# CHARACTERIZATION AND SIMULATION OF DISCRETE FRACTURE NETWORKS IN UNCONVENTIONAL SHALE RESERVOIRS

A Dissertation

by

JIANLEI SUN

Submitted to the Office of Graduate and Professional Studies of
Texas A&M University
in partial fulfillment of the requirements for the degree of

DOCTOR OF PHILOSOPHY

| | |
|---|---|
| Chair of Committee, | David Schechter |
| Committee Members, | Wolfgang Bangerth |
| | John Killough |
| | Michael King |
| Head of Department, | A. Daniel Hill |

August 2016

Major Subject: Petroleum Engineering

# ABSTRACT

Fracture characterization and simulation of complex fracture networks are investigated with the emphasis on better and faster approaches to generate fractures by conforming to available data resources, and on accurate, robust, and efficient techniques to grid and discretize complex fracture networks.

Three fracture characterization techniques such as fractal-based, microseismic-constrained, and outcrop-based are presented. Natural fractures are generated either stochastically from fractal-based theory, or constrained by microseismic information, or from outcrop maps. Hydraulic fractures are computed from a fast proxy model for fracture propagation that incooperates material balance and lab-measured conductivity data. Then, optimization-based unstructured gridding and discretization technique is developed to handle complex fracture networks with extensively fracture clustering, nonorthogonal and low-angle fracture intersections, and nonuniform fracture aperture distributions. Moreover, through fracture simulation, sensitivity analysis of natural fracture related parameters, nonuniform fracture aperture, and unstructured gridding related parameters on well production performance are investigated, which are followed by well testing behaviors and $CO_2$ EOR of complex fracture networks.

This work presents an integrated workflow to model discrete fractures in unconventional shale reservoirs, together with detailed illustrations of each critical component using both synthetic and field application examples.

DEDICATION

*To my wife, Shuhua Lin,*

*for being with me and sharing happiness and joy.*

*To my parents and relatives,*

*for their unconditional love and support.*

*To my colleagues and friends,*

*for their discussions and insights through my study.*

ACKNOWLEDGEMENTS

I would like to thank my committee chair, Dr. David Schechter, and my committee members, Dr. John Killough, Dr. Michael King, and Dr. Wolfgang Bangerth, for their guidance and support throughout the course of this research.

Thanks also go to my friends and colleagues and the department faculty and staff for making my time at Texas A&M University a great experience. I also want to extend my gratitude to the Crisman Institute for Petroleum Research, which provided financial support and warm discussions from the petroleum industry.

Finally, thanks to my parents for their encouragement and to my wife for her patience and love.

# NOMENCLATURE

| | |
|---|---|
| BHP | Bottom-Hole Flowing Pressure |
| DFN | Discrete Fracture Network |
| DT | Delaunay Triangulation |
| EOR | Enhanced Oil Recovery |
| EDFM | Embedded Discrete Fracture Modeling |
| FVM | Finite Volume Method |
| FDFN | Fractal Discrete Fracture Network |
| IFD | Integral Finite Difference Method |
| NNC | Non Neighbor Connections |
| PEBI | Perpendicular Bisector |
| SRV | Stimulated Reservoir Volume |
| TPFA | Two-Point Flux Approximation |
| PDF | Probability Density Function |
| CDF | Cumulative Distribution Function |
| DP | Pressure Difference |
| DPDT | Pressure Derivative |

TABLE OF CONTENTS

Page

LIST OF FIGURES

Page

LIST OF TABLES

Page

# CHAPTER I

# INTRODUCTION AND LITERATURE REVIEW

Unconventional liquid and gas resource plays require extensive hydraulic fracturing treatments in order to produce at commercially viable rates. Before, during and after hydraulic fracturing, the evolving technology of microseismic combined with outcrop, core and image log analysis coupled with production logging technology provides the basis for development of discrete fracture networks (DFNs). Combination of these measurements can be used to develop multiple realizations of the complex geometry of both hydraulic and natural fractures. Therefore, it is extremely important to analyze and characterize accurately the geometry and properties of discrete fractures networks (Dershowitz et al. 2004).

In the context of hydraulic fracturing in naturally fractured reservoirs, the heterogeneous nature of fracture patterns renders it almost impossible to apply deterministic approaches to extract realistic DFNs. Part of the reason is from non-planar fracture propagation around the well-bore due to complex interactions between the hydraulic fractures and natural fractures. Abass et al. (1996) did experimental work to investigate the complex nonplanar fracture geometries related to a hydraulically fractured horizontal well. Numerical geomechanics modeling was also performed by other researchers (Olson and Wu 2012, Warpinski and Branagan 1989, Xue and Ghassemi 2009), demonstrating the vital effect of wellbore orientation and stress shadow near hydraulic fractures on the fracture propagation path as well as induced complex

fracture network geometries. Microseismic monitoring data is also widely used by researchers (Mirzaei and Cipolla 2012, Warpinski et al. 2013) to analyze both stimulated reservoir volume (SRV), and post-fracturing fracture properties such as fracture strike and fracture failure mode. However, an important factor in determining fracture complexity arises from the uncertainty of the interaction of hydraulic fractures with the stochastic distribution of natural fractures.

Numerous stochastic approaches (Priest 1993, Tamagawa et al. 2002) have been proposed to characterize naturally fractured reservoirs (NFRs) in terms of complex DFNs. Most of the fracture models assume unrealistically smooth fracture surfaces or parallel plate fractures, from which fracture properties such as permeability could be easily estimated. Such idealized models need further improvements to honor available geologic and well logging data. We also observe that there is a lack of discussion regarding aperture distribution in the literature. One has to inquire whether large aperture, long fractures dominate performance compared to short, small aperture micro-fractures. It is a logical progression to generate more realistic fracture networks with non-uniform aperture distributions to investigate the effect on reservoir performance. To that end, Muralidharan, Chakravarthy, et al. (2004) and Kim et al. (2007) investigated aperture distributions in fractured cores and showed that fracture aperture follows lognormal distribution at all stress conditions using X-ray CT scanning to image the fracture surfaces at variable overburden pressure. Later, Kim and Schechter (2009) introduced fractal theory to generate multiple realizations of 2D and 3D fracture

networks, and to construct fracture networks with lognormal aperture distributions as well as fractal-based aperture distributions.

Once a discrete fracture network with log-normally distributed aperture size is constructed from fracture characterization, the next step is to perform flow simulation as well as performance analysis. It is very important to evaluate post-fracturing production performance of the complex fracture networks in order to facilitate hydraulic fracturing treatment design. In the following, we will discuss about available numerical approaches for modeling complex fracture networks.

The first approach to simulate well production performance is to use continuum approaches such as the dual porosity (DP), dual permeability (DPDK) or multiple porosity (MP) models. Warren and Root (1963) introduced the dual-porosity or sugar-cube models for single-phase systems to the petroleum industry, where interconnected fractures contribute to the fluid flow, and matrix provides only storage to fractures. Later, DP was extended to DPDK by Rossen (1977) and Kazemi et al. (1976), and single-phase flow was generalized to multiphase flow by Dean and Lo (1988). Both DP and DPDK have been implemented in most commercial reservoir simulators. Yu et al. (2014) and Wan and Sheng (2015) extensively studied the capabilities of DP/DPDK in commercial tools for simulating fractured reservoirs. Furthermore, in order to capture both transient and gravity segregation effects on individual matrix blocks, more variations of dual continuum approaches were developed, such as MINC (Wu and Pruess 1988) and SUBDOMAIN (Beckner et al. 1991). Each matrix gridblock is divided into nested rings for MINC, into layers for SUBMODAIN, and thus matrix-to-matrix

transient effect can be resolved. Recently, multiple porosity systems (Yan et al. 2013) were used to better model fluid flow mechanisms in different pore types such as kerogen, inorganic minerals, and natural fractures. However, such approaches are based on assumptions that fractures are very well connected and uniformly distributed. It cannot resolve the scenario where there exist large-scale fractures and high-localized anisotropies dominating fluid flow paths.

In order to overcome the above disadvantages of DP and DPDK models, a collection of meshfree or non-conformal approaches were developed, such as embedded discrete fracture model (EDFM), extended finite element method (XFEM), and multi-segment wells (MSW). These approaches incooperate fracture information implicitly into background grid systems, and thus avoid meshing and remeshing of complex fracture networks. For example, EDFM (Li and Lee 2008, Moinfar et al. 2013) computes transmissibilities for both matrix-to-fracture and fracture-to-fracture fluid flows, and then the computed transmissibility values are imported to reservoir simulators as additional non-neighbor connections. Similarly, Du et al. (2015) applied the concept of MSW to implicitly model hydraulic fractures, and he demonstrated MSW's advantages on fracture geometry description, infill drilling and refracturing. Furthermore, XFEM as a new technique was first developed by Belytschko et al. (2000) for geomechanics and fracture mechanics in the context of modeling crack propagation. Later, XFEM was used by Sheng et al. (2012) for modeling multi-scale flow in fracture shale gas reservoirs.

The third approach – discrete fracture model (DFM) is to represent fracture geometry explicitly. Fracture gridblocks are differentiated from matrix gridblocks by assigning different petrophysical properties. For DFM, the critical step is to generate unstructured meshes for complex fracture networks. In essential, the discretization problem is converted to a meshing problem. In order to conform accurately to fracture geometries, unstructured PEBI (perpendicular bisector) or Voronoi grid was introduced to the petroleum industry by Heinemann et al. (1991). Such a grid system is flexible, locally conforming to the fracture networks, but also capable to reduce grid orientation effect. In **Fig. 1**, blue points represent cell centers. Red triangles comprise a triangular mesh, which is constructed by connecting all the cell centers. Black polygons form a polygon mesh or 2D PEBI mesh, which is constructed by making perpendicular bisectors of the triangular mesh. Therefore, the 2D PEBI mesh is considered as the dual mesh of the 2D triangular mesh. Besides, the shape of the 2D PEBI is very flexible, and thus PEBI grids are widely used to model complex fracture networks. In order to model geological layers, the 2D PEBI grid is projected and extruded to each geological layer to yield a 2.5D PEBI grid. Furthermore, not only the fracture geometry but also the fracture aperture requires to be accurately modeled. Muralidharan, Schechter, et al. (2004) demonstrated the importance of non-uniform fracture aperture through CT-scanning fracture aperture changes under different stress conditions. On one hand, Karimi-Fard et al. (2003) introduced a lower-dimensional approach to represent each fracture gridblock with a 2D line segment with “zero” aperture. Such approach has been widely used by many researchers (Branets et al. 2008, Fung et al. 2014, Jiang and Younis 2015, KURC

2015, Moog 2013, Romain et al. 2011, Verma and Aziz 1997, Vestergaard et al. 2008). On the other hand, fracture aperture can be explicitly represented and gridded (Cipolla et al. 2011, Olorode et al. 2012, Sun and Schechter 2015a,b, Sun et al. 2016, Wang and Shahvali 2016). One advantage of the explicit approach is to model and visualize non-uniform aperture very straightforward.

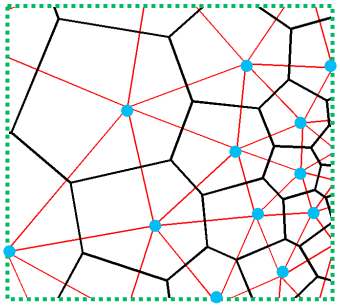

**Fig. 1 – Unstructured PEBI grid and Delaunay Triangulation.**

However, there is not much discussion about the effect of characteristics of natural fractures on production performance of hydraulic fractured wells when unstructured grids are used for reservoir simulation. Besides, as the geometry of discrete fracture networks becomes more complex, unstructured mesh generation tends to be more difficult to deal with, especially with increasing demand of local grid refinement around fractures, non-orthogonal intersection gridding, and incorporation of non-uniform aperture distributions. To our knowledge, no one has tried to simulate realistic fracture networks by explicitly gridding natural fractures and applying actual aperture models using unstructured grids. Therefore, we will first revisit how to generate realistic DFNs based on fractal theory. Different characterization parameters will be incorporated

into the mathematic model such as fracture fractal density, fracture fractal length distribution, fracture fractal center distribution, fracture strike, and non-uniform fracture aperture distribution. The following gridding and discretization sections with unstructured grids will be devoted to detailed algorithms and code implementation, which lead to discussing the advantages of the proposed method. Sensitivity analysis and visualization of fluid flow regimes as well as discussion of the effect of natural fracture parameters (aperture, spacing, length and strike) on well performance will be investigated as well.

Besides, for all the numerical approaches, it is important to present sensitivity analysis of input parameters especially fracture characterization properties on well production performance. However, besides of the properties of natural fractures, unstructured mesh itself might introduce uncertainties or inaccuracies on simulation results. For example, unstructured mesh density, background grid type, refinement method around fractures might have either significant or slight effects on production performance, which are required to be investigated. Moreover, reservoir engineers might be more interested in how much the difference is between the conventional grid solutions such as Tartan grid or LGR girds, and unstructured PEBI grid for both synthetic and real reservoir models, and in whether or not the unstructured PEBI grid can accurately reproduce the results of the conventional grid solutions. Most importantly, in terms of the advantages of using unstructured PEBI grids, not only do we need to present its flexibility, but also carry out a detailed CPU performance analysis to investigate if flexibility will yield better CPU performance, or we have to compromise CPU

performance by using more flexible unstructured grids. To these ends, a new gridding and discretization workflow with unstructured grids will be proposed for characterization and simulation of unconventional shale reservoirs. Then we will study whether or not the unstructured grids are accurate enough to reproduce conventional grid solutions by comparing to the tartar grid, whether or not robust enough to model a real field problem by comparing to the LGR grid, whether or not flexible enough to vary meshing-related parameters on a field problem, and finally whether or not efficient enough to improve CPU performance.

Moreover, Kuchuk and Biryukov (2015) presented a good summary of pressure-transient behaviors of fractured reservoirs for vertical wells. Not too much discussion is given to well testing behaviors of complex fracture networks stimulated with multistage hydraulically fractured wells. For the proposed simple well testing models in commercial software, there is lack of public benchmarking with numerical solutions of complex fracture networks. It would be beneficial if we could provide a rigorous comparison between numerical solutions of complex fracture networks and matched well testing models.

Furthermore, one goal of this work is to investigate the potential of $CO_2$ EOR (Enhanced Oil Recovery) in unconventional liquid reservoirs (ULRs). Multi-stage hydraulic fractured horizontal wells have enabled commercial oil and gas production from unconventional shale reservoirs. One of the characteristics of such reservoirs is very low recovery factor and high production declining rate, and enhanced oil recovery techniques are thus necessary. In addition, previous lab and numerical results have

already shown $CO_2$ EOR might be an option for unconventional liquid reservoirs. However, the intersections of induced hydraulic fractures with in-situ stochastically distributed natural fractures usually yield complex discrete fracture networks, which require unstructured gridding techniques to better discretize the reservoir domain and more accurately simulate well production performance. Therefore, it is very important to investigate the potential of $CO_2$ EOR for unconventional liquid reservoirs in complex fracture networks. A single well for $CO_2$ huff-n-puff will be investigated where we have a horizontal well and 40 orthogonal hydraulic fractures. A comparison of $CO_2$ huff-n-puff between structured grids and unstructured grids for this case is provided to validate the proposed workflow. Then $CO_2$ huff-n-puff in three complex fracture networks are investigated, and compared with the dual porosity approach. Complex fracture networks are generated from a fractal-based stochastic approach. We will demonstrate how to apply $CO_2$ EOR in complex fracture networks using unstructured grids. Implementation algorithms as well as application considerations will be included. Preliminary simulation results provide fundamental understanding of the key parameters on $CO_2$ EOR for unconventional liquid reservoirs.

In summary, throughout this work, we will try to resolve the following questions:

1) What would be the general seismic-to-simulation workflow for modeling unconventional shale reservoirs? What are the main components and challenges in this workflow that we should pay special attention to?

2) How do we grid up complex fracture networks with extensively fracture clustering, non-uniform fracture aperture, and low-angle fracture intersections? How do we improve the existing meshing algorithms for fracture networks?

3) How do we incooperate non-uniform fracture aperture into fracture simulation? Is there any significant difference in production performance between nonuniform and uniform fracture apertures?

4) How much is the impact of both natural fracture parameters and unstructured gridding parameters on production performance? How do we perform detailed sensitivity analysis on those parameters?

5) How do we evaluate well testing behaviors of complex fracture networks? How do we simulate $CO_2$ EOR in unconventional liquid reservoirs in complex fracture networks?

# CHAPTER II

# WORKFLOW FOR CHARACTERIZATION AND SIMULATION OF DISCRETE FRACTURE NETWORKS

## *2.1 Seismic-to-Simulation workflow*

In the context of developing unconventional shale reservoirs, it is crucial to have a reasonable description of in-situ natural fracture distributions, an accurate estimation of intersections between natural and hydraulic fractures, and finally a robust gridding and discretization technique to simulate and predict well production performance.

As mentioned in the previous Introduction, literature documentation only shows several components of the whole workflow, or abstract workflow concept without practical field examples.

### 2.1.1 Previous Workflows

Cipolla et al. (2011) introduced the seismic-to-simulation workflow by implementing three new important components such as Hydraulic Fracture Models, Automatic Grid Generation, and Completion Advisor. The key focus of the workflow is related to geomechanics and well completion design. Microseismic mapping is only used as a validation tool for the shape of discrete fracture networks. In addition, in terms of natural fracture distributions, stochastic fracture networks are used to demonstrate how to be coupled with the geomechanics fracture propagation module. However, not too

much attention is paid to characterization of natural fracture networks. On the other hand, KURC (2015) investigated discrete fracture networks from the standpoint of well testing and single-well application. Only gridding and reservoir simulation modules are extensively studied, leaving open areas in fracture characterization and fracture geomechanics. The rest published workflows only highlight several components at a time, especially the component of fracture propagation with completely or partially ignoring the geology and geophysics associated with naturally fractured reservoirs.

### 2.1.2 Proposed Workflow

The proposed workflow in **Fig. 2** consists of five main components - fracture and reservoir characterization, preprocessor, reservoir simulator, postprocessor, and sensitivity analysis and history matching. After characterization, the preprocessor takes reservoir properties, fracture properties, and user-defined meshing parameters and generates input files for finite-volume based simulators. The postprocessor prepares appropriate format and visualizes simulation output. Sensitivity analysis yields numerous realizations of discrete fracture networks to investigate the effect of wide-range parameters on reservoir production performance. Among those realizations, the best realization can be selected by history matching against production data, and then used for future prediction forecast.

The proposed workflow focuses not only on gridding and discretization, but also the geological and geophysical aspects – natural fracture characterization. Less focus is made on fracture geomechanics, or in other words, fracture propagation models. Instead,

we will apply a simple proxy model based on geological concepts to approximate hydraulic fracture geometries.

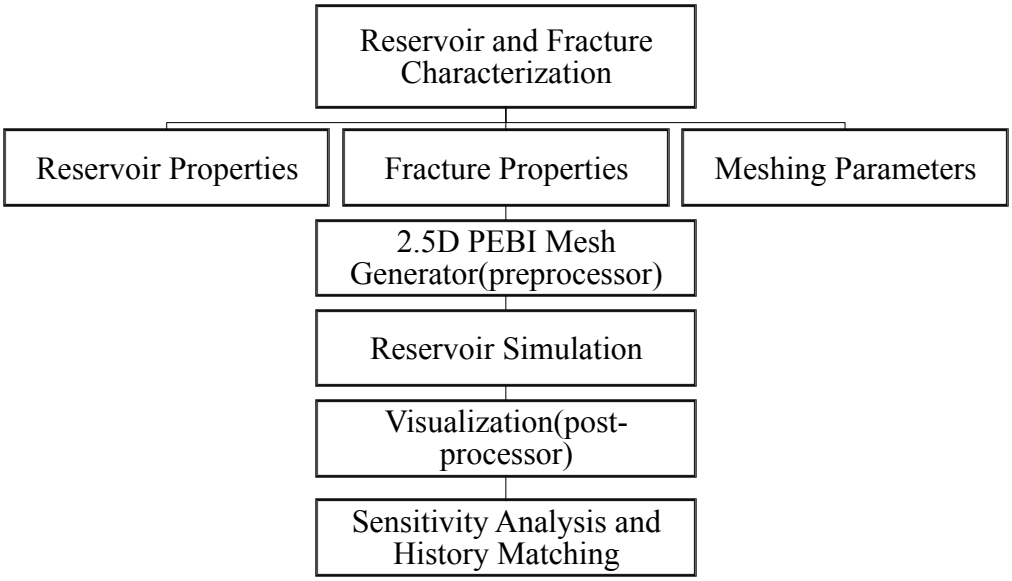


**Fig. 2 – Workflow chart of the proposed fracture characterization and simulation approach.**

### *2.2 Fracture Characterization*

As seen in **Fig. 2**, the starting point is the fracture and reservoir characterization, among which the challenge part based on our previous knowledge is to incorporate given outcrop, log, and core data, seismic data to come up with a reasonable fracture description.

First, stochastic algorithms have been applied to generate fracture networks. However, fractal based stochastic algorithms haven't drawn enough attention, even though field observation has proven natural fractures mostly follow fractal patterns (Kim and Schechter 2009). Second, microseismic monitoring outputs after hydraulic fracturing if properly being interpreted can be used to constrain the shape of discrete fracture networks, whereas researchers tend to consider them only as a validation tool. For example, the location of microseismic events was used to define the stimulated reservoir volume (SRV), in which dual continuum models could be assigned with enhanced reservoir properties such as larger fracture permeability. On the other hand, microseismic-inversion techniques could be employed to obtain discrete fracture network, which was then followed by upscaling techniques to yield enhanced reservoir properties for dual continuum models. Either way had to resort to dual continuum models, and thus might introduce inaccuracies for reservoir simulations. In this study, we propose to generate stochastic discrete fracture networks constrained by stochastic algorithms and/or microseismic modeling information. And then direct reservoir

simulation will be then performed on the discrete fracture networks without applying ambiguous fracture upscaling techniques.

### *2.3 Fracture Simulation*

As discussed in the Introduction, fracture simulation approaches for fractured reservoirs are summarized into three main categories. Neither do we want to perform upscaling on discrete fracture networks, nor to implement techniques such as embedded discrete fracture network (EDFM) or multi-segment wells (MSW), which still require a certain degree of approximation. We decide to choose the unstructured gridding approach. Note that unstructured gridding approach might not yield the most efficient outcome, when compare to EDFM. However, it should be the most accurate, since each fracture will be modeled individually and accurately in terms of both geometry and properties. The trade-off is to develop a better fracture gridding and discretization algorithms, which are not straightforward even though we have been using unstructured grids since 1960s. The main challenge is to honor extensive non-orthogonal fracture intersections, with low intersection angle and non-uniform fracture apertures. Fracture refinement is critical in order to capture transient behaviors between fracture and matrix gridblocks, because unconventional shale reservoirs present extremely low permeability, and flow regime throughout the whole well life belongs to the linear flow.

### *2.4 Uncertainty Analysis*

So far, the most important while frequently missed component is the uncertainty analysis. First, natural fracture characterization involves a whole range of parameters such as fracture density, fracture length distribution, and fracture orientation. If outcrop and/or core data is not available, slight variation in these parameters might result in completely different production performance. Second, lognormal fracture aperture distribution has been proven by previous work (Muralidharan, Schechter, et al. 2004) to be stress-dependent. Most researchers have assumed uniform fracture aperture distribution. In order to incorporate non-uniform proppant displacement and thus non-uniform fracture conductivity distribution, large constant fracture aperture is used together with corresponding non-uniform fracture permeability based on the assumption that same fracture conductivity will yield the same fracture production performance. This assumption is true for a single fracture with uniform fracture properties. However, no publication has been done to validate whether or not the same fracture conductivity will still yield the same production performance for non-uniform fracture apertures. Third, when it comes to gridding and discretization, not too much sensitivity analysis has been carried out for grid density and type especially for field-scale applications. This is extremely important if we want to apply unstructured gridding algorithms to model discrete fracture networks. Too much grid resolution might improve simulation results, but inevitably cause more time assumption. A guideline is necessary regarding how to select an optimized unstructured grid for modeling discrete fracture networks, ensuring

good CPU performance in the meantime without compromising too much accuracy of the results.

# CHAPTER III

# GRIDDING AND DISCRETIZATION OF DISCRETE FRACTURE NETWORKS

## *3.1 Previous Fracture Gridding and Discretization Approaches*

As mentioned in the Introduction, there are three categories of approaches to model discrete fracture networks. Dual Continuum approach considers uniform distributed fracture networks, without explicit modeling each individual fractures, which might introduce inaccuracies if there are a few large fractures dominate the flow paths. Embedded discrete fracture modeling is essentially a dual continuum approach with additional Non Neighbor Connections (NNCs) to model fluid flux between matrix gridblocks and several individual fractures. Similarly, Multi-segment well approach resorts to NNCs to consider fluid flow between fractures and matrix.

On the other hand, unstructured gridding approach is to honor individual fractures as accurate as possible. As a result, special gridding techniques have to been designed to handle complex fracture networks with low-angle intersections, extensively fracture clustering, non-uniform fracture aperture, and so on.

### *3.2 Proposed Fracture Gridding Approach*

The main idea of the proposed approach is to apply unstructured grids only to necessary locations, for instance, around the fractures or faults. Because there exist complex fracture geometries or special topology structure, for which flexible shapes of the unstructured grids come into playing a key role. For other locations such as reservoir background, we might want to use structured grids since we have been using them for many years. It might be much easier for us to populate geostatistic properties in structured grids than in unstructured grids. With that being said, we propose the following optimization – based unstructured gridding algorithms. When it comes to gridding complex fracture networks, two general approaches were taken in the literatures:

- The fracture geometry is conformed exactly by using straight lines segments, or only approximated by edges of unstructured grids, which in most cases will result in a zigzag shape of fractures, which significantly change fracture geometry and connectivity.
- The fracture aperture is explicitly modeled with simulation gridblocks, or is assumed a zero aperture value in the geometric domain with simplified approaches to compute transmissibilities in the computational domain. For the case with non - zero aperture, each fracture gridblock is defined by a 2D polygon, whereas for the case with zero aperture by a line segment.

### 3.2.1 Fixed-Points Computation

This work chooses to honor both fracture geometry and nonuniform fracture aperture distributions as accurate as possible, since we intend to perform a detailed sensitivity analysis of the effect of stress-dependent fracture aperture on production performance. To this end, we have to design an approach to place fix Voronoi cell or PEBI cell centers.

#### *3.2.1.1 Compute Intersections of the Connected Fracture Network*

Once a discrete fracture network is obtained, mesh generation starts with determination of fracture intersection points in 2D geometry. Almost all the gridding algorithms involving complex fracture geometries need to determine intersection points either explicitly or implicitly. First of all, intersection information helps the mesh generation algorithms to better conform to the input of complex fracture geometry and therefore will ensure good mesh quality. Second, for the approaches where no fracture gridblocks are explicitly defined, the intersection points are still needed to compute the inter-cell transmissibilities; for the approaches where fractures are not described exactly as straight line segments, the intersection points are considered as background information to guide the mesh generation algorithms. In this study, not only do we compute intersection points, but also define the intersections into five types, which offer us additional freedom to manipulate fracture connectivity through intersections. The following is a list of possible intersections where N stands for natural fractures, H for hydraulic fractures, and W for the horizontal well:

- NN – natural fractures with natural fractures
- NH – natural fractures with hydraulic fractures
- NW – natural fractures with the horizontal well
- HH – hydraulic fractures with hydraulic fractures
- HW – hydraulic fractures with horizontal wells

For simplicity in this study, we choose to assign higher permeability values to intersections. For instance, for NH type of intersection, permeability of the hydraulic fracture will be assigned to the intersection, similarly for NW and HW where well block permeability (a relatively higher value) will be used for intersection gridblocks.

*3.2.1.2 Compute Locations of the Fixed Voronoi Cell Centers around Fracture Intersections and Fracture Tips*

In order to model non-uniform fracture aperture distribution, protection area (pairs of nodes around each fracture) has to be used. In the previous study, Syihab et al. (2014) tried to generate Voronoi cells conforming to fracture line segments without explicitly modeling fracture thickness, and then applied volume correction for each fracture gridblocks. Such approach inevitably involved significant manual intervention, and inaccuracies in both volume and transmissibility calculation, especially when the number of fractures increases. In this study, instead of modifying connection-list information after mesh generation, we pre-placed fixed Voronoi cell centers to yield given aperture distributions as seen in **Fig. 3 (a)**, where the x axis is the length along each natural fracture, and the y axis is the fracture aperture values; and **Fig. 3 (b)**,

showing two natural fractures with non-uniform apertures intersecting at the same location.

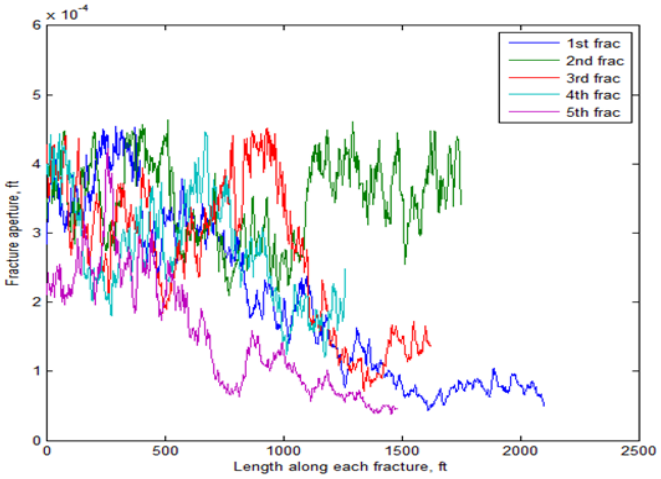


**(a)**

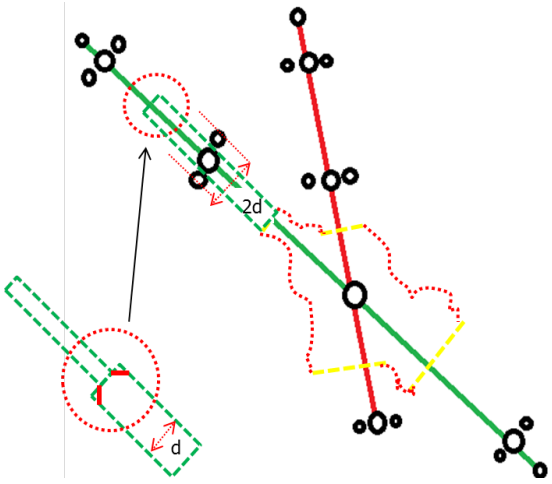


**(b)**

**Fig. 3 – Input non-uniform aperture distributions for fractures (a); Assign the non-uniform fracture aperture distribution to corresponding fracture segments along each fractures (b).**

The following procedure is implemented to model the non-uniform aperture distributions:

- First of all, each single fracture is divided into fracture segments at intersections, and fixed Voronoi nodes are placed at fracture intersections and fracture tips;
- Then, we loop over all fracture segments of each single fracture, and further divided each fracture segment into fracture sub segments based on user-defined interval size or minimum grid size;
- For each fracture sub segment, we retrieve the corresponding aperture distribution from fracture characterization data, and compute a mean value as the averaged aperture value "d", which will be used to guide placement of a pair of fracture nodes in the distance of "2d". At each fracture gridblock location, there will be three fixed Voronoi cell nodes, one for the fracture gridblock and the other two for matrix gridblock. If more refinement around fractures is required by the users, more than one pair of fixed points will be placed. In addition, if fracture aperture is input as lognormal distribution parameters such as standard deviation and mean values, at each fracture sub segment, a sampled value from the lognormal distribution will be used instead of taking an average from the pre-computed fracture aperture distributions. In this study, we will present both approaches for assign non-uniform fracture apertures to discrete fracture networks.
- Repeat the previous step to place fixed Voronoi cell centers for all fracture segments; hydraulic fractures should be treated in the same manner with a

different user-defined interval size. If we want to model horizontal wellbore effect, the same approach will be applied to the horizontal well, for which a wellbore diameter will replace fracture aperture. Otherwise, horizontal well trajectory will only be used for defining wellbore perforations, and the proposed gridding approach won't honor the horizontal well trajectory.

- Such approach will honor fracture aperture distributions as accurate as possible, except that there might exist two "shoulder edges" around the interface between two fracture gridblocks as seen in **Fig. 3 (b)** because of the aperture change.

### 3.2.2 Flexible-Points Optimization

*3.2.2.1 Define Refinement around each Fracture with Initial Flexible Points*

Complex fracture networks are too complicated to place fixed points for the entire reservoir domain as we did for honoring fracture aperture distribution. If all horizontal wells were stimulated with orthogonal hydraulic fractures, it would be much easier to compute exact locations of Voronoi cell centers and implement LGR features for capturing pressure transient behavior. However, in reality, the non-planar and non-orthogonal features of the post-stimulation fracture network with lower-angle fracture intersections prevent us from developing a simple fixed-point scheme. Instead, optimization of the Voronoi cell locations is necessary to yield not only the LGR features around fractures but also good mesh quality. In this study, we simply generate denser Voronoi point clouds around fractures, and sparser Voronoi point clouds away from the fractures. This way, the optimization algorithms will take the initial points, and

rearrange them to generate good mesh quality with LGR features around fractures. In order to speed up the convergence of the optimization algorithm, the rejection method is applied to obtain an initial point distribution.

*3.2.2.2 Optimize Location of the Initial Flexible Points*

Mesh generation and optimization belongs to the subject of Computational Geometry. Schneiders (2014) summarized most of the available programs in both the public domain and commercial mesh generators. In this study, we applied the force-based algorithm proposed by Persson and Strang (2004) to optimize locations of the flexible points to yield better refinement features around complex fracture networks. The force-based optimization algorithms assume a mechanical analogy between a triangular mesh and a truss structure. Given a set of initial Voronoi cell centers of both fixed and flexible points in the reservoir domain, Delaunay Triangulation algorithms can be applied to determine the topology of the triangular mesh. Edges of the triangles are considered as bars of the truss structure, while vertices of the triangles as joints. The force displacement of each bar is calculated based on the length difference between the current bar and its desirable size. The desirable edge length or Voronoi cell size increases away from mesh objects such as natural fractures, hydraulic fractures, and/or horizontal wells following pre-defined distance functions. At any given location in the reservoir domain, we can first compute distances from all the mesh objects, and then determine a desirable grid size from pre-defined distance-size relationships. Once all the force displacements of the bars are determined, at each joint, corresponding bar forces will be assembled together to yield a displacement direction and distance for this joint.

In order to solve the above analogical problem numerically, a system of ODEs is introduced to convert the optimization problem to a time-dependent problem with the locations of all the Voronoi cell centers evolving with time.

$$\frac{d\vec{p}}{dt} = \vec{F}(\vec{P}), t \geq 0 \quad or \quad \vec{p}_{n+1} = \vec{p}_n + \Delta t\, \vec{F}(\vec{p}_n),\ t_n = n\Delta t \geq 0 \quad \text{(Eq. 1)}$$

The point location $\vec{P} = [\vec{x}, \vec{y}]$ is an N-by-2 vector array containing the locations of all the Voronoi cell centers. The force displacement $\vec{F}$ is an N-by-2 vector array, which contains the displacement vectors at all the locations. The Forward Euler method can be applied to approximate the differential equation into a discretized form as seen above, in which new locations $\vec{p}_{n+1}$ of the Voronoi centers are computed with locations $\vec{p}_n$ at the previous time step. In terms of the calculation of $\vec{F}(\vec{p}_n)$, once the triangular mesh topology is constructed by the Delaunay Triangulation algorithms, a scalar force displacement array $f(l_0, l)$ of all triangle edges is computed by assuming a simple model of ordinary liner springs.

$$f(l_0, l) = \begin{cases} k(l_0 - l) & if\ l < l_0 \\ 0 & if\ l \geq l_0 \end{cases} \quad \text{(Eq. 2)}$$

In which,

$l$, current length array of all the triangle edges;

$l_0$, desirable length array which are computed at the interesting locations such as middle points of all the current triangular edges;

K, a constant unit conversion factor.

Note that $f(l_0, l)$ is defined to always be positive so that corresponding repulsive forces help the initial Voronoi cell centers spread out across the whole reservoir domain. The scalar force displacement array $f(l_0, l)$ is used to assemble the force displacement vector array $\vec{F}(\vec{p}_n)$ at all Voronoi cell centers.

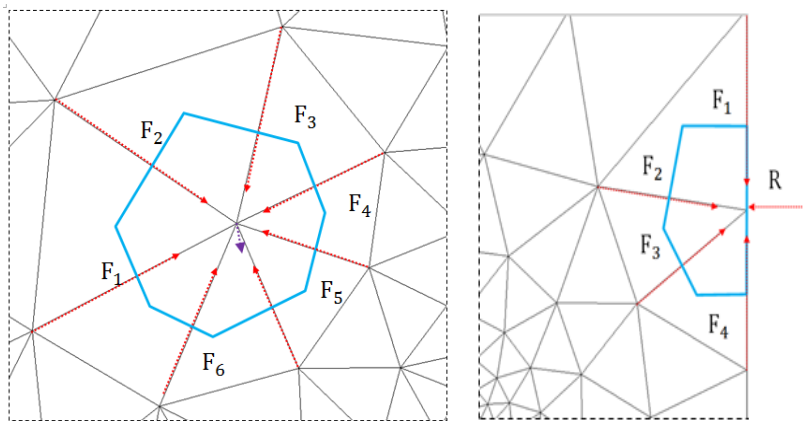


**Fig. 4 – Internal force calculation around a Voronoi cell center (a) and treatment of an out-of-boundary Voronoi center (b); Blue polygon highlights a Voronoi cell, black lines indicate edges of Delaunay triangles, and red arrows stand for bar forces exerted on triangle edges, purple arrow shows displacement direction toward the new Voronoi cell center.**

For example, six Delaunay triangles as seen in **Fig. 4 (a)** are connected at the same Voronoi cell center, toward which all the displacement vectors add up to a final displacement vector as indicated by the purple arrow. With this displacement vector, the Voronoi cell center moves to the lower right corner of this cell, resulting in a non-

uniform Voronoi cell with smaller edges on the lower right corner and large edges on the upper-left corner. If a uniform mesh size function h (x, y) were used for the reservoir domain, the results would be uniform Voronoi cells with all edges almost the same length. **Fig. 4(b)** shows how the out-of-boundary points are treated with an imaginary force vector array $\vec{R}(\vec{p}_n)$. Once any Voronoi cell center goes out of the boundary, an imaginary force is applied orthogonal to the boundary, and then displacement direction and distance are computed to bring the out-of-boundary point back onto the boundary. Finally, once the new point location vector $\vec{p}_{n+1}$ is computed, the triangular topology will be reconstructed to compute $\vec{p}_{n+2}$. This loop continues until reaching the given stopping criteria and the final point locations $\vec{p}_{n+1}$, which will be used for Voronoi tessellation and output to specific mesh formats.

Once the locations of all the flexible points are determined from the optimization loop, Voronoi grids can be computed, which is followed by clipping faces of the Voronoi grids at the model boundary, and by removing duplicate vertices of each Voronoi cell. In the geometric domain, each unstructured cell is stored in terms of number of vertices and an index array storing the entire vertex IDs of the cell.

*3.3 Proposed Fracture Discretization Approach*

### 3.3.1 Finite Volume Fracture Discretization Approach

The fracture discretization approach implemented in this study is the Integral Finite Difference Method (IFD) or Finite Volume Method (FVM). This approach combines the traditional finite difference method with flexible geometry of the unstructured grids. As seen in the following, after discretization, the continuum equation is very similar as that of finite difference method. In addition, a connection - list related information will be used to represent underlying grid geometry. There is no difference in terms of discretization between fracture and matrix gridblocks except that being assigned with different properties.

*3.3.1.1 Derivation of Governing Equations*

Following Pruess et al. (1999), mass balance considerations in every gridblock into which the simulation domain is subdivided by the Finite Volume Method dictates that

$$\frac{d}{dt}\int_{V_n} M^k dV = \int_{\Gamma_n} F^k \cdot n \, d\check{A} + \int_{V_n} q^k dV \quad \text{..... (Eq. 3)}$$

In which,

$V, V_n$, volume of subdomain n, in $ft^3$;

$M^k$, mass accumulation term of component k, in lbm;

$\Gamma_n, A$, surface area of subdomain n, in $ft^2$;

$F^k$ , Darcy flux vector of component k, in lbm/day;

$n$ , inward unit normal vector;

$q^k$ , source or sink term of component k, in lbm/day;

$t$ , time, in days.

The mass accumulation terms can be expanded as follows:

$M^k = \sum_{\beta \equiv A,G,O} \emptyset S_\beta \rho_\beta X_\beta^o,\ k \equiv w, g, o$ ……..……. (Eq. *4*)

In which,

$\varphi$, porosity;

$\rho_\beta$, density of phase β, $\frac{\text{lbm}}{\text{ft}^3}$;

$S_\beta$, saturation of phase β;

$X_\beta^k$, mass fraction of component $k \equiv w, g, o$ in phase β;

A, G, O, Aqueous, Gaseous, and Organic phases;

w, g, o, water, gas, oil components, and so on.

The flux terms can be derived as follows:

$F^k = \sum_{\beta \equiv A,G,O} F_\beta^k , k \equiv w, g, o$ ……..…..……. (Eq. 5)

The source or sink terms can be written as follows:

$q^k = \sum_{\beta \equiv A,G,O} X_\beta^k q_\beta \, , k \equiv w, g, o$ ……..……. (Eq. 6)

In which,

$q_\beta$, production rate of the phase β, in lbm/day.

*3.3.1.2 Discretization of the Governing Equations*

The fracture discretization approach implemented in this study is the Integral Finite Difference Method (IFD) or Finite Volume Method (FVM). This approach combines the traditional finite difference method with flexible geometry of the unstructured grids. In addition, this approach applies Two-Point Flux Approximation (TPFA) to approximation transmissibilities between two cells. As seen in the following, after discretization, the continuum equation is very similar as that of finite difference method. In addition, a connection - list related information will be used to represent underlying grid geometry.

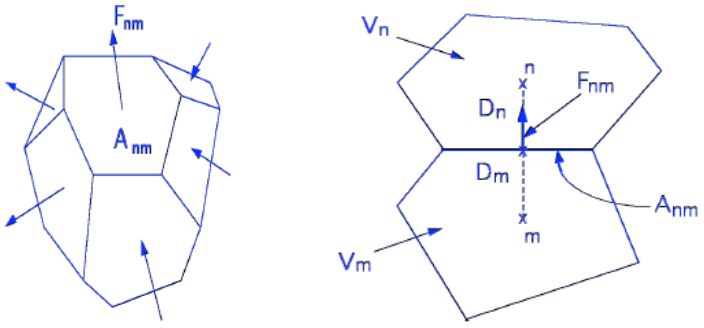


**Fig. 5 – Space discretization in finite volume method (a); and the flux computation between two cells using two-point flux approximation (b).**

First, the governing equation in **Eq. 2** is discretized in spacing using the finite volume method. With appropriate volume averages, we get

$\int_{V_n} M dV = V_n M_n$ ..... (Eq. 7)

In which,

$M$ is a volume-normalized quality, and $M_n$ is the average volume of $M$ over $V_n$.

Then, we approximate surface integrals with a discrete sum of averages over surface segments $A_{nm}$ as seen in **Fig. 5**.

$\int_{\Gamma_n} F^k \cdot n \, d\check{A} = \sum_m A_{nm} F_{nm}$ ..... (Eq. 8)

In which,

$F_{nm}$ is the average value of the inward normal component of flux $F^k$ over the surface segments $A_{nm}$ between volume elements $V_n$ and $V_m$.

Substituting **Eq. 7** and **Eq. 8** into the governing equation, we have the following a set of first-order ordinary differential equations in time.

$\frac{dM_n^k}{dt} = \frac{1}{V_n} \sum_m A_{nm} F_{nm}^k + q_n^k$ ..... (Eq. 9)

Fully implicit approach is applied for the above equation in order to solve strongly nonlinear problems. **Eq. 10** is the final formula after time discretization. Time is discretized as a first-order finite difference, and the right-hand terms such as flux and

sink/source are evaluated at the new time level. For each gridblock $V_n$, there are $N_k$ equations equal to number of components. For a system discretized into $N_g$ gridblocks, there are total $N_g * N_k$ non-linear equations, which can be solved using the Newton-Raphson Iteration approaches.

$$R_n^{k,i+1} = M_n^{k,i+1} - M_n^{k,i} - \frac{\Delta t}{V_n}\left(\sum_m A_{nm} F_{nm}^{k,i+1} + V_n q_n^{k,i+1}\right) = 0 \quad \text{..... (Eq. 10)}$$

In which

$t^{i+1} = t^i + \Delta t$;

$R_n^{k,i+1}$, residual of the discretized continuum equation.

### 3.3.2 Computation of Connection-List Parameters

From the previous sections on gridding and discretization, grid geometry will be implicitly represented by a number of vertices and an index array storing the entire vertex IDs of the cell. However, in order to prepare simulation input, a connection-list is required, which includes pore volume of each cell, cell center depth, transmissibilities between two adjacent cells, and well-related information. In the following, we will briefly discuss about data structure and workflow of the gridding and discretization algorithms.

### *3.4 Workflow Chart of the Proposed Algorithms*

**Fig. 6** summarizes the previous gridding and discretization. From input files, 3D fracture geometry is first reduced to 2D by projecting to the horizontal plane. Such treatment is valid if fractures are perpendicular to bedding layers, which is usually the case in fractured shale reservoirs. Then fractures and reservoir background will be meshed separately. For the fractures, fixed Voronoi cell centers are computed to deal with fracture refinement, fracture intersection and clustering, as well as variable fracture aperture. Moreover, flexible Voronoi cell centers are computed for reservoir background from the forced-based optimization algorithms, where different reservoir background mesh density, orientation, and type can be achieved by iteratively updating flexible Voronoi cell centers. After all the Voronoi cell centers are calculated, 2D Voronoi grid is constructed and extruded onto geological layers to yield the 2.5D Voronoi grid. Finally, simulator input files are calculated as a connection-list including pore volume of each Voronoi cell, transmissibility between two Voronoi cells, cell center depth, as well as well-related properties.

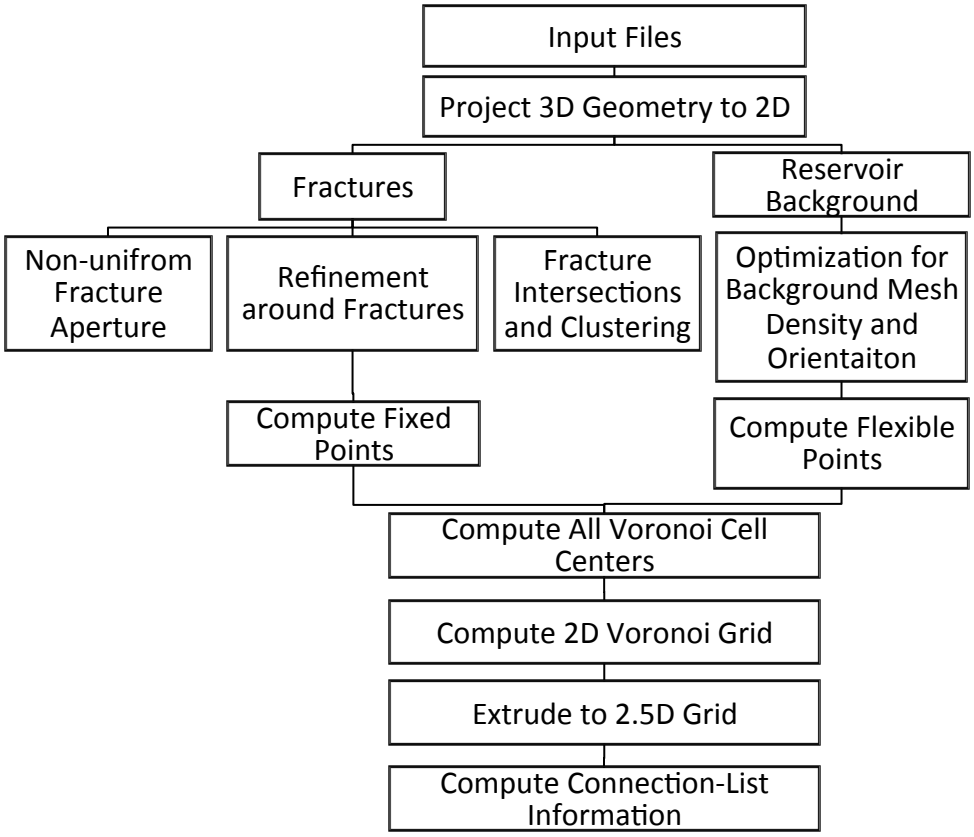


**Fig. 6 – Workflow chart of the proposed gridding and discretization scheme.**

# CHAPTER IV

# APPLICATION OF FRACTURE CHARACTERIZATION TECHNIQUES IN DISCRETE FRACTURE NETWORKS

## *4.1 Fractal-Based Characterization Approach*

During characterization, fracture properties can be determined from outcrop studies, image logs and core samples, especially horizontal core with the trajectory of the core perpendicular to the fracture network. However, measured data comes from different scales, which require a scale-independent approach to combine such data for generating more realistic stochastic fracture network models. It has been shown that fractures do present self-affine fractal features in several studies (Fardin et al. 2001, Kulatilake and Um 1999). Therefore, fractal theory was introduced to reduce uncertainty and inevitable discrepancies among different scales. The main advantage of fractal discrete fracture network is independence of scale, which allows to utilize available data as much as possible regardless of the measurement scale. Besides, fractal aperture distribution can be generated to mimic more realistic fracture roughness rather than a single value throughout the fracture plane.

Kim and Schechter (2009) previously developed both 2D and 3D FDFN generation code. However, there is no hydraulic fractures, well trajectory or simulation studies performed for the generated natural fractures. In this paper, we will combine the 2D FDFN algorithms with the developed gridding and discretization techniques, and

investigate production performance of FDFN. The 2D FDFN algorithms are organized into two modules, one for FDFN geometry generation and the other for fracture aperture generation. A corrected successive random addition (SRA) algorithm based on fractal theory was implemented to generate fractal aperture distributions. On the other hand, fracture aperture can be assumed to either be a constant value or follow a certain distribution function, such as a log normal distribution. We will perform a detailed comparison between constant aperture and lognormal aperture distributions at the end of this chapter.

### 4.1.1 FDFN Test Problem

In this section, we will illustrate the proposed workflow for characterization and simulation of discrete fracture networks using the 2D FDFN model. From outcrop maps, core samples, and image logs, it is conceivable to generate statistical properties of natural fracture networks. We can, thus, analyze and extract information to prepare input parameters of FDFN as seen in **Table 1**. During fracture stimulation, hydraulic fractures propagate and intersect natural fractures, forming complex discrete fracture networks. Even though for conventional reservoirs, discrete fractures might be considered as conductors or barriers, in the context of unconventional reservoirs only proppant fractures or connected fracture networks contribute to production performance (Mirzaei and Cipolla 2012). Some natural fractures are directly connected to the horizontal wellbore or indirectly connected by either hydraulic fractures or other natural fractures, but all connected fractures will contribute to well performance. For those isolated natural

fractures, production contribution may be negligible. Based on such simplifications, it is important to combine stimulation monitoring data such as microseismic events, well trajectory, and stochastic algorithms to prepare a reasonable fracture network that conforms to the data obtained from microseismic and natural fracture characterization. In section 4.2, we will show how to incorporate microseismic data (if available) into the process of fracture characterization.

*4.1.1.1 Extract the Complex Fracture Network*

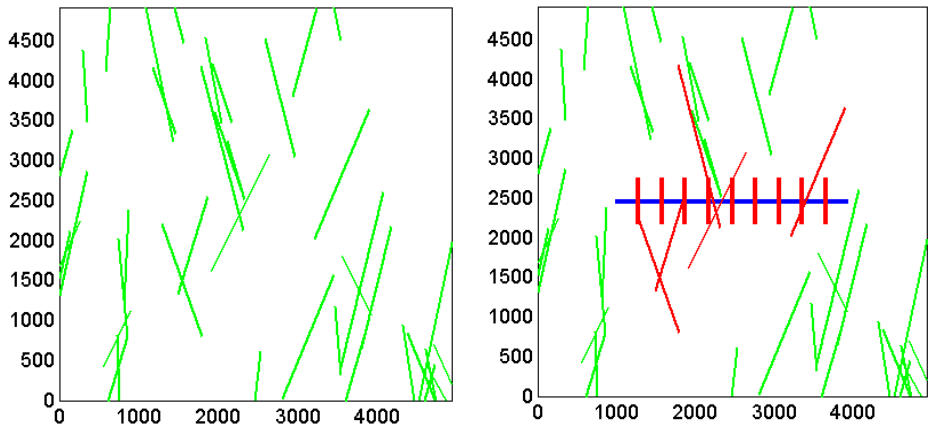


**(a)** **(b)**

**Fig. 7 – Fractal discrete fracture network (a) and the extracted complex fracture network (b) (blue lines for horizontal well, wide red lines for hydraulic fractures, narrow red lines for connected natural factures, and green lines for isolated natural fractures).**

| | |
|---|---|
| Number of Natural Fracture Sets | 1 |
| Minimum Fracture Length (ft.) | 0.05 * L |
| Fracture Fractal Density | 1.9 |
| Fracture Fractal Length | 1.8 |
| Constant Density Term | 1.5 |
| Scale Ratio | 3 |
| Multifractal Dimension | 2 |
| Aperture Density | 100 |
| Aperture Amplitude | 0.1269 |
| Hurst Exponent | 0.45 |
| Maximum Aperture (ft.) | 4.4554E-4 |
| Minimum Aperture (ft.) | 2.7559E-5 |
| Standard Deviation | 0.011 |

**Table 1 – Input parameters for generating discrete fracture networks and fracture aperture distributions, where L represents the reservoir length equal to 4921 ft.**

However, in this section, for the lack of microseismic monitoring data, we simply overlay hydraulic fractures with the FDFN, and then evaluate production performance of the connected fracture networks. Regarding the geometry of hydraulic fractures, we choose a straight horizontal wellbore and nine hydraulic fractures orthogonal to the well trajectory. **Fig. 7** shows the FDFN generated by using input parameters in **Table 1**, and the extracted simple fracture network.

*4.1.1.2 The Impact of Optimization on Locations of Flexible Points.*

Based on the input parameters in **Table 1** and the extracted complex fracture network in **Fig. 7**, the optimization algorithms proposed in section 3.2.2.2 are applied to generate a series of Delaunay Triangulations (DT), among which three are shown in **Fig. 8**. **Fig. 8 (a)** shows the initial point distribution after the rejection method. Note that there exist denser point clouds around mesh objects such as fractures and wellbore trajectory, even though the initial Delaunay Triangulation ends up with very skewed triangles.

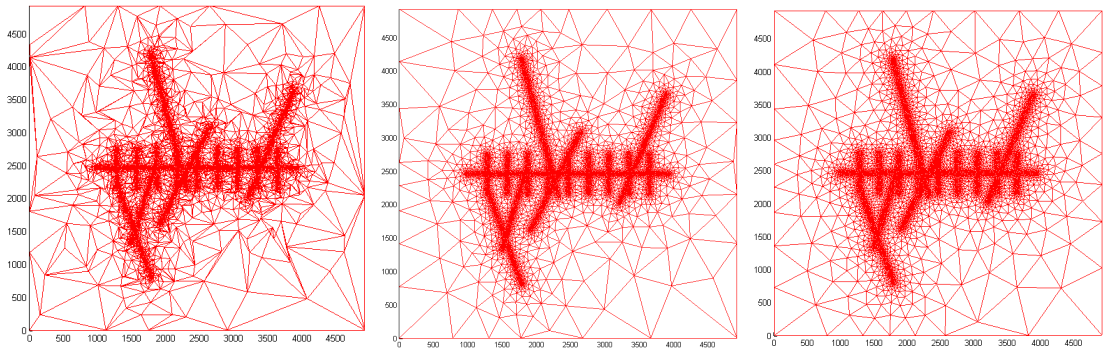

**(a)** **(b)** **(c)**

**Fig. 8 – Delaunay Triangulations of Voronoi centers for one iteration after applying the rejection method (a), 20 iterations of the force-based algorithm (b) and 400 iterations of the final output (c).**

After 20 iterations, most of the flexible points in the regions far away from the mesh objects in **Fig. 8 (b)** are very close to their final positions when compared to the final network in **Fig. 8 (c)** after around 400 iterations. The implemented algorithms used

in development of **Fig. 8** are for optimization of the Voronoi locations at each iteration. From **Fig. 8 (c)**, we obtain a good quality mesh, capturing desirable refinement features around both the fractures and well trajectory.

*4.1.1.3 Enlarged Views of the Simulation Grid.*

**Fig. 9** and **Fig. 10** illustrate the details of the Voronoi grid in the FDFN test problem. In **Fig. 9 (a)**, cell size increases away from the mesh objects, and on the reservoir boundary we see the largest cell size, because in this study we set the maximum cell size as a very large number to reduce the total number of simulation gridblocks. In **Fig. 9 (b)** and **(c)**, we show how the algorithm treats non-orthogonal fracture intersections. Between the regions of intersecting fractures, we observe Voronoi cells oriented almost perpendicular to the fractures, because of both the force-based optimization and usage of the fixed points. The proposed point-placement scheme to honor non-uniform fracture aperture distributions is not only easy to implement, but also able to handle lower-angle intersections automatically by the flexible points, which avoids the complicated point-placement procedure around intersections. **Fig. 9 (d)** demonstrates how grid refinement features appear around fracture tips and at the heel and toe of the horizontal wellbore. Voronoi cells are oriented in a radial pattern so that a radial flow regime in addition to linear flow regimes can be observed during flow simulations. **Fig. 10** shows how a non-uniform fracture aperture distribution looks like along a natural fracture in the geometric domain. Later in section 4.4, we will present a detailed study on non-uniform fracture aperture, highlighting its importance on production romance.

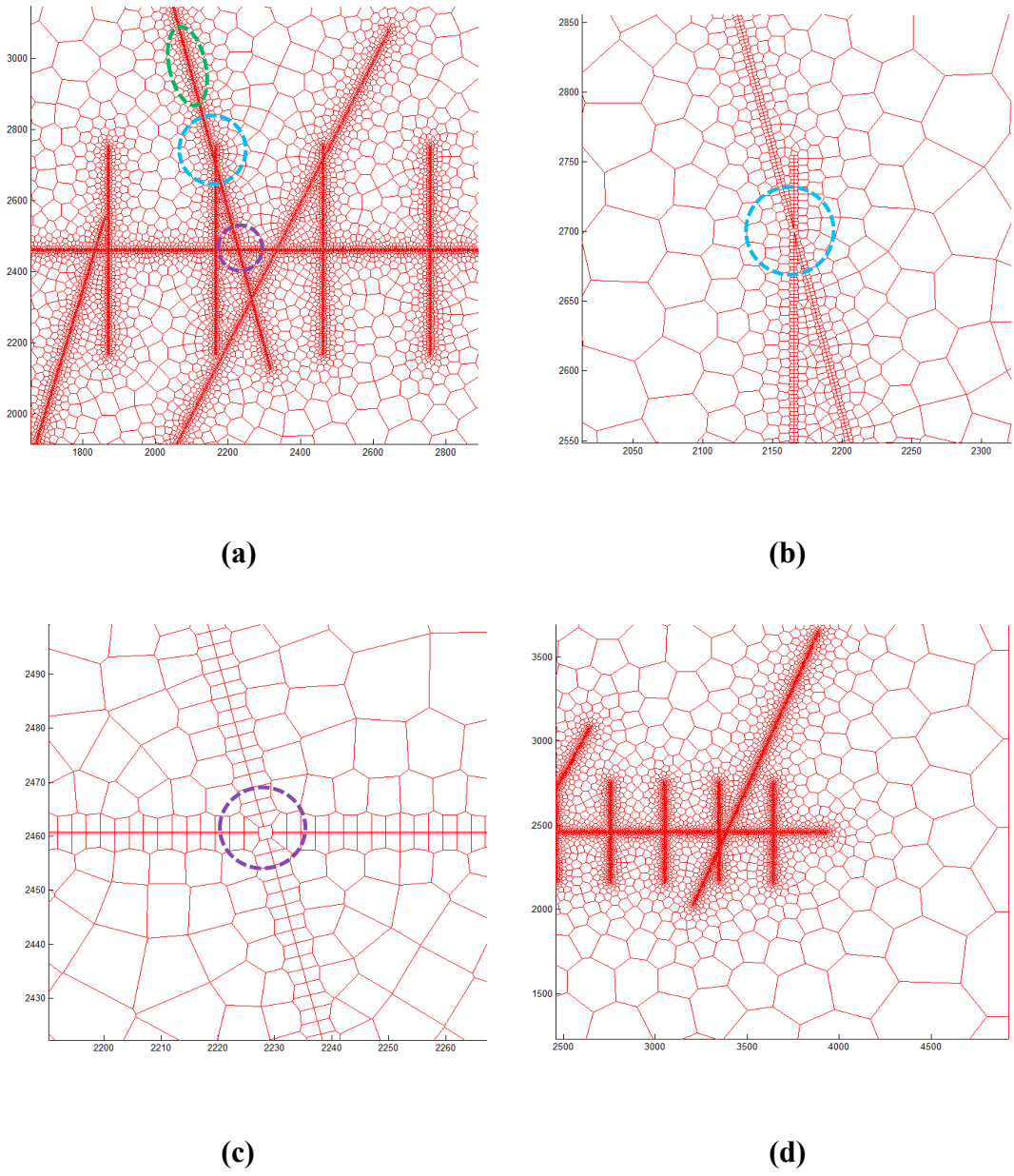


**(a)** **(b)**

**(c)** **(d)**

**Fig. 9 – Enlarged view of the intersected fractures of the Voronoi grid (a); the refinement around a lower-angle intersection between a vertical hydraulic fracture and a natural fracture indicated by the blue circle (b); around a non-orthogonal intersection between the horizontal well and a natural fracture indicated by the purple circle (c); around the horizontal heel and toe and fracture tips (d).**

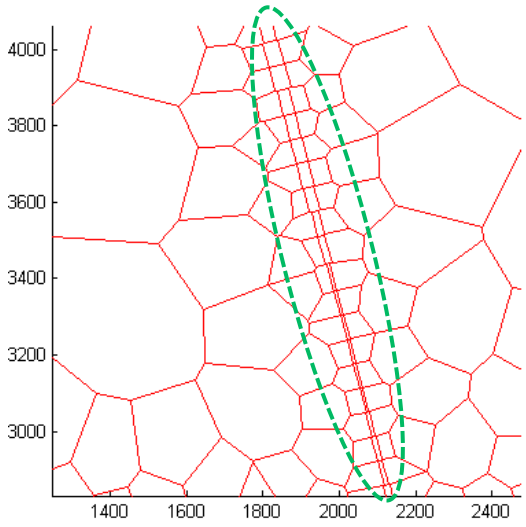


**Fig. 10 – Enlarged view of non-uniform fracture aperture indicated by the green dotted ellipse. In order to facilitate visualization, the picture was prepared by increasing fracture aperture by 10^5 times and fracture segment length by 27 times.**

*4.1.1.4 Comparison between Finite Fracture Conductivity with Infinite Fracture Conductivity*

**Table 2** summarizes all the simulation input parameters. One case (Case 4) is prepared with a constant fracture aperture equal to 3 mm or 9.84E-3 ft., which will be compared with another case (Case 7) with a non-uniform aperture distribution (**Fig. 3)**. We will study the effect of non-uniform aperture vs. uniform aperture, and finite fracture conductivity vs. infinite fracture conductivity. For all simulation runs, we set locations of perforations at the intersections between the horizontal wellbore and hydraulic or natural fractures.

| | | | |
|---|---|---|---|
| Reservoir Length, ft. | 4921 | Hydraulic Fracture Length, ft. | 590 |
| Reservoir Thickness, ft. | 164 | Hydraulic Fracture Width, ft. | 9.84E-3 |
| Reservoir Pressure, psi | 5004 | Hydraulic Fracture Spacing, ft. | 295 |
| Reservoir Temperature, $^{o}$F | 200 | Hydraulic Fracture Perm, mD | 50000 |
| Well BHP, psi | 500 | Hydraulic Fracture Porosity | 0.33 |
| Well Radius, ft. | 0.328 | Natural Fracture Perm, mD | 500 |
| Well Length, ft. | 2953 | Natural Fracture Porosity | 0.33 |
| # of Hydraulic Fractures | 9 | Natural Fracture Width, ft. | 9.84E-3 |
| Matrix Porosity | 0.04 | Matrix Permeability, mD | 0.0001 |

**Table 2 – Input reservoir and fracture properties for single-phase gas simulations.**

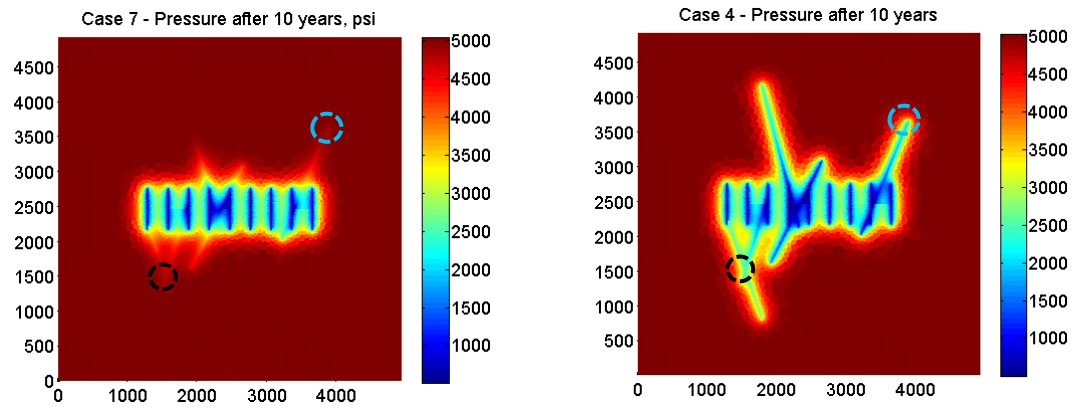


**(a)** **(b)**

**Fig. 11 – Single-phase gas simulation pressure graphs of both non-uniform aperture distribution (a) with averaged fracture conductivity equal to 0.125 mD-ft vs. constant fracture aperture (b) with fracture conductivity equal to 4.92 mD-ft.**

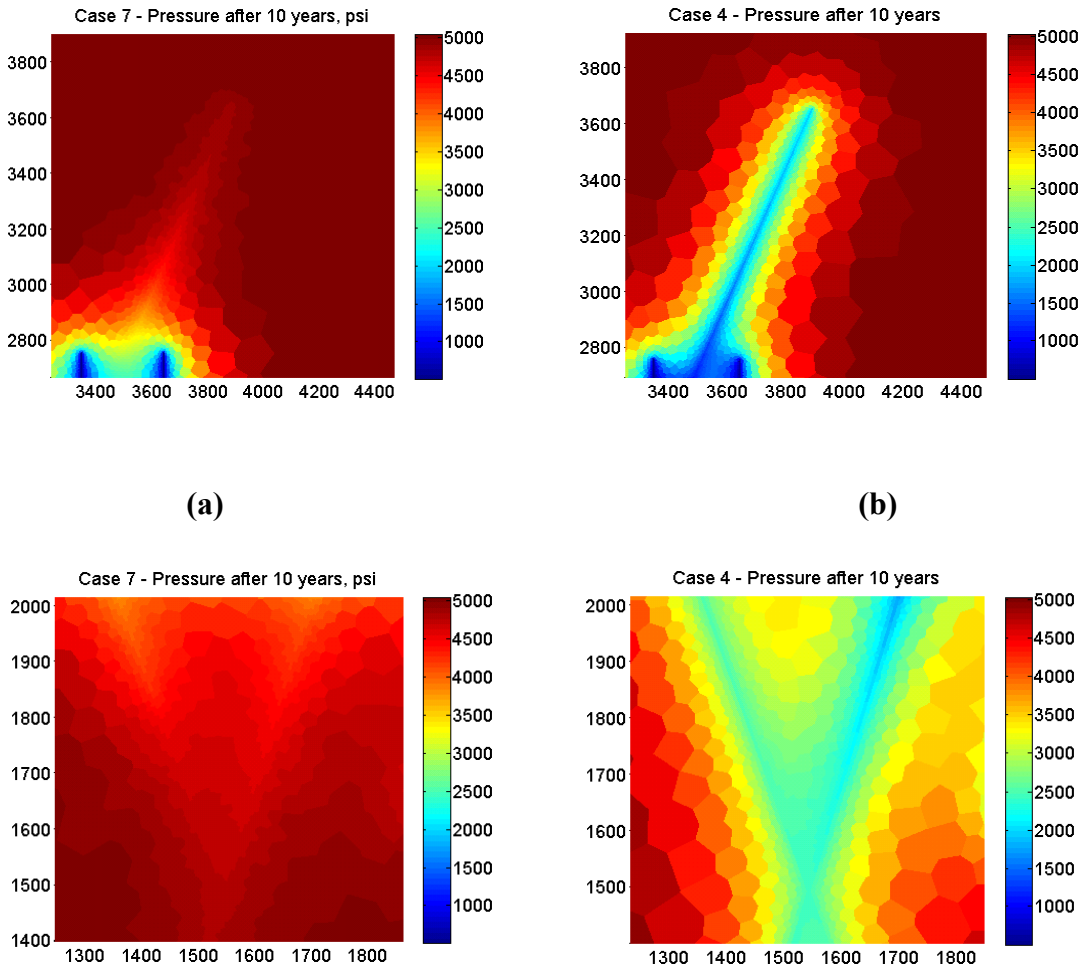


**Fig. 12 – Zoom-in view of the blue circle in Fig. 11 showing pressure depletion around a fracture tip for finite fracture conductivity (a), infinite fracture conductivity (b), zoom-in view of the black circle around a fracture intersection for finite fracture conductivity (c), and infinite fracture conductivity (d).**

After 10 years' single-phase gas simulation, we plot pressure graphs as seen from **Fig. 11** to **Fig. 12**. From **Table 2**, matrix conductivity is readily calculated as 2.95E-2

mD-ft. For the non-uniform aperture case, the averaged fracture conductivity equals to 2.5E-4 ft. * 500 md = 0.125 mD-ft, whereas for the constant fracture aperture case, the fracture conductivity equals to 9.84E-03 ft. * 500 md = 4.92 mD-ft. Therefore, dimensionless fracture conductivity is 4.23 and 167 for non-uniform and constant aperture, respectively. As mentioned by Olorode et al. (2013), infinite-conductivity for natural fractures exists when the dimensionless fracture conductivity is more than 55.6, and finite-conductivity dominates the flow when the dimensionless fracture conductivity is less than 11.1. Therefore, the former non-uniform case corresponds to finite fracture conductivity, and the latter to infinite fracture conductivity.

**Fig. 11** compares the simulation results of finite fracture conductivity with infinite fracture conductivity. Obviously, the latter case results in a greater SRV, and around fractures we see significant pressure depletion. However, for the finite conductivity case, we observe a more limited SRV. Similar conclusions can be reached from **Fig. 12**, which shows an enlarged view around intersecting fractures. **Fig. 12** shows the zoomed-in details around the blue circle (fracture tip) and black circle (fracture intersection) shown in **Fig. 11**.

To sum up this test case, not only natural fracture geometry but also fracture conductivity significantly affects the SRV and ultimately, production performance. However, natural fracture networks are usually distributed stochastically, and it is almost impossible to apply a deterministic method to accurately extract complex DFNs from hydraulic fracturing treatment. Besides, no unique DFN for natural fractures could be

obtained even from the same input parameters because of the stochastic nature of both the real natural fractures as well as the developed DFN generation code.

*4.1.1.5 Comparison Fractal Non-uniform Fracture Aperture with Constant Fracture Aperture.*

In **Table 3**, four approaches such as arithmetic, harmonic, maximum and minimum are used to average non-uniform apertures along five natural fractures, respectively. For example, the third column corresponds to the arithmetic mean along each natural fracture, and the average of the third column yields 2.5E-4 ft., which is already used for the previous comparison between finite fracture conductivity and infinite fracture conductivity. Besides, the descending order of average aperture values for each natural fracture is maximum > arithmetic > harmonic > minimum.

| Fracture Number | Maximum (ft.) | Arithmetic (ft.) | Harmonic (ft.) | Minimum (ft.) |
|---|---|---|---|---|
| 1 | 4.54E-04 | 2.04E-04 | 1.33E-04 | 4.37E-05 |
| 2 | 4.64E-04 | 3.48E-04 | 3.37E-04 | 2.10E-04 |
| 3 | 4.52E-04 | 2.67E-04 | 2.14E-04 | 7.15E-05 |
| 4 | 4.46E-04 | 2.75E-04 | 2.53E-04 | 1.20E-04 |
| 5 | 4.22E-04 | 1.55E-04 | 1.08E-04 | 3.76E-05 |

**Table 3 – Average natural fracture apertures.**

**Fig. 13** shows production performance of four different averaging approaches, which are compared with the previous case with non-uniform fracture aperture (Case 7).

The descending order of production performance is maximum > arithmetic > non-uniform > harmonic > minimum, which is the same as that of average aperture values of each natural fracture. Moreover, Case 7 falls between arithmetic and harmonic, even though their production performance is similar to each other for the single-phase gas simulation up to 10 years. At the end of 10 years' simulation, cumulative gas production differences of arithmetic minus nonuniform and nonuniform minus harmonic are 0.674 MMSCF and 0.487 MMSCF, respectively. Such differences correspond to 0.9% and 0.6% differences from the non-uniform Case 7, which is not a negligible difference. When more physics are involved such as multiphase flow and liquid condensation, we speculate that accurate modeling of non-uniform fracture behavior becomes even more important.

Therefore, sensitivity analysis of natural fracture properties is extremely important. First, it is necessary to better understand the reservoir, and extract more representative DFNs. Second, once the high impact parameters are obtained, they can be used as variables to history match production data, or better yet, target more intensive fracture characterization directed to higher impact parameters. Finally, high impact parameters can be varied to generate more precise realizations of DFNs, which could help the optimization of hydraulic fracture design.

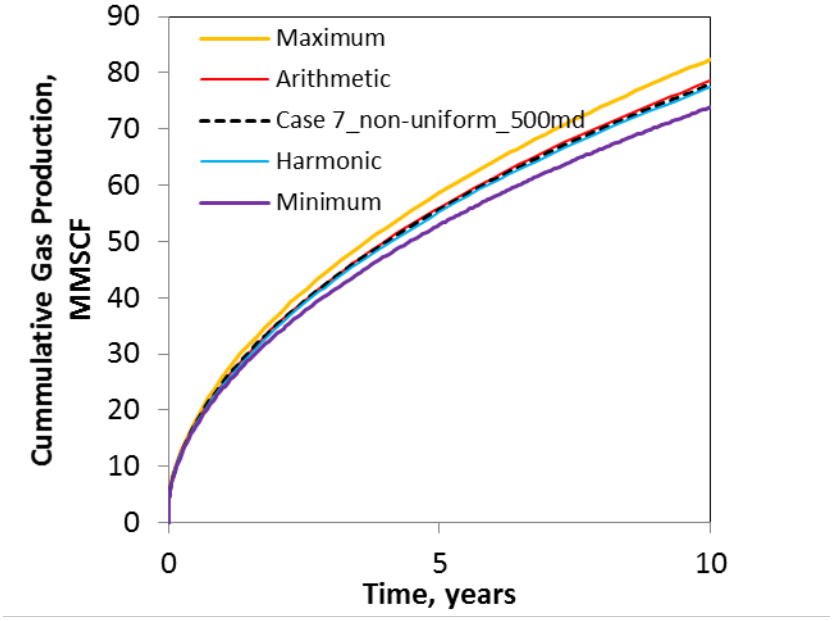


**Fig. 13 – Effect of nonuniform natural fracture aperture vs. averaged uniform natural fracture apertures on production performance.**

### 4.1.2 Sensitivity Analysis of Natural Fracture Parameters

The complex fracture network after hydraulic fracturing consists of natural fractures and induced hydraulic fractures. Even though the effect of natural fractures on production has been investigated, there is no numerical study of stochastic generated natural fractures on production performance due to gridding and discretization difficulties of complex fracture networks. In this study, we will perform sensitivity analysis of properties of natural fractures which are broken down into four categories, including natural fracture aperture and permeability, fracture density, fracture length, and strike of fracture sets. We will discuss about DFN graphs, generated Voronoi

meshes, and single-phase gas simulation results with the same reservoir and fluid properties as were used in the previous section.

*4.1.2.1 Natural Fracture Aperture and Permeability*

**Table 4** tabulates natural fracture aperture (wf), fracture permeability (kfrac), fracture conductivity (Cf), and dimensionless fracture conductivity (CfD). Case 4 and Case 7 were already discussed in the previous section for demonstrating the effect of fracture conductivity (finite fracture conductivity vs. infinite fracture conductivity) on production performance of hydraulically fractured wells. Fracture aperture ranges from 0.003 mm up to 3 mm, resulting in fracture permeability values from 500 mD to 5000 mD. Fracture conductivity varies from 4.92E-3 mD-ft to 49.2 mD-ft. Dimensionless fracture conductivity changes from 0.167 to 1670.

| Case Number | wf (mm) | kfrac (md) | Cf (mD-ft) | CfD |
|---|---|---|---|---|
| 1 | 0.003 | 500 | 0.00492 | 0.167 |
| 2 | 0.03 | 500 | 0.0492 | 1.67 |
| 3 | 0.3 | 500 | 0.492 | 16.7 |
| 4 | 3 | 500 | 4.92 | 167 |
| 5 | 0.3 | 5000 | 4.92 | 167 |
| 6 | 3 | 5000 | 49.2 | 1670 |
| 7 | Non-uniform | 500 | 0.125 | 4.23 |

**Table 4 – Sensitivity analysis of natural fracture aperture and permeabilities.**

**Fig. 14** and **Fig. 15** are cumulative production and production rate for up to ten years. For all the cases with 500 md for fracture permeability, when the fracture aperture is increasing from 0.003 mm up to 3 mm, we observe doubling of cumulative production as shown in **Fig. 14**.

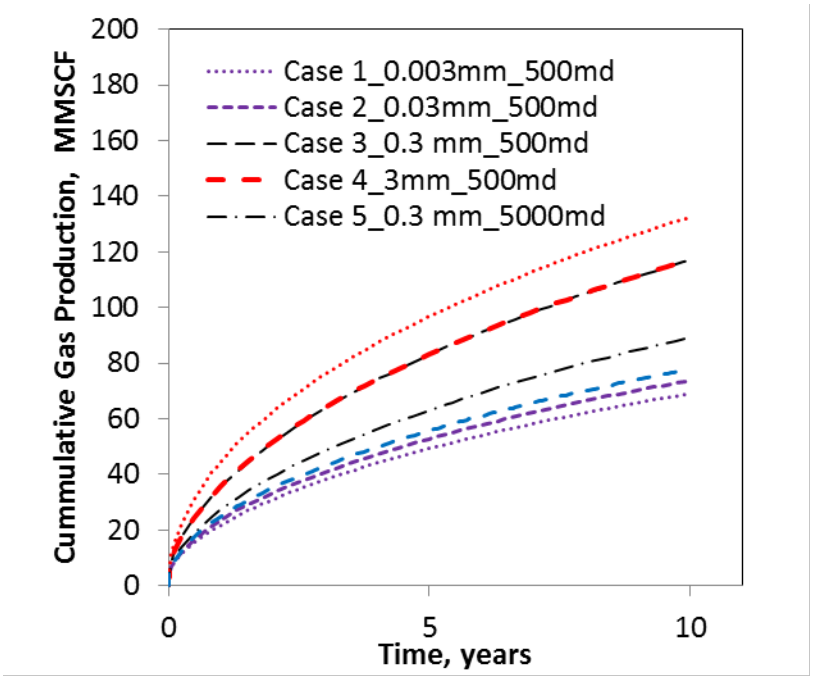


**Fig. 14 – Sensitivity analysis of the effect of fracture width and permeability on production performance. For example, "Case 1_0.003mm_500md" indicates cumulative gas production for Case 1 with 0.003 mm fracture width and 500 md fracture permeability.**

*4.1.2.2 Flow Regime Analysis of the 2D FDFN Test Problem*

In **Fig. 15**, gas production vs. production time is plotted on a log-log scale. We observe five transition periods, which are indicated by red dotted circles. In this study, we set a constant bottom-hole pressure for the grid block located at the heel of the horizontal well with the reservoir coordinate around (1000 ft., 2500 ft.). Besides, the horizontal wellbore gridblocks are explicitly modeled with a higher permeability value of 5000 Darcies, which are two orders of magnitude higher than the hydraulic fracture permeability as seen in **Table 2**. Therefore, as observed from **Fig. 15**, from 1E-8 day to 1E-6 day, we have a unit slope which corresponds to wellbore storage from the gridblock where we impose the pressure constraint. From 1E-6 day to 1E-3 day, a half-slope is observed which indicates linear flow along the horizontal well. Hydraulic fractures start flowing to the horizontal wellbore from 1E-3 day up to 1E-2 day, and then natural fractures continue production contribution up to 1 day. At this point, all the fluid in the well and fracture systems has been produced. However, at field conditions, because of flow back of fracturing fluids and other issues, we may not observe these transitions. Instead, field production data with the half slope is usually observed after at least several days of production. In this study, we observe that linear flow from the matrix to the complex DFN happens from 1 day up to around 300 days. Because of natural fracture interference in the early stage of the linear flow regime, the slope deviates slowly from a half slope to a relatively larger value between one-half and one. If there were no natural fractures, the slope would be more or less a half slope until hydraulic fracture interference occurs. Similar behavior is observed for natural fractures

with orthogonal intersections with larger fracture spacing. However, if extensive natural fracture clustering with non-orthogonal and lower-angle intersections exists, much greater natural fracture interference might occur, which would delay and perhaps alter the half-slope regime.

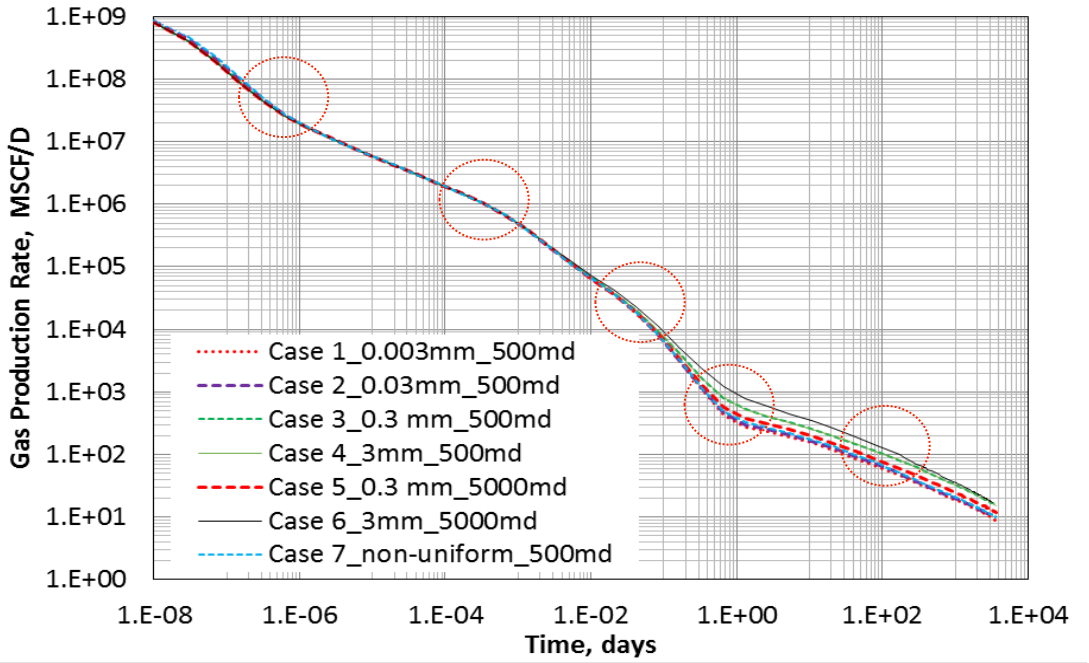


**Fig. 15 – Sensitivity analysis of the effect of fracture width and permeability on production performance. For example, "Case 1_0.003mm_500md" indicates gas production rate for Case 1 with 0.003 mm fracture width and 500 md fracture permeability.**

In **Fig. 16**, we illustrate the last three transitions that we might observe in the field. At around 0.01 day, hydraulic fractures have already been depleted, and natural fracture drainage is observed at intersections between hydraulic and natural fractures as

indicated by four yellow circles in **Fig 16 (a)**. At around 1 day in **Fig 16 (b)**, fracture networks have finished contributing to production and we observe very low pressure in both hydraulic and natural fractures. Gas begins to flow from the matrix rock towards the complex DFN in a linear pattern. At around 300 days in **Fig 16 (c)**, fracture interference results in the deviation from the half-slope as shown by the last red circle in **Fig. 15** at around 100 days. At the end of the simulation in **Fig 16 (d)**, we observe pressure depletion throughout the whole SRV. Comparing **Fig. 11** with **Fig. 16**, there is an obvious difference in depletion of natural fractures for Case 3, Case 4 and Case 7, which results in different production rates and cumulative production. One last observation regarding fracture aperture is that computational time for smaller aperture values is very large. For 0.003 mm, it took several days to complete even the single-phase simulation run up to 10 years. Increasing the aperture value to 3 mm with the same fracture permeability only took 30 minutes. So as long as the fracture conductivity of natural fractures remains the same, one might want to use a larger nominal aperture value to speed up the simulation. In this study, we found that 3 mm aperture is a good value to use without introducing obvious inaccuracies for the simulation results. A larger aperture value might need additional modifications of fracture porosity in order to produce reasonable results for early flow periods.

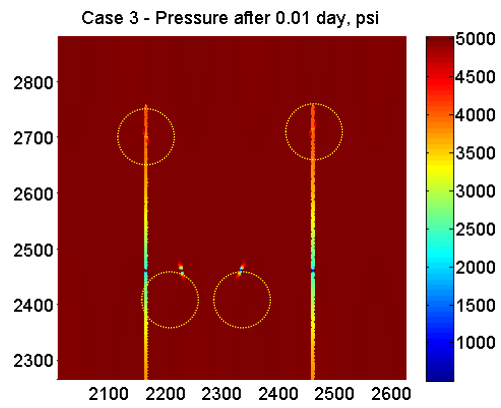


**(a)**

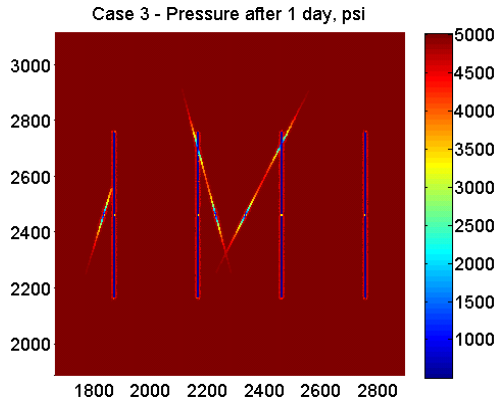


**(b)**

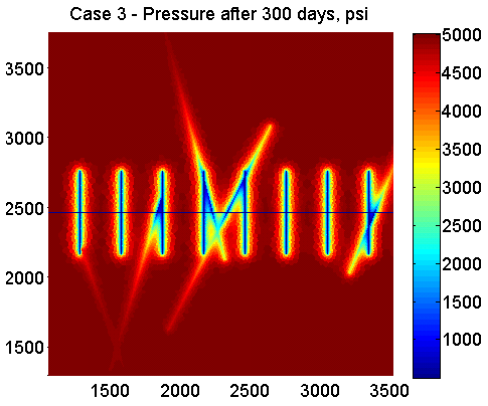


**(c)**

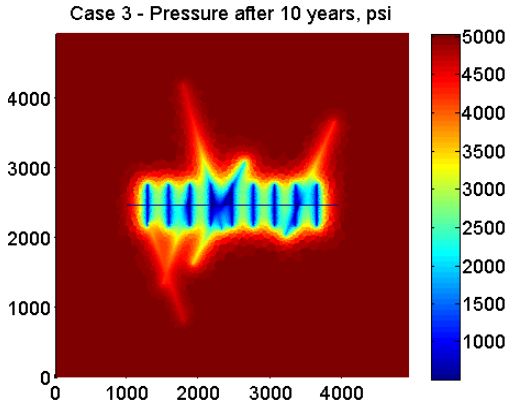


**(d)**

**Fig. 16 – Selected four production times at 0.01 day (a), 1 day (b), 300 days (c), and 10 years (d), showing transitions from hydraulic fracture drainage, to linear flow around the complex DFN, to fracture interference, and to complete drainage around SRV.**

*4.1.2.3 Natural Fracture Spacing*

In **Table 5**, we will investigate five cases from Case 8 to Case 12 for low to high fracture density parameter alpha from 0.5 to 4.5. **Fig. 17** shows the extracted DFN for each case. Since we used the same random seed as well as the same fractal center distribution (FDc) and fractal length distribution (FDl), the generated natural fracture networks follow a similar clustering pattern around the hydraulic fractures near the toe of the well at the location of around (3500 ft., 2500 ft.). For each case, we then create a Voronoi mesh using the previous developed unstructured grid generation algorithms, and perform reservoir simulation. For the purpose of illustration, we only present the Voronoi mesh for the most complicated, high intensity natural fracture version of this study – Case 12.

| Case Number | FDc | FDl | lmin | alpha |
|---|---|---|---|---|
| 8 | 1.9 | 1.8 | 0.03 L | 0.5 |
| 9 | 1.9 | 1.8 | 0.03 L | 1.5 |
| 10 | 1.9 | 1.8 | 0.03 L | 2.5 |
| 11 | 1.9 | 1.8 | 0.03 L | 3.5 |
| 12 | 1.9 | 1.8 | 0.03 L | 4.5 |

**Table 5 – Sensitivity analysis of natural fracture density.**

As seen in **Fig. 18**, 103,045 cells are used to resolve 129 natural fractures. The challenge of this case is that the natural fractures are closely spaced and not easily

resolved using Voronoi cells. The minimum fracture spacing is only half of the pre-defined Voronoi mesh size.

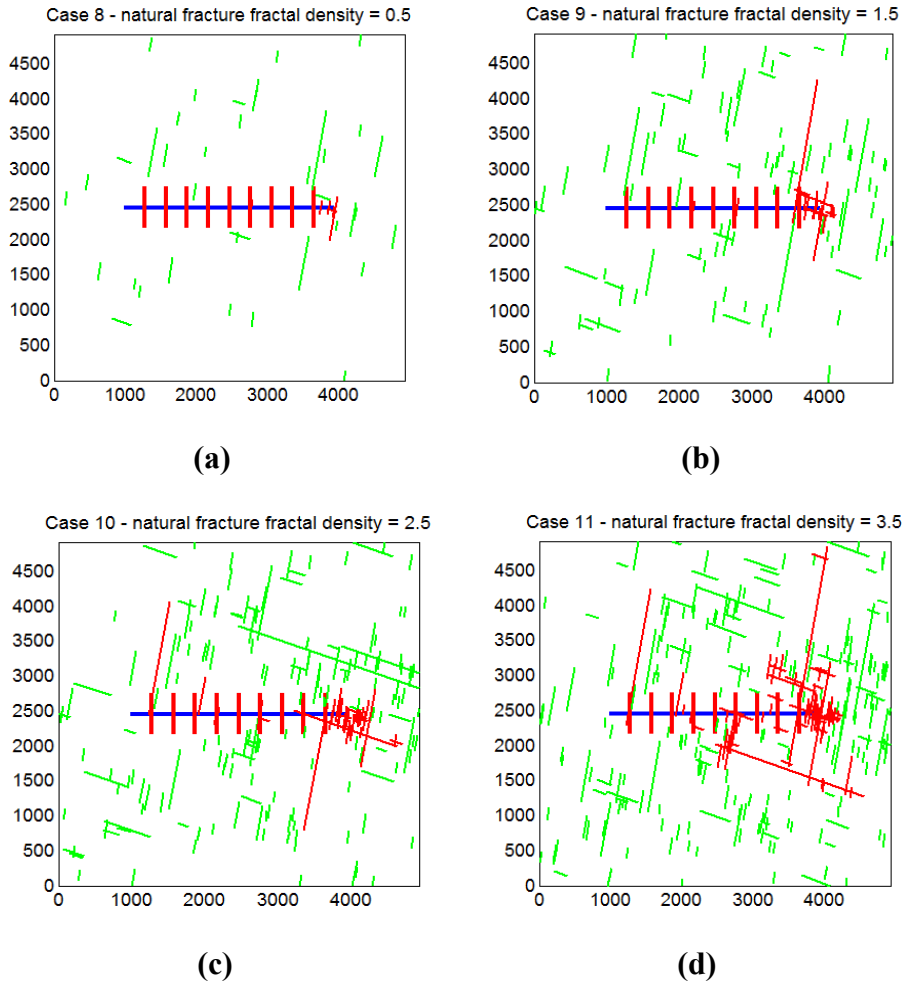


**Fig. 17 – Sensitivity analysis of fracture density for Case 8 to Case 12. Fracture fractal density parameter (alpha) increases from 0.5 in Case 8 up to 4.5 in Case 12. Green line segments represent natural fractures, narrow red line for natural fractures which are connected to the horizontal well represented by the blue line, and wide red line for hydraulic fractures.**

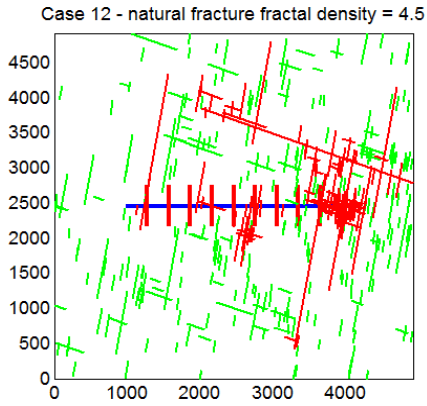


**(e)**

**Fig. 17 – Continued.**

Besides, fracture intersections are intensely distributed so that if one cell shape was distorted, it might affect the connectivity of the entire fracture network. Moreover, fracture tips tend to be very close to an adjacent fracture body so that the pre-defined fixed points might intercept adjacent fracture connectivity. All of these issues are solved with the algorithms developed and described in previous sections. Several enlarged views of the Voronoi mesh are shown to demonstrate how grid refinement features are implemented to capture all the details of the complex DFN.

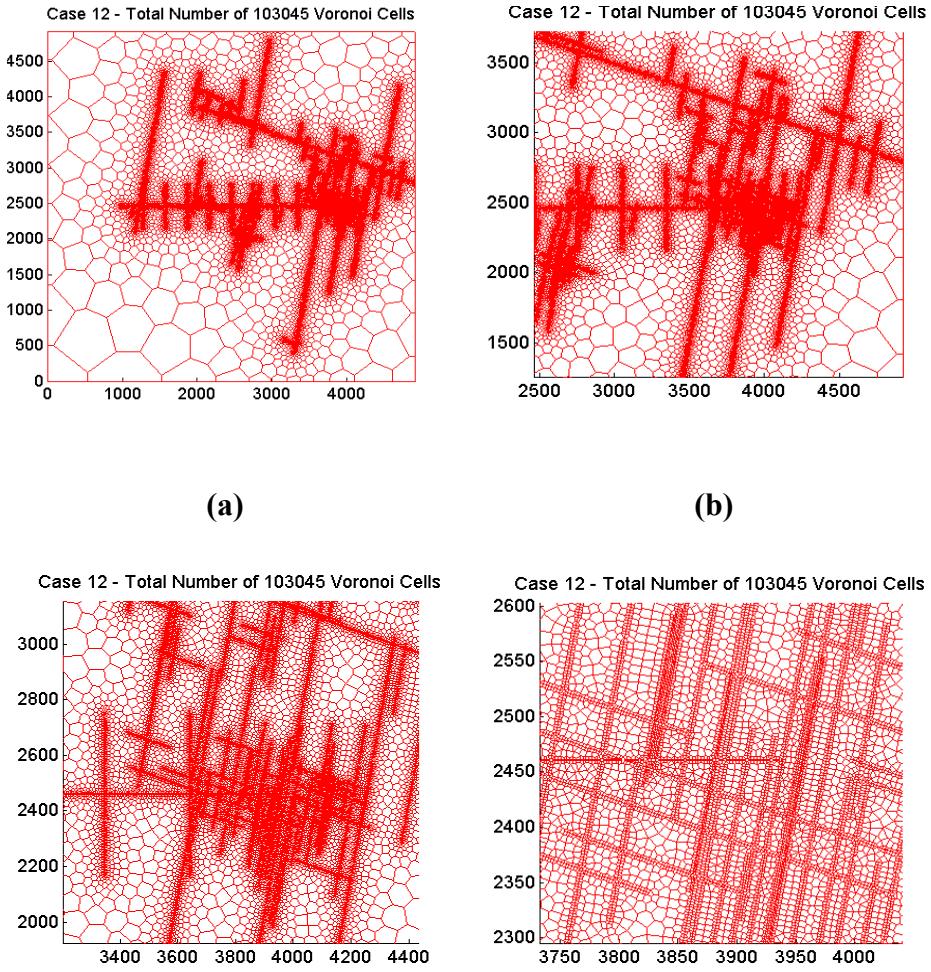


**Fig. 18 – Generated Voronoi mesh for Case 12 with 129 natural fractures, and enlarged views around the toe of the horizontal well where exists extensive natural fracture clustering and intersection.**

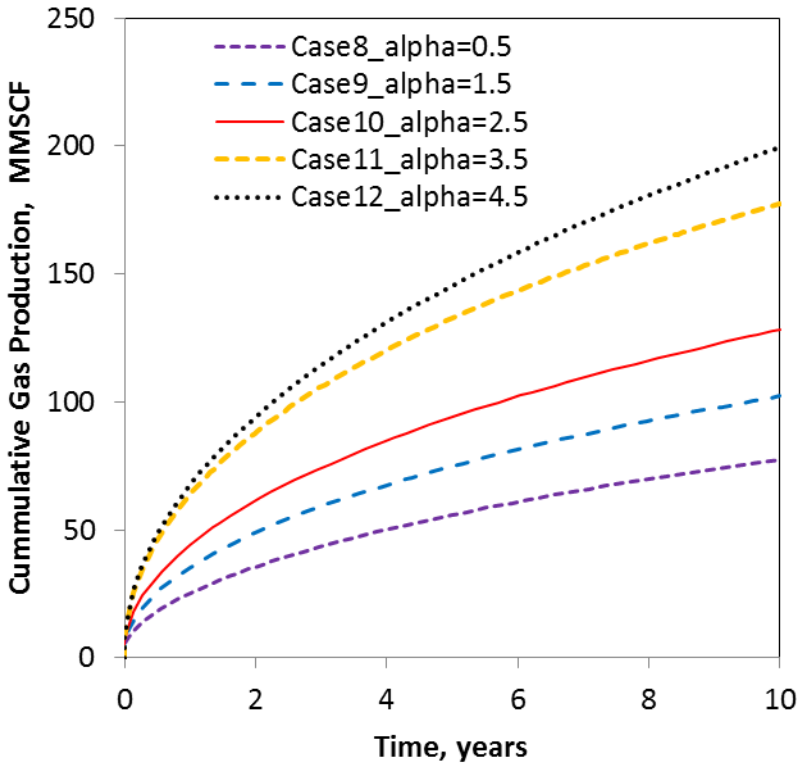


**(a)**

**Fig. 19 – Sensitivity analysis of the effect of fracture density on production performance. "Case 8_alpha = 0.5" indicates cumulative gas production or gas production rate for Case 8 with fracture density parameter alpha equal to 0.5. Two dashed arrows indicate the linear flow regime starts from 3 days for Case 8 or 4 days for Case 12.**

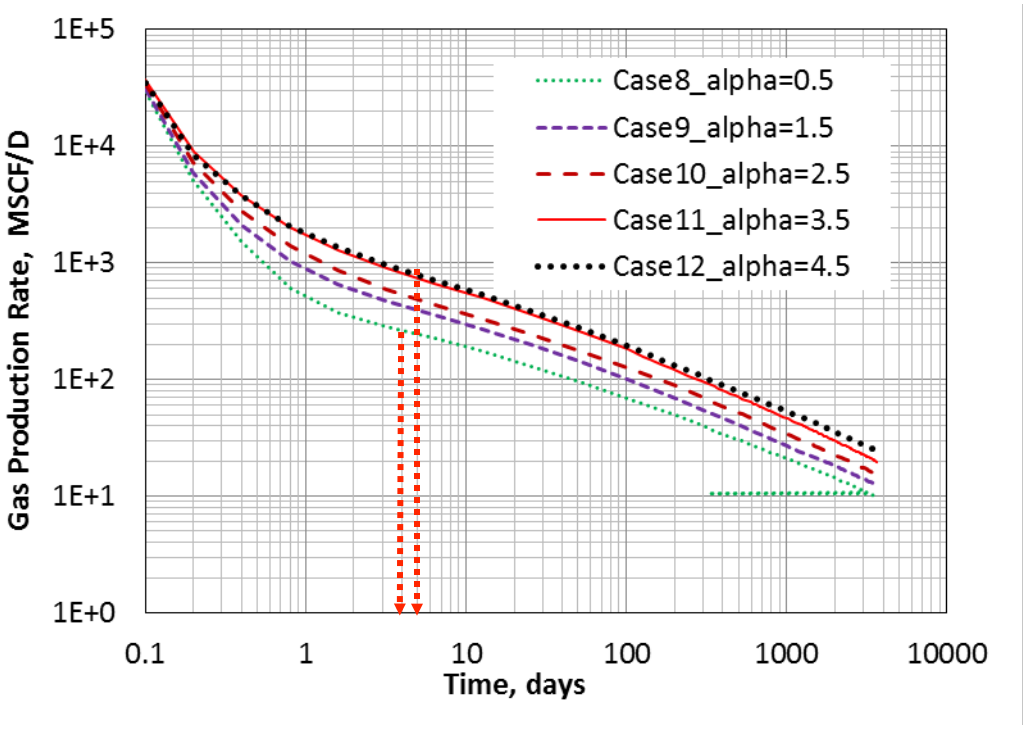


**(b)**

**Fig. 19 – Continued.**

**Fig. 19** shows the simulation results. As expected, the higher the fracture density, the better the rate and cumulative production performance. Note that the time it takes to deplete the complex DFN in the higher fracture density grid (Case 12) requires slightly longer time than that of the lower fracture density grid (Case 8). Case 8 requires 3 days vs. 4 days for Case 12 as indicated by the dashed arrows in **Fig. 19(b)**. In **Fig. 20**, several enlarged views of the simulation results for Case 12 are prepared to illustrate how pressure depletion occurs in complex DFNs. Note that Case 10 is the base case

which would be used for the following sensitivity analysis of fracture minimum length and fracture strike.

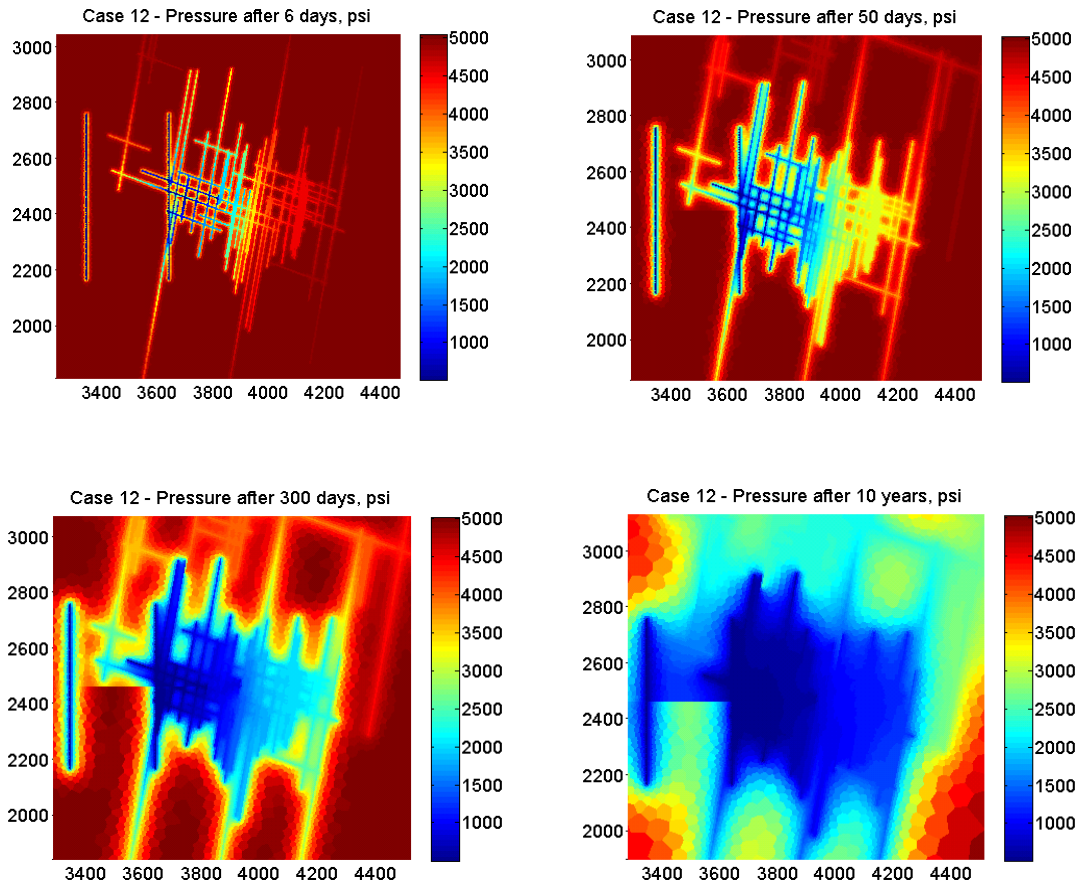


**Fig. 20 – Pressure graphs around the toe of the horizontal well for Case 10 after 6 days (a), 50 days (b), 300 days (c), and 10 years' production (d).**

*4.1.2.4 Natural Fracture Length*

In **Table 6**, fracture minimum length changes from 0.02 L up to 0.07 L, where L denotes the reservoir domain length and equals to 4921.3 ft. for this study. **Fig. 21** shows the DFN plan views for four cases, and together with base Case 10 there are a total of

five cases. Since the fracture density remains the same for all the five cases, we observe sparse distribution of natural fractures as the minimum length increases.

| Case # | FDc | FDl | lmin | alpha |
|---|---|---|---|---|
| 10 | 1.9 | 1.8 | 0.03 L | 2.5 |
| 13 | 1.9 | 1.8 | 0.02 L | 2.5 |
| 14 | 1.9 | 1.8 | 0.04 L | 2.5 |
| 15 | 1.9 | 1.8 | 0.05 L | 2.5 |
| 16 | 1.9 | 1.8 | 0.07 L | 2.5 |

**Table 6 – Sensitivity analysis of natural fracture minimum length.**

From **Fig. 22**, Case 14 yields the best production performance after a ten-year simulation run. The ratio of the natural fracture minimum length of the Case 14 to the hydraulic fracture half-length is (0.04*4921.3) to 295.3, which is around 2:3. For smaller fracture length (Case 10 and 13), natural fractures are too short to be connected into a complex DFN. Similarly, for larger fracture length with the same fracture density, natural fractures are too sparsely distributed to be connected. For a given naturally fractured reservoir, there should exist a desirable length (e.g., 2:3 for this study) to yield the most complex DFN and the largest SRV. However, we cannot control how the secondary natural fractures are distributed, and the best we could do is optimize the hydraulic fracture half-length. Thus, the characterization of length distributions of

natural fracture is extremely important since it is closed related to the optimization, which would bring the best production performance for a given reservoir.

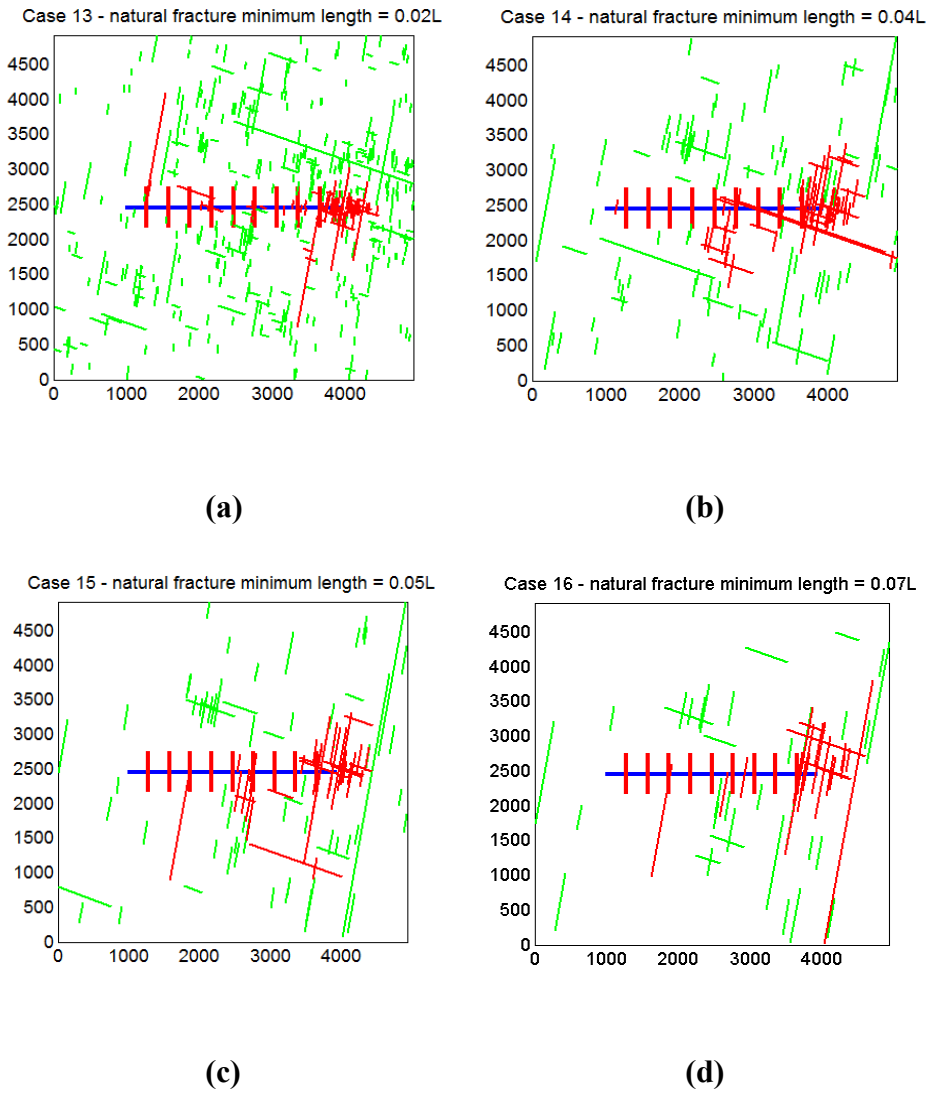


**Fig. 21 – Sensitivity analysis of natural fracture minimum length. The minimum length increases from 0.02 L up to 0.07 L where L stands for the reservoir domain length. The color scheme is the same as Fig. 17.**

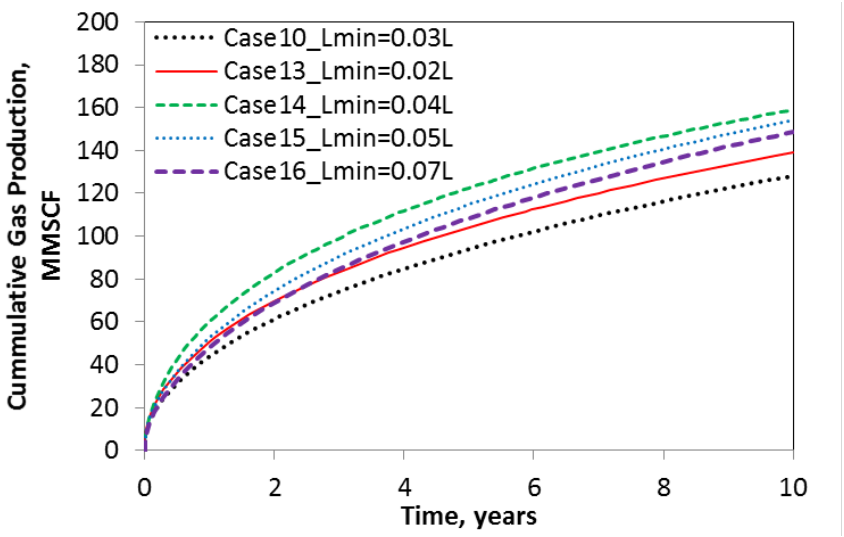


**(a)**

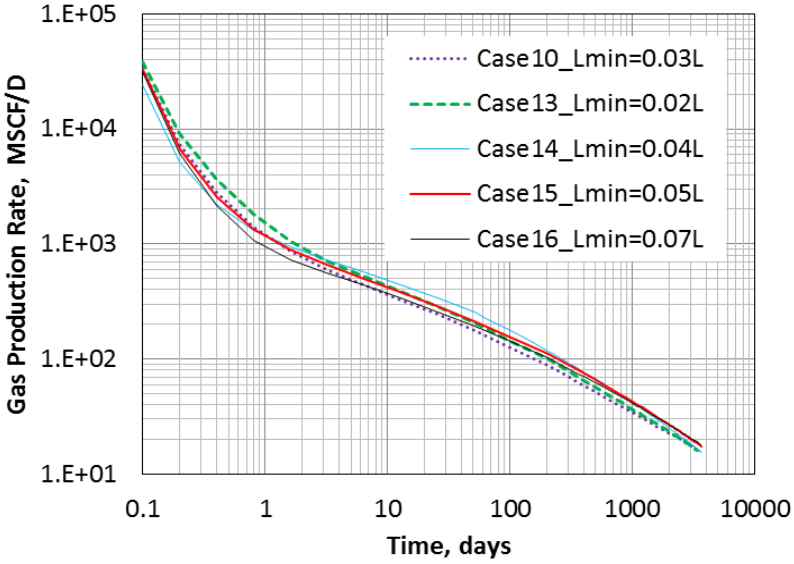


**(b)**

**Fig. 22 – Sensitivity analysis of the effect of fracture length on production performance. "Case 10_Lmin=0.03 L" indicates cumulative gas production or production rate for Case 10 with fracture minimum length equal to 0.03 of the reservoir domain size.**

*4.1.2.5 Natural Fracture Orientation and Strike*

Finally, in **Table 7**, the effect of natural fracture strike and Fisher parameter (i.e., a standard deviation term from the mean value of the fracture strike) is investigated. In total, there are four cases. For the base Case 10, 80 percent of natural fractures are oriented in the direction of the first fracture set (80 degrees from the horizontal), and the rest 20 percent of fractures in the direction of the second fracture set (160 degrees from the horizontal). An "Inf" value of Fisher constant in this study means that there is no standard deviation from input strikes of fracture sets. Case 18 is different from Case 10 in that 80 percent of fractures are oriented in the second fracture set. Case 17 sets half of the natural fractures in each fracture set. Case 19 introduces a perturbation of fracture strike using a value of 20 for the Fisher constant. The rest of the parameters such as fracture spacing, fracture length, fracture permeability and aperture remain the same as Case 10.

| Case Number | Fisher K1 | Orientation Prob1 | Fracture Angle1 | Fisher ParK2 | Orientation Prob2 | Fracture Angle2 |
|---|---|---|---|---|---|---|
| 10 | inf | 0.8 | 80 | inf | 0.2 | 160 |
| 17 | inf | 0.5 | 80 | inf | 0.5 | 160 |
| 18 | inf | 0.2 | 80 | inf | 0.8 | 160 |
| 19 | 20 | 0.8 | 80 | 20 | 0.2 | 160 |

**Table 7 – Sensitivity analysis of natural fracture strike related parameters.**

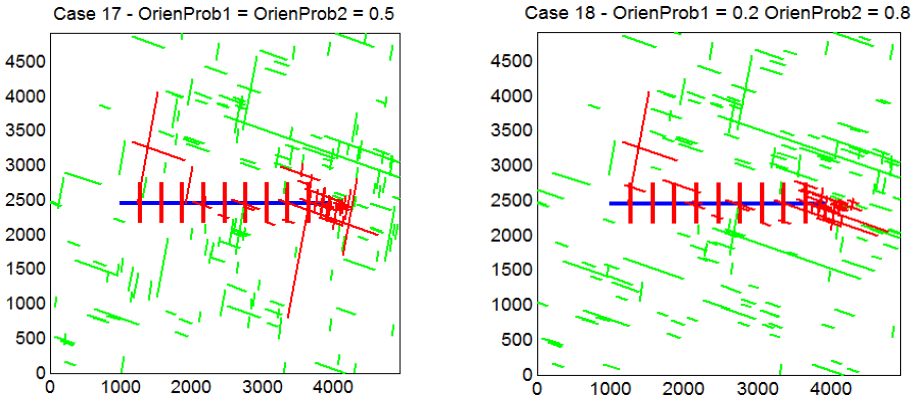


**(a)** **(b)**

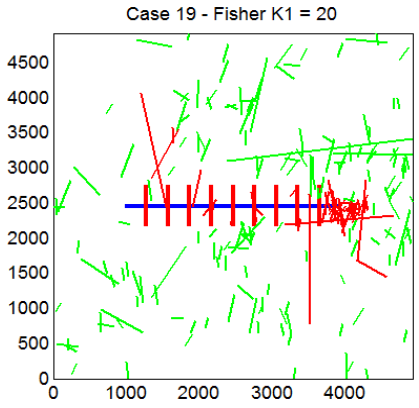


**(c)**

**Fig. 23 – Sensitivity analysis of fracture strike for Case 17 to Case 19. In Case 17, half of the fractures are orientated in one fracture set, and half in the other. In Case 18, 20% of the fractures are oriented in the first fracture set, and 80% in the other. In Case 19, a value of fisher constant 20 is given to the base Case 10.**

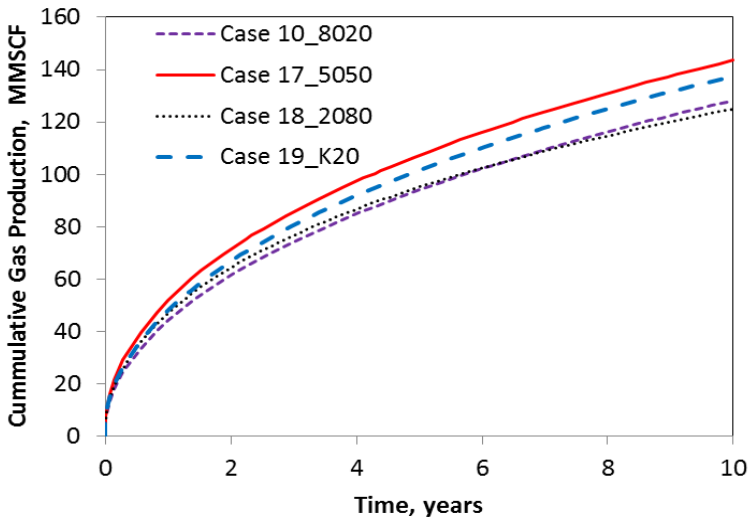


**(a)**

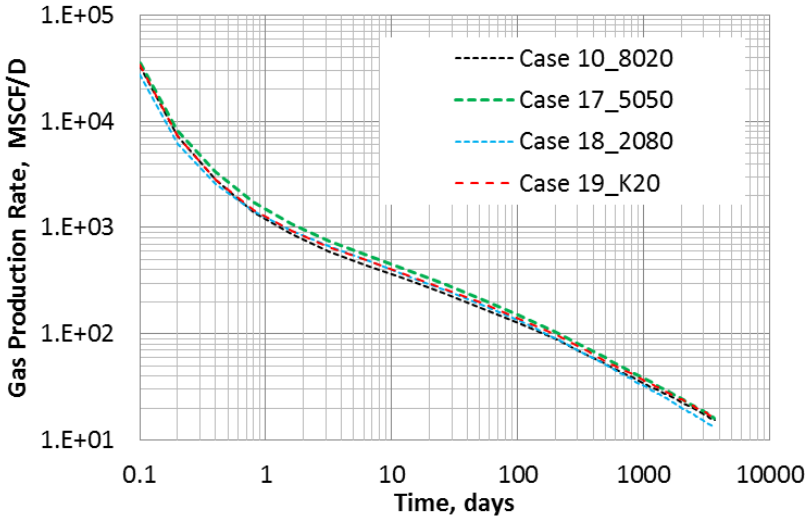


**(b)**

**Fig. 24 – Sensitivity analysis of the effect of fracture strike on production performance. "Case 10_8020" indicates cumulative gas production or production rate for Case 10 with two fracture sets, in which 80% of total natural fractures belong to the first fracture set, and the rest 20% to the second fracture set.**

**Fig. 23** summarizes DFN plan views for the three cases. Comparing Case 19 with Case 10, most of the fractures in Case 19 are still generated in the same locations with the same length and general trend as Case 10, whereas with only a small angle perturbation.

From **Fig. 24**, Case 17 and Case 19 show the best production performance than the other cases. Case 17 with equally distributed fractures in each fracture set increases the chance of creating a complex DFN with a larger SRV. Similarly, even though we see poor performance in the base Case 10, a small angle perturbation in Case 19 creates a more complex DFN and thus better production performance. Case 18 is the poorest performing case because most of the natural fractures are oriented along the direction of the horizontal well. Therefore, in order to optimize production performance, it is preferable to have natural fractures equally distributed in each fracture set. Strike uncertainty reflected by the Fisher constant will help increase the SRV of the DFN. Obviously, horizontal wells should be drilled in the direction perpendicular to the fracture strike of the most dominant fracture set provided a bottom water aquifer is not present.

## *4.2 Microseismic-Based Characterization Approach*

Microseismic data recorded during hydraulic fracturing treatments is commonly used to constrain the modeling of pre-existing natural fractures. To include microseismicity in the DFN modeling, it is reasonable to assume that microseismic event locations constrain the location of natural fractures, since, reactivation of plane of weaknesses is regarded as one of the main mechanisms of induced microseismicity (Warpinski et al. 2013). This assumption is incorporated in the proposed microseismic-constrained DFN generation approach by considering that only one fracture can pass through an event location. Regarding fracture geometrical properties, fractures are assumed to be planes that are perpendicular and fully penetrating to a horizontal pay layer, in consequence fracture size and orientation are completely described by its fracture trace length and strike, respectively.

In the section 4.2.1, we will briefly discuss about pros and cons of the previous microseismic-constrained DFN generation technique developed by Gamboa (2014). More details can be referred to Gamboa's thesis. Then, section 4.2.2 to section 4.2.4 will be devoted to a field example from Lower Spraberry, through which we will illustrate how to apply the developed approach to model and simulate a single-stage DFN, and most importantly, perform uncertainty analysis on a new important concept – fluid-producing DFN (FP-DFN).

### 4.2.1 Microseismic-Constraint Discrete Fracture Network

Gamboa (2014) proposed a technique to incooperate microseismic information into the process of the DFN generation. The main advantage is to generate stochastic natural fracture DFN models honoring both microseismic event locations and core data (e.g., fracture length and density distributions). However, no actual hydraulic propagation mechanics are implemented. Instead, hydraulic fractures are generated by randomly connecting existing natural fractures. Therefore, it is extremely important to evaluate the uncertainty of the resulting DFN, from which we expect to obtain a range of production performance corresponding to different uncertainty levels.

The first step of DFN generation is to allocate microseismic event locations to different fracture sets with the following two assumptions. For a system with two fracture sets, the total number of microseismic events is assumed to equal to the sum of natural fractures of each set. The other assumption is that the ratio between the numbers of microseismic events for each set is the same as the ratio between the numbers of fractures per set. This way, we can compute the number of fractures in each set. After obtaining the number of events for each fracture set, the second step is that microseismic locations are assigned randomly to a fracture set until the required number and ratio are completed. The third step is to generate the fracture orientation and length, which are sampled from respective distributions. Finally, natural fractures are then interconnected with hydraulic fracture branches, which are generated perpendicular to the well trajectory.

Since unconnected fractures to the hydraulic-natural fracture network can be considered as unable to contribute to production due to the negligible flow-transport capability of the matrix. In consequence, permeability estimations are only necessary for the interconnected hydraulic-natural fracture network, identified hereafter as the fluid-producing DFN (FP-DFN). The area of the FP-DFN is proposed as the representative output of a DFN realization since it provides a quantitative result that reflects the extent of interconnectivity between natural and hydraulic fractures.

### 4.2.2 Input Data of Lower Spraberry Case

**Fig. 25** shows two natural fracture sets in the Lower Spraberry Formation. One set is striking EW in average, parallel to the current maximum horizontal stress. The second set is striking N 35º E in average. A horizontal well was drilled close to 180 º and was hydraulically fractured with 15 stages. A receiver array placed in a nearby vertical was used to record induced microseismicity. The microseismic event locations are shown in **Fig. 26**, from which we see that the average azimuthal direction of the microseismic cloud induced by the stimulation treatment follows the direction of the maximum horizontal stress.

Stage 8 of the stimulation treatment is chosen as a representative to apply the pervious microseismic-constraint DFN generation and DFN simulation techniques for evaluating the impact of fracture parameter uncertainties on the FP-DFN and production performance. Different DFN realizations are generated for stage 8 using input values in **Table 8**.

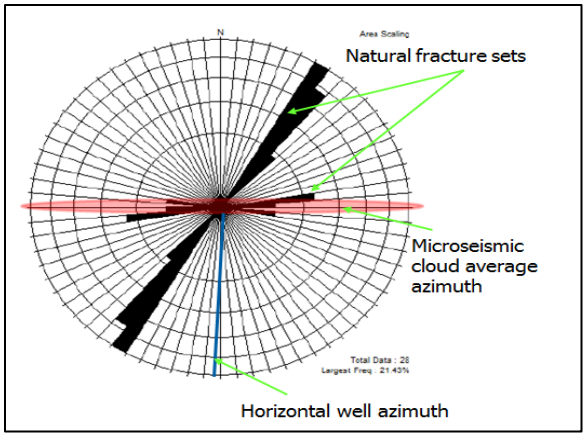


**Fig. 25 – The azimuth of the two natural fracture sets present in the reservoir as well as the azimuth direction of the stimulated well and the average direction of the induced microseismic cloud.**

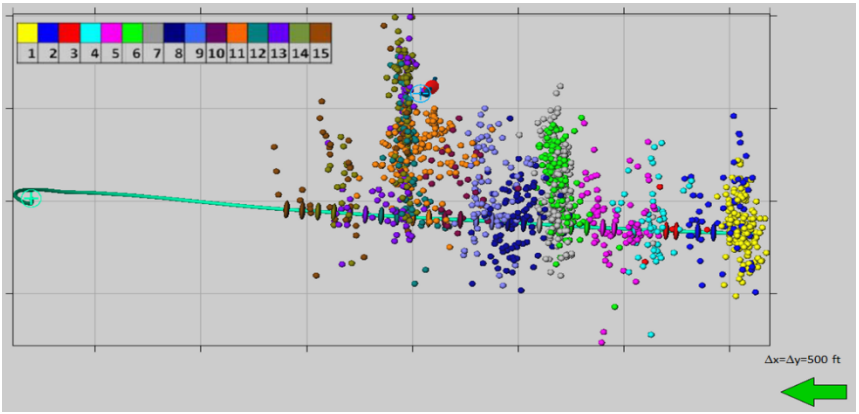


**Fig. 26 – The locations of the microseismic events induced by the hydraulic fracturing stimulation treatment. Event locations for the 15 stages are differentiated by color and the green arrow points toward North.**

| Fracture Sets | Set 1 (N 35 deg. E) | Set 2 (E-W) |
|---|---|---|
| Mean Strike | 35 deg. | 90 deg. |
| Fisher Parameter | 120 | 80 |
| Minimum Fracture Length | 10 ft. | 10 ft. |
| Maximum Fracture Length | 150 ft. | 150 ft. |
| Power Law Exponent | 0.8 | 0.9 |

**Table 8 – The input parameters for the PDF of the stage 8 DFN model.**

| | | | |
|---|---|---|---|
| Matrix Porosity | 0.06 | Initial Reservoir Pressure (psi) | 8000 |
| Matrix Permeability (md) | 0.0001 | Reference Pressure (psi) | 8000 |
| Rock compressibility (1/psi) | 3.40E-06 | Reference Datum Depth (ft.) | 10150 |
| Reservoir Length (ft.) | 1011 | Saturation Pressure (psi) | 4000 |
| Reservoir Width (ft.) | 451 | Water Density (lb./ft3) | 62.4 |
| Reservoir Height (ft.) | 300 | Water Compressibility (1/psi) | 3.36E-6 |
| Reservoir Top Depth (ft.) | 10000 | Water Viscosity (cp) | 0.2053 |
| Hydraulic Fracture width (ft.) | 0.01 | Water Formation Volume Factor | 1.0803 |
| Hydraulic Fracture porosity | 0.3 | Three-phase Calculation Model | STONE 2 |

**Table 9 – Reservoir and fluid parameters for DFN simulation.**

**Table 9** and **Table 10** summarize the reservoir, rock, and fluid parameters for DFN simulation. A black-oil model is built to evaluate and compare production performance of different DFN realizations.

**Table 11** and **Table 12** show a volatile black-oil fluid model with PVT properties of both the saturated and unsaturated oil tables. A horizontal well produces from the single stage 8 at a constant rate of 100 bbl./d, together with the minimum bottom-hole flowing pressure constraint at 3000 psi. All DFN simulations are run up to around 10 years.

| Sw | Krw | Krow | Sg | Krg | Krog |
|---|---|---|---|---|---|
| 0.25 | 0 | 1 | 0 | 0 | 1 |
| 0.3 | 0 | 0.656 | 0.05 | 0.001 | 0.826 |
| 0.356 | 0.002 | 0.385 | 0.113 | 0.009 | 0.633 |
| 0.413 | 0.009 | 0.208 | 0.175 | 0.038 | 0.465 |
| 0.469 | 0.021 | 0.1 | 0.238 | 0.084 | 0.323 |
| 0.525 | 0.038 | 0.041 | 0.3 | 0.15 | 0.207 |
| 0.581 | 0.059 | 0.013 | 0.363 | 0.234 | 0.116 |
| 0.625 | 0.079 | 0.005 | 0.375 | 0.255 | 0.103 |
| 0.638 | 0.084 | 0.003 | 0.425 | 0.338 | 0.052 |
| 0.694 | 0.115 | 0 | 0.488 | 0.459 | 0.013 |
| 0.75 | 0.15 | 0 | 0.55 | 0.6 | 0 |
| 1 | 1 | 0 | 0.75 | 0.8 | 0 |

**Table 10 – Input oil and gas relative permeability curves.**

| Pressure (psia) | $B_o$ (RB/STB) | $\mu_o$ (cp) |
|---|---|---|
| 4962 | 2.4309 | 0.0858 |
| 5824 | 2.3733 | 0.0925 |
| 6686 | 2.3248 | 0.0993 |
| 7548 | 2.2831 | 0.1061 |
| 8410 | 2.2464 | 0.1128 |
| 9272 | 2.2139 | 0.1196 |
| 10134 | 2.1847 | 0.1263 |

**Table 11 – PVT properties of the unsaturated oil table.**

| P (psia) | $B_o$ (RB/STB) | $\mu_o$ (cp) | $R_s$ (MSCF/STB) | $B_g$ (RB/MSCF) | $\mu_g$ (cp) |
|---|---|---|---|---|---|
| 15 | 1.098 | 0.5305 | 0.0185 | 260.4 | 0.0127 |
| 468.9 | 1.204 | 0.3711 | 0.2327 | 7.783 | 0.0135 |
| 922.8 | 1.35 | 0.296 | 0.4343 | 3.711 | 0.0151 |
| 1377 | 1.522 | 0.2522 | 0.649 | 2.365 | 0.0173 |
| 1831 | 1.715 | 0.2228 | 0.8806 | 1.728 | 0.0202 |
| 2284 | 1.927 | 0.2013 | 1.131 | 1.382 | 0.0237 |
| 2738 | 2.161 | 0.1847 | 1.401 | 1.177 | 0.0275 |
| 3192 | 2.398 | 0.1714 | 1.694 | 1.048 | 0.0312 |
| 3646 | 2.629 | 0.1605 | 2.009 | 0.9599 | 0.0348 |
| 4100 | 2.855 | 0.1513 | 2.35 | 0.8966 | 0.0383 |

**Table 12 – PVT properties of the saturated oil table.**

### 4.2.3 Uncertainty Analysis

In the context of stochastic modeling, it is important to evaluate two types of uncertainties. The first type of uncertainty arises from the stochastic nature of the proposed algorithms, i.e., the same input parameter in **Table 8** will produce different DFN realizations. The second type of uncertainty results from the lack of perfect knowledge of model input parameters in **Table 8**, and thus we need to vary each parameter and investigate their impact on production performance. Monte Carlo (MC) based techniques are used for uncertainty analysis in this example with Latin hypercube design as the sampling approach. In addition, fracture conductivity is interpreted from lab measurement based on proppant concentration and stress.

In section 4.2.3.1, we will introduce the methodology to obtain the mean FP-DFN area, which is considered to be representative of the stochastic modeling based on

input parameters in **Table 8**. In the following section, we will address uncertainties of input parameters. Each parameter is assumed to follow a predefined probabilistic density function, and for each combination of the sampled parameters, the mean FP-DFN is estimated. At the end a cumulative distribution function (CDF) is obtained which incorporates combined uncertainties into production estimation.

*4.2.3.1 The Mean FP-DFN Model*

After 50-batch runs (where each batch represents 10 Monte Carlo simulations) of DFN generation algorithms with the input parameters in **Table 8**, the histogram of the FP-DFN area is shown in **Fig. 27**. For simplicity, we express FP-DFN results as a ratio of the estimated FP-DFN area divided by the area of a reference straight hydraulic fracture, which is equal to 240,000 $ft^2$. Note that the histogram is fitted very well with a normal PDF, from which the mean and the mean +/-2 standard deviations are summarized in **Table 13**, together with the interpolated conductivity values. The DFN realization with the closest FP-DFN area to the mean is selected as the expected realization in **Fig. 28**. The realizations corresponding to the mean +/- 2 standard deviation are presented in **Fig. 29** and **Fig. 30**, respectively. **Fig. 31** shows the gridded models for the three FP-DFN models, and **Fig. 32** plots corresponding cumulative oil production up to 10 years.

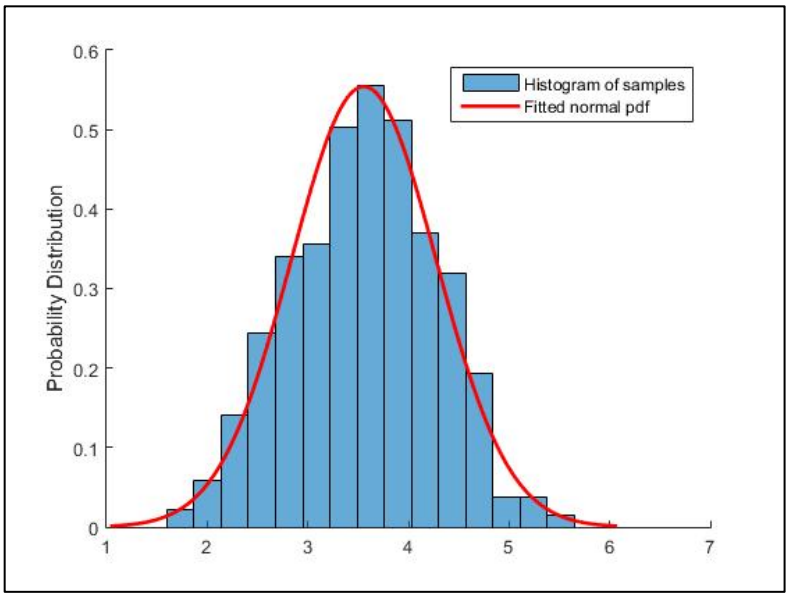


**Fig. 27 – The histogram of the FP-DFN area after 50 batches run and the respective fitted normal PDF.**

| | Area Ratio | Conductivity (mD-ft.) |
|---|---|---|
| Reference Hydraulic Fracture | 1.00 | 124.95 |
| Mean DFN Area | 3.56 | 39.84 |
| Mean DFN Area + 2 std | 4.98 | 28.60 |
| Mean DFN Area - 2 std | 2.12 | 58.37 |

**Table 13 – The estimated FP-DFN areas corresponding to mean, mean +/- 2 standard deviation, and the reference hydraulic fracture.**

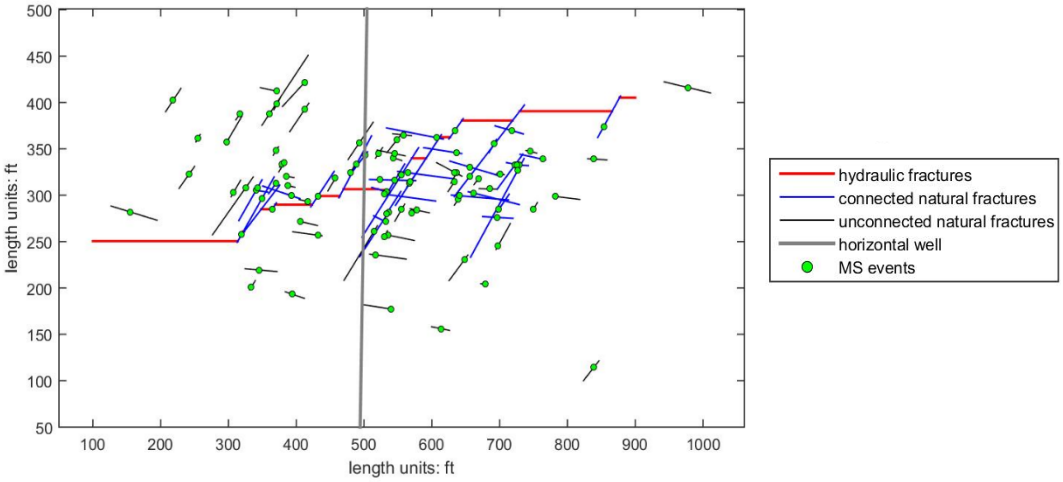


**Fig. 28 – The top view of fracture geometry for the mean FP-DFN.**

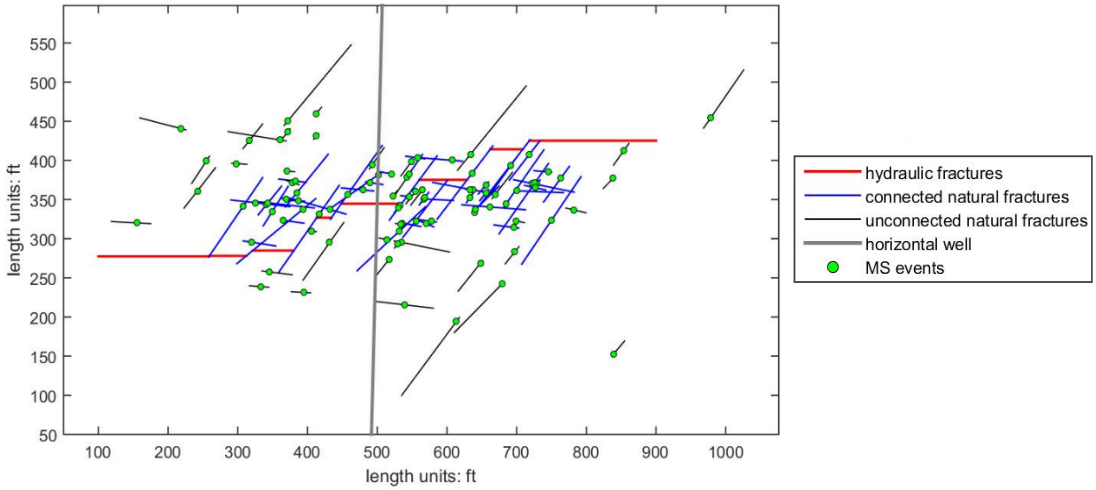


**Fig. 29 – The DFN geometry of the FP-DFN area corresponding to mean + 2 standard deviation.**

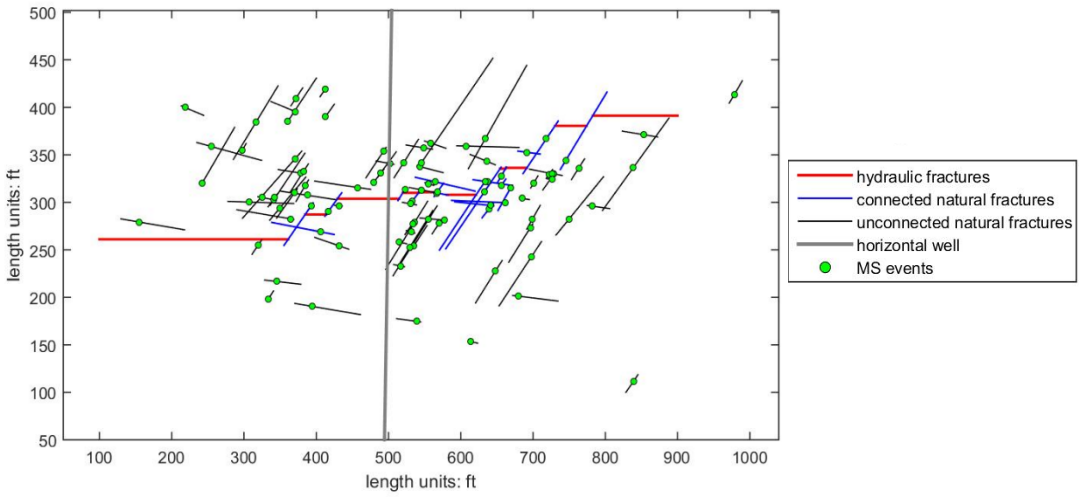


**Fig. 30 – The DFN geometry of the FP-DFN area corresponding to mean - 2 standard deviation**

According to the 10 year production simulation as shown in **Fig. 32** and **Fig. 33**, the difference in production between + and -2 standard deviation is a little larger than 10 MSTB, revealing the impact of uncertainty on production. The highest value (mean FP-DFN +2 standard deviation) and lowest value (mean FP-DFN -2 standard deviation) of production estimates would correspond approximately to P2 and P97 of the DFN occurrences respectively, covering 95% of the possible DFN realizations, and the expected production forecast would correspond to P50 of the FP-DFN area occurrences.

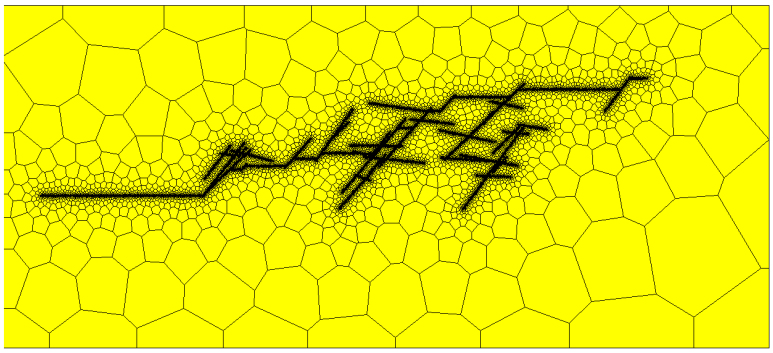

**(a)**

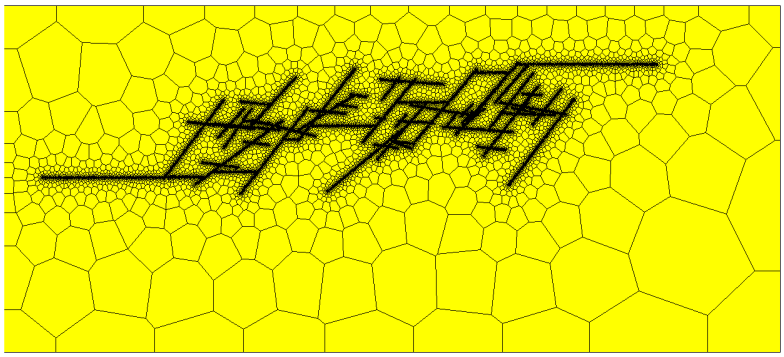

**(b)**

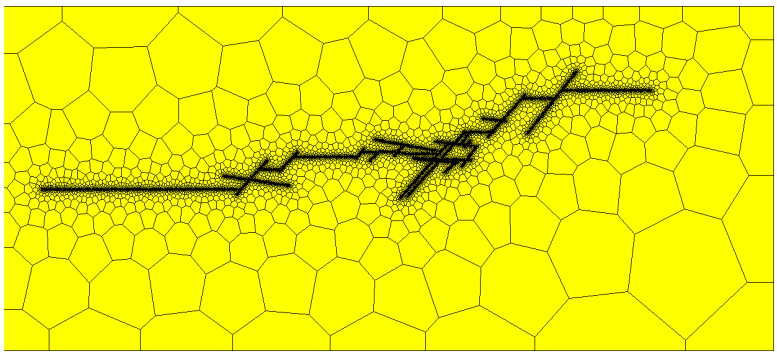

**(c)**

**Fig. 31 – The gridded unstructured models for FP-DFN realizations (mean (a), plus 2 standard deviation (b), and minus 2 standard deviation (c)).**

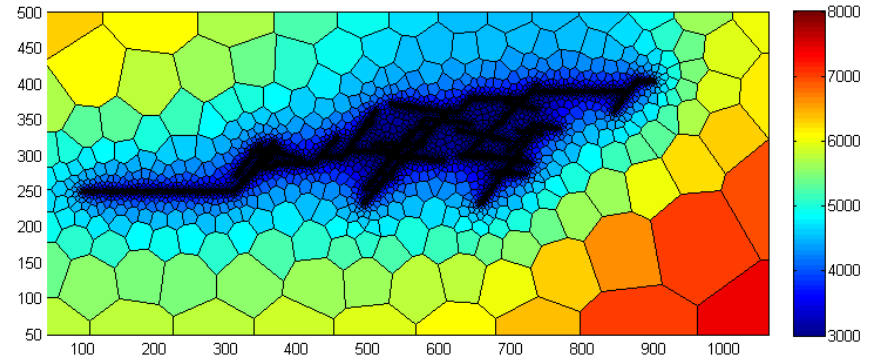


**(a)**

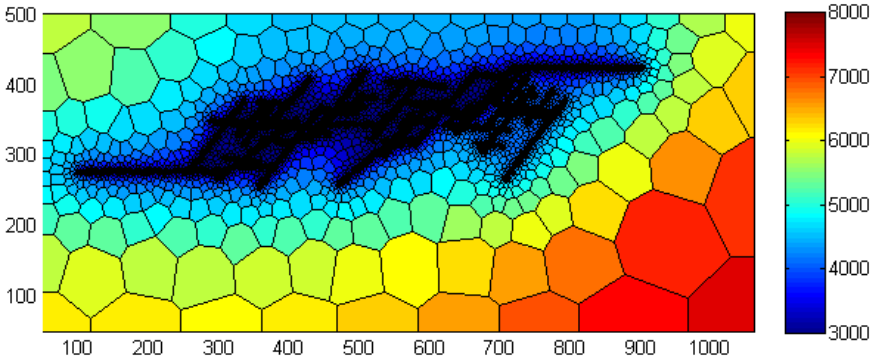


**(b)**

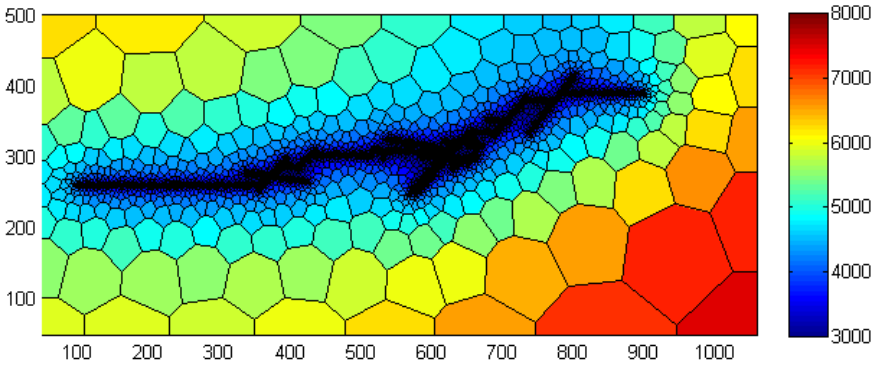


**(c)**

**Fig. 32 – The pressure graphs at the end of 10 years' simulation for FP-DFN (mean (a), plus 2 standard deviation(b), and minus 2 standard deviation(c) ).**

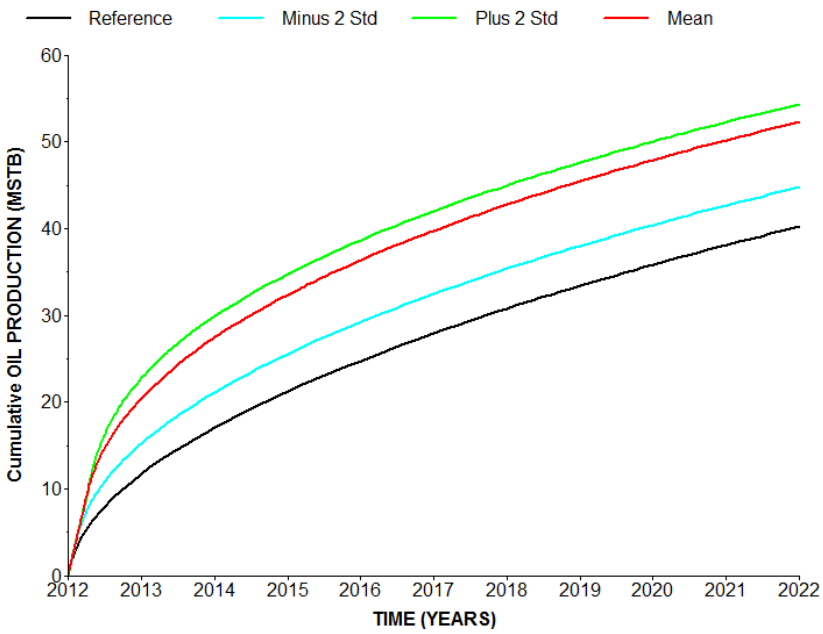


**Fig. 33 – The cumulative oil production for FP-DFN realizations (mean, plus 2 standard deviation, and minus 2 standard deviation) and the reference model.**

*4.2.3.2 Sensitivity Analysis of Input Parameters*

The sensitivity analysis is performed by varying one input parameter at a time from 0.5 to 1.5 times of its reference value in increments of 0.1. For each value that this parameter can take, Monte Carlo simulations are run until the mean of the FP-DFN area converges within 1%. For this case, we assume that the minimum length for the power law is a known constant for both fracture sets as well as the mean strikes. Results indicate that the Maximum length is the parameter that produces the most variations in the expected FP-DFN area in both fracture sets. Therefore, the effect of uncertainties of maximum length is analyzed since this is the parameter that has the highest impact in the variation of expected FP-DFN area.

Uncertainties in the maximum length for each fracture set is represented by a uniform distribution with equal probability for values from 0.5 to 1.5 times the reference maximum length. To quantify the effect of these uncertainties, a CDF is built by Monte Carlo simulations, from which 5 percentiles are estimated and shown in **Table 14**.

Finally, a 10-year production is simulated for the selected percentiles in **Table 14**. For the five DFN models (**Fig. 34**) corresponding to five different percentiles, similar simulation approach as the previous section is applied to evaluate production performance. **Fig. 35** and **Fig. 36** show the gridded models and the cumulative oil production plots, respectively. Notice that there does not exist a linear relationship among the percentiles, and that there is a difference of at least 10 MSTB between P5 and P95, the lowest and highest percentiles. The initial oil in place is around 499.6 MSTB, so recovery factors are around 9% to 12% for P5 and P95, respectively. Note that recovery factors depend on production time and reservoir dimensions, which explain why we have relatively higher recovery factors for these cases.

| Percentiles | P5 | P10 | P50 | P90 | P95 |
|---|---|---|---|---|---|
| FP-DFN Area | 2.16 | 2.33 | 3.26 | 4.84 | 5.15 |
| Conductivity (mD-ft.) | 58.1 | 55.7 | 43.2 | 29.5 | 27.9 |

**Table 14 – The percentiles selected for simulation, and the respective FP-DFN area and conductivity values.**

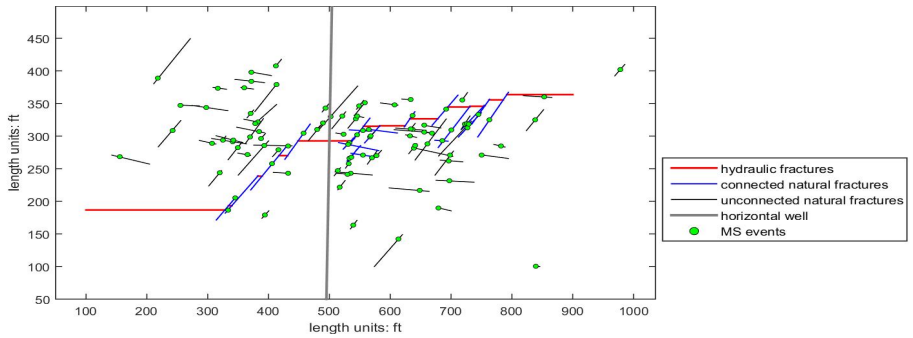


**(a)**

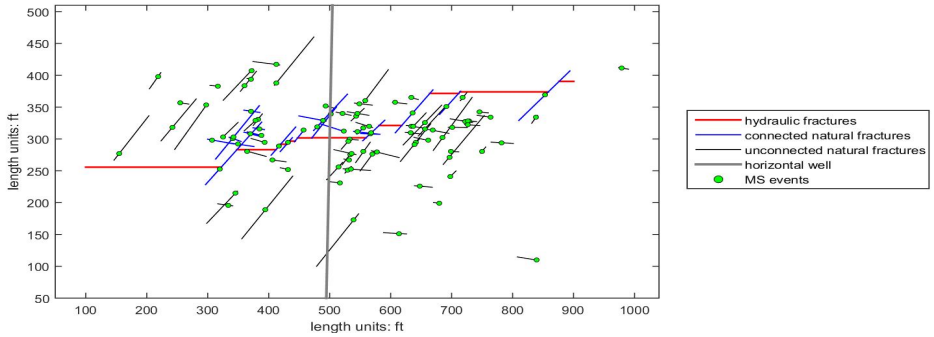


**(b)**

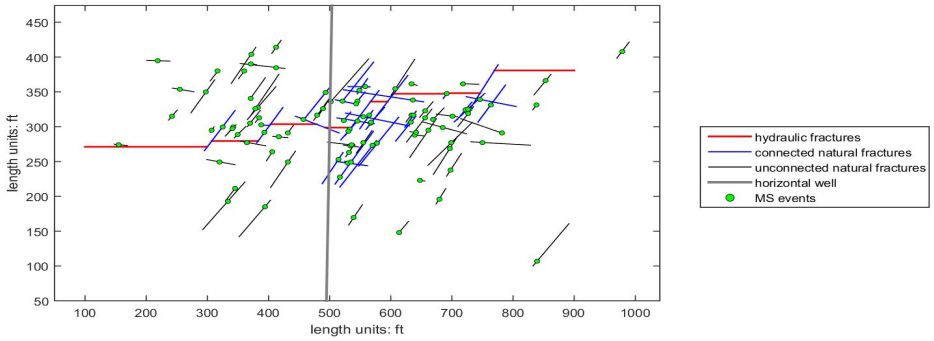


**(c)**

**Fig. 34 – The FP-DFN geometry corresponding to the P5 (a), P10 (b), P50 (c), P90 (d), and P95 (e) FP-DFN areas.**

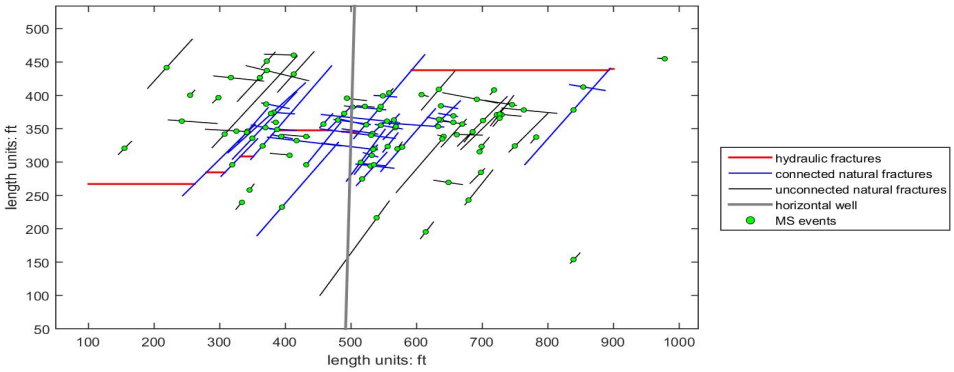


**(d)**

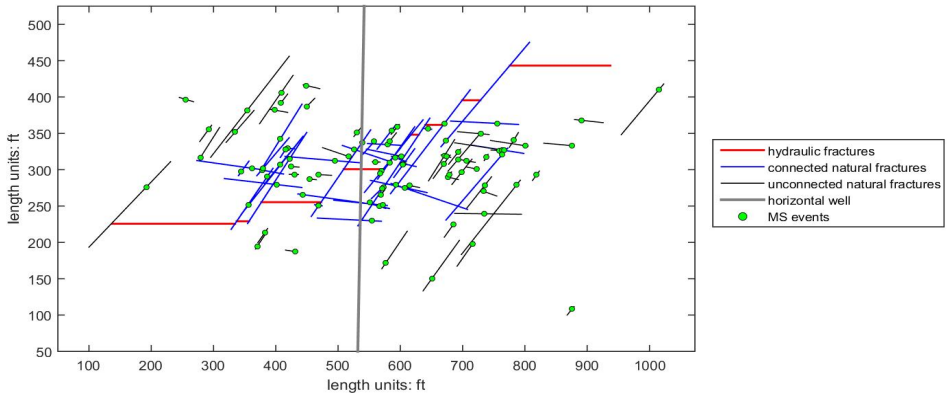


**(e)**

**Fig. 34 – Continued**

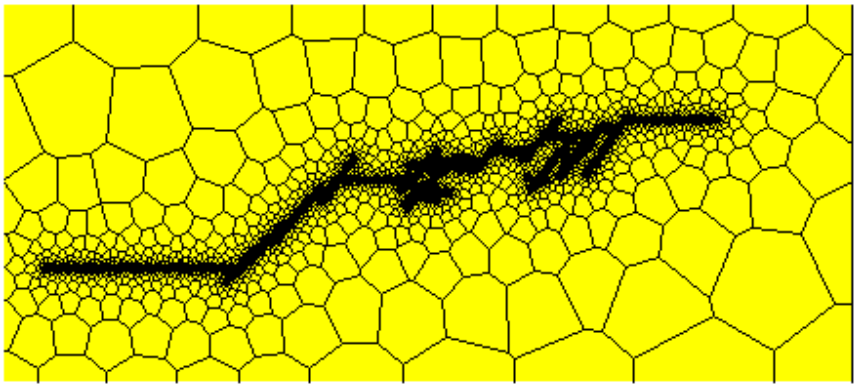

**(a)**

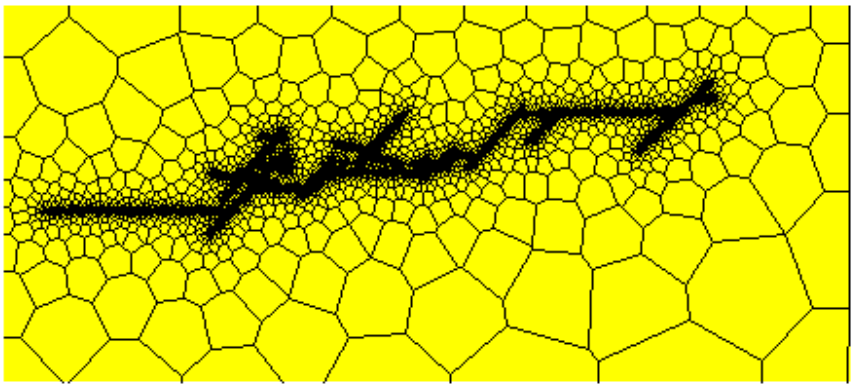

**(b)**

**Fig. 35 – The gridded models for the DFN realizations corresponding to 5 (a), 10 (b), 50 (c), 90 (d), and 95 (e) percentiles.**

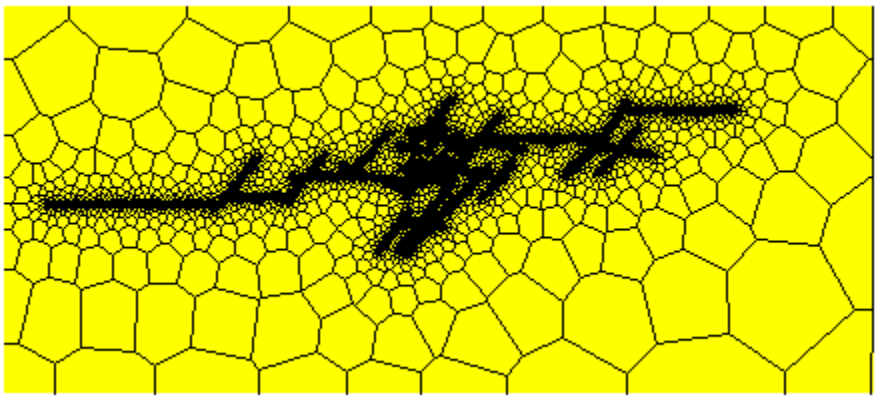

**(c)**

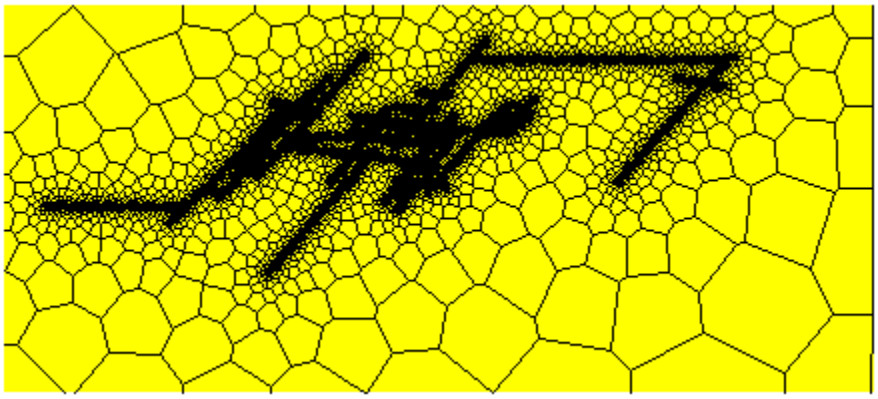

**(d)**

**Fig. 35 – Continued.**

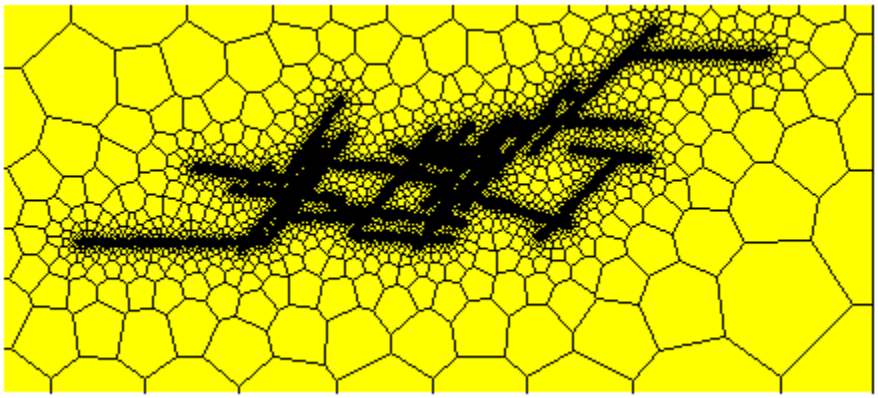

**(e)**

**Fig. 35 – Continued.**

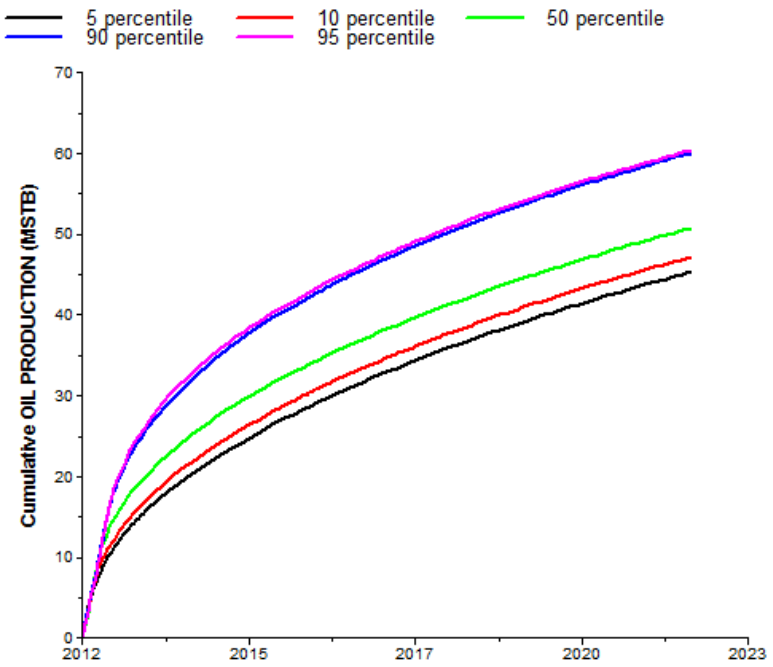


**Fig. 36 – The fluid flow simulations for the DFN realizations corresponding to 5, 10, 50, 90, and 95 percentiles.**

*4.3 Outcrop-Based Characterization Approach*

Outcrop maps present useful information regarding how natural fractures are distributed underground. In this section, we will take the Eagle Ford outcrop maps as an example to demonstrate how to incooperate available outcrop data into fracture characterization and simulation process.

### 4.3.1 Outcrop Maps for the Eagle Ford Formation

Mode I extension fractures are very common in outcrop maps. Ferrill et al. (2014) outlines the outcrop maps for the Eagle Ford Formation. **Fig. 37** shows the west pavement of the mapped outcrop. Bed I, II and III show very well formed fracture networks, which contributes to well production if being hydraulically fractured. Fractures in Bed 1 are composed of two main fracture sets. The first fracture set strikes around N50°E, and the other around N310°E or N50°W. In addition, two fracture sets observed in the outcrop exposure were barren of mineral fill as determined by hand lens inspection, and thus we expect there exist similar extensive and open natural fractures underground which contribute significantly to production performance. The longest and most consistently oriented fractures are the N50°E-striking set, which are interpreted to be the first formed joints. The approximately orthogonal N310°E-striking set appear to be the last formed joints, abutting the N50°E set.

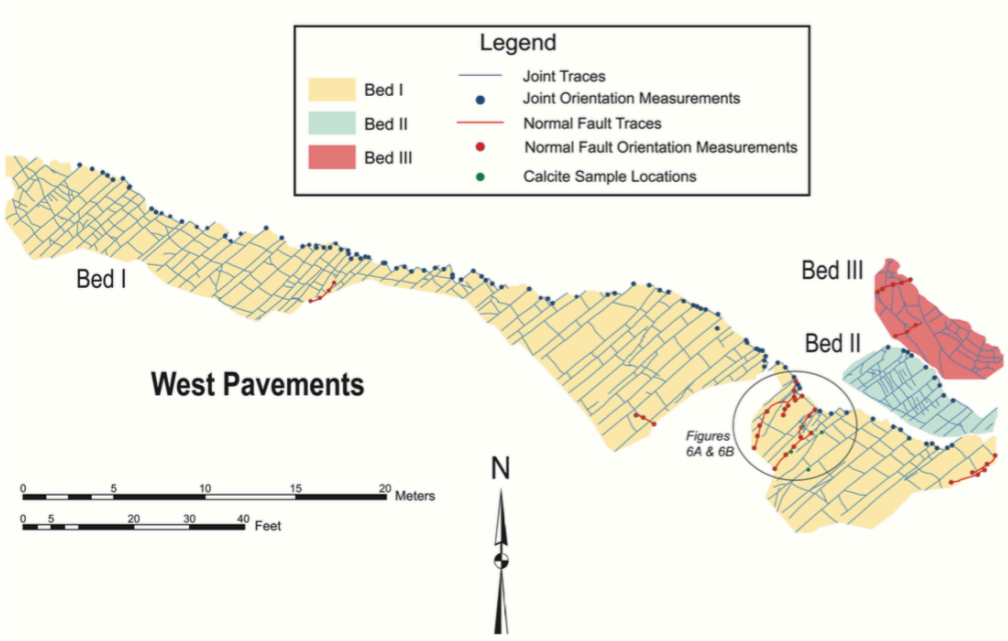


**Fig. 37 – Pavement maps and data from competent Beds I, II, and III, respectively Ferrill et al. (2014).**

### 4.3.2 Production Performance on a Single Outcrop Map Pattern

**Fig. 38** illustrates how to digitize the region highlighted by the red dotted cycle. According to the scale on the map, we first define both x and y scales, which is then followed by a line by line digitization. The final output consists of an N-by-4 matrix array, where N represents the number of fractures and each row corresponds to four coordinates of each fracture line segment. **Fig. 39** plots the digitized fracture geometry.

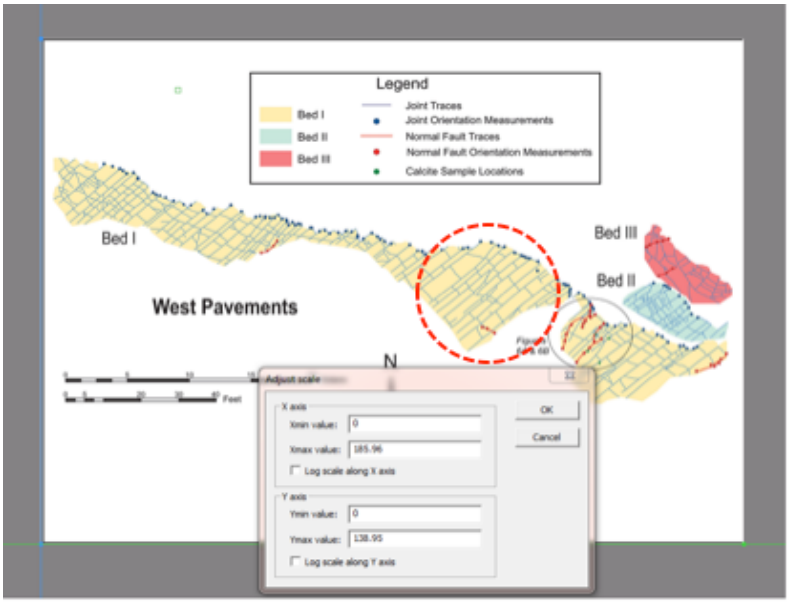


**Fig. 38 – X and Y unit scale, and the red-dotted circle highlights the outcrop region that will be digitized and simulated.**

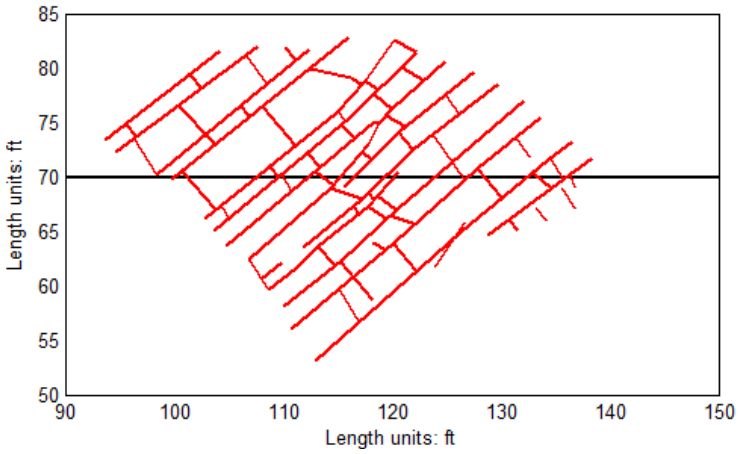


**Fig. 39 – Top view of the digitized outcrop map, and the horizontal well trajectory indicated by the black line.**

As seen in **Fig. 39**, natural fracture network presents a very dense distribution. And thus we neither overlay hydraulic fractures as what we did in the fractal-based characterization workflow, nor do we generate hydraulic fractures as what we did in the microseismic-based approach. Instead, we simply assume the horizontal well will produce from the whole natural fracture network. By applying the previous gridding and discretization technique, the single-pattern outcrop map in **Fig. 39** is gridded up with unstructured grids in **Fig. 40**.

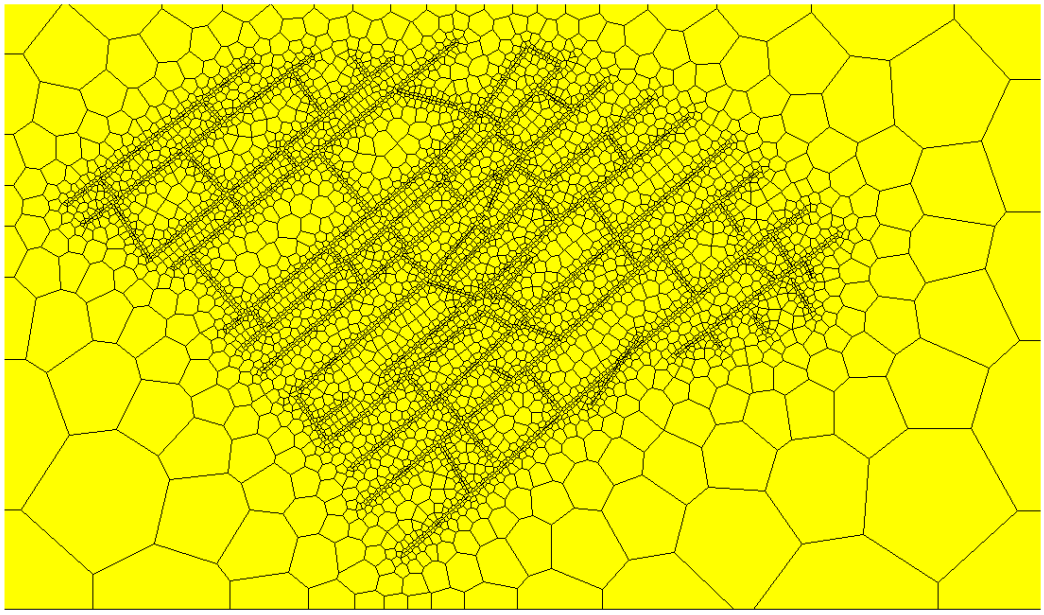

**Fig. 40 – Top view of the gridded outcrop pattern.**

With the same reservoir and fluid properties as the previous section 4.2.2, we will evaluate production performance from the outcrop map in **Fig. 40**. Instead of using a production rate constraint of 100 STB/day, we reduce the production to 10 STB/day

because the dimension of the reservoir in **Fig. 40** is relatively small. **Fig. 41** shows the cumulative oil production and production rate plots after around 1827 days' simulation. Note that oil production rate remains 10 STB/days for up to around 37 days, and then decline significantly because the bottom-hole flowing pressure constraint is set at 3000 psi and the fracture fluids have already been produced out.

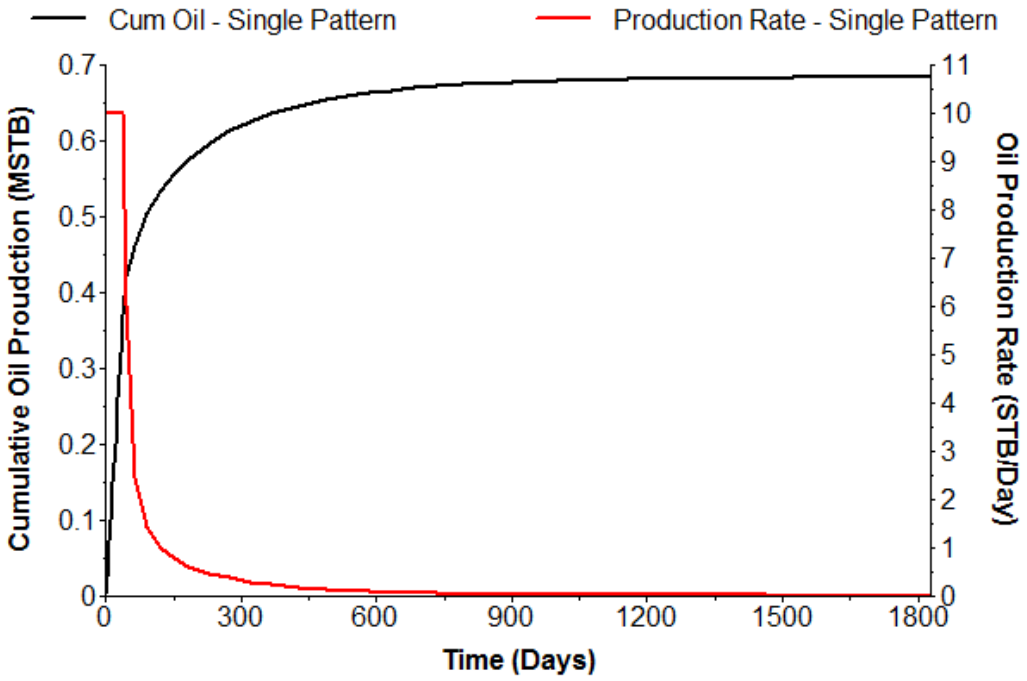


**Fig. 41 – Production performance of the single outcrop map pattern.**

**Fig. 42** and **Fig. 43** shows pressure graphs at 0.1 day, 37 days and 1827 days at the end of the simulation. During the early period less than 0.1 day, fractures contribute to well production. At around 37 days, the pressure propagation fronts hit the reservoir boundary, and thus 10 STB/day production rate cannot be satisfied any more. At the end

of the simulation, the whole reservoir reaches almost the bottom-hole flowing pressure of 3000 psi.

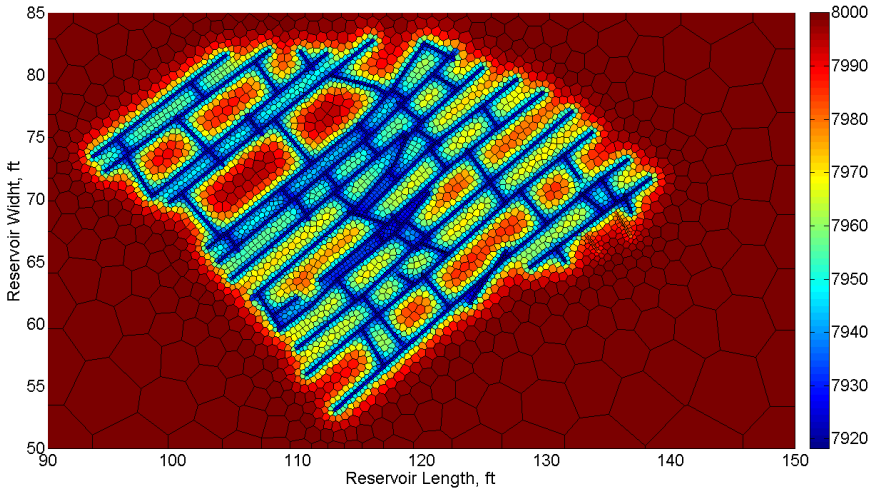


**Fig. 42 – Top view of the pressure graph after 0.1 days' simulation.**

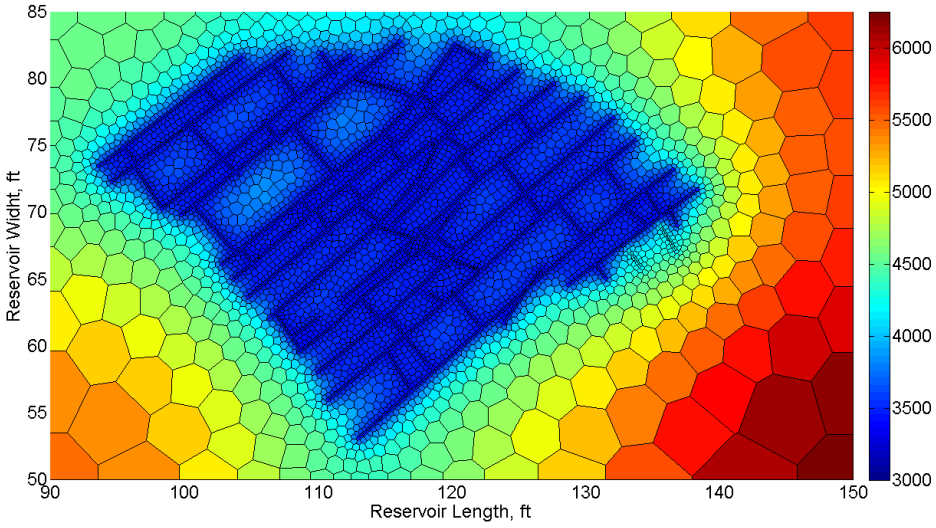


**Fig. 43 – Top view of the pressure graph after 37 days' simulation.**

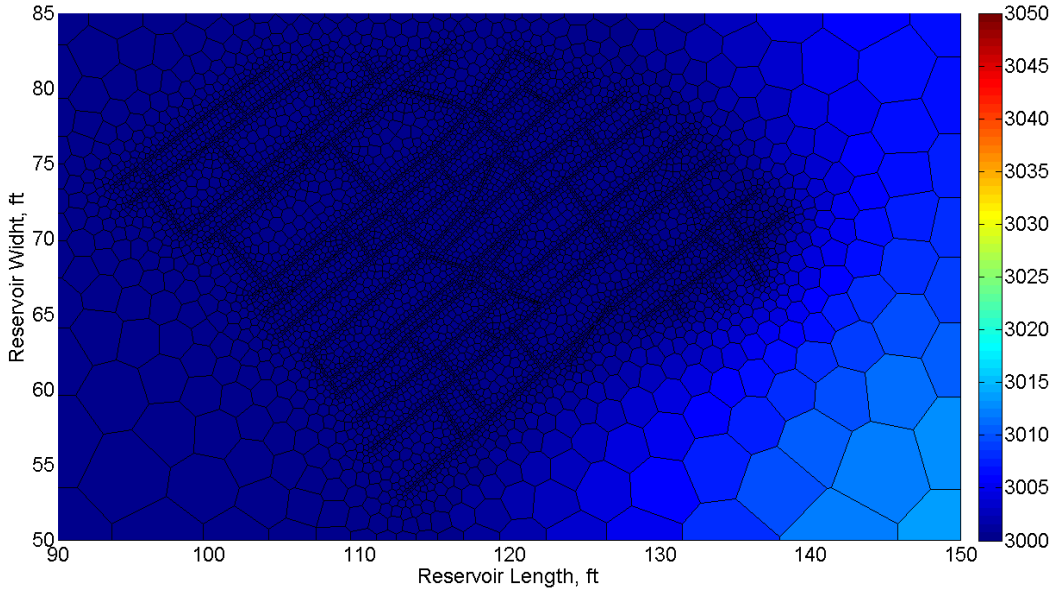


**Fig. 44 – Top view of the pressure graph at the end of the 1827 days' simulation.**

### 4.3.3 Production Performance on Duplicated Outcrop Map Pattern

In the previous example, we only show how to simulate production performance on one natural fracture pattern. However, in the field scale, we actually have hundreds and thousands of the same outcrop patterns as the one in **Fig. 39**. Therefore, in the section, we will extend the outcrop map both in the horizontal and vertical directions. **Fig. 45** shows a larger outcrop map, which consists of three patterns along the horizontal direction, and four patterns along the vertical direction.

Similarly, **Fig. 45** is gridded and discretized, and then used for simulation with reservoir and fluid properties in section 4.2.2. **Fig. 46** is the gridded model with 186,255 unstructured cells. **Fig. 47** is the enlarged view of the gridded model. **Fig. 48** is the

cumulative oil and production rate of both the duplicated outcrop map pattern and the previous single outcrop map pattern.

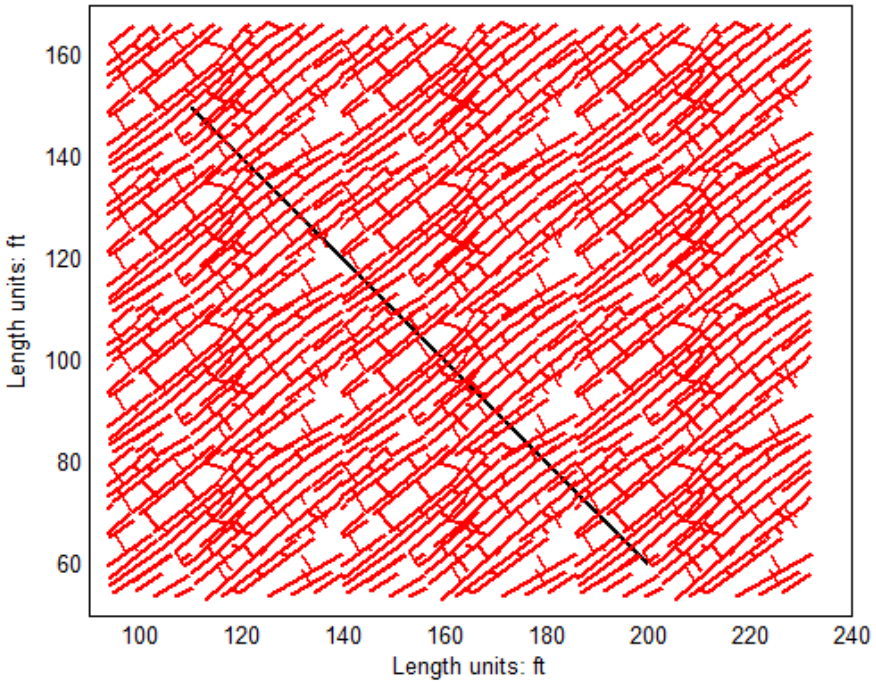


**Fig. 45 – Top view of the duplicated outcrop map, and the horizontal well trajectory indicated by the black line.**

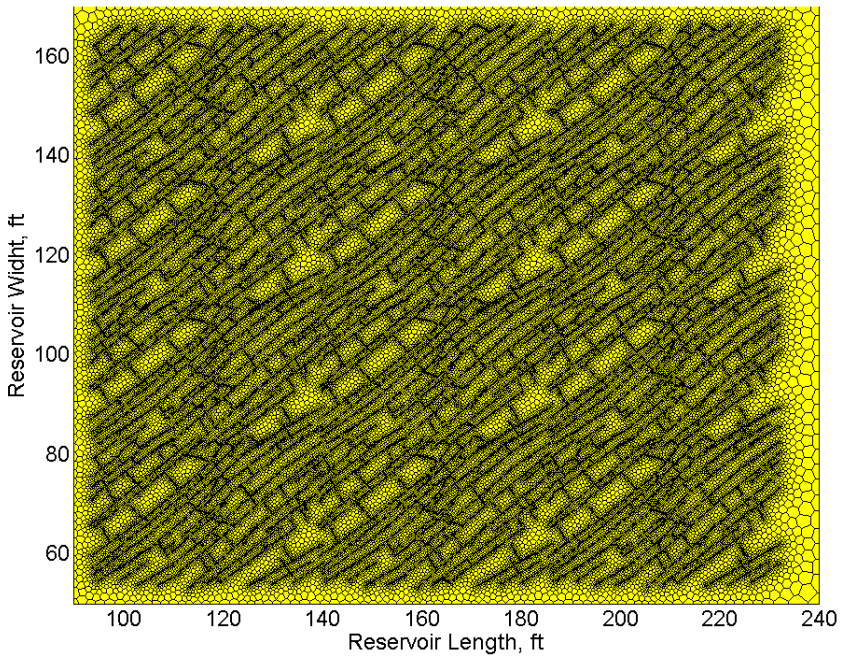


**Fig. 46 – Top view of the gridded outcrop pattern with 186255 unstructured cells.**

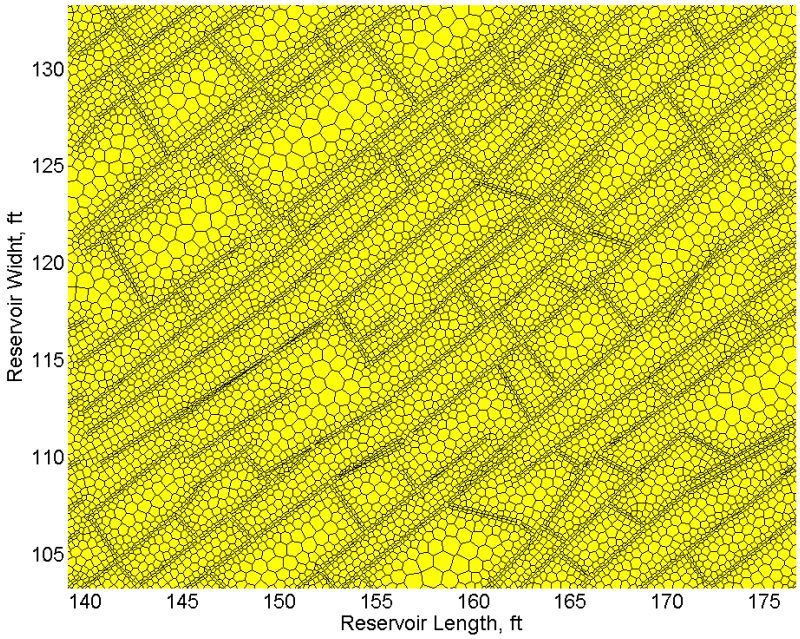


**Fig. 47 – Enlarged view of the unstructured grid for duplicated outcrop pattern.**

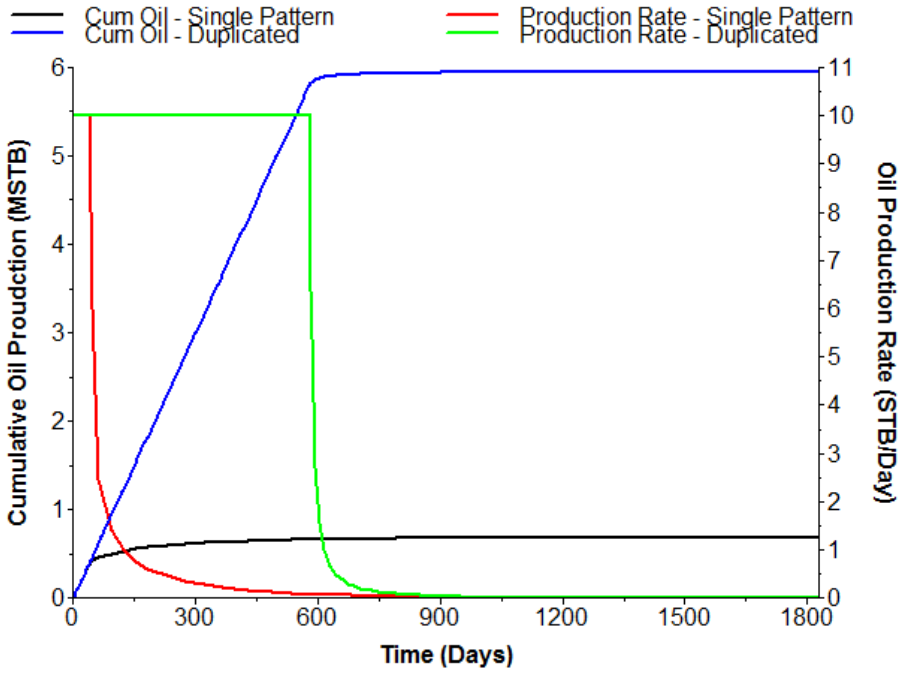


**Fig. 48 – Production performance of both the single and duplicated outcrop map patterns.**

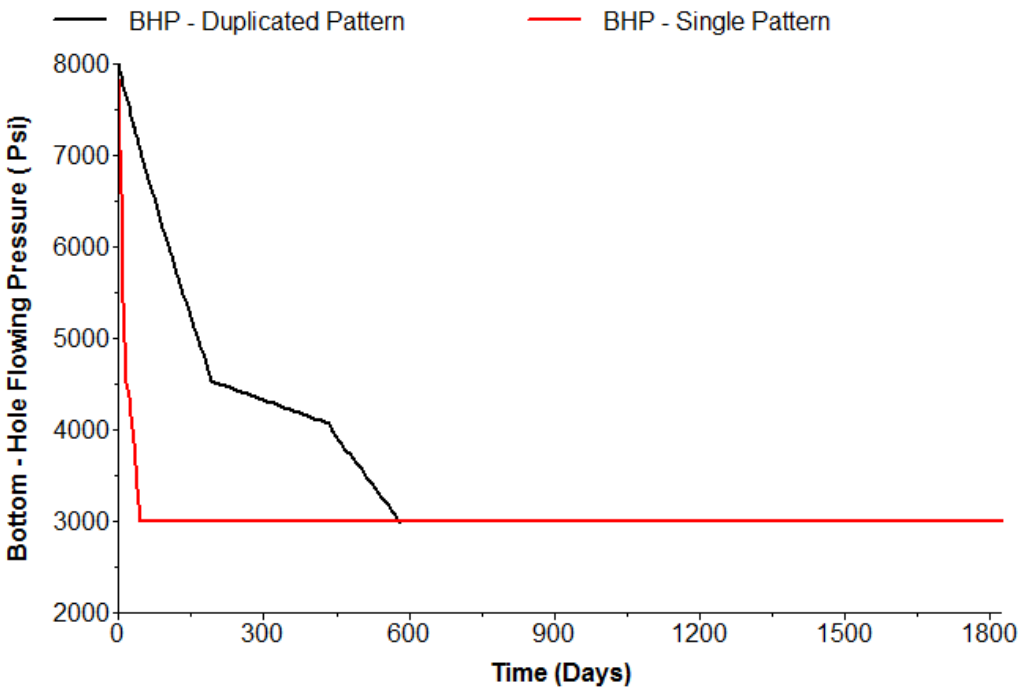


**Fig. 49 – Top view of the pressure graph after 1827 days' simulation.**

As seem in **Fig. 48**, the duplicated outcrop model remains the constant production rate of 10 STB/day until around 580 days, and then present a steep decline in production rate. Correspondingly, cumulative oil production shows straight-line production behavior, and then quickly approaches the plateau. Because the reservoir dimension is relatively too small to show the transient flow regime. After linear flow regime which corresponds to fracture flow, pressure propagation front reaches the reservoir boundary very quickly, and thus doesn't show a long period of the transient flow regime as seen in **Fig. 41**.

**Fig. 49** plots the bottom–hole flowing pressure (BHP) vs. production time. Up to 580 days (when the well constraint switches from the constant rate to the constant

pressure), we observe a linear flow behavior, because BHP decreases almost linearly with production time.

**Fig. 50** to **Fig. 53** plot pressure behavior at 0.1 day, 1 day, 580 days, and 1827 days. Fracture plays a dominant role in production performance. A linear flow production behavior is observed up to 580 days, during which the whole reservoir is nearly depleted as seen from the pressure graph in **Fig. 52.** After 600 days, the production rate is very small around less than 1 STB/day for a long time up to 1827 days.

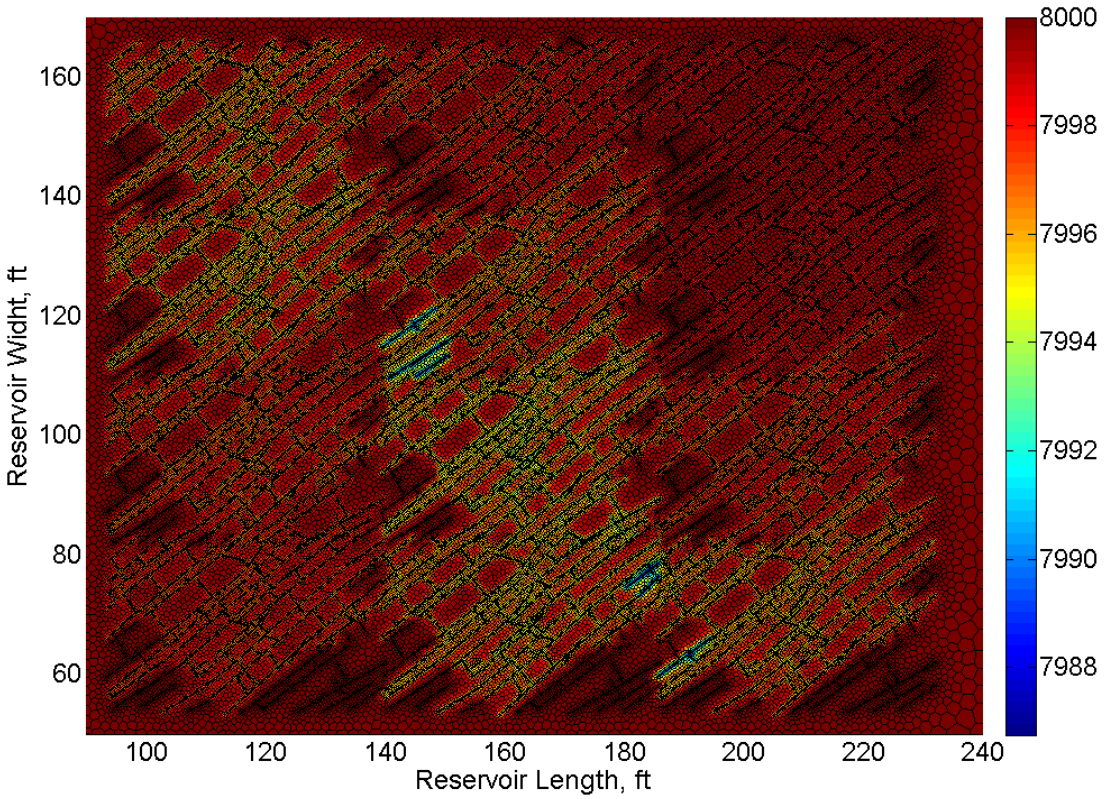


**Fig. 50 – Top view of the pressure graph after 0.1 days' simulation.**

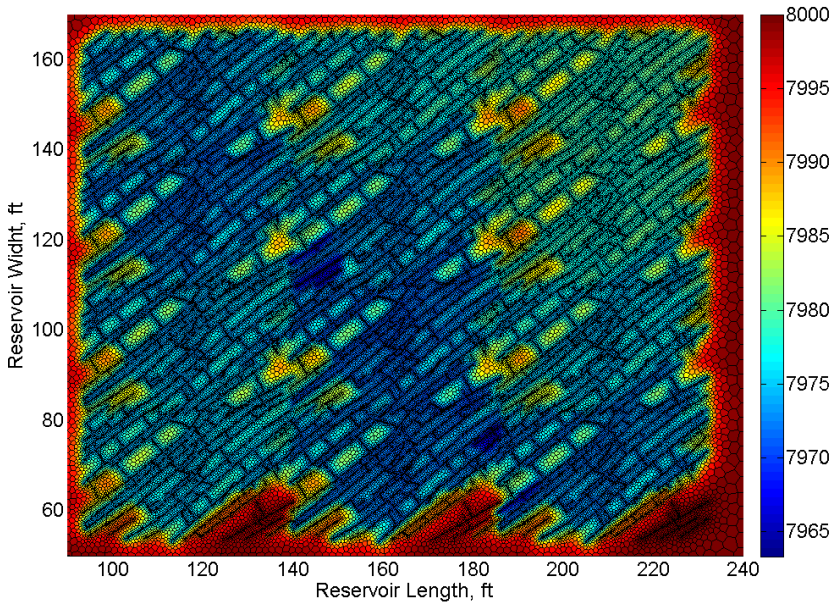


**Fig. 51 – Top view of the pressure graph after 1 days' simulation.**

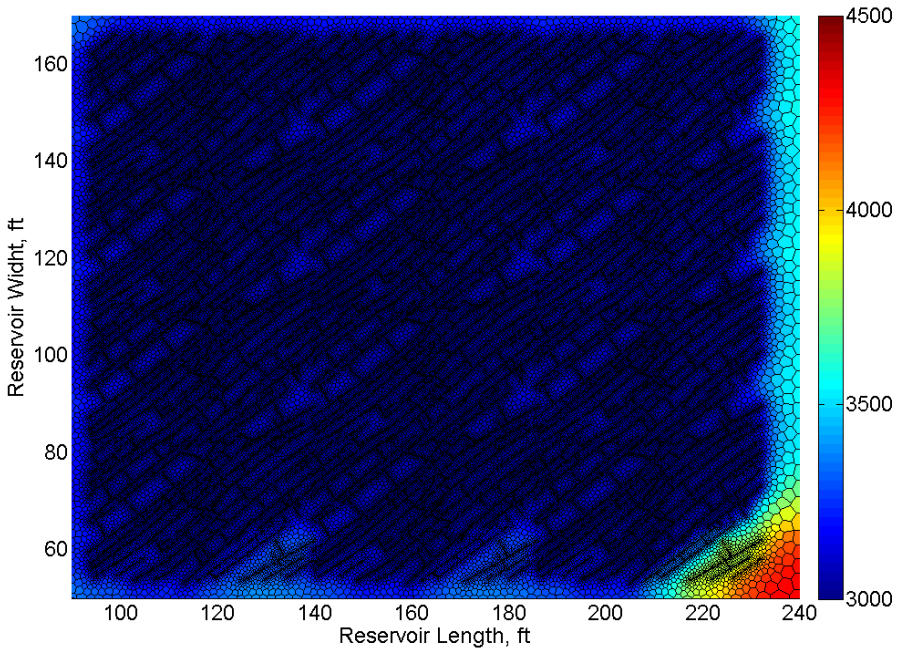


**Fig. 52 – Top view of the pressure graph after 580 days' simulation.**

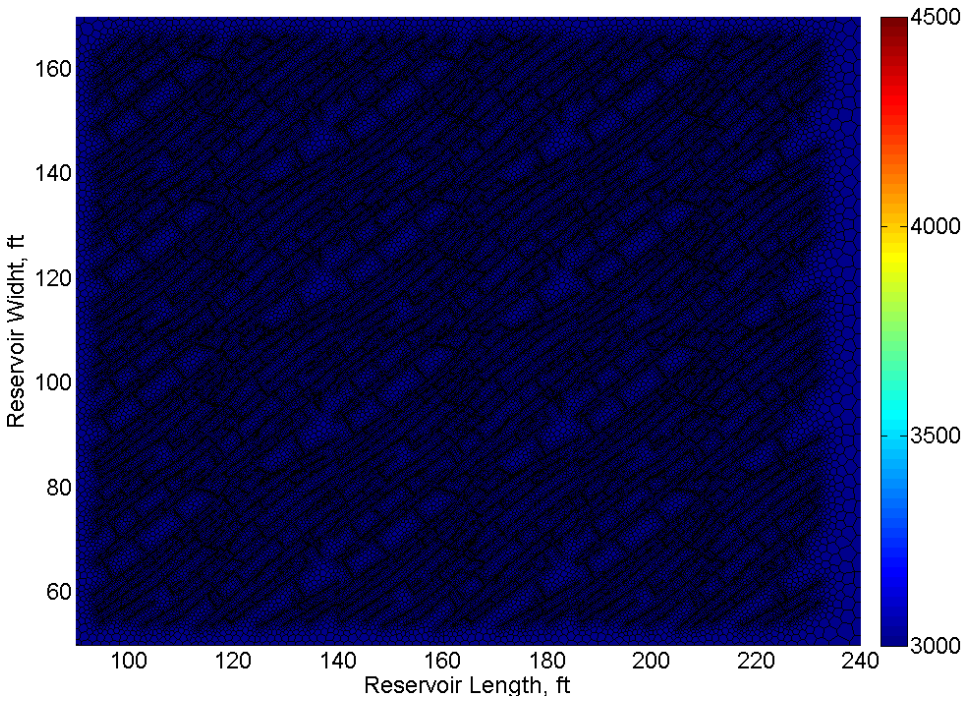


**Fig. 53 – Top view of the pressure graph after 1827 days' simulation.**

### 4.4.1 Fracture Aperture Distributions under Various Overburden Pressure

Muralidharan, Schechter, et al. (2004) investigated the impact of overburden pressure on aperture distributions using X – Ray CT scanner. They concluded that even under various stresses, the fracture aperture still follows lognormal distributions. **Fig. 54** is reproduced from Muralidharan, Schechter, et al. (2004). With the increase in stresses from 500 psi up to 1500 psi, the lognormal peak shifts to the left. One interesting follow-up question is whether or not the non-uniform aperture will affect fluid flow simulations under various stresses. We will consider variations in fracture permeability, fracture width, and fracture conductivity. First, sampling from a lognormal distribution will end up with multiple fracture aperture realizations. Second, different lognormal distributions yield different fracture apertures realizations. Finally, same fracture conductivity means either variation in fracture aperture or in fracture permeability. In this section, we will use the discrete fracture network in **Fig. 31a** (P5 model) to investigate various scenarios.

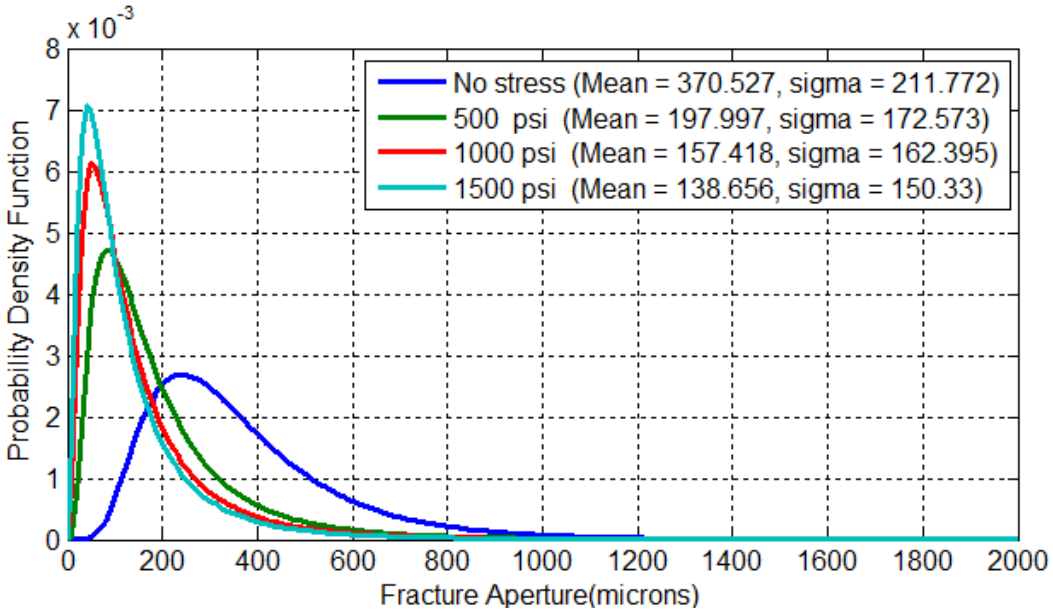


**Fig. 54 – Various non-uniform aperture distributions under four different overburden pressures.**

### 4.4.2 From a Single Lognormal Aperture Distribution

As seen in **Fig. 54**, without overburden pressure, fracture aperture follows a lognormal distribution with the mean of 370.527, and standard deviation of 211.772. For this lognormal distribution, we generate three fracture aperture realizations each one with 1000 points, which are plotted in **Fig. 55**. Notice that fracture aperture varies a lot. However, the histograms of the three cases (**Fig. 56**) still roughly follow the same lognormal distribution given by the input mean and standard deviation.

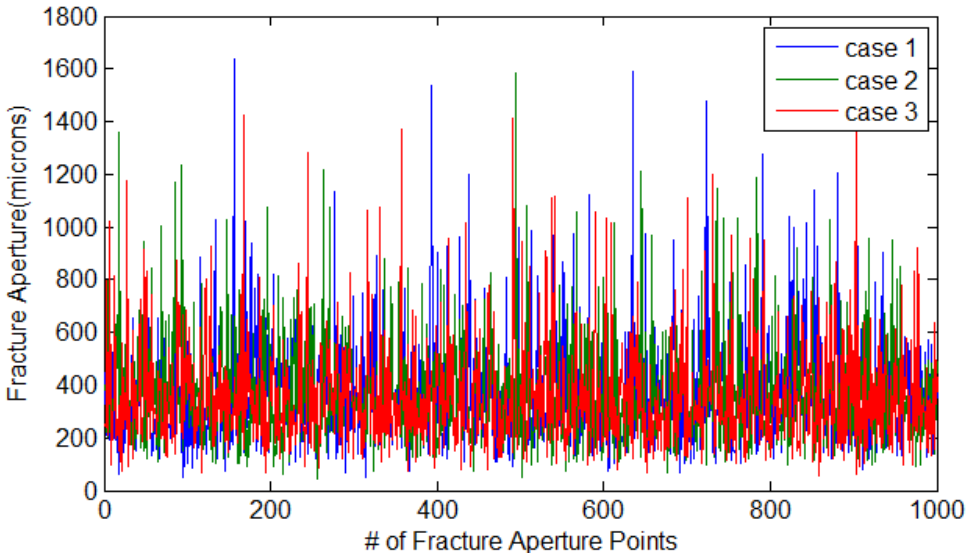


**Fig. 55 – Three fracture aperture realizations with mean equal to 370.527 and standard deviation equals to 211.772 under zero overburden stress.**

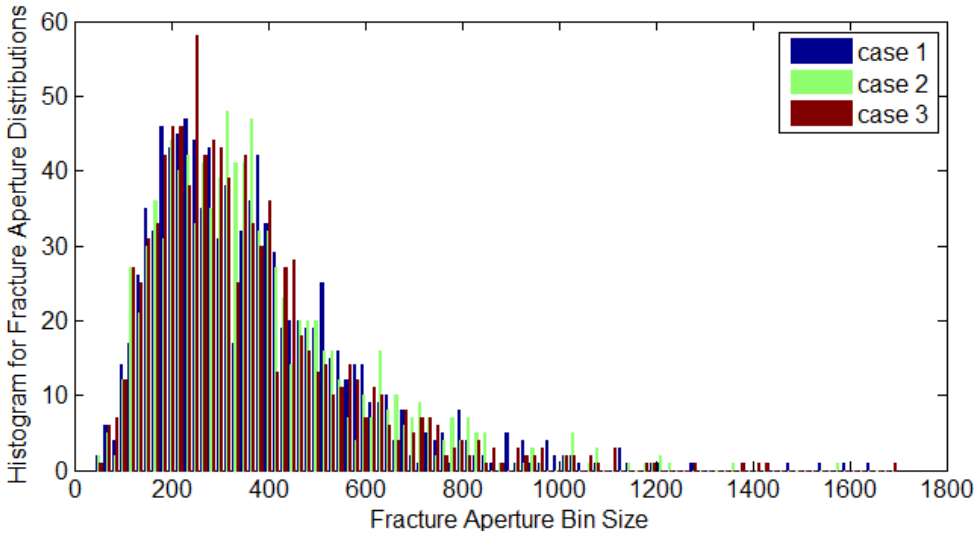


**Fig. 56 – Histogram of three fracture aperture distributions with mean equal to 370.527 and standard deviation equals to 211.772 under zero overburden stress.**

In order to evaluate the effect of fracture aperture on production performance, fluid flow simulations are performed in the discrete fracture network in **Fig. 31a.** The technique to incooperate non-uniform fracture aperture is described in the following. As mentioned previously in the Gridding and Discretization Chapter, each fracture is divided into sub fracture segments. The fracture aperture value of each segment can be selected from the pre-computed 1000 values in **Fig. 55** and **Fig. 56**. For example, if two fractures are divided into 10 and 20 sub segments respectively, the first 30 values of fracture apertures will be retrieved and assigned to the fracture sub segments. If the total number of fracture sub segments is more than 1000, e.g. 2004, the 4$^{th}$ value is retrieved and assigned for the fracture sub segment.

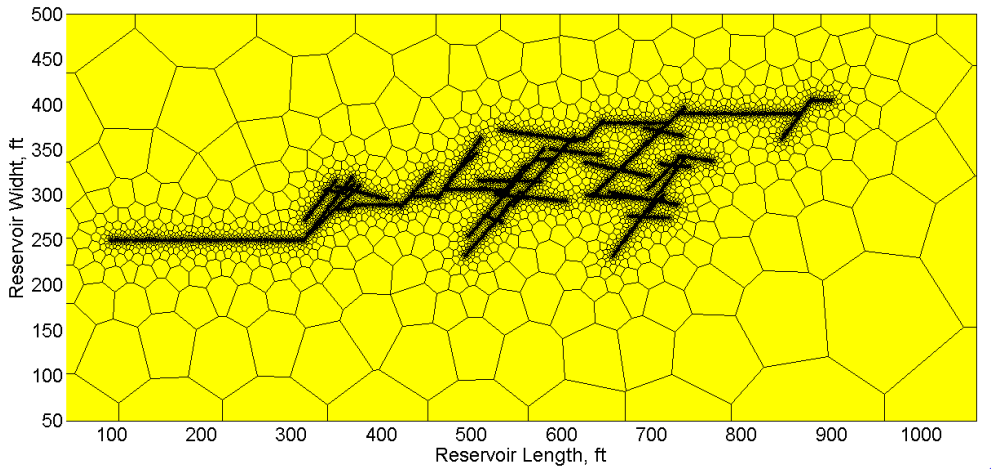


**Fig. 57 – Gridded reservoir model for case 1 with unstructured PEBI grids.**

**Fig. 57** shows the gridded reservoir model of the case 1. There is no distinct difference in the grid geometry between case 1 and the other two cases, as well as

between case 1 and **Fig. 31a** with uniform fracture aperture, because of small fracture aperture values, which are between 1.1643e-5 ft. and 6.3e-3 ft.

**Fig. 58** shows the cumulative oil plots for case 1 to case 3. No significant difference is observed among the three cases, since the same lognormal input parameters are applied to generate aperture distributions.

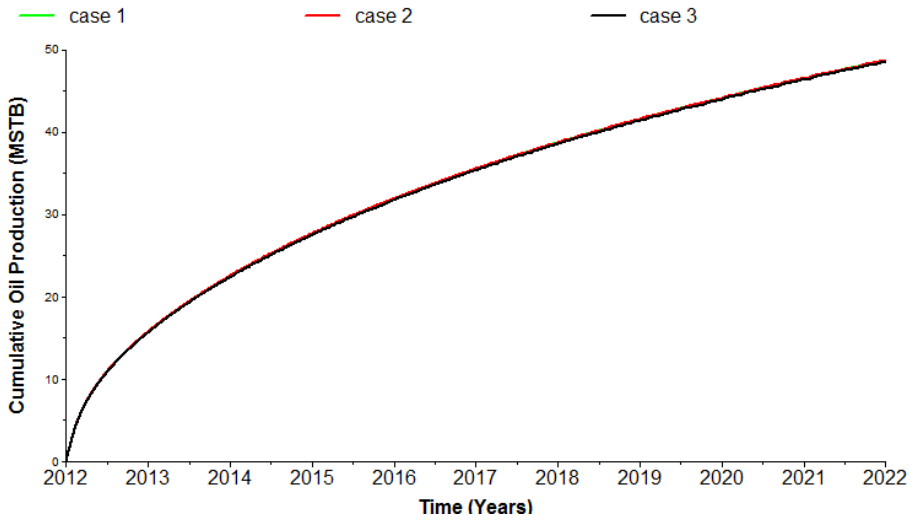


**Fig. 58 – Comparison of cumulative oil production for case 1 to case 3 with the same lognormal aperture input parameters.**

### 4.4.3 From Four Lognormal Aperture Distributions under Different Overburden Pressures

With the input parameters of lognormal distributions for overburden stress 500, 1000, and 1500 psi, three fracture aperture distributions are generated, which corresponds to case 4, case 5, and case 6. **Fig. 59** and **Fig. 60** show the aperture distributions and histograms. Compared with **Fig. 55** and **Fig. 56**, fracture aperture

values are much lower with the histograms being shifted to the left with the increase of overburden stresses. As expected in **Fig. 61**, the cumulative oil production plot shows reduced production performance with the increase of overburden pressure, or with the decrease of fracture aperture values.

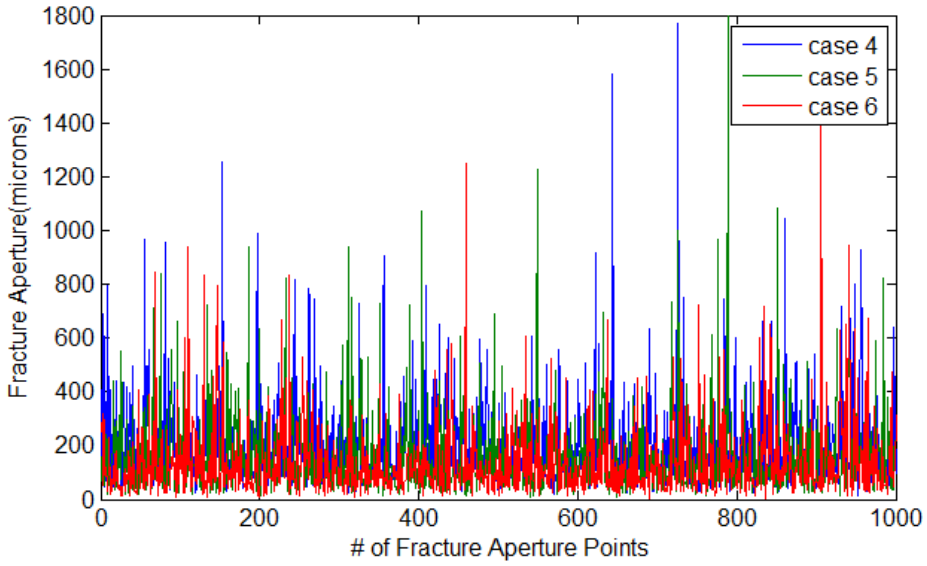


**Fig. 59 – Three fracture aperture realizations under 500, 1000, and 1500 psi overburden stress, respectively.**

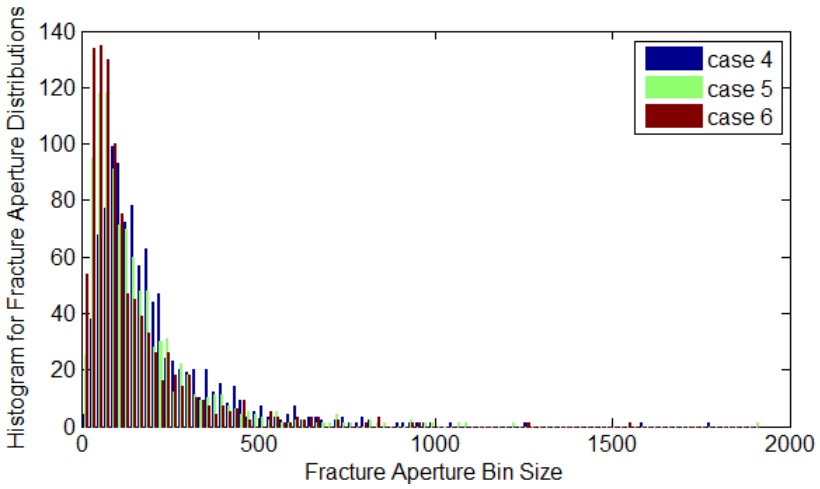


**Fig. 60 – Histograms of three fracture aperture distributions under 500, 1000, and 1500 psi overburden stress, respectively.**

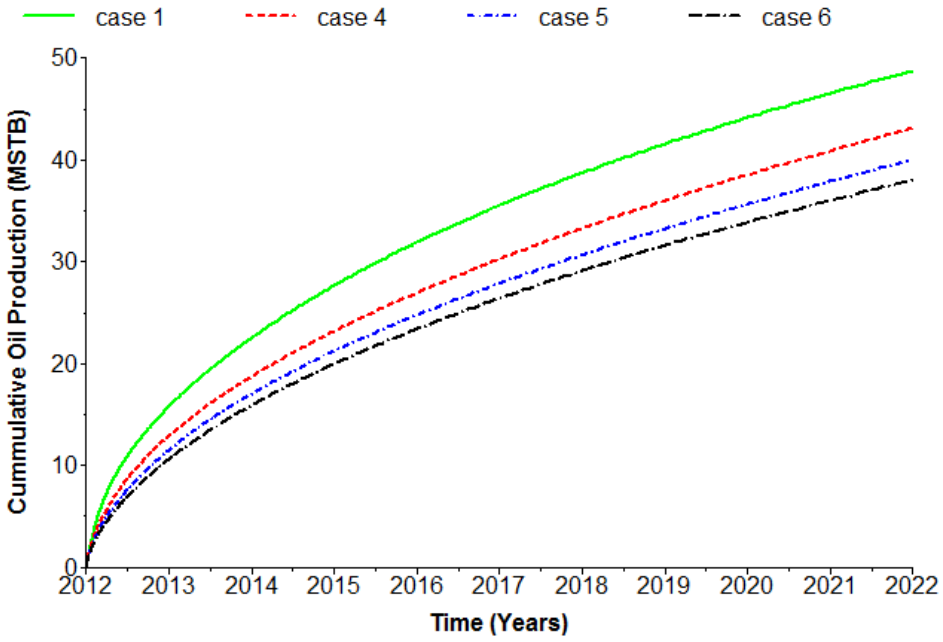


**Fig. 61 – Comparison of cumulative oil production between case 1 without overburden pressure, and case 4 to case 6 with overburden pressure.**

### 4.4.4 From the Same Fracture Conductivity Distribution by Varying Fracture Aperture or/and Fracture Permeability

If the fracture conductivity remains the same, it is possible to vary either fracture aperture or fracture permeability, or vary both. In the following, we will take a look at these three scenarios. Case 1 will be taken as the base case. **Fig. 62** plots the fracture conductivity distribution along fracture element indices for case 1. In total, there are 10728 fracture elements, and thus around 11 repeated patterns of fracture aperture distribution.

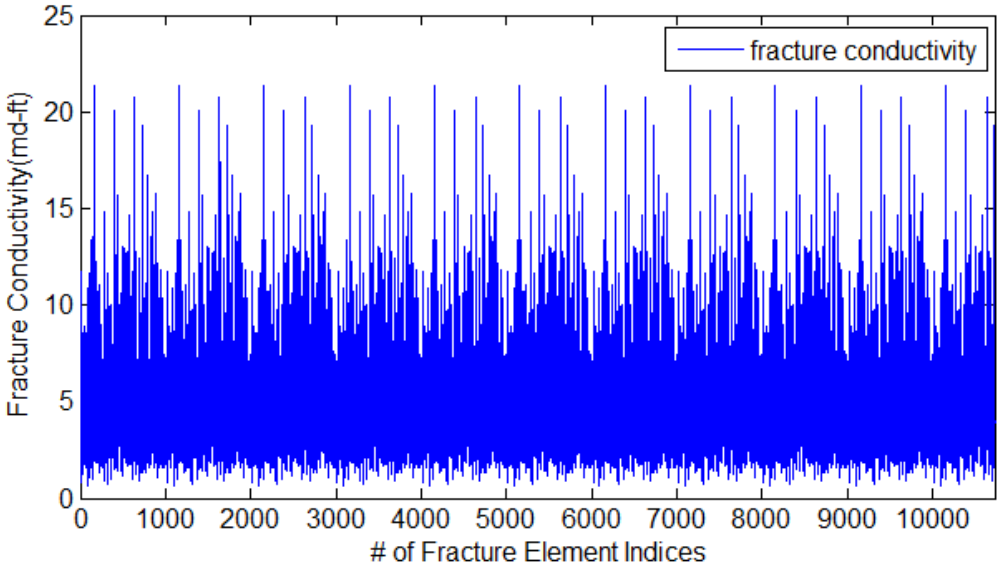


**Fig. 62 – Fracture conductivity distribution of all the fracture elements in case 1.**

*4.4.4.1 Non-Uniform Fracture Aperture and Constant Fracture Permeability*

This scenario has already been investigated in the previous case 1, where a constant fracture permeability of 3984 md is used as the input.

*4.4.4.2 Uniform Fracture Aperture and Varying Fracture Permeability*

**4.4.4.2.1 Arithmetic Averaged Aperture**

The arithmetic average of lognormal fracture aperture in case 1 is computed as 1.2e-3 ft. In addition. Fracture permeability of each fracture element is back computed from the fracture conductivity. Note that this averaging option yields the same fracture pore volume between the lognormal fracture aperture and arithmetic averaged aperture. After fracture permeability and fracture aperture are updated, the reservoir model is remeshed with the unstructured PEBI grids, and similar reservoir simulation as case 1 is then performed for the arithmetic mean (case 7).

**4.4.4.2.2 Geometric and Harmonic Averaged Aperture**

The geometric average of lognormal fracture aperture in case 1 is 1e-3 ft. The harmonic average is 8.97e-04 ft., which shows the lower bound of the lognormal fracture aperture. Similar procedure is carried out for gridding and reservoir simulation for geometric mean (case 8) and harmonic mean (case 9).

*4.4.4.3 Non-Uniform Fracture Aperture and Varying Fracture Permeability being correlated by the Cubic Law*

Based on the Cubic law, fracture conductivity is proportional to the fracture aperture raised to the power of three. From the fracture conductivity values of all the fracture elements, we can back calculate the fracture aperture (**Fig. 63**) and corresponding fracture permeability. Again, the same simulation process is performed for the case 10 based on the Cubic law.

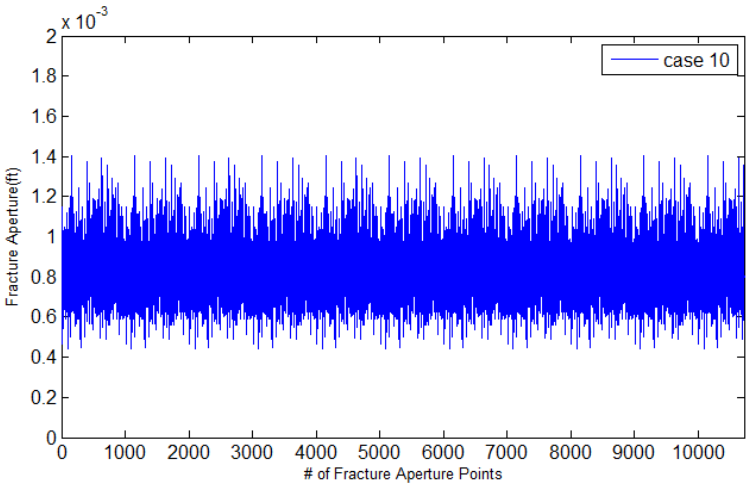


**Fig. 63 – Fracture aperture distribution that is estimated from the Cubic law.**

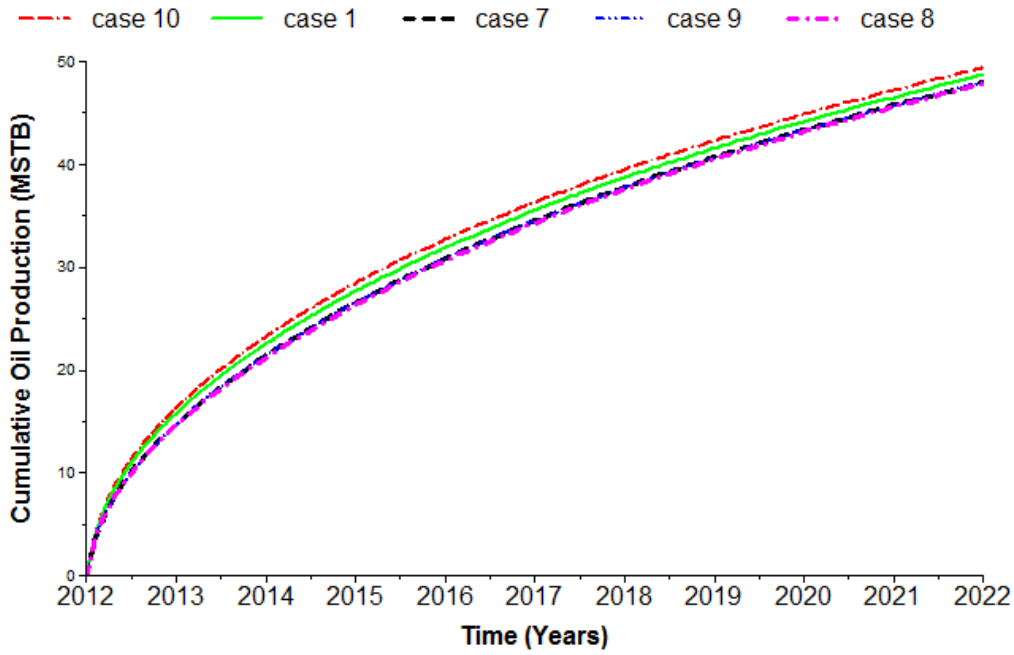


**Fig. 64 – Comparison of cumulative oil production between different averaging approaches (case 7 to case 10) and case 1.**

**Fig. 64** shows a summary of cumulative oil production for cases with the same fracture conductivity. Note that case 10 where the aperture and permeability are estimated from the Cubic law yields the best production performance. The base case 1 is in the middle of the range. If fracture conductivity remains the same, averaging approaches such as arithmetic, geometric and harmonic provide us with less cumulative oil production. Special attention has to pay to the averaging techniques when we deal with non-uniform fracture aperture distributions.

### 4.4.5 From the Simple Aperture Averaging Approaches

With the case 1 as the base case, we will try different aperture averaging approaches without honoring the given fracture conductivity distribution. From the previous sections, we know that averaged fracture aperture values equal to 1.2e-3 ft., 1e-3 ft., 8.97e-4 ft., for arithmetic, geometric, and harmonic averaged values, respectively. In addition, fracture permeability equals to 3984 mD. Uniform fracture aperture and fracture permeability will be assigned to the discrete fracture network. The difference between 4.4.5 and 4.4.4 is that this section doesn't assume non-uniform fracture permeability in order to yield the same fracture conductivity as seen in case 1. Case 11 to case 13 correspond to arithmetic, geometric and harmonic average, respectively.

From **Fig. 65**, we reach conclusions very similar as we usually expect for different averaging approaches. The arithmetic averaging approach (case 11) gives the best performance, which is followed by the base case 1, geometric averaging approach (case 12), and harmonic averaging approach (case 13). Note that both case 7 and case 11

are based on arithmetic averaging approaches. Whether or not honoring fracture conductivity gives us distinctly different results, with case 7 being worse and case 11 being better than the base case 1.

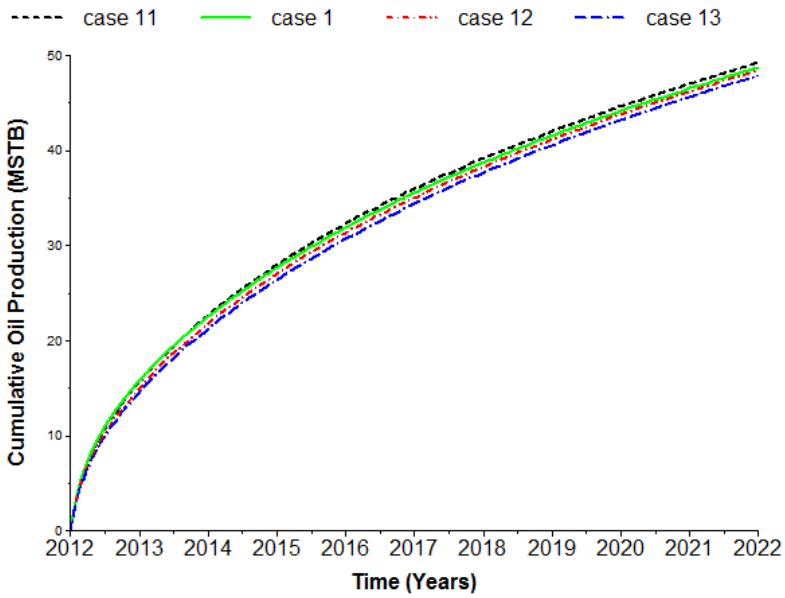


**Fig. 65 – Comparison of cumulative oil production between simple averaging approaches (case 11 to case 13) and case 1.**

# CHAPTER V

# APPLICATION OF WELL-TESTING TECHNIQUES IN DISCRETE FRACTURE NETWORKS

## *5.1 Build-up Pressure Transient Analysis*

Well testing in fractured reservoirs has been summarized for vertical wells by Kuchuk and Biryukov (2015). However, only few publications (Al-Kobaisi et al. 2006, Kim and Lee 2015) focus on pressure transient behaviors of multi-stage horizontally fractured (MSHF) wells in naturally fractured unconventional shale reservoirs, especially for complex fracture networks as presented in this study. To this end, in this section, we will present preliminary results of build-up analysis of complex fracture networks.

Since pressure transient analysis deals with analytical solutions, a water-oil model with residual water saturation is used for both numerical simulations and well testing analysis. First of all, we perform numerical pressure build-up simulations on the single outcrop map in **Fig. 39** with two scenarios - limited reservoir boundary and "infinite" reservoir boundary conditions. And then, pressure response is analyzed with well testing software – Saphir (a module of the software package Ecrin). The final outputs will be dual continuum equivalent parameters, and fracture-related parameters.

The build-up study consists of 1 day of production at a rate of 10 STB/day, which is followed by around 624 day's build-up. In total, the elapsed time is around 15,000 hours. A large build-up period of around 624 days is used because of low

permeability. The PVT properties are similar as the previous section 4.2.2, except that we remove the gas-related properties.

### 5.1.1 The Impact of Reservoir Boundary on Build-up Curves

For boundary-dominated reservoir, we use the reservoir geometry and gridded model in **Fig. 40** for the pressure build-up analysis. **Fig. 66** plots pressure response vs. elapsed time. Note that pressure goes to plateau very quickly, and pressure at the plateau is far less than 8000 psi. **Fig. 67** shows the zoom-in view around the beginning of the build-up period. At 1 day, pressure builds up from around 7540 psi.

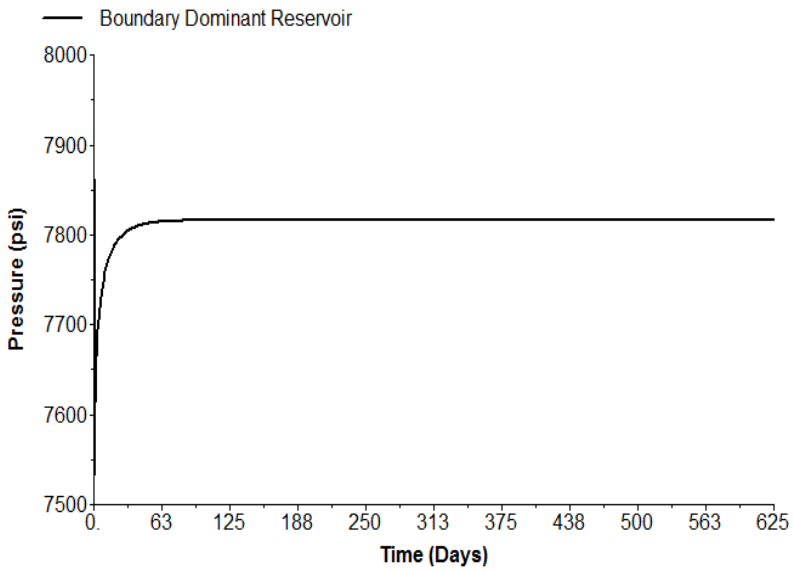


**Fig. 66 – Pressure response of the build-up analysis for both boundary dominated reservoir and infinite acting reservoir.**

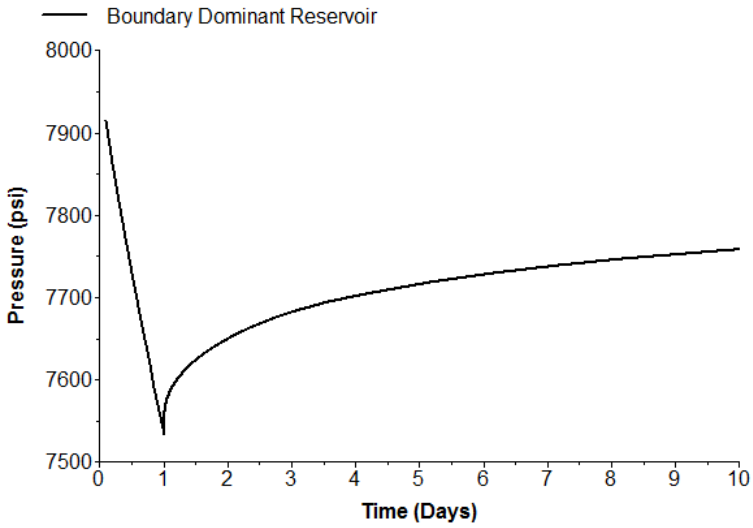


**Fig. 67 – Enlarged view of pressure response of the build-up analysis for boundary-dominated reservoir.**

### 5.1.2 The Impact of Infinite-Acting Reservoir on Build-up Curves

In order to mimic an infinite-acting reservoir, we extend the reservoir boundary in **Fig. 39** by 400 ft. along both X and Y dimensions. **Fig. 68** draws both the reservoir dimension and complex fracture networks. In the middle is the fracture network from **Fig. 40**. Compared with the fracture dimensions, the model can be considered as an infinite acting reservoir.

**Fig. 69** and **Fig. 70** show the gridded model and zoom-in view around the fractures. Similarly, a pressure build-up simulation is performed in this model. **Fig. 71** and **Fig. 72** plot pressure response for both the infinite acting and the previous boundary dominant reservoirs. Note that at 625 days, pressure approaches to almost the initial reservoir pressure of 8000 psi. However, in the boundary dominant reservoir, the build-

up pressure is much less than 8000 psi. In addition, less than 1 day, both models show almost the same production profile.

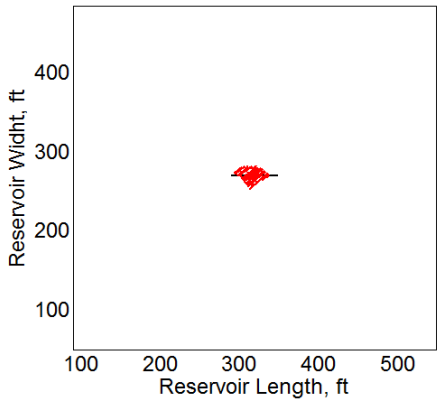


**Fig. 68 – Reservoir dimensions of the infinite acting reservoir with the fracture geometry of Fig. 40 in the middle.**

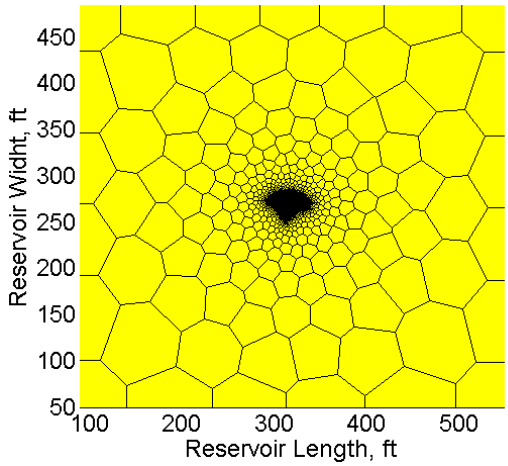


**Fig. 69 – Gridded model of the infinite acting reservoir with the fracture geometry of Fig. 40 in the middle.**

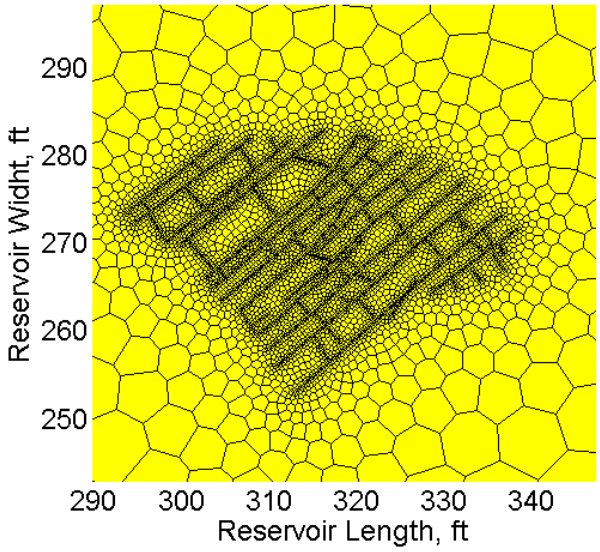


**Fig. 70 – Zoom-in view of the gridded model around the fractures.**

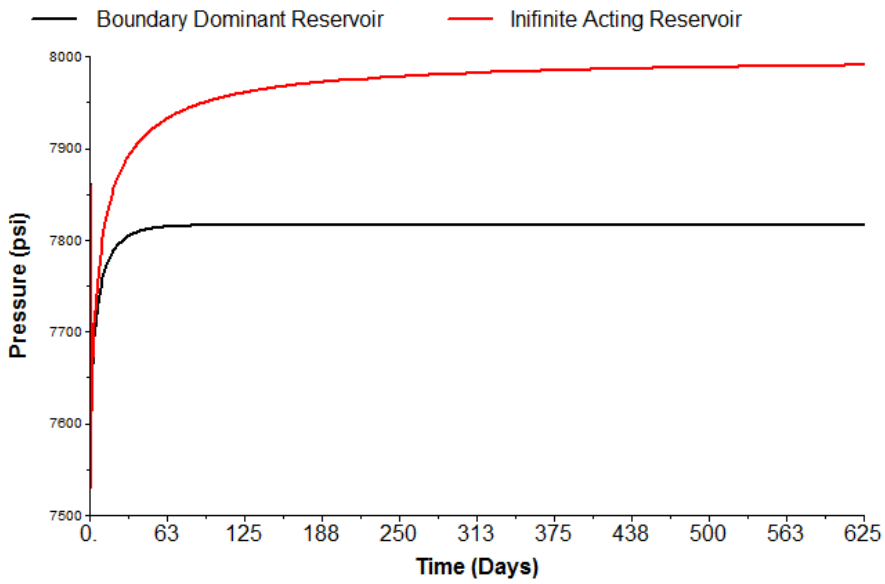


**Fig. 71 – Pressure response of the build-up analysis for both boundary-dominated and infinite acting reservoirs.**

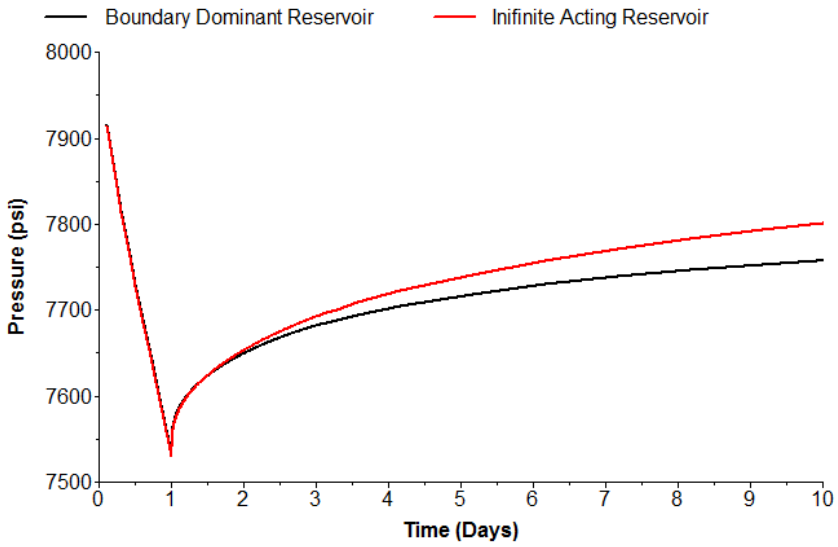


**Fig. 72 – Enlarged view of pressure response of the build-up analysis for both boundary-dominated and infinite acting reservoirs.**

### 5.2.1 Fractured Horizontal Well and Dual Continuum Model

The selection of well testing models is very important to yield a reasonable match between history production data (i.e. numerical simulation results in section 5.1) and prediction of well testing models. For the model, not only do we need a horizontal well, but also hydraulic and natural fractures. However, current well testing models can only deal with hydraulic fractures with orthogonal intersection. Natural fractures can only be incorporated through the concept of dual continuum model. Therefore, the best model we can use is the Fractured Horizontal Well with Dual Continuum Model, for which the reservoir boundary can be model as either closed rectangle or infinite acting.

### 5.2.2 Build-up Analysis for the Boundary-Dominant Reservoir

*5.2.2.1 Data Interpretation and Comparison with Numerical Simulation*

**Fig. 73** shows the model selection menu. Note that there is no wellbore storage effect; well is set as the Fractured Horizontal; reservoir is set as the Two Porosity PSS; and the boundary is set as the Rectangle. **Fig. 74** and **Fig. 75** show the history-matched model input parameters to achieve a reasonable match between the numerical simulation and well testing model. Note that there is no unique solution to this problem, since we are trying to match the complex fracture network with the simplified analytical model. During regression, the software might randomly vary the parameters within the given range without honoring physics behind it. In addition, we use numerical simulation data

up to around 83.33 days or 2000 hours, since after that pressure response already shows significant boundary effect.

Since the well testing model is built with one layer, well depth ($Z_w$) is input as 150 ft. Flow type is assumed only within the fractures. Fracture conductivity is input as infinite fracture conductivity. We assume that the number of equivalent hydraulic fractures equals to 15. Fracture height $H_f$ is input the same as the reservoir thickness, which is 300 ft. The rest of the parameters are generated automatically from the regression algorithms of the software package.

In **Fig. 74**, there is a very small skin factor. Horizontal well perforation length ($h_w$) is computed as 169.956 ft. Fracture half-length is estimated as 27.1344 ft. Fracture angle with the horizontal well is calculated as 62.9232 degree.

In **Fig. 75**, initial reservoir pressure is estimated as 7842.7 psi, which is less than 8000 psi. Reservoir flow capacity (kh) is around 0.22 $md * ft$. Reservoir permeability ratio between vertical and horizontal is about 5.37. For dual continuum parameters, storage ratio Omega is around 0.035, and inter-porosity flow parameter is around 1.282 E-8. The distances between the horizontal well and four boundaries are equal to 184.526 ft. to the South boundary, 257.374 to the East boundary, 184.313 to the North boundary, and 203.528 to the West boundary. From **Fig. 76** to **Fig. 78,** we compare the numerical simulation with the well testing interpretation. A good match is observed for both pressure and pressure derivative vs. build-up time on the log-log plot in **Fig. 76**, for pressure vs. superposition time on the semi-log plot in **Fig. 77**, and for pressure and rate vs. elapsed time plot in **Fig. 78**.

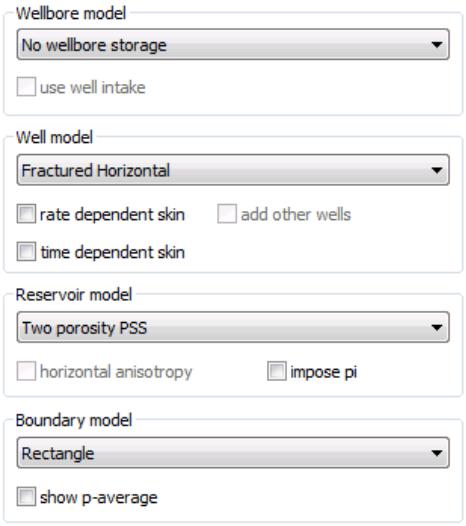


**Fig. 73 – Model selection for the boundary-dominated reservoir (Kappa 2016).**

| | | |
|---|---|---|
| Skin | 0.00169629 | |
| Flow type | Flow in fractures onl | |
| hw | 169.956 | ft |
| Zw | 150 | ft |
| Theta | 0 | ° |
| Number of fractu | 15 | |
| Xf | 27.1344 | ft |
| Hf | 300 | ft |
| Fracture angle | 62.9232 | ° |
| Fracture model | Infinite conductivity | |

**Fig. 74 – Model parameters for well and wellbore for the boundary-dominated reservoir.**

| | | | |
|---|---|---|---|
| h | | 300 | ft |
| Pi | | 7842.7 | psia |
| k.h | | 0.220221 | md.ft |
| kro | | 1 | |
| krw | | 0 | |
| kz/kr | | 5.37053 | |
| Omega | | 0.0352857 | |
| Lambda | | 1.28204E-8 | |
| Top | | No flow | |
| Bottom | | No flow | |
| S | No flow | 184.526 | ft |
| E | No flow | 257.374 | ft |
| N | No flow | 184.313 | ft |
| W | No flow | 203.528 | ft |

**Fig. 75 – Model parameters for boundary-dominated reservoir and boundary.**

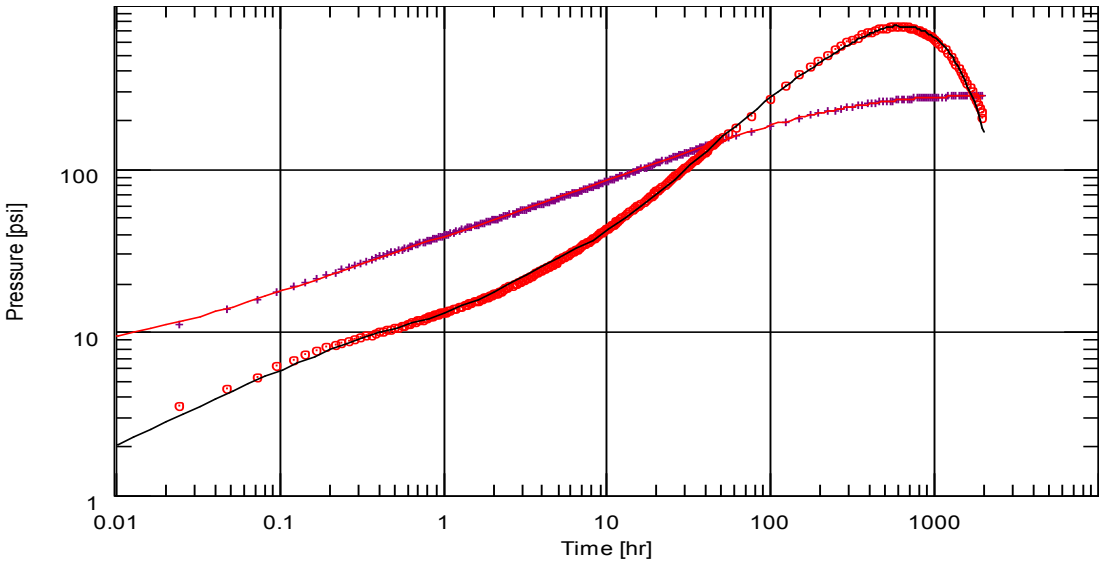


**Fig. 76 – Comparison between the numerical simulation model and well testing model for log-log plots of both pressure difference (DP) and pressure derivative (DPDT) vs. time. Solid red and black are the DP and DPDT of well testing, respectively. Dotted curves are corresponding numerical simulation results.**

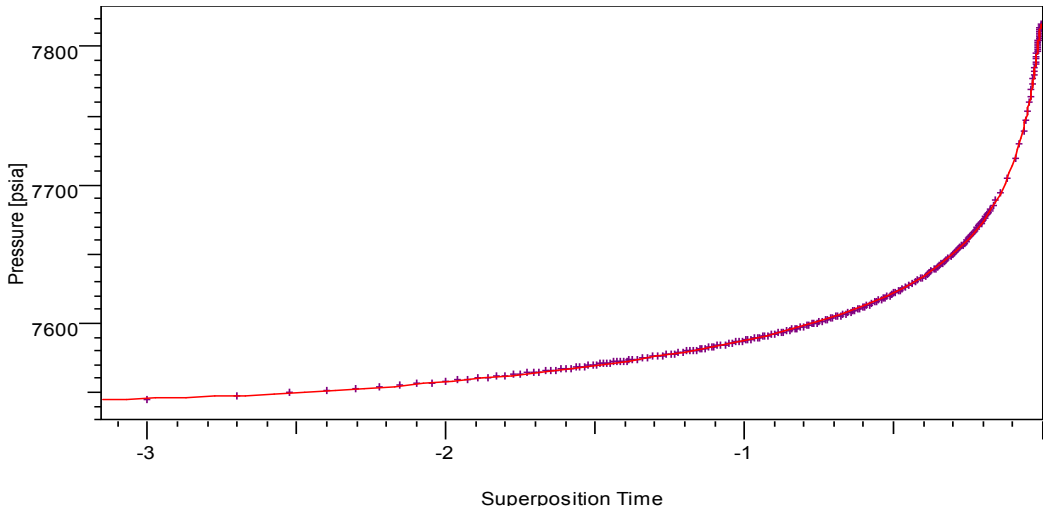


**Fig. 77 – Comparison between the numerical simulation model and well testing model for semi-log plot of pressure vs. superposition time. Solid red is for well testing, and dotted black curve for numerical simulation model.**

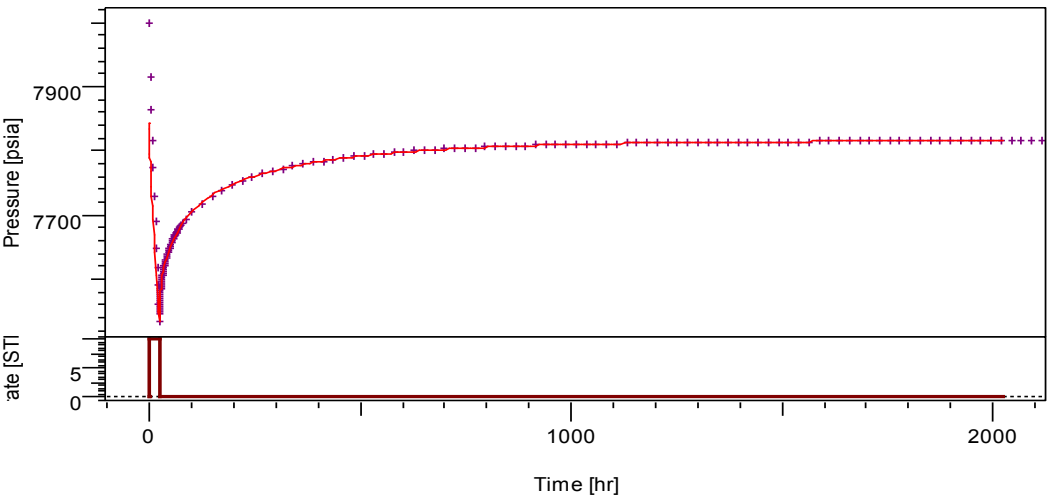


**Fig. 78 – Comparison between the numerical simulation model and well testing model for pressure response and rate vs. elapsed time. Solid red is for well testing, and dotted black curve for numerical simulation model.**

*5.2.2.2 Sensitivity Analysis for Parameters of the Well Testing Model*

Sensitivity analysis is designed not only to reveal the most important model parameters, but also to provide guidance on how to adjust them in order to reach reasonable matches with historic production data.

| **Model Parameters** | **Default** | **Case I** | **Case II** | **Case III** | **Trends** |
|---|---|---|---|---|---|
| Skin Factor (s) | 0.00169629 | 0 | 0.01 | 0.1 | Upwards |
| Fracture Half Length (Xf), ft. | 27.13444 | 1 | 10 | 100 | Downwards |
| Fracture Angle, degree | 62.9232 | 20 | 40 | 80 | - |
| Reservoir Flow Capacity (kh), md-ft | 0.220221 | 0.01 | 0.1 | 0.5 | Downwards |
| Permeability Anisotropy (Kz/kz) | 5.37053 | 0.5 | 50 | 500 | - |
| Storage Ratio, Omega | 0.0352857 | 0.01 | 0.1 | 0.5 | Downwards |
| Inter-Porosity Flow, Lambda | 1.28E-08 | 1.00E-10 | 1.00E-05 | 1.00E-03 | Downwards |
| South Distance, ft. | 184.526 | 50 | 100 | 250 | Downwards |
| East Distance, ft. | 257.374 | 90 | 150 | 300 | - |
| North Distance, ft. | 184.313 | 50 | 100 | 250 | Downwards |
| West Distance, ft. | 203.528 | 90 | 150 | 300 | - |

**Table 15 – Sensitivity analysis of the well testing model parameters for the boundary-dominated reservoir.**

**Table 15** tabulates all the sensitivity cases, among which the default column shows the model input parameters in the previous section (**Fig. 74** and **Fig. 75**). Each parameter is varied to yield three more cases corresponding to Column Case I, Case II and Case III. The last column (Trends) indicates the impact of each parameter on log-log plot of the pressure difference vs. build-up time curve. For instance, with the increase of the skin factor, the pressure difference vs. build-up time curve moves upwards.

**Fig. 79** to **Fig 89** show log-log plots of both DP and DPDT vs. build-up time for all the sensitivity cases. Together with **Table 15**, it is found that fracture angle, permeability anisotropy ratio, and east and west distances to the boundary have slight or negligible impact on the build-up curves. The rest of the parameters except skin factor show important impact, e.g., with the increase of fracture half-length, the build-up curve moves downwards. In the following, we will visit each sensitivity case to draw specific conclusions.

**Fig. 79** shows that skin factor affects the early stage of DP curves. There is almost no impact on DPDT curves. The linear flow regime is also observed from the half slope in the early stage of the build-up curve. The existence of large skin factor completely disturbs the appearance of the linear flow period.

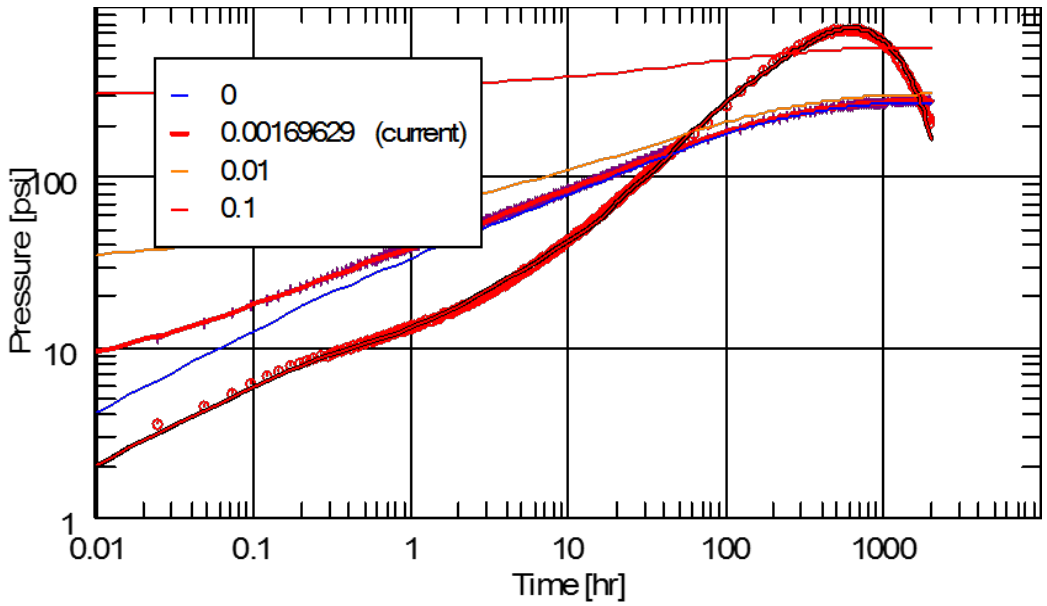


**Fig. 79 – The impact of skin factor on DP and DPDT vs. build-up time.**

The sensitivity analysis of fracture half-length in **Fig. 80** illustrates its crucial impact on both DP and DPDT plots. The shorter the fracture length, the shorter the linear flow regime. When fracture half-length equals to 1 ft., we see that its linear flow regime is less than that of the default case. In addition, with the increase of fracture half length, the transition from the linear flow regime to the closed boundary effect become more severe, i.e., the 'V' shape becomes more significant for longer fracture half length. The peak DP value of larger fracture half-length also becomes smaller.

**Fig. 81** shows that fracture angle has almost zero effect. From the perspective of the numerical simulation model, we use a single preformation location, which is located within a fracture gridblock in the center of the outcrop map, and thus fracture angle

won't affect the numerical simulation model. Similarly, the well testing model is to be designed to mimic the numerical model, and we expect negligible effect from the angle.

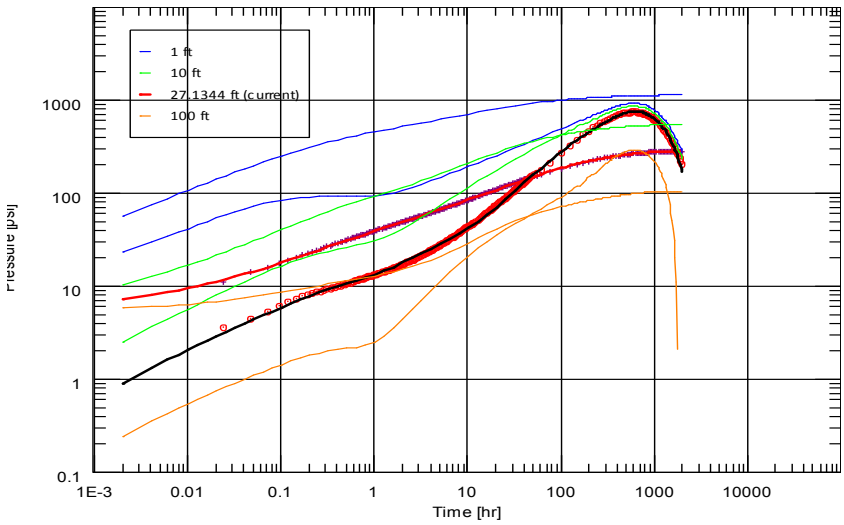


**Fig. 80 – The impact of fracture half-length on DP and DPDT vs. build-up time.**

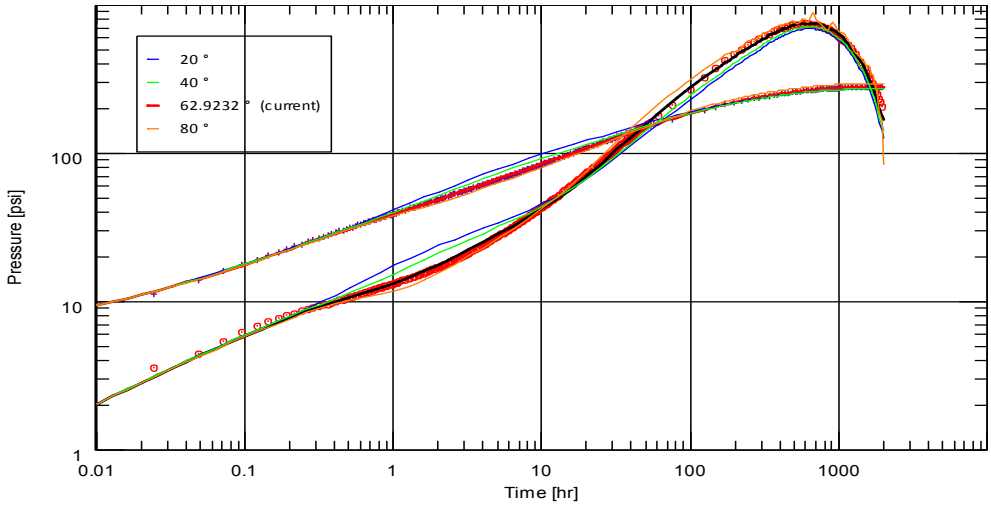


**Fig. 81 – The impact of fracture angle on DP and DPDT vs. build up time.**

The higher of the reservoir flow capacity, the smaller the DP. In **Fig. 82**, the DP and DPDT curves for 0.5 mD-ft are the lowest. Besides, the lower the fracture flow capacity, the longer the linear flow regime (e.g. 0.01 mD-ft vs. the 0.5 mD-ft), and the later of the peak DP.

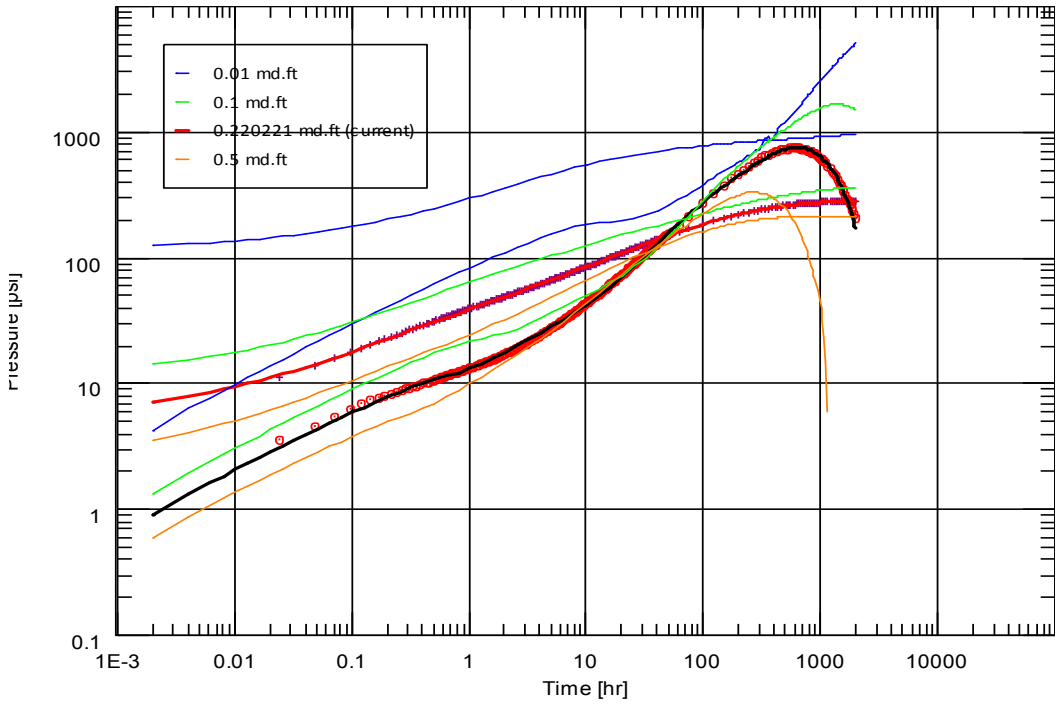


**Fig. 82 – The impact of reservoir flow capacity on DP and DPDT vs. build-up time.**

Permeability anisotropy ratio shows negligible effect as seen in **Fig. 83**, because the numerical outcrop model is highly fractured. Fractures play the key role in production performance, rather than the reservoir matrix permeability values.

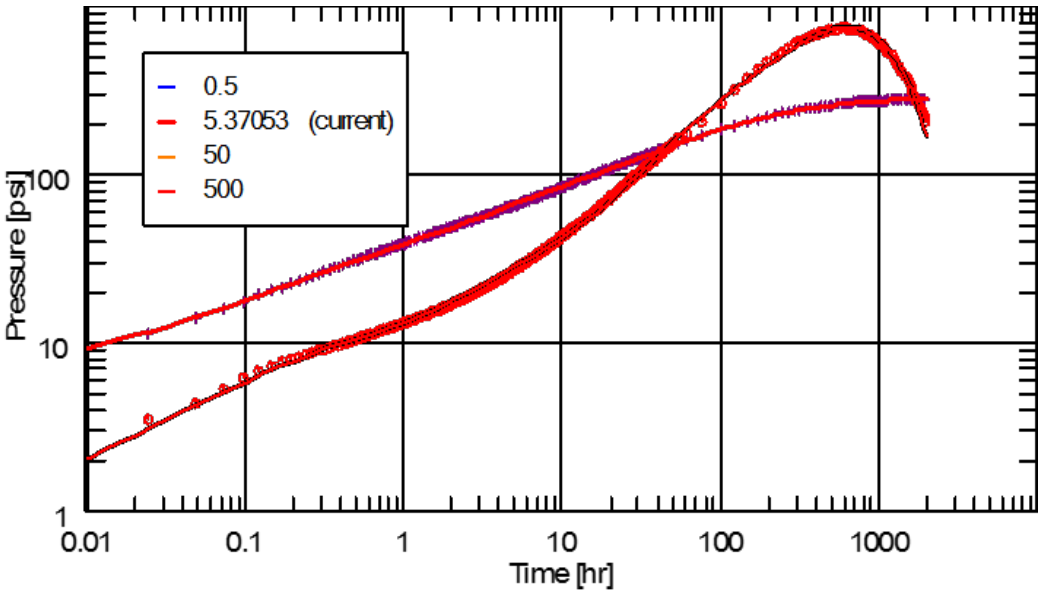


**Fig. 83 – The impact of permeability anisotropy on DP and DPDT vs. build-up time.**

**Fig. 84** and **Fig. 85** show the impact of dual porosity parameters – storage ratio and inter-porosity flow capacity. The higher the fracture storage ratio, the more fractures exist in the model, and the lower the DP. Correspondingly, the DP peak shifts to the right. The Inter-Porosity flow capacity is extremely small around the order of magnitude 1E-8 for the default value. The increase up to 1E-5 won't affect the DP and DPDT too much. When the value is increased to around 1E-3, we start to observe the classic well-testing feature of dual porosity reservoirs – the "V" shape. However, with 1E-3, both DP and DPDP are completely off the trend.

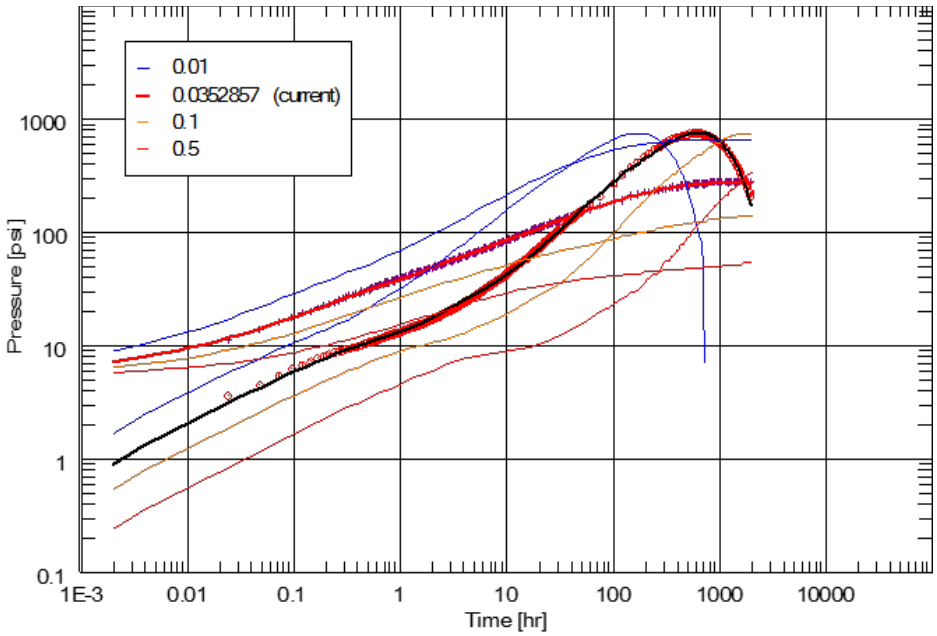


**Fig. 84 – The impact of omega on DP and DPDT vs. build-up time.**

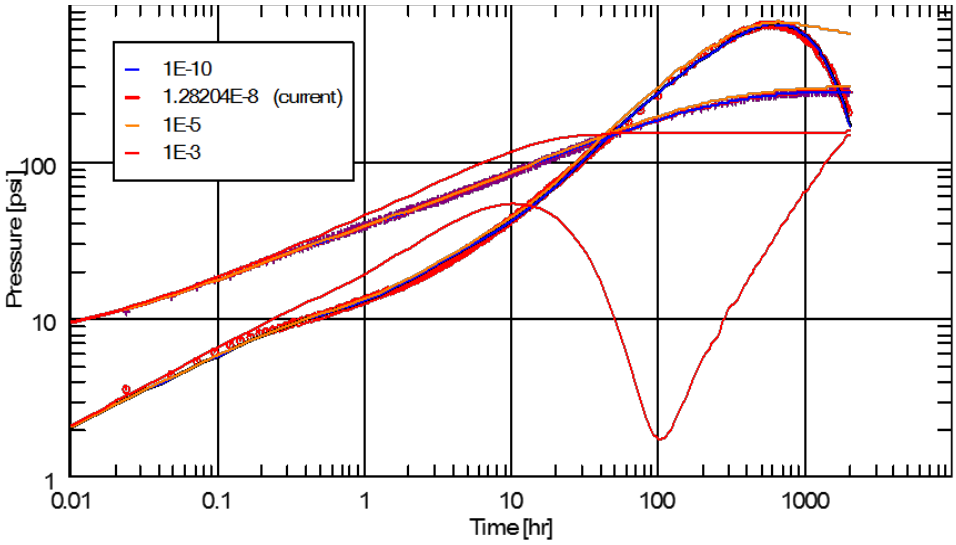


**Fig. 85 – The impact of lambda on DP and DPDT vs. build-up time.**

Since the well testing model consists of boundary-dominated reservoir, it might be able to provide information regarding the distance between the horizontal well and four boundaries. In addition, the DP and DPDT response from the boundary effect occurs at the later period as seen from **Fig. 86** to **Fig. 89**.

From **Fig. 86** and **Fig. 87**, when the distance to the north and south is less or equal to 50 ft., the DP peak becomes higher and shifts slightly to the right. When the distance to the north and south is more than 100 ft., the differences become smaller compared with the default case.

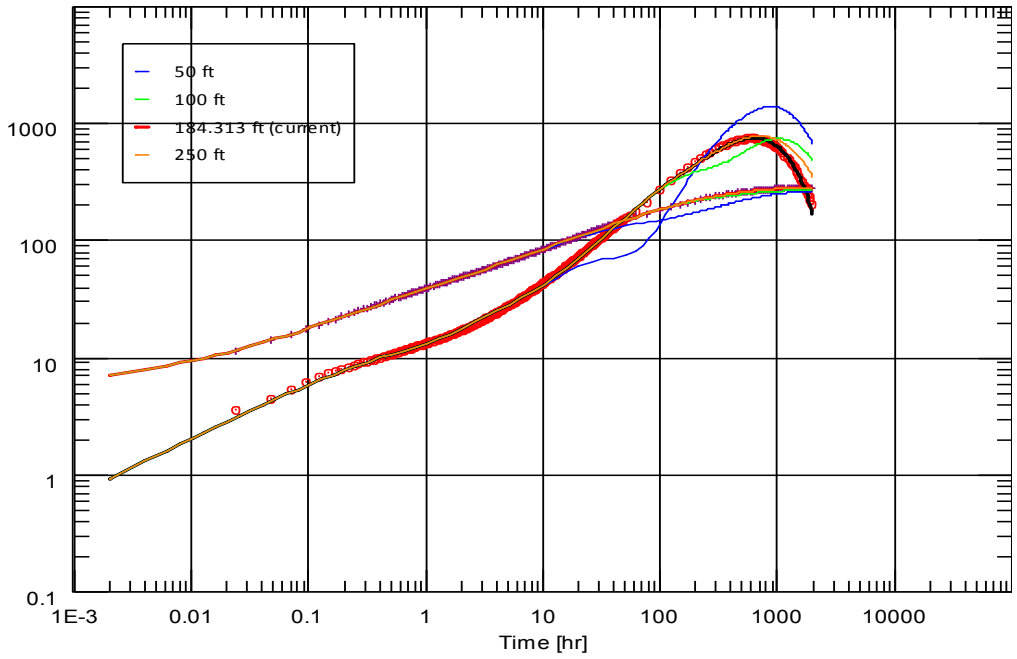


**Fig. 86 – The impact of north distance on DP and DPDT vs. build-up time.**

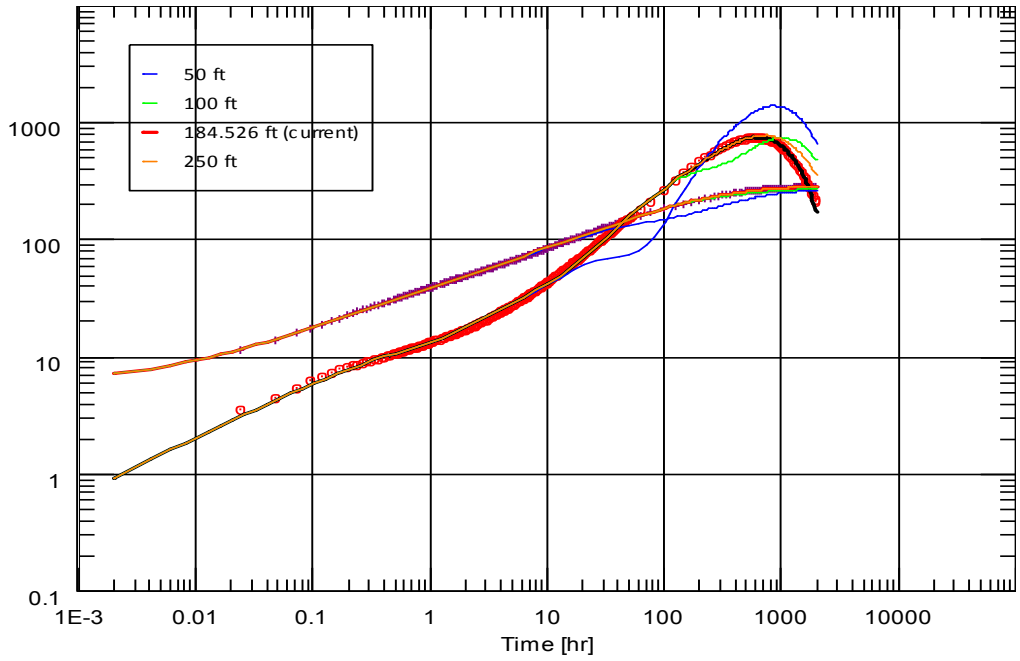


**Fig. 87 – The impact of south distance on DP and DPDT vs. build-up time.**

From **Fig. 88** and **Fig 89**, the distance to the west and north is not so sensitive as for the north and south.

Note that the outcrop map shown in **Fig. 39** gives us the lambda dimension around 35 ft. by 60 ft. The discrepancy between the numerical model and well testing model indicates that it might not be accurate to obtain boundary information from the well testing model. Furthermore, unconventional shale reservoirs produce mainly in the pressure transient stage, and usually won't be necessary to obtain boundary information.

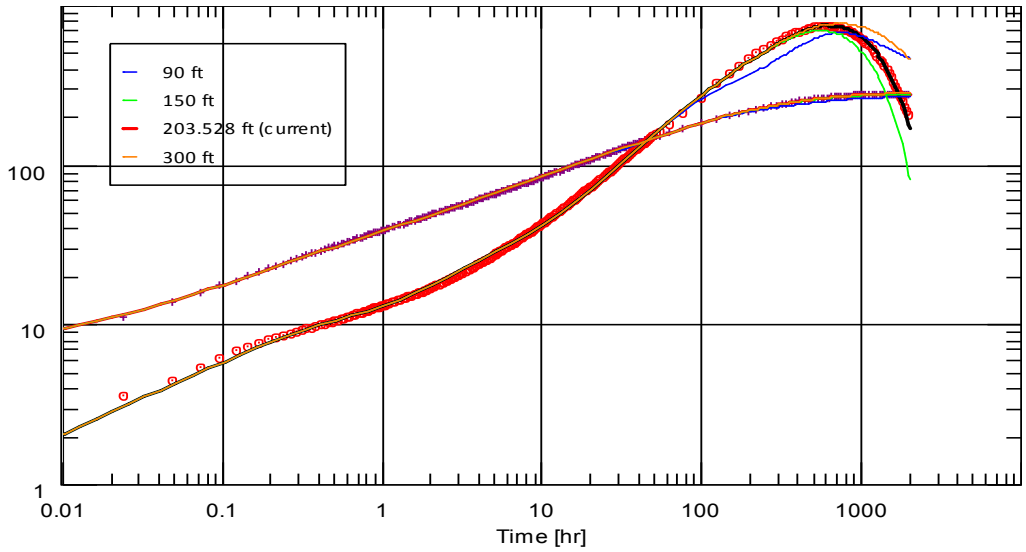


**Fig. 88 – The impact of west distance on DP and DPDT vs. build-up time.**

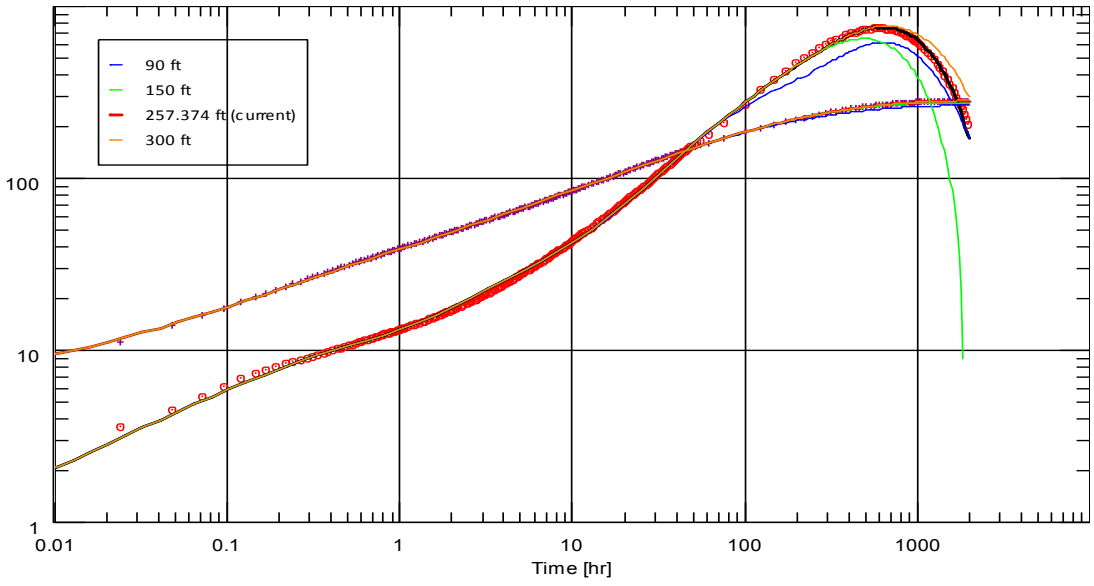


**Fig. 89 – The impact of east distance on DP and DPDT vs. build-up time.**

### 5.2.3 Build-up Analysis for the Infinite-Acting Reservoir

As mentioned before, infinite acting reservoir might be a more representative boundary model, since most of the hydraulically fractured horizontal wells produce most of the time in the pressure transient stage without showing boundary effect or the pseudo steady-state behavior.

For the pressure responses in **Fig. 71** and **Fig. 72**, a fractured horizontal well with dual continuum and infinite acting features is built in software Saphir to match both DP and DPDT responses.

#### *5.2.3.1 Data Interpretation and Comparison with Numerical Simulation*

**Fig. 90** and **Fig. 91** summarize the model parameters. Note that horizontal well depth $Z_w$, number of fracture, fracture half-length $X_f$, reservoir thickness h, and permeability anisotropy ratio are given, since these parameters are either from input data or the previous well testing analysis of the boundary dominated reservoirs. On the other hand, skin factor, perforation interval, fracture angle, initial reservoir pressure, reservoir flow capacity, and dual continuum parameters are available to vary during the regression process.

| | | |
|---|---|---|
| Skin | 1.09992E-4 | |
| Flow type | Flow in fractures on | |
| hw | 76.9133 | ft |
| Zw | 150 | ft |
| Number of fractu | 15 | |
| Xf | 27.1344 | ft |
| Hf | 300 | ft |
| Fracture angle | 90 | ° |
| Fracture model | Infinite conductivity | |

**Fig. 90 – Model parameters for well and wellbore for the infinite acting reservoir**

| | | |
|---|---|---|
| h | 300 | ft |
| Pi | 7997.03 | psia |
| k.h | 0.0666442 | md.ft |
| kro | 1 | |
| krw | 0 | |
| kz/kr | 5.37053 | |
| Omega | 0.0721077 | |
| Lambda | 1.28213E-8 | |
| Top | No flow | |
| Bottom | No flow | |

**Fig. 91 – Model parameters for the infinite acting reservoir**

**Fig. 92** to **Fig. 94** compare the matches between numerical simulation (from **Fig. 71** and **Fig. 72**) and the well testing model (input parameters from **Fig. 90** and **Fig. 91**). A good agreement is observed for the DP and DPDT vs. built-up time on the log-log plot in **Fig. 92**, for DP vs. superposition time on the semi-log plot in **Fig. 93**, and for DP and rate vs. elapsed time in **Fig. 94**.

Comparing the interpretation results of infinite acting model (**Fig. 90** and **Fig. 91**) with the previous boundary dominated model (**Fig. 74** and **Fig. 75**), skin factor and perforation interval, reservoir flow capacity are relatively lower for the infinite acting model. In addition, the estimated reservoir pressure equal to 7997.03 psi is closer to 8000 psi of the initial reservoir pressure. Dual continuum parameter omega is in the same of order of magnitude for two models, and Lambda is almost the same.

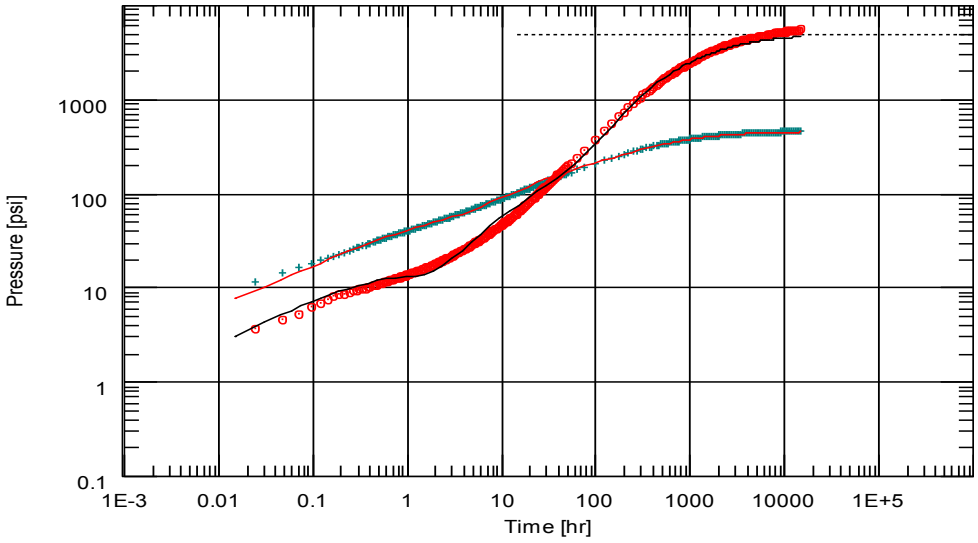


**Fig. 92 – Comparison between the numerical simulation model and well testing model for log-log plots of both DP and DPDT vs. time. Solid red and black are the DP and DPDT of well testing, respectively. Dotted curves are corresponding numerical simulation results.**

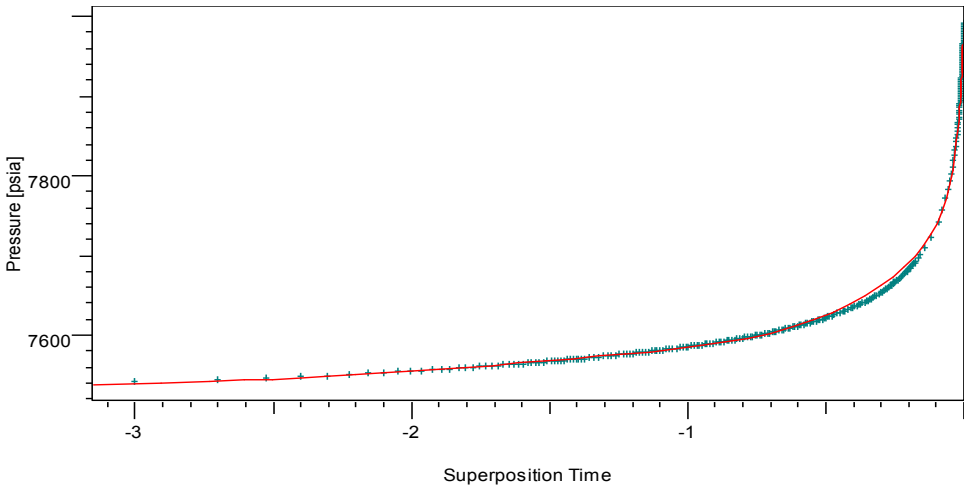


**Fig. 93 – Comparison between the numerical simulation model and well testing model for semi-log plot of pressure vs. superposition time. Solid red is for well testing, and dotted black curve for numerical simulation model.**

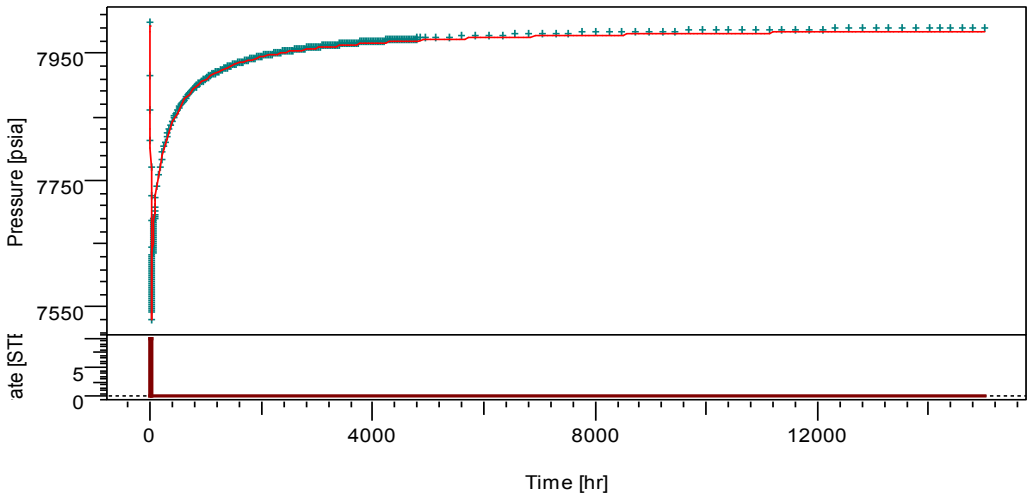


**Fig. 94 – Comparison between the numerical simulation model and well testing model for pressure response and rate vs. elapsed time. Solid red is for well testing, and dotted black curve for numerical simulation model.**

*5.2.3.2 Sensitivity Analysis for Parameters of the Well Testing Model*

Similarly as section 5.2.2.2, another group of sensitivity analysis is performed for well testing model parameters. **Table 16** tabulates all the sensitivity cases. A similar range of parameters in **Table 15** is used for **Table 16** in order to compare different model responses due to two reservoir boundary conditions.

| **Model Parameters** | **Default** | **Case I** | **Case II** | **Case III** | **Trends** |
|---|---|---|---|---|---|
| Skin Factor (s) | 1.09992E-4 | 0 | 0.01 | 0.1 | Upwards |
| Fracture Half Length (Xf), ft. | 27.13444 | 1 | 10 | 100 | Downwards |
| Fracture Angle, degree | 90 | 60 | 70 | 80 | - |
| Reservoir Flow Capacity (kh), mD-ft | 0.0666442 | 0.01 | 0.1 | 0.5 | Downwards |
| Permeability Anisotropy (Kz/kz) | 5.37053 | 0.5 | 50 | 500 | - |
| Storage Ratio, Omega | 0.0721077 | 0.01 | 0.1 | 0.5 | Downwards |
| Inter-Porosity Flow, Lambda | 1.28213E-8 | 1.00E-10 | 1.00E-05 | 1.00E-03 | Downwards |

**Table 16 – Sensitivity analysis of the well testing model parameters for the infinite acting reservoir.**

Trends in **Table 16** are very similar as those in **Table 15**. Specifically speaking, fracture angle and permeability anisotropy ratio have slight impact on both DP and DPDT curves. DPDT is not sensitive to the skin factors. With the increase of fracture half-length, the DP curves shift almost paralleled downward, similarly for Omega. The 'V' shape becomes severer with the increase in fracture half-length, lambda and omega, and decrease in reservoir flow capacity.

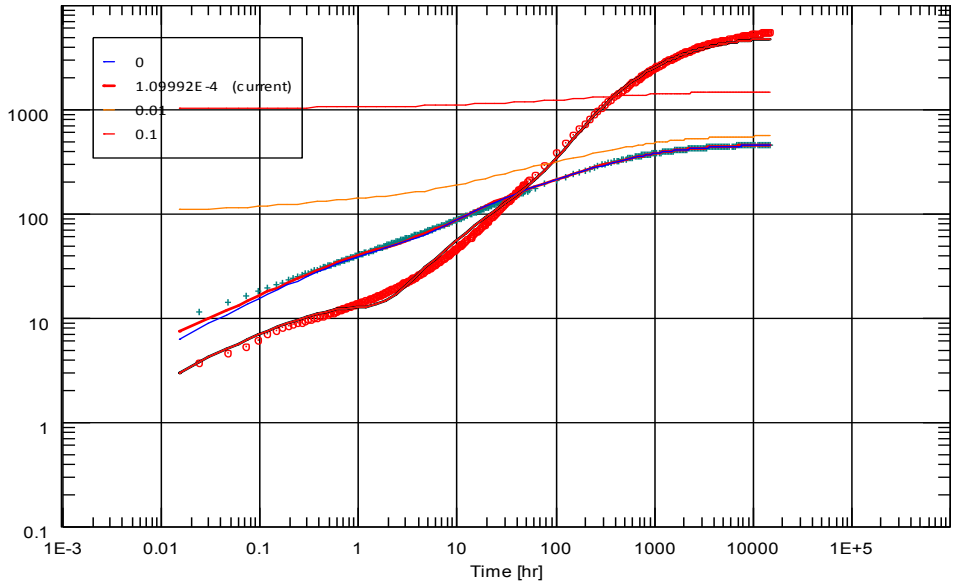


**Fig. 95 – The impact of skin factor on DP and DPDT vs. build-up time.**

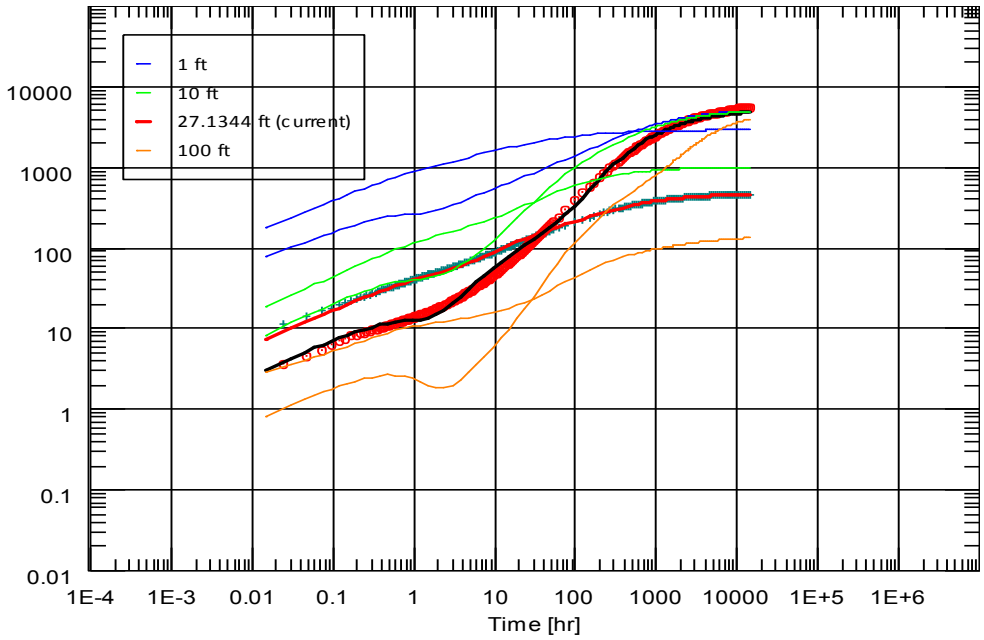


**Fig. 96 – The impact of fracture half-length on DP and DPDT vs. build-up time.**

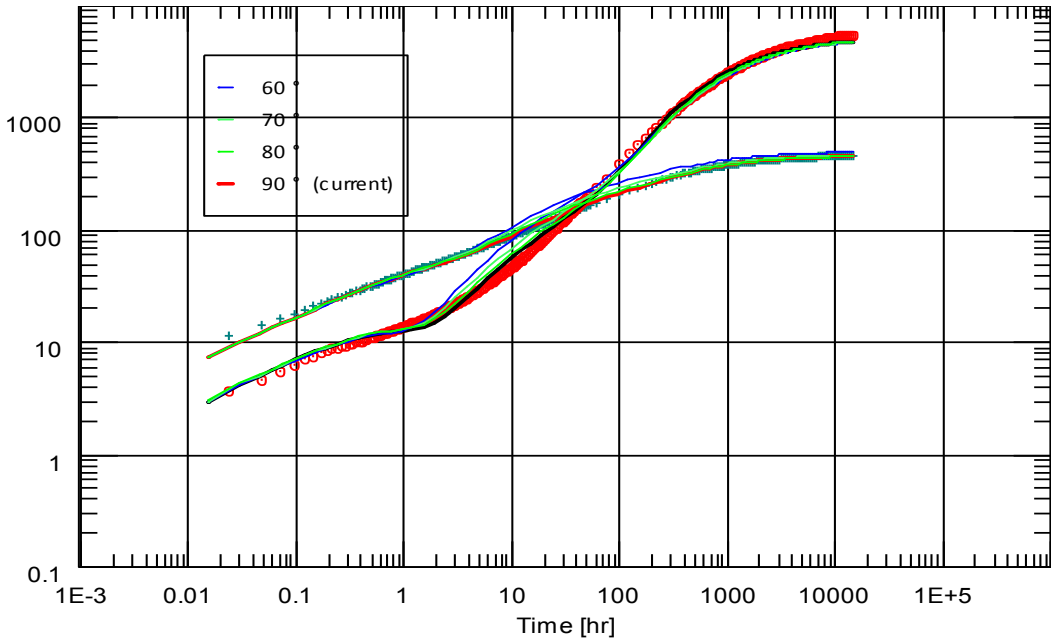


**Fig. 97 – The impact of fracture angle on DP and DPDT vs. build-up time.**

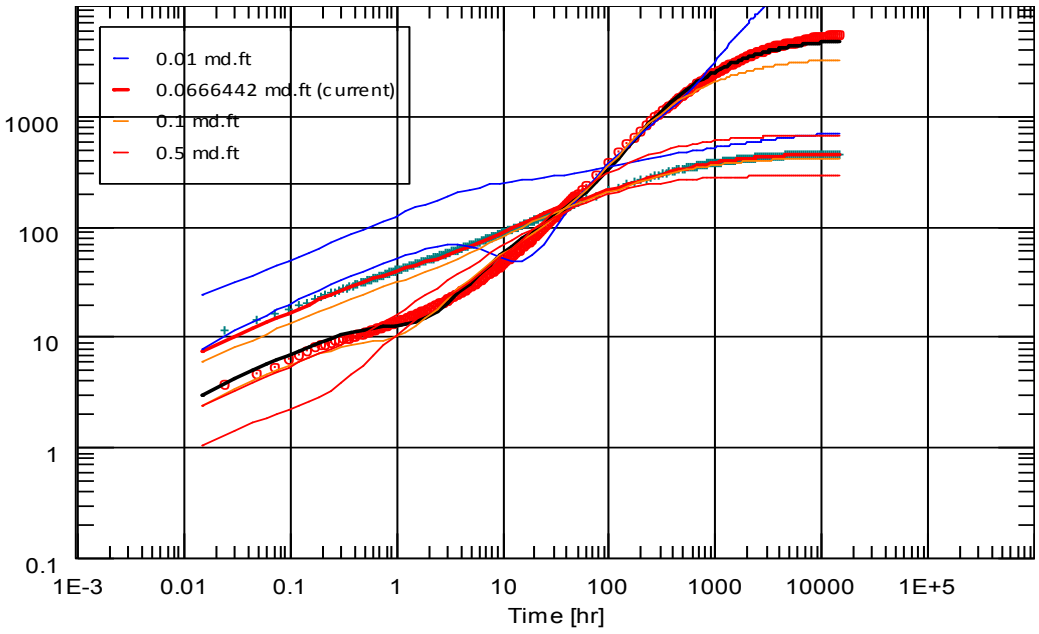


**Fig. 98 – The impact of reservoir flow capacity on DP and DPDT vs. build-up time.**

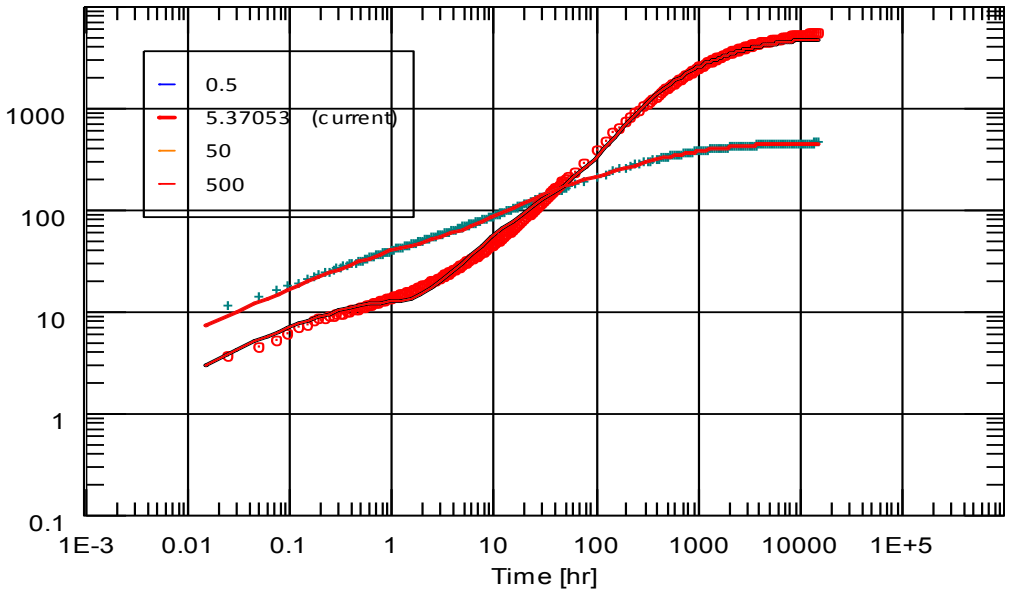


**Fig. 99 – The impact of permeability anisotropy on DP and DPDT vs. build-up time.**

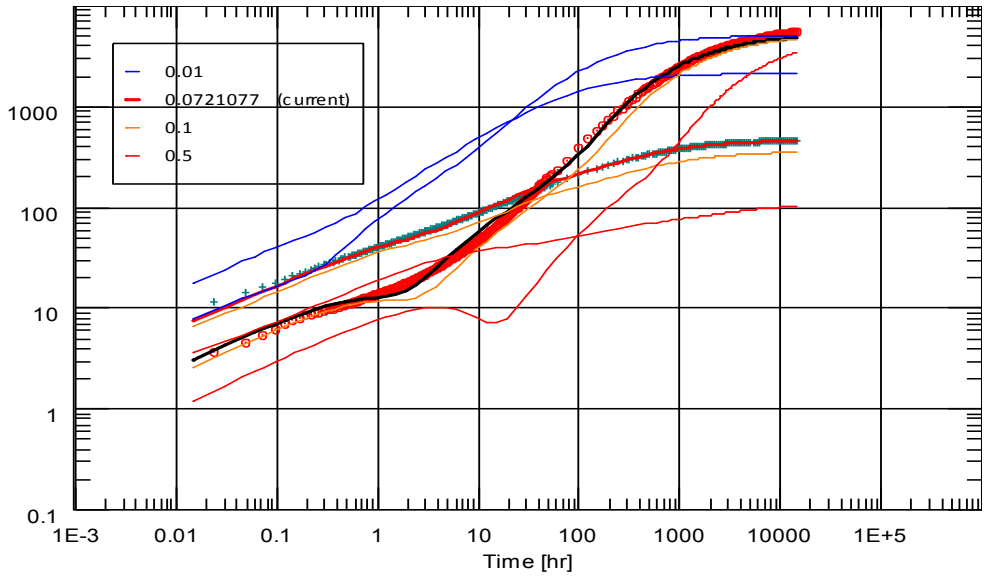


**Fig. 100 – The impact of omega on DP and DPDT vs. build-up time.**

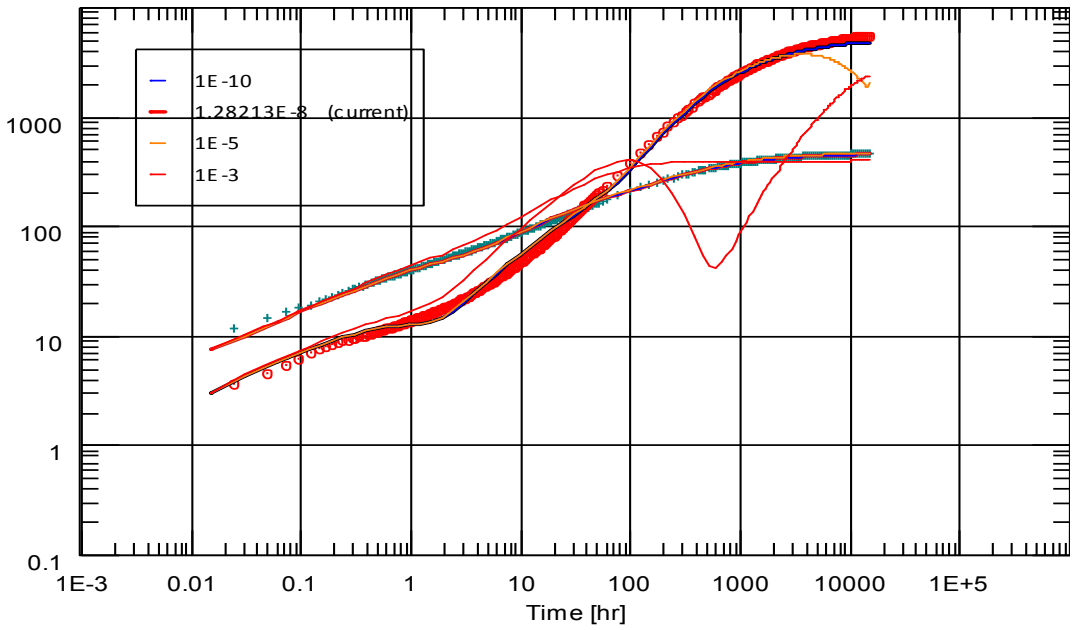


**Fig. 101 – The impact of lambda on DP and DPDT vs. build-up time.**

# CHAPTER VI

# APPLICATION OF OPTIMIZATION-BASED GRIDDING TECHNIQUES IN DISCRETE FRACTURE NETWORKS

In section 4.1.1, we present a sensitivity study on natural fracture related properties on well production performance such as natural fracture density or spacing, length, and strike. However, besides of the properties of natural fractures, the proposed optimization-gridding approach in Chapter III might introduce uncertainties or inaccuracies on numerical simulation.

For example, unstructured mesh density, background grid type, refinement method around fractures might have either significant or slight effect on production performance, which is required to be investigated. Moreover, reservoir engineers might be more interested in how much is the difference between the conventional grid solutions such as Tartan grid or LGR girds, and unstructured PEBI grid for both synthetic and real reservoir models, and in whether or not the unstructured PEBI grid can accurately reproduce the results of the conventional grid solutions. Most importantly, in terms of the advantages of using unstructured PEBI grids, not only do we need to present its flexibility, but also carry out a detailed CPU performance analysis to investigate if flexibility will yield better CPU performance, or we have to compromise CPU performance by using more flexible unstructured grids.

To these ends, we will study whether or not the unstructured grids are accurate enough to reproduce conventional grid solutions by comparing them to the tartar grid,

whether or not robust enough to model a real Eagle Ford field problem by comparing them to the LGR grid, whether or not flexible enough to vary meshing-related parameters, and finally whether or not efficient enough to improve CPU performance.

### *6.1 Model Validation with 2D Synthetic Case*

For simple fracture geometry with several fractures, it is feasible to benchmark numerical solutions against analytical solutions. However, it is difficult to derive analytical solutions to complex fracture geometries in order to validate the proposed gridding and discretization approach. Instead, we will validate it by comparing with known tartan grid solutions, which will be produced by an in-house reservoir simulator using the IFD discretization approach in section 3.3.

As seen in **Fig. 102**, a 2D synthetic model is built with a horizontal well and 55 vertical hydraulic fractures. The fracture network is gridded and discretized by both the tartan gridding and proposed unstructured gridding approach. For the tartan grid (around 29K cells), refinement around fractures has to be used in order to capture liquid condensate front around fractures. Inevitably, it results in a large number of cells for the reservoir background, which cannot be easily coarsened because of limitations of the structured grid system. On the other hand, for the PEBI grid, not only do we see a significant decrease in cell count from 29K to 19K, but also a reduction in grid-orientation effect because of the implemented force-based optimization algorithms. Besides, a condensate fluid PVT table is used for both models, and reservoir and fracture

properties are summarized in **Table 17**. In terms of accuracy, two models will be compared for oil rate, characteristic flow regimes, and pressure graphs throughout a 20 years' production at a constant bottom-hole flowing pressure (BHP).

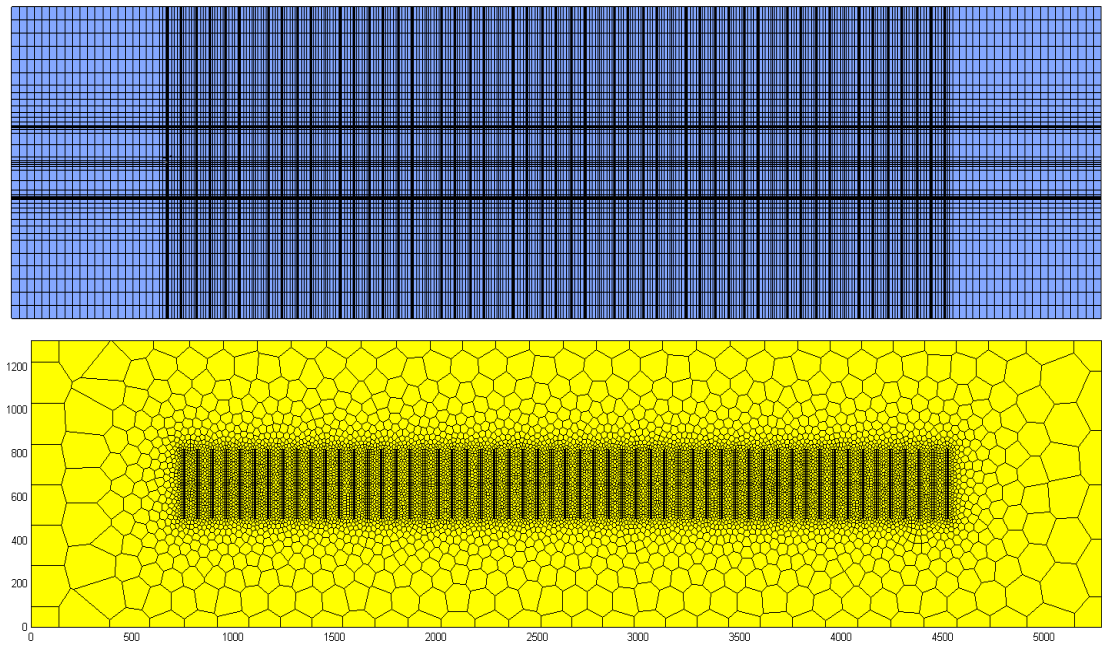


**Fig. 102 – Comparison of a 2D synthetic model between the Tartan grid and 2D PEBI grid.**

After 20 years' production at a constant BHP, oil rate vs. time is plotted on a log-log scale in **Fig. 103**. In addition, pressure graphs are prepared at 1 day, 10 days, 100 days, and at the end of 20 years' production for both the tartan grid and unstructured PEBI grid. The top pressure graph is for tartan grid, and the bottom one is for PEBI grid.

| | |
|---|---|
| Reservoir perm, md | 0.009 |
| Reservoir porosity | 0.055 |
| Reservoir length, ft. | 5280 |
| Reservoir width, ft. | 1320 |
| Fracture perm, md | 2754 |
| Fracture length, ft. | 302.6 |
| Fracture porosity | 0.3 |
| Fracture aperture, ft. | 0.083 |

**Table 17 – Reservoir and fracture properties for a 2D synthetic model.**

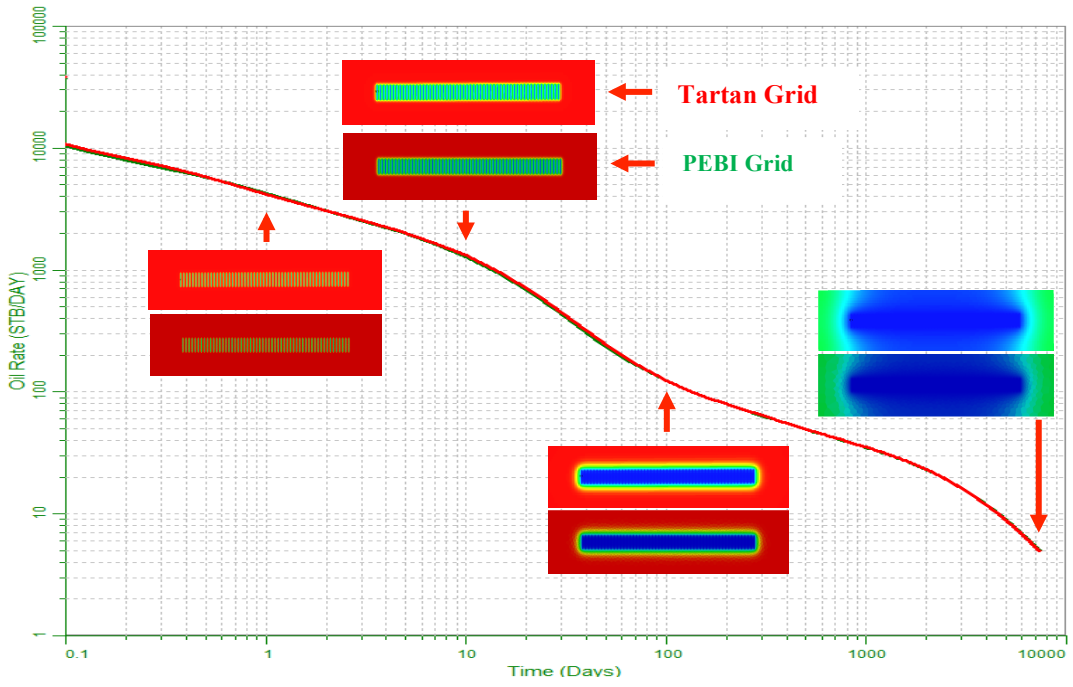


**Fig. 103 – Comparison of flow regimes between the Tartan mesh and 2D PEBI mesh.**

Almost the same pressure graph is observed between two grids throughout the whole simulation period. Moreover, from 0.1 day up to 10 days, a half-slope is found, which represents the linear flow regime. From 10 days up to 100 days, significant pressure depletion is noticed around the hydraulic fractures, corresponding to fracture interference. At the end of 20 years' production, a complete pressure depletion of the whole reservoir occurs, representing the boundary-dominated fluid flow. For all the flow regimes, good matches between the tartan grid and the PEBI grid for both oil rate and pressure graphs are observed. Therefore, it is concluded that the proposed gridding and discretization approach is accurate enough to reproduce reference solutions. Lastly, for both models, reservoir simulations take only a few minutes to finish, and thus it makes no sense to compare CPU performance. Instead, we will take a look at a detailed analysis of CPU performance for the following field case.

## *6.2 Eagle Ford Field Model*

Once the proposed algorithms are validated by the synthetic model, an Eagle Ford field model with complex fracture geometries will be studied and presented in this section to compare PEBI grids with a Schlumberger E&P software platform-generated LGR grid. The objective of this comparison is to determine if the developed unstructured gridding approach is sufficiently robust and flexible to handle complicated field problems. In the meantime, the effect of gridding-related parameters on both accuracy and CPU performance will be thoroughly investigated.

### 6.2.1 Reservoir and Fracture Properties

The Eagle Ford field model consists of three horizontal wells corresponding to Well #1, Well #2, and Well #3, 40 nonorthogonal hydraulic fractures per well, and 8 reservoir layers with a small dipping angle. To reveal differences between PEBI meshes and the LGR mesh, several snapshots of the same reservoir locations are shown in **Fig. 104**. First of all, from the two snapshots at the top, the proposed gridding approach represents fractures around the intersection using straight-line segments, whereas the LGR model intersected fractures using a zigzag shape of line segments, which causes inaccuracy in the fracture length.

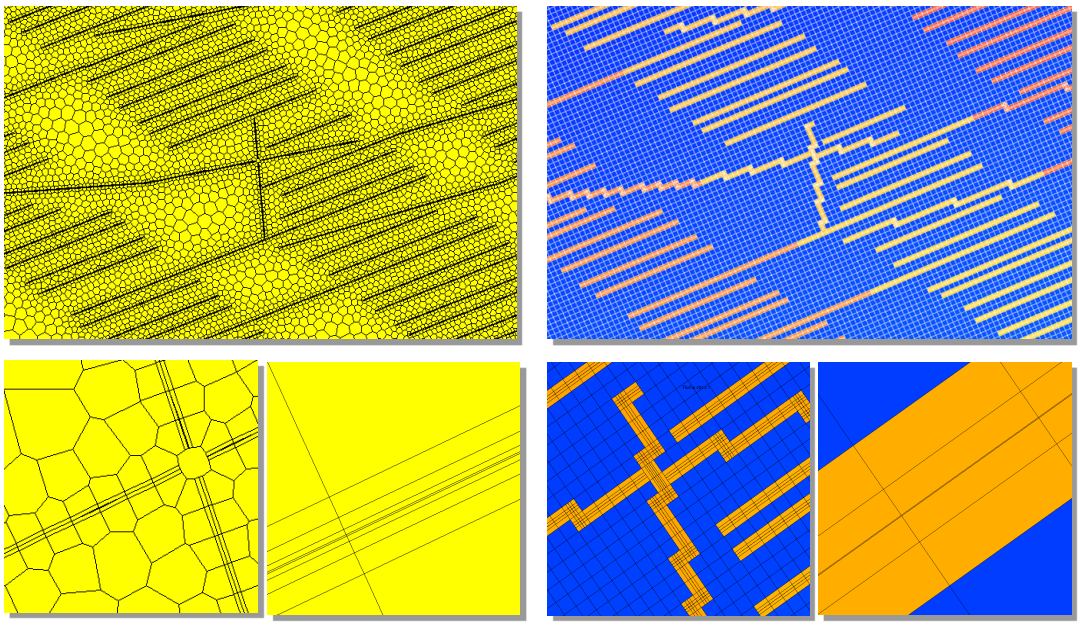

**Fig. 104 – Comparison between 2.5D PEBI grid (left) and E&P software platform-generated LGR grid (right).**

| Layer | Thickness (ft.) | Porosity | Kx = Ky (md) | Kz (md) |
|---|---|---|---|---|
| 1 | 36.003 | 0.08 | 1.50E-04 | 5.00E-07 |
| 2 | 35.025 | 0.099 | 1.50E-04 | 5.00E-07 |
| 3 | 17.075 | 0.119 | 1.50E-04 | 5.00E-07 |
| 4 | 38.173 | 0.129 | 1.50E-04 | 5.00E-07 |
| 5 | 19.307 | 0.139 | 1.50E-04 | 5.00E-07 |
| 6 | 38.98 | 0.113 | 1.50E-04 | 5.00E-07 |
| 7 | 23.25 | 0.123 | 1.50E-04 | 5.00E-07 |
| 8 | 29.748 | 0.106 | 1.50E-04 | 5.00E-07 |

**Table 18 – Reservoir and rock data.**

| Sw | krw | krow | Sg | krg | krog |
|---|---|---|---|---|---|
| 0.25 | 0 | 1 | 0 | 0 | 1 |
| 0.3 | 0 | 0.656 | 0.05 | 0.001 | 0.826 |
| 0.356 | 0.002 | 0.385 | 0.113 | 0.009 | 0.633 |
| 0.413 | 0.009 | 0.208 | 0.175 | 0.038 | 0.465 |
| 0.469 | 0.021 | 0.1 | 0.238 | 0.084 | 0.323 |
| 0.525 | 0.038 | 0.041 | 0.3 | 0.15 | 0.207 |
| 0.581 | 0.059 | 0.013 | 0.363 | 0.234 | 0.116 |
| 0.625 | 0.079 | 0.005 | 0.375 | 0.255 | 0.103 |
| 0.638 | 0.084 | 0.003 | 0.425 | 0.338 | 0.052 |
| 0.694 | 0.115 | 0 | 0.488 | 0.459 | 0.013 |
| 0.75 | 0.15 | 0 | 0.55 | 0.6 | 0 |
| 1 | 1 | 0 | 0.75 | 0.8 | 0 |

**Table 19 – Oil and gas relative permeability data.**

Secondly, the two snapshots at the bottom of **Fig. 104** show enlarged views around the fracture intersection. The LGR model implements complicated non-neighbor connections to model fluid flow around the intersection. However, this study adds a single gridblock to model the intersection, which is more straightforward to understand. Thirdly, the background mesh generated by LGR model depends on the fracture gridblock size, which produces unnecessary refinement for reservoir background. Nevertheless, the proposed gridding method uses fine mesh around the fractures and coarse mesh far away from the fractures. On the other hand, both the PEBI grid and the LGR grid use rectangular cells for both fracture gridblocks and surrounding fracture

refinement, which is required to model linear flow regimes during the early production period.

| Pressure (psi) | Bg (res. bbl./stb) | Vg (cp) | Rs (scf/stb) | Bo@Pb (res. bbl./stb) |
|---|---|---|---|---|
| 15 | 2.604E-01 | 1.271E-02 | 18.5 | 0.992 |
| 469 | 7.783E-03 | 1.354E-02 | 232.7 | 1.120 |
| 923 | 3.711E-03 | 1.506E-02 | 434.3 | 1.253 |
| 1377 | 2.365E-03 | 1.729E-02 | 649.0 | 1.399 |
| 1831 | 1.728E-03 | 2.024E-02 | 880.6 | 1.558 |
| 2284 | 1.382E-03 | 2.373E-02 | 1130.9 | 1.728 |
| 2738 | 1.177E-03 | 2.747E-02 | 1401.5 | 1.908 |
| 3192 | 1.048E-03 | 3.122E-02 | 1693.8 | 2.097 |
| 3646 | 9.599E-04 | 3.484E-02 | 2009.5 | 2.295 |
| 4100 | 8.966E-04 | 3.830E-02 | 2350.1 | 2.501 |
| 4962 | 8.149E-04 | 4.440E-02 | | |
| 5824 | 7.608E-04 | 4.997E-02 | | |
| 6686 | 7.219E-04 | 5.511E-02 | | |
| 7548 | 6.922E-04 | 5.990E-02 | | |
| 8410 | 6.685E-04 | 6.442E-02 | | |
| 9272 | 6.490E-04 | 6.870E-02 | | |
| 10134 | 6.326E-04 | 7.278E-02 | | |
| 10996 | 6.186E-04 | 7.669E-02 | | |
| 11858 | 6.063E-04 | 8.046E-02 | | |
| 12720 | 5.955E-04 | 8.409E-02 | | |

**Table 20 – PVT data.**

**Table 18** summarizes the reservoir and rock data. Hydraulic fracture permeability values are equal to 250 md, 500 md, and 300 md for three horizontal wells, respectively. Hydraulic fracture porosity is equal to 0.3. The horizontal well is completed in the sixth layer, and hydraulic fractures fully penetrate all the layers. **Table 19** and **Table 20** show the input oil/water and gas/water two-phase relative permeability data. The Stone 1 method modified by Fayers (Fayers 1989) is used for the three-phase oil relative permeability model. **Table 20** illustrates gas formation volume factor and viscosity vs. pressure. Gas formation volume factor (Bg) ranges from 2.6E-01 to 5.96E-04 between 15 psi and 12,720 psi. Correspondingly, gas viscosity (Vg) ranges from 1.27E-02 to 8.41E-02. Furthermore, solution gas/oil ratio (Rs), and oil formation volume factor (Bo) at variable bubble point pressures are tabulated in the last two columns, which are used for computing PVT properties along the envelope. For instance, at the bubble point of 2284 psi, Rs and Bo equal to 1130.9 and 1.728, respectively.

Furthermore, laboratory pressure/volume/temperature (PVT) measurement shows a volatile oil where the bubble points are very close to the critical point. In total, there are 10 saturation pressures ranging from 15 psi to 4,100 psi in **Table 20**.

### 6.2.2 Sensitivity of Background Grid Density

One advantage of the unstructured PEBI grid is its flexibility with regard to cell shape and size; thus, a large background grid size can be chosen to reduce the total number of simulation cells and simulation time. The goal in this section is to investigate the lowest background grid density we can achieve without compromising the accuracy

of simulation results. In conventional grid systems such as tartan and LGR grids, it is very difficult to coarsen the reservoir background because the background grid size depends on the fracture gridblock size.

By applying the developed unstructured gridding workflow, five meshes were generated as shown in **Fig. 105**. The total number of cells is reduced by 1/2 from around 410,000 to 190,000 by using a large initial gridblock size and mesh-size progression ratio (two input parameters for the 2.5D PEBI mesh generator). For the four PEBI meshes as well as the LGR mesh, a history production of approximately 0.65 year is first simulated, which is then followed by a 20-year prediction at a constant rate until the BHP reaches 100 psi using an in-house black-oil simulator. After simulating all of the cases, the post-processor is applied to plot and compare the pressure plots as shown in **Fig. 106**.

A good match in pressure graph is observed between the LGR model and the PEBI fine model. Both models have approximately 400,000 cells. The LGR grid use larger grid size for the reservoir background; otherwise, there will not be enough gridblocks between two fractures to capture the fracture interference effect. On the other hand, with the help of the developed unstructured gridding algorithms, the cell number is reduced to approximately 255,000 without compromising the accuracy of the pressure responses.

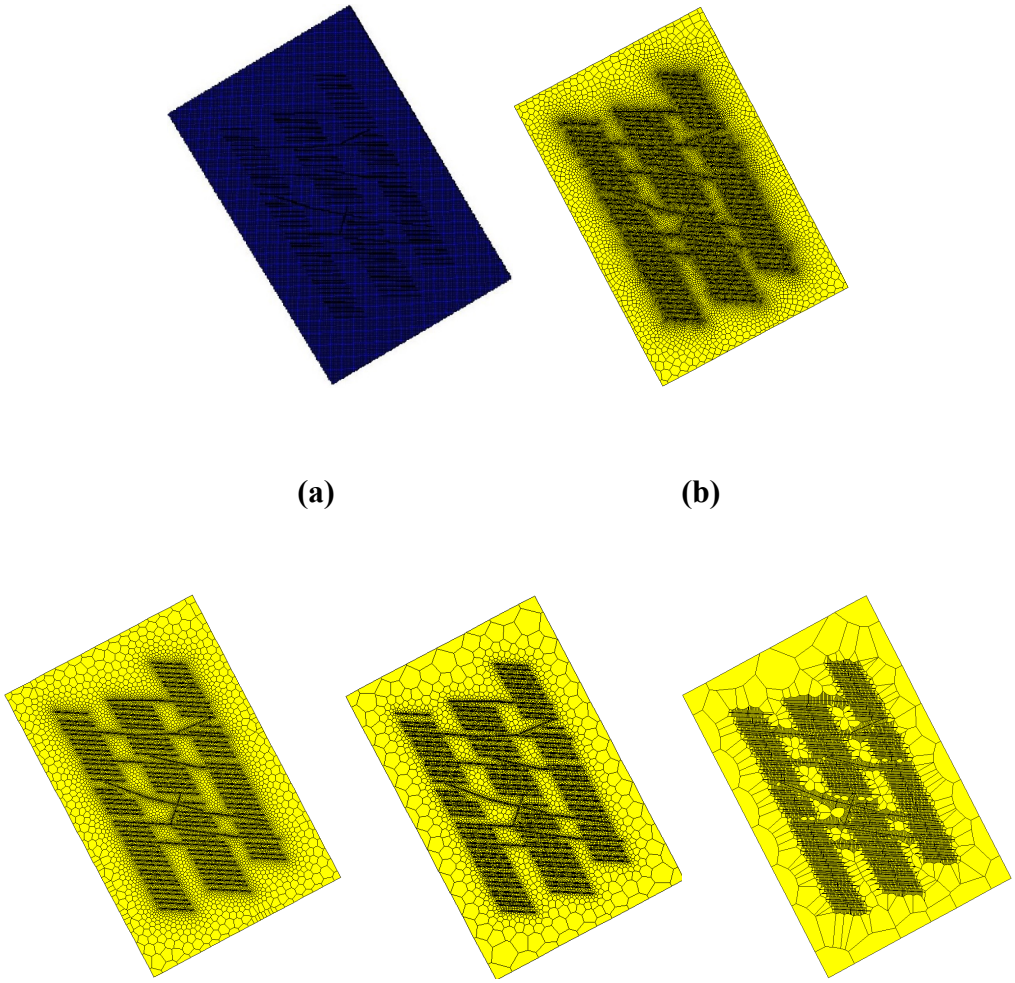

**(a)** **(b)**

**(c)** **(d)** **(e)**

**Fig. 105 – Comparison of simulation grids between LGR and 2.5D PEBI meshes with different background grid densities; from the upper left to the lower right are an LGR mesh with 401,384 cells (a), a PEBI fine mesh with 409,920 cells (b), two PEBI meshes with 281,336 (c) and 255,088 cells (d), and a PEBI coarse mesh with 190,440 cells (e).**

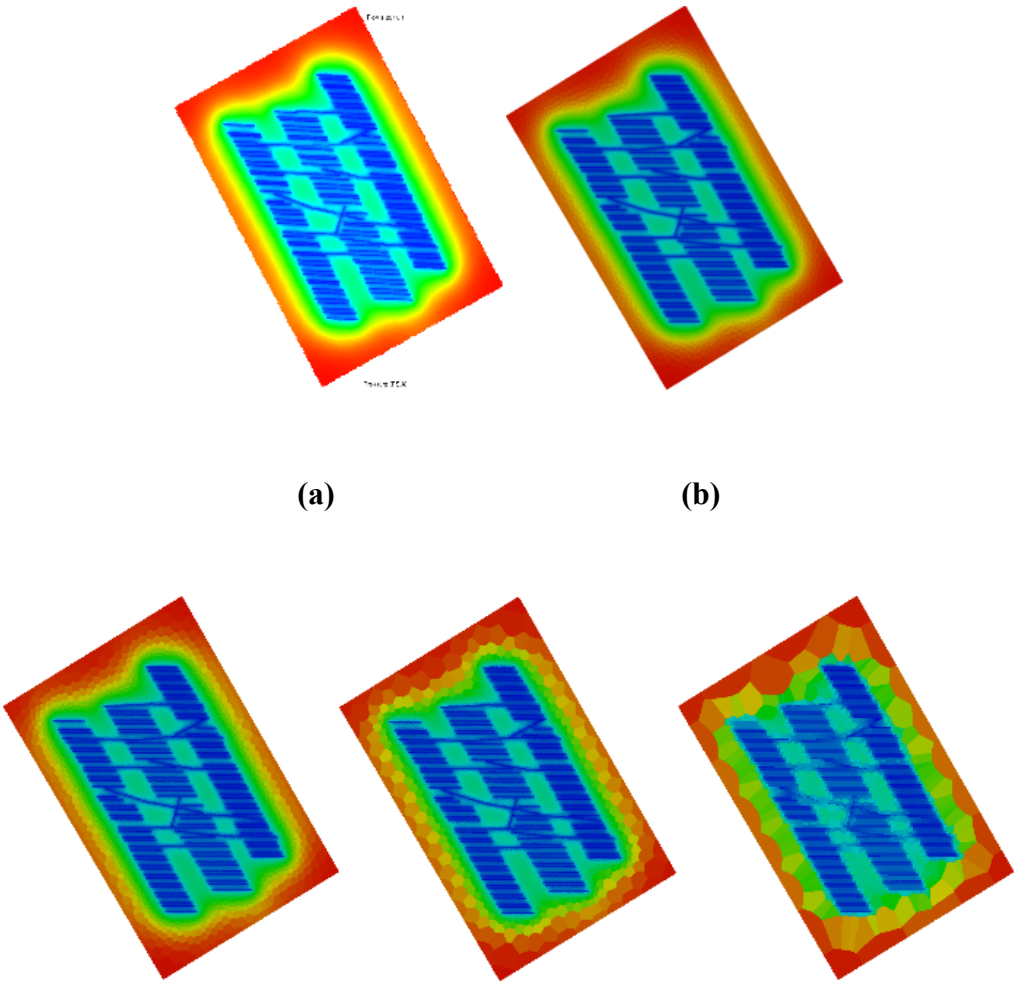

**(a)** **(b)**

**(c)** **(d)** **(e)**

**Fig. 106 – Comparison of pressure graphs between LGR and 2.5D PEBI meshes with different background grid densities; from the upper left to the lower right are an LGR mesh with 401,384 cells (a), a PEBI fine mesh with 409,920 cells (b), two PEBI meshes with 281,336 (c) and 255,088 cells (d), and a PEBI coarse mesh with 190,440 cells (e).**

Moreover, the background grid density plays an important effect in long-term production. For example, the PEBI model with 190,440 cells is too coarse to accurately capture the pressure front. However, for other PEBI models, a reasonable match with the LGR model is observed, even though the LGR grid is different from PEBI grids, especially in the fracture intersection areas.

The BHP comparison between the LGR model and four PEBI models are shown in **Figs. 107**, **108**, and **109**. For example, in **Fig. 107a**, the BHP responses are shown for long-term production up to 20 years, and **Fig. 107b** shows a close-up view during the early production period up to 0.65 year. Furthermore, the LGR model has been history matched with production data up to 0.65 year; thus, it was taken as the reference model. The remainder of the PEBI models will be compared versus the LGR model for accuracy of the results.

The PEBI coarse mesh with 190,440 cells shows large discrepancy in results compared to other refined ones (e.g., PEBI models with 255,088 and 409,920 cells). We don't see any improvement in the results with the refinement in the background mesh from 255,088 to 409,920 cells during early as well as late production period. When the production time is less than 0.3 year, the PEBI coarse model with less background density shows a reasonable BHP match with other PEBI models and LGR model. However, from both the early production after 0.3 year (e.g., 0.5 to 0.6 year in **Figs. 107** to **109**) and long-term production up to 20 years, the PEBI coarse model shows significantly lower BHP responses than the other three PEBI models that have a similar BHP response throughout the entire production period.

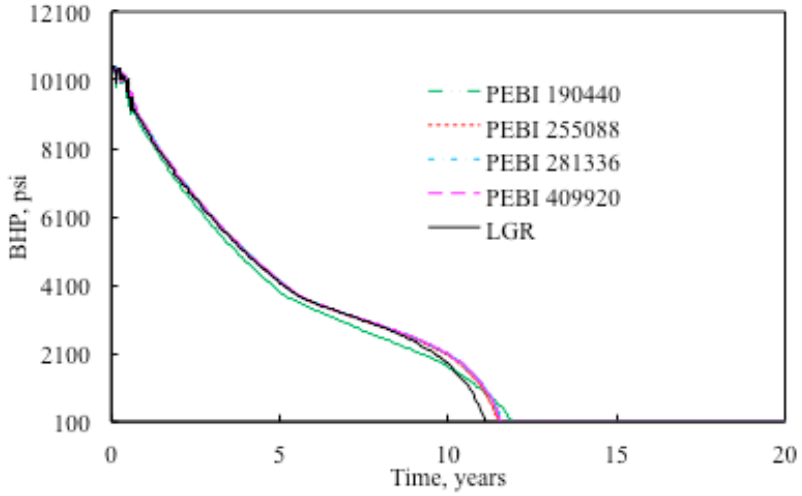


**(a)**

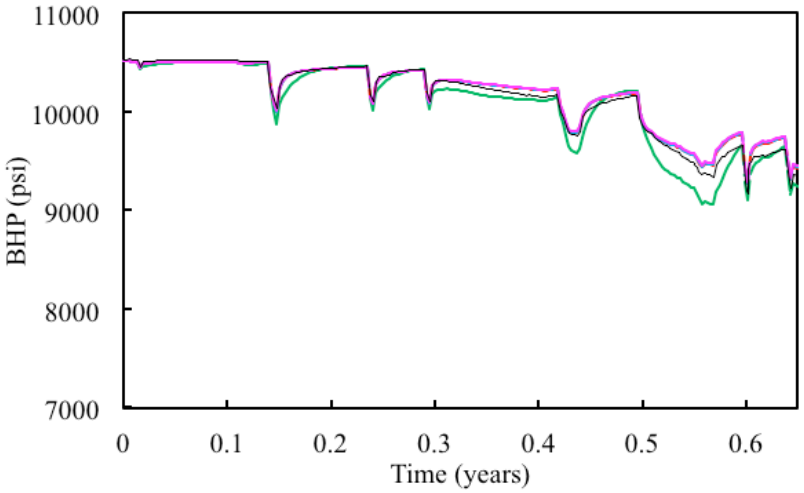


**(b)**

**Fig. 107 – Well #1 BHP comparison between the LGR grid and PEBI grids with different background densities.**

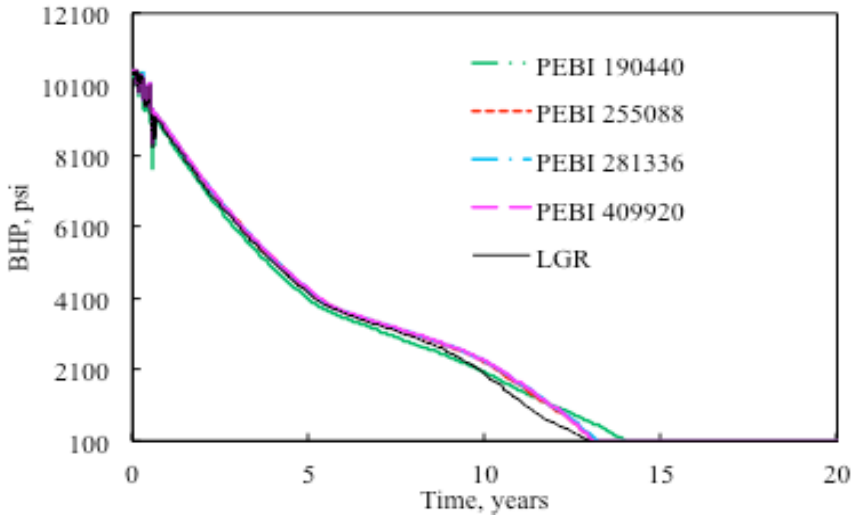


**(a)**

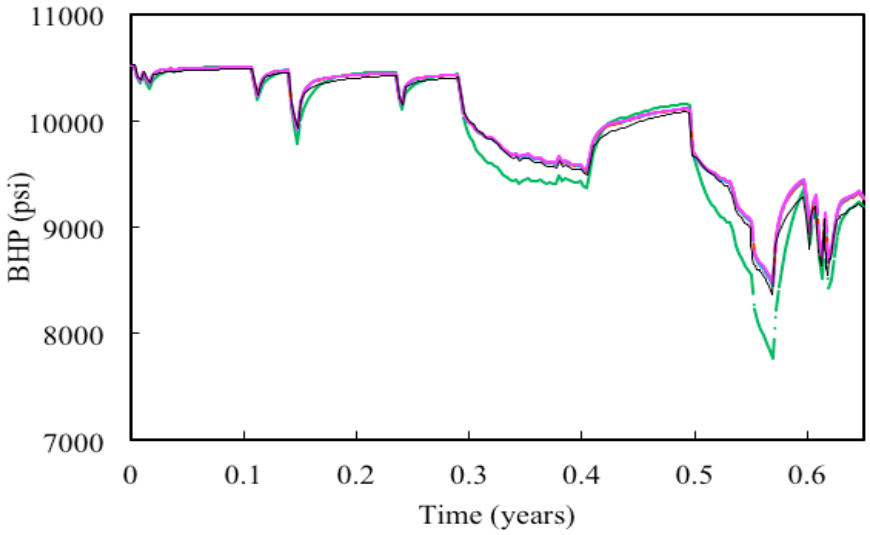


**(b)**

**Fig. 108 – Well #2 BHP comparison between the LGR grid and PEBI grids with different background densities.**

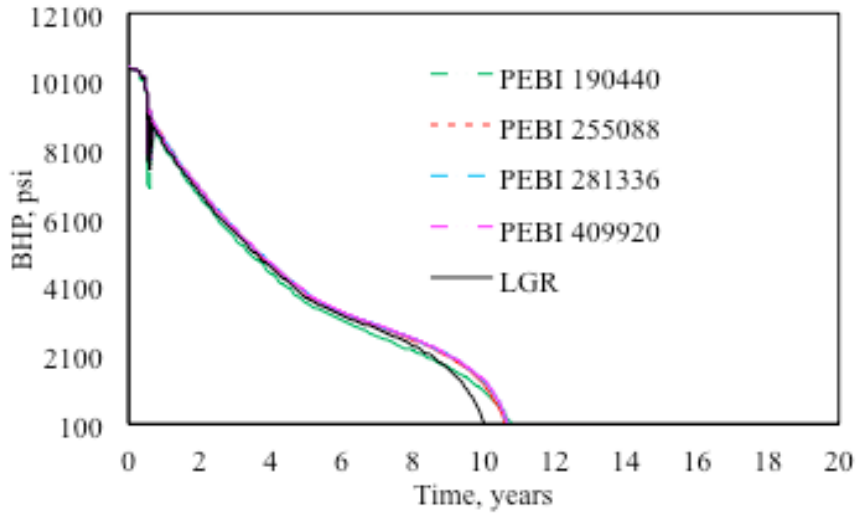


**(a)**

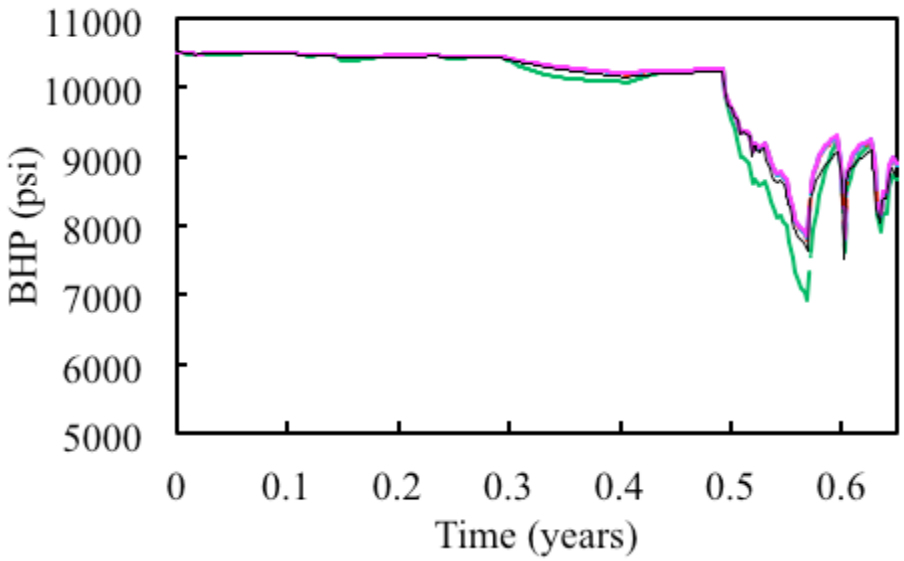


**(b)**

**Fig. 109 – Well #3 BHP comparison between the LGR grid and PEBI grids with different background densities.**

The reason for this result is all four PEBI models are created with the same fracture gridblock size; thus, early production behaves almost the same. For the PEBI coarse model with 190,440 cells as shown in **Fig. 105**, there is only one cell between fractures, and two cells between the fractures and the reservoir boundary, which results in early fracture interference and boundary effect. This issue can be resolved by adding additional refinement to the reservoir background (e.g., using a smaller initial gridblock size and lowering the mesh-size progression ratio between two adjacent cells), making certain there are enough cells to capture the pressure transient effect between fractures, and between fractures and boundaries. In this field case, as long as the total number of PEBI cells are greater than approximately 255,000, the same accurate BHP responses and pressure graphs as the LGR model can be achieved with the less number of cells.

### 6.2.3 Sensitivity of Background Grid Type

Even though the PEBI grid is flexible and has demonstrated its capability to reduce the total number of simulation gridblocks, the Jacobian matrix formulated from unstructured PEBI grids usually concludes with unequal bandwidth; thus, compromised computational efficiency. One possible solution to this problem is to replace the background unstructured grids with either Cartesian or hexagonal grids. The result is the Jacobian matrix might be as narrow in bandwidth as possible without compromising accuracy requirement around the fractures.

As shown in **Fig. 110**, a region boundary indicated by the red dotted box indicates the same distance to the inner fracture. A hybrid gridding approach is

implemented in this study, for which within this region, unstructured PEBI grids will be used; and outside this region, either structured rectangles or hexagons will be used.

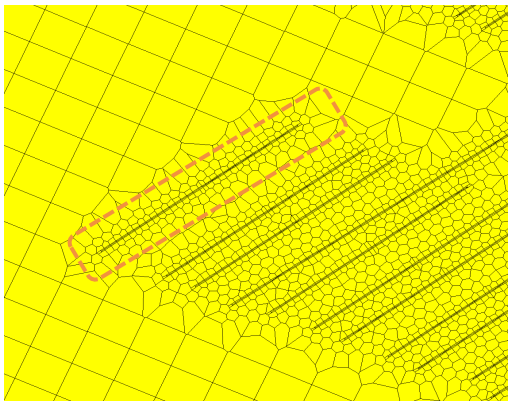

**Fig. 110 – Hybrid gridding approach with the PEBI grid around fractures and the structured Cartesian grid for the reservoir background.**

In **Fig. 111**, three different background grid types are shown—from left to right, default unstructured PEBI grid, PEBI-rectangle grid, and PEBI-hexagonal grid. The default PEBI grid with 255,088 cells is taken from the previous section. The hybrid gridding approach yields 231,048 cells for the PEBI-rectangle model, and 232,080 for the PEBI-hexagonal model. A lesser number of cells are obtained for the hybrid gridding approach than the default gridding approach because a small region is defined around each fracture. If a large region were defined, it would finish with more cells than the default gridding approach. In a similar manner, two hybrid PEBI models are simulated with the previous rock and fluid properties in **Tables 18** to **20**, and simulation results will be compared with the LGR model and the default PEBI model.

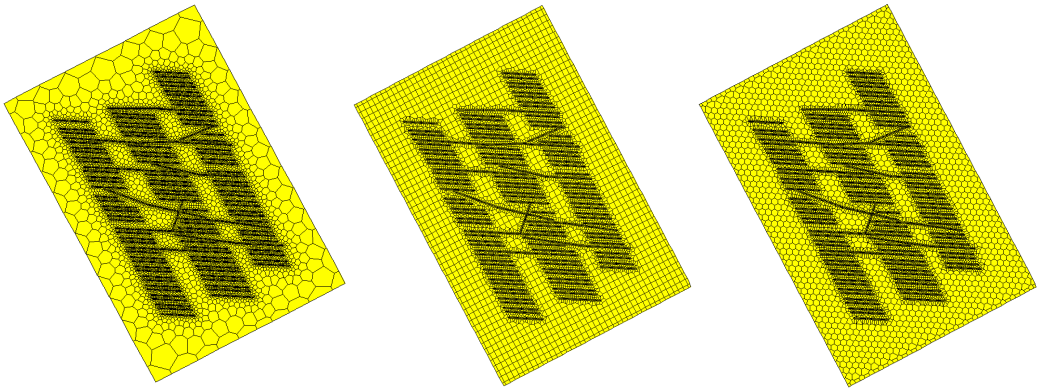

**(a)** **(b)** **(c)**

**Fig. 111 – Comparison of 2.5D PEBI meshes with different background grid types; from left to right, the default PEBI model with 255,088 cells (a), PEBI-rectangle model with 231,048 cells (b), and PEBI-hexagonal model with 232,080 cells (c).**

From the pressure plots shown in **Fig. 112**, the hybrid gridding approach produces even better results than did the default gridding approach. Hybrid gridding not only reduces the total cell number, but also yields better resolution of simulation results for the reservoir background. For instance, because of the lower resolution in the reservoir background for default gridding produce, there is a clear transition in pressure graph, which follows the shape of the PEBI grid. Such a transition becomes much smoother in the hybrid gridding approach, which shows even closer results to the LGR grid. Furthermore, very little difference is observed between the hexagonal and rectangle background. Both cases yield almost the same pressure curves because of the same background density.

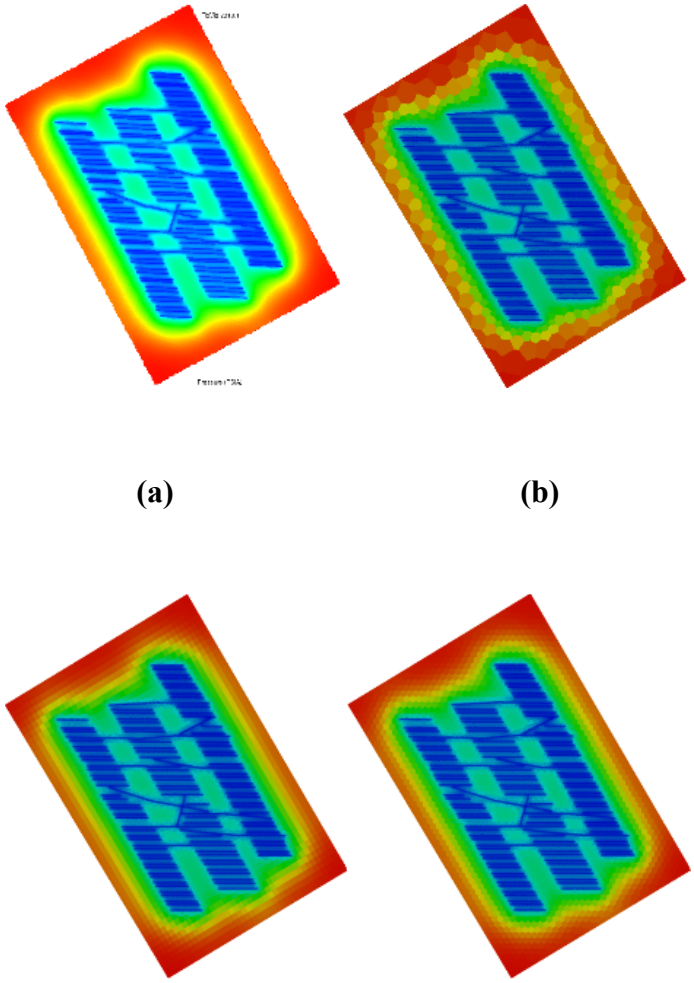

**(a)** **(b)**

**(c)** **(d)**

**Fig. 112 – Pressure comparison between the LGR grid and PEBI grids with different background grid types; from upper left to lower right, the LGR model with 401,384 cells (a), default PEBI model with 255,088 cells (b), PEBI-rectangle model with 231,048 cells (c), and PEBI-hexagonal model with 232,080 cells (d).**

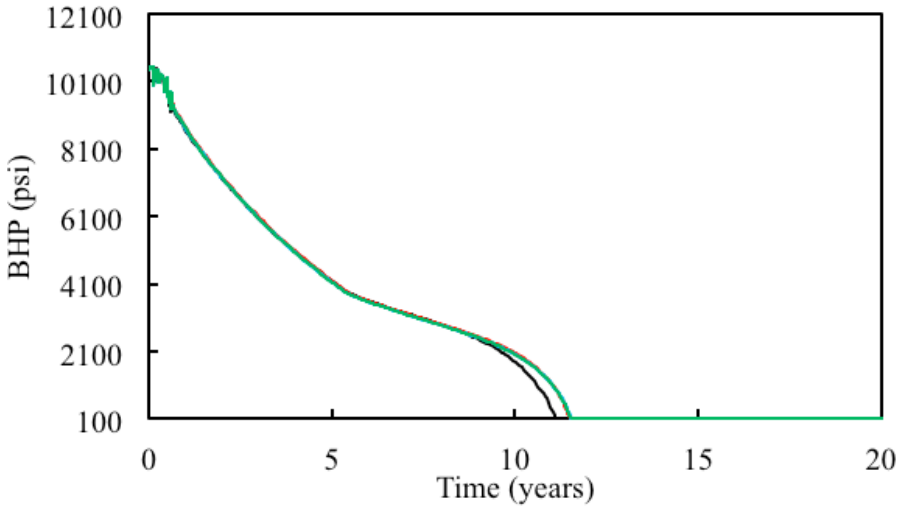


**(a)**

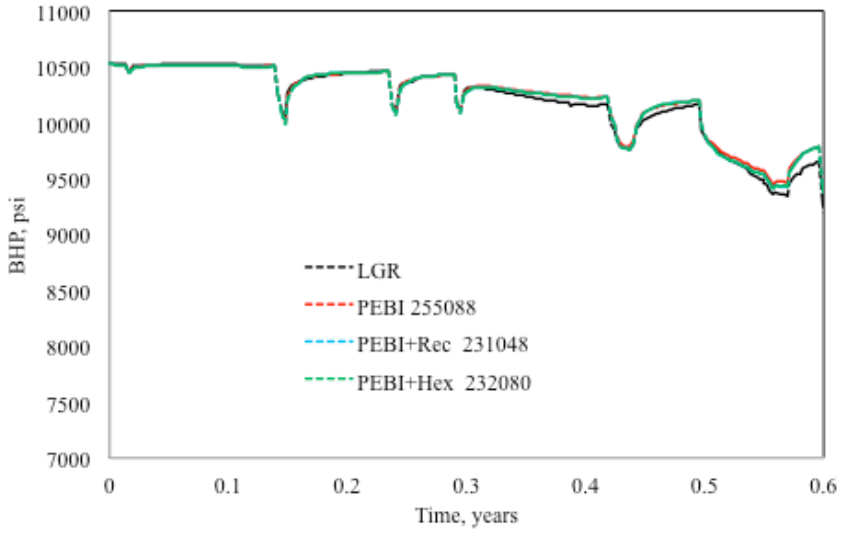


**(b)**

**Fig. 113 – Well #1 BHP comparison between the LGR grid and PEBI grids with different background types.**

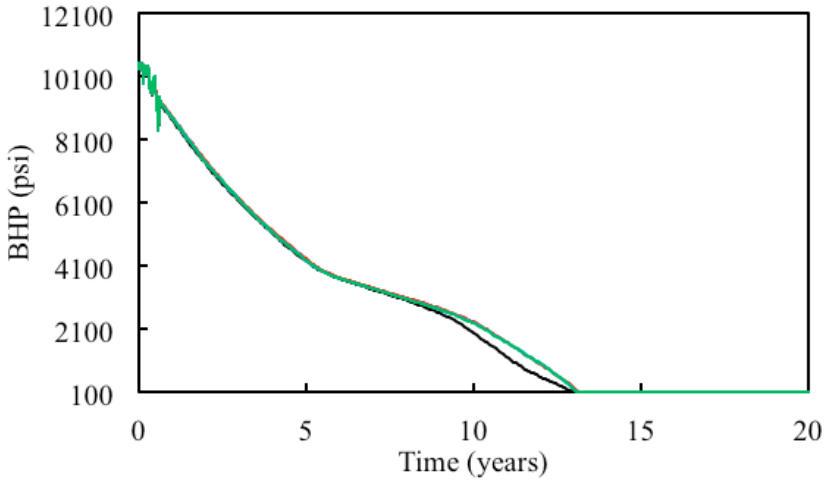


**(a)**

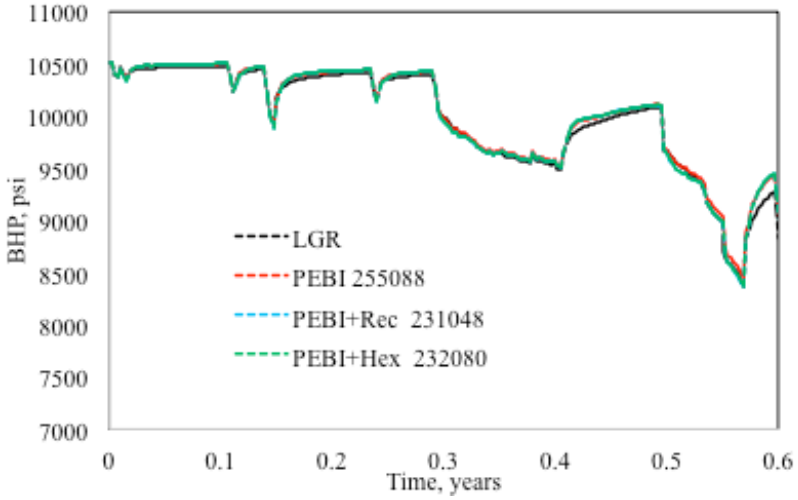


**(b)**

**Fig. 114 – Well #2 BHP comparison between the LGR grid and PEBI grids with different background types.**

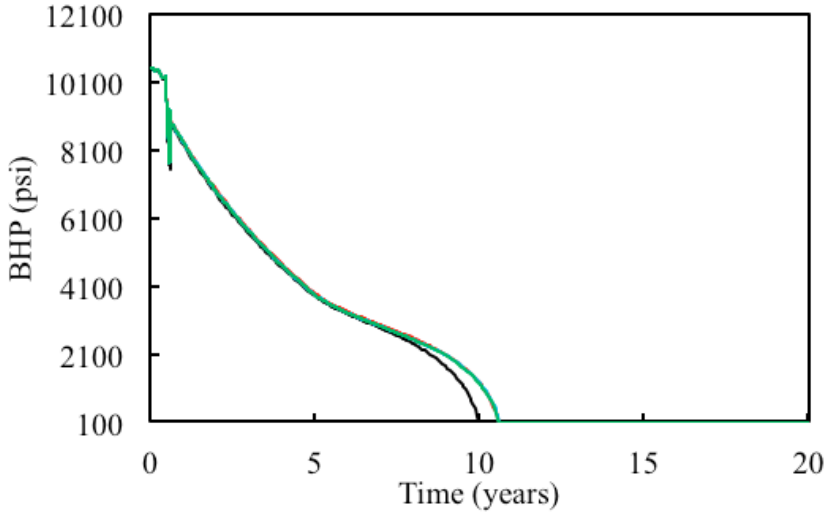


**(a)**

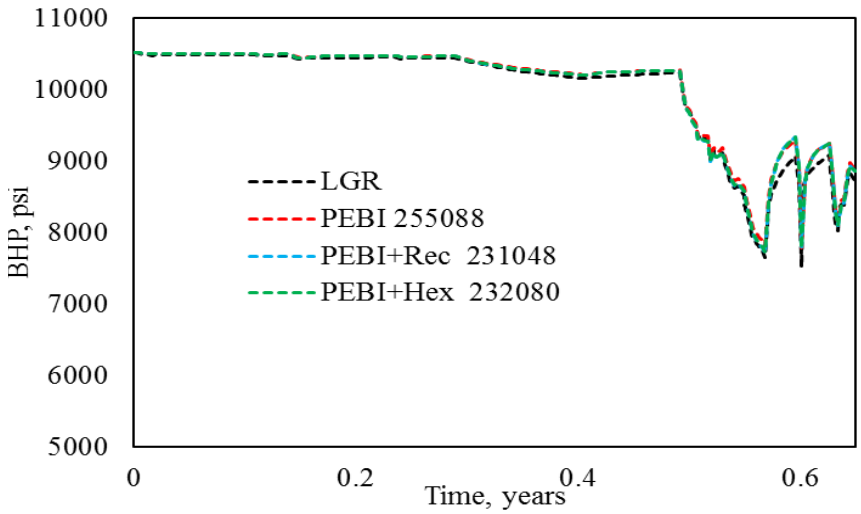


**(b)**

**Fig. 115 – Well #3 BHP comparison between the LGR grid and PEBI grids with different background types.**

BHP response comparisons between the LGR model, the default PEBI model, PEBI-rectangle model, and PEBI-hexagonal model are shown in **Figs. 113** to **115**. All of the PEBI models show almost the same BHP responses throughout the entire production period. Furthermore, all of the PEBI models are very similar to the LGR model for both the early and long-term production periods. At approximately 8 years of production when the BHP decreases to 2,100 psi, there is a small discrepancy between the PEBI models and the LGR model, which might due to different grid refinement around the fractures. Thus, the BHP responses and pressure curves are insensitive to background grid type if the background grid density is approximately the same.

### 6.2.4 Sensitivity of Background Grid Refinement

In terms of well testing analysis, fracture refinement is necessary to accurately capture early flow regimes. In this section, the effect of fracture refinement on both short-term and long-term production will be investigated. Illustrations of two hybrid meshes without refinement and with three refinement gridblocks on both sides of fractures are shown in **Fig. 116**. For instance, in the case with refinement, the tartan grid is first applied to resolve refinement, then the PEBI grid for conforming to complex fracture geometry, and finally the structured Cartesian grid for modeling reservoir background.

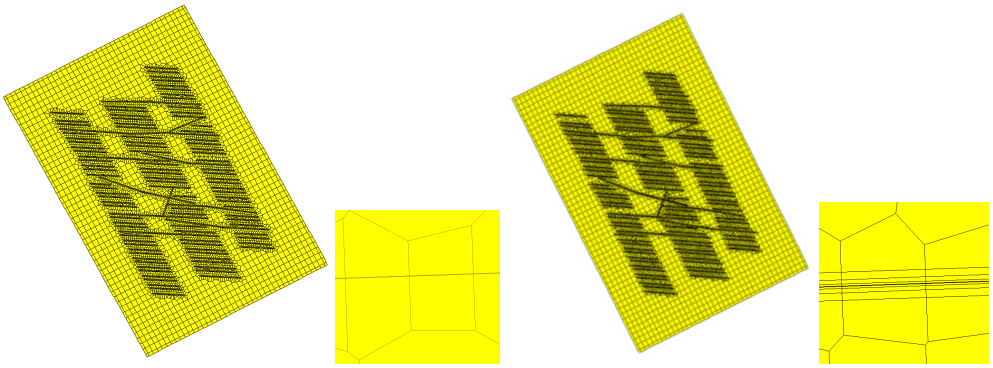

**(a)** **(b)** **(c)** **(d)**

**Fig. 116 – Fracture refinement comparison; PEBI-rectangle model without fracture refinement (a), enlarged-view of a fracture without refinement (b), PEBI-rectangle model with fracture refinement (c), and a magnified view of a fracture with refinement (d).**

From the pressure graphs shown in **Fig. 117**, very small discrepancy in the pressure graph is observed in either the reservoir background or around the fractures. The PEBI model with only 155,080 cells can approximate simulation results of the LGR model and PEBI model with 388,008 cells.

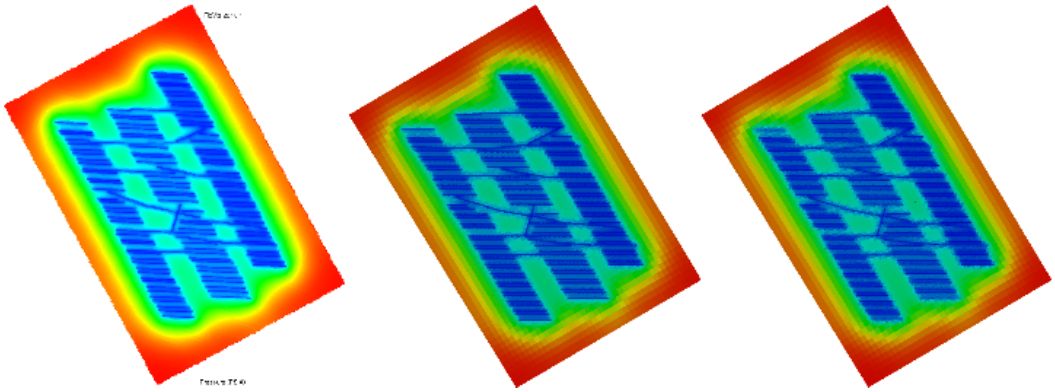

**(a)** **(b)** **(c)**

**Fig. 117 – Pressure comparison between the LGR model (a), PEBI-rectangle model without refinement (b), and PEBI-rectangle model with refinement (c).**

BHP responses in the LGR model, PEBI-rectangle model without refinement, and PEBI-rectangle model with refinement are shown in **Figs. 118** to **121**. However, we do observe an improvement in the results with the fracture refinement during early and late production period. For instance, during the early production period between 0.5 and 0.65 year, the PEBI model without refinement fluctuates more than the PEBI model with refinement (higher during pressure buildup, and lower during pressure drawdown) due to lack of refinement around the fractures. At the later period when BHP is below around 2,100 psi, the PEBI model without refinement overestimates the pressure more than the model with refinement.

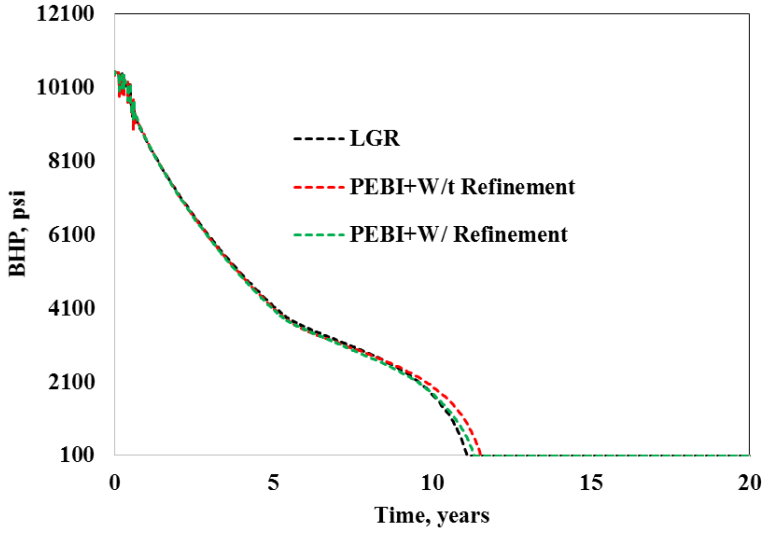


**(a)**

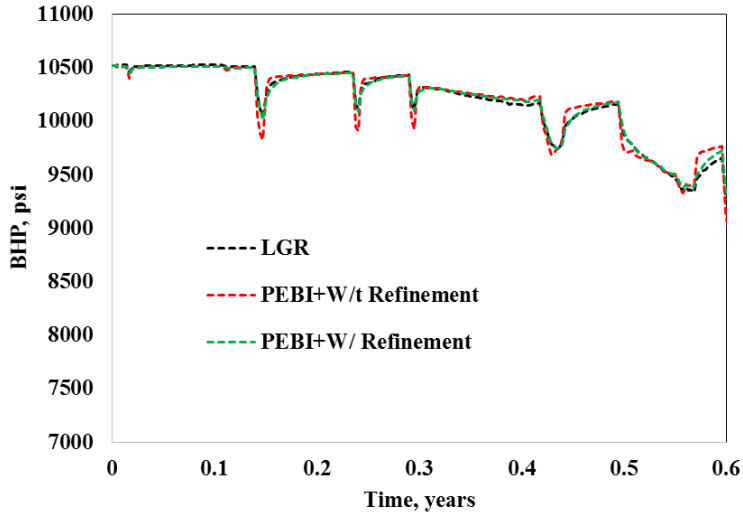


**(b)**

**Fig. 118 – Well #1 pressure comparison between the LGR model, PEBI-rectangle model without refinement, and PEBI-rectangle model with refinement.**

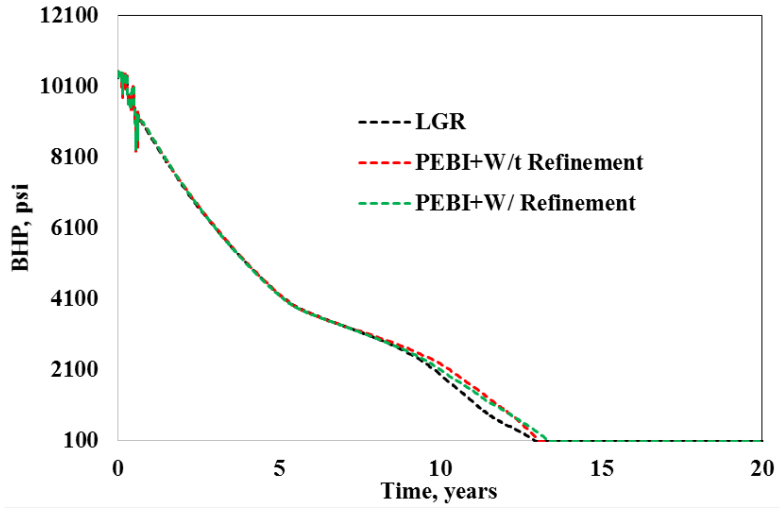


**(a)**

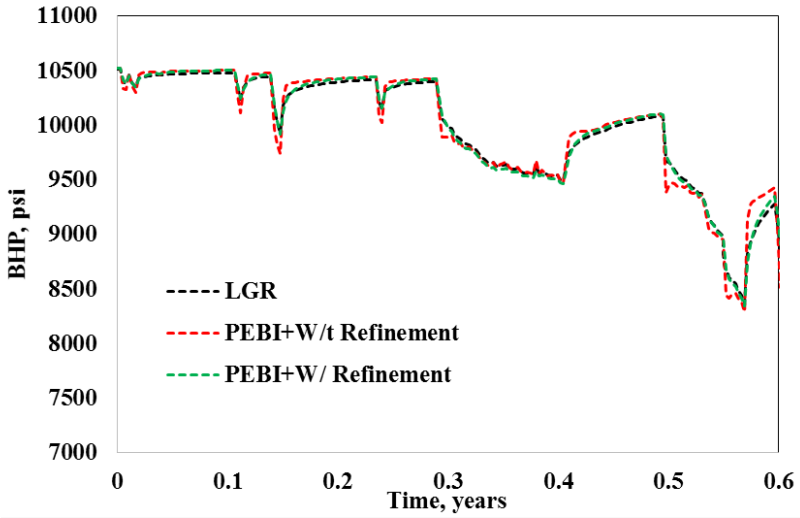


**(b)**

**Fig. 119 – Well #2 pressure comparison between the LGR model, PEBI-rectangle model without refinement, and PEBI-rectangle model with refinement.**

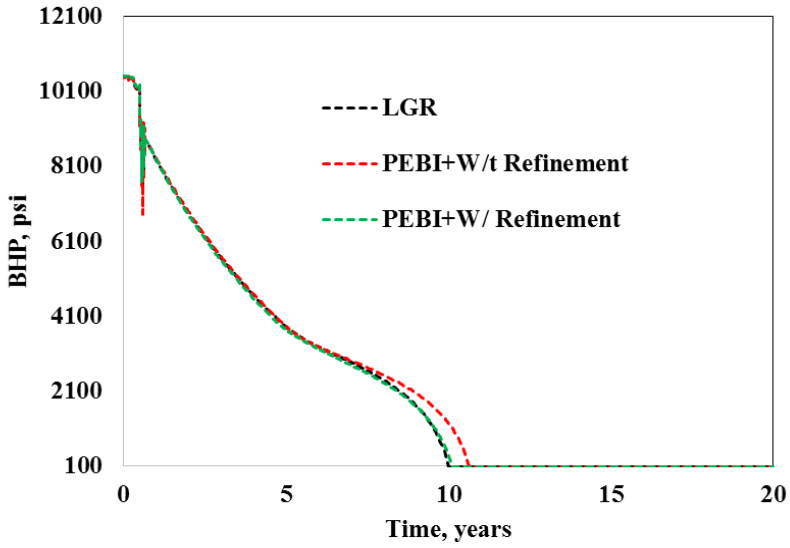


**(a)**

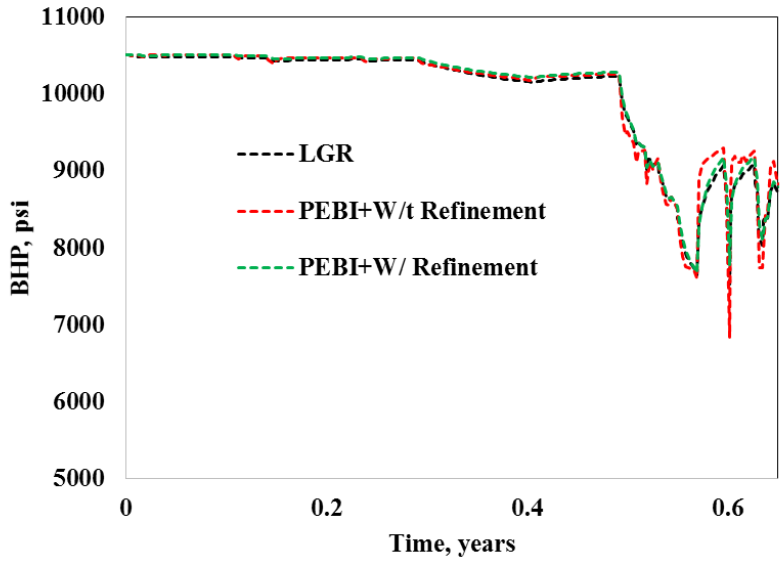


**(b)**

**Fig. 120 – Well #3 pressure comparison between the LGR model, PEBI-rectangle model without refinement, and PEBI-rectangle model with refinement.**

### 6.2.5 Comparison of CPU Performance

In **Fig. 121**, the CPU performance is compared between the LGR model and eight PEBI models from the previous sensitivity studies. Each model is run on a single-core central processing unit (CPU) of a 64-bit desktop computer. During the simulation, all other computer applications are closed to avoid simulator overhead time. The CPU time is scaled according to the LGR model in which the CPU time equals to 1. From left to right, scaled CPU time bars represent the LGR model, four PEBI models with different background densities, two PEBI models with different background types, and the last two PEBI models with different fracture refinement. As shown, the less the number of cells, the better the CPU performance because a linear solver is applied for the black-oil simulator. Furthermore, not too much difference in CPU performance is found between the rectangle and hexagonal background because the number of cells is almost the same. Furthermore, the PEBI model with 155,080 cells yields the best CPU performance even though the accuracy is a little bit compromised due to the lack of enough fracture refinement. Therefore, the PEBI-rectangle hybrid grid without fracture refinement is considered to be the best mesh for both history matching and production prediction.

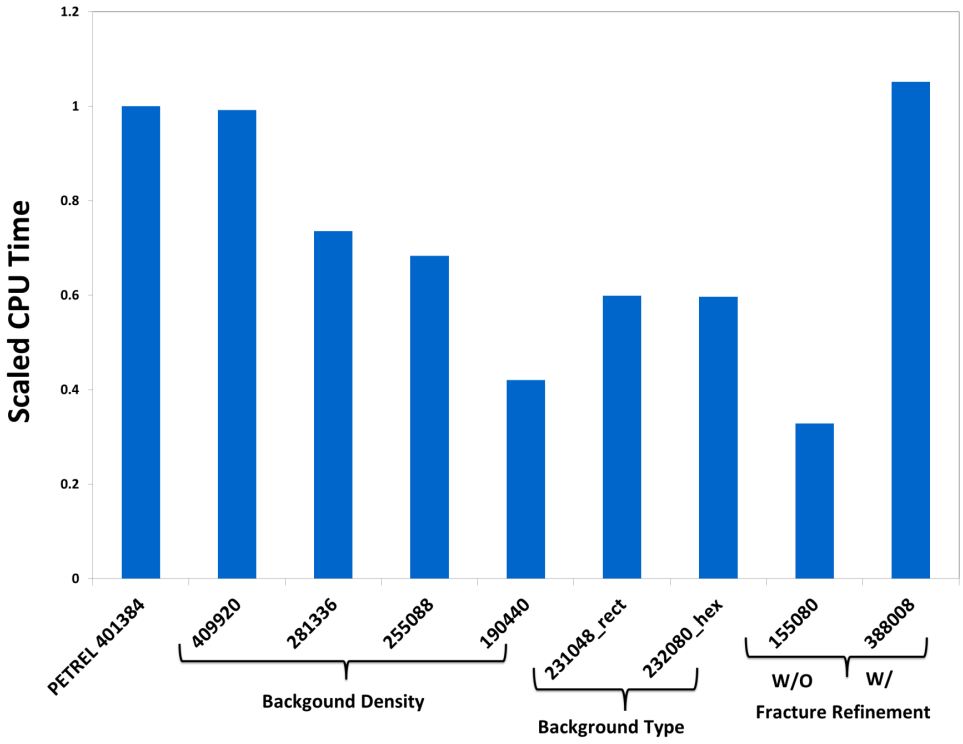


**Fig. 121 – CPU comparison between the LGR model and eight PEBI models.**

### 6.2.6 Sensitivity of Natural Fracture Density

In the previous Eagle Ford field case, natural fractures were not taken into account during fracture characterization, and well production only came from the hydraulic fractures. However, Gale et al. (2014) reviewed 18 shale resource plays and proved the existence of natural fractures in unconventional shale reservoirs. Natural factures might be reactivated during hydraulic fracturing; thus, reservoir fluids from faraway regions might also be stimulated by horizontal wells. In this study, natural fractures are characterized from a seismic covariance map shown in **Fig. 122** in which trajectories of three horizontal wells in addition to 120 hydraulic fractures are plotted.

The grey scale in **Fig. 122** represents the possibilities for the existence of natural fractures. In other words, the lighter the color, the higher the probability for the existence of natural fractures. Based on this assumption, three scenarios of natural fractures are generated, which correspond to 40, 80, and 120 natural fractures.

The developed gridding and discretization algorithms are then applied in **Fig. 123** to generate unstructured PEBI meshes. As expected, the greater the number of fractures, the more cells we have to use to discretize the fractured reservoir domain. The cell number ranges from 228,752 to 826,288 for cases without and with 80 natural fractures, respectively. Moreover, for simplicity, the same properties as applies to hydraulic fractures are assigned for natural fractures. After the reservoir simulation, pressure graphs are summarized as shown in **Fig. 124**.

Note that characterization of natural fractures is extremely important to accurately estimate the stimulated reservoir volume (SRV). With the increase in the number of natural fractures, a significant increase in SRV is observed. The three horizontal wells produce reservoir fluids from distant regions with the help of the opened natural fractures. Furthermore, CPU consumption is approximately 12.9 hours for the model with 80 natural fractures, compared to 2.7 hours for the model without natural fractures. A linear trend is also observed between CPU consumption (simulation time) and the total number of simulation cells; thus, it is important to reduce the cell count whenever possible to achieve the best CPU performance when modeling complex fracture networks.

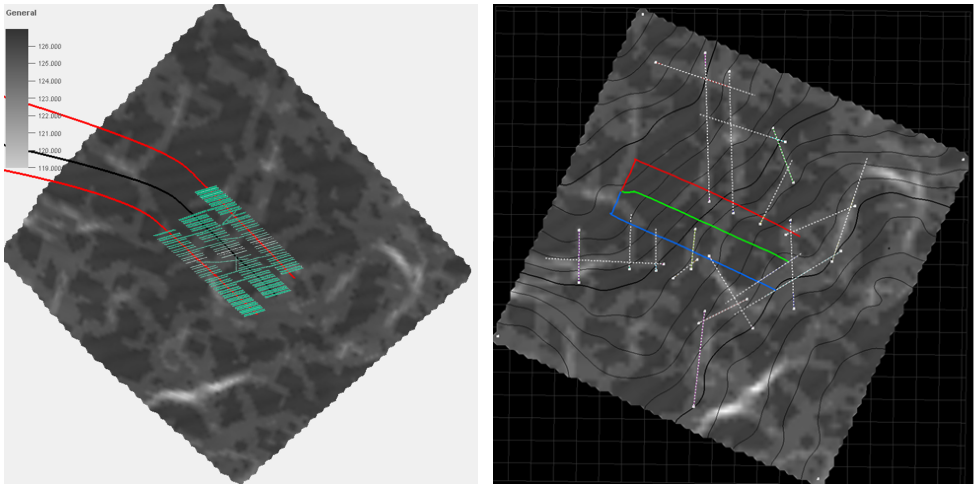


**(a)** **(b)**

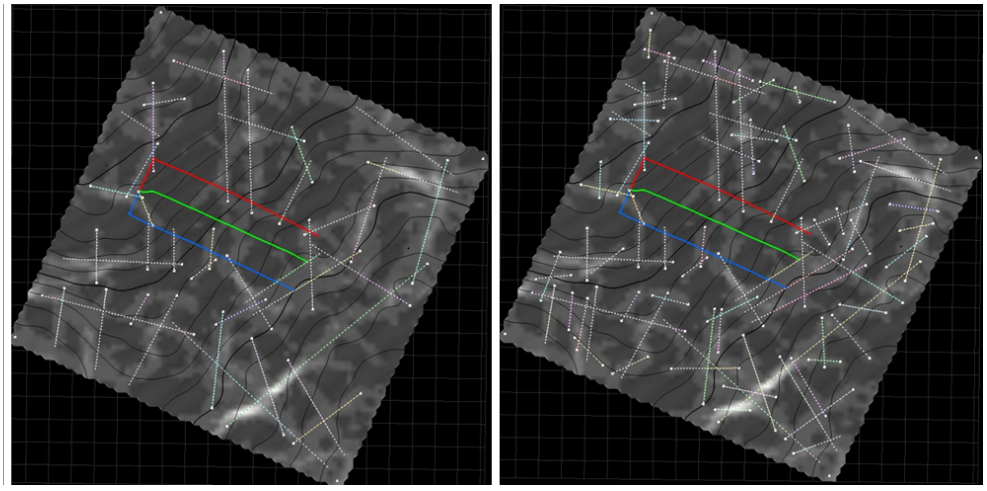

**(c)** **(d)**

**Fig. 122 – The top view of a seismic map for the Eagle Ford field model (a) is shown; and three natural fracture scenarios are generated from the seismic map corresponding to 20 (b), 40 (c), and 80 (d) natural fractures, respectively.**

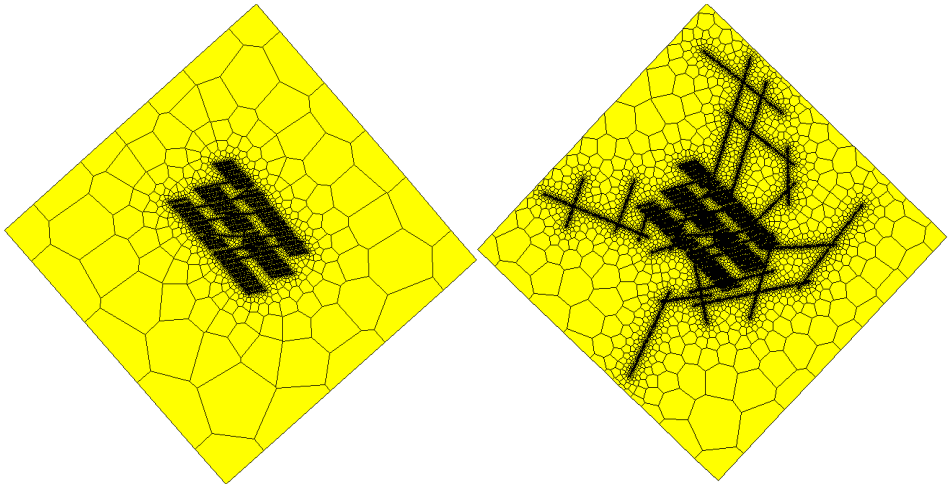

**(a)** **(b)**

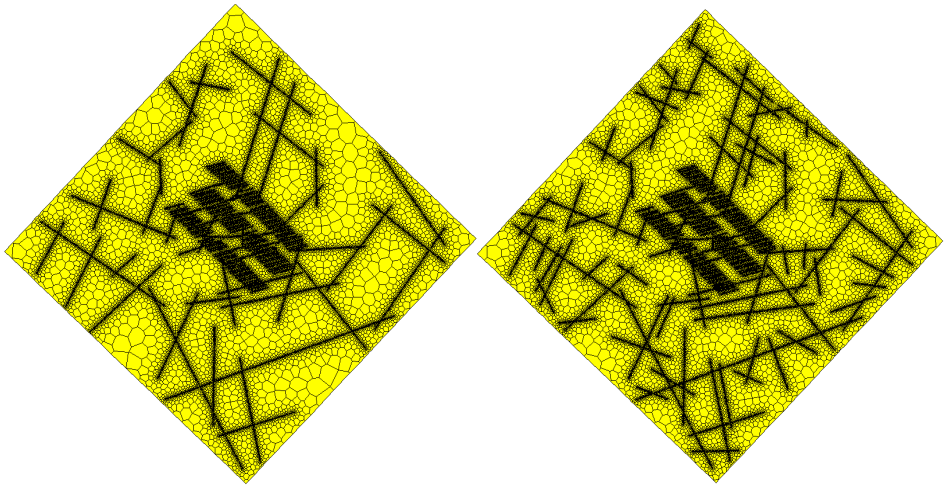

**(c)** **(d)**

**Fig. 123 – 2.5D PEBI grid comparison for different natural fractures (NF) scenarios; no NF with 228,752 cells (a), 20 NFs with 426,576 cells (b), 40 NFs with 636,440 cells (c), and 80 NFs with 826,288 cells (d).**

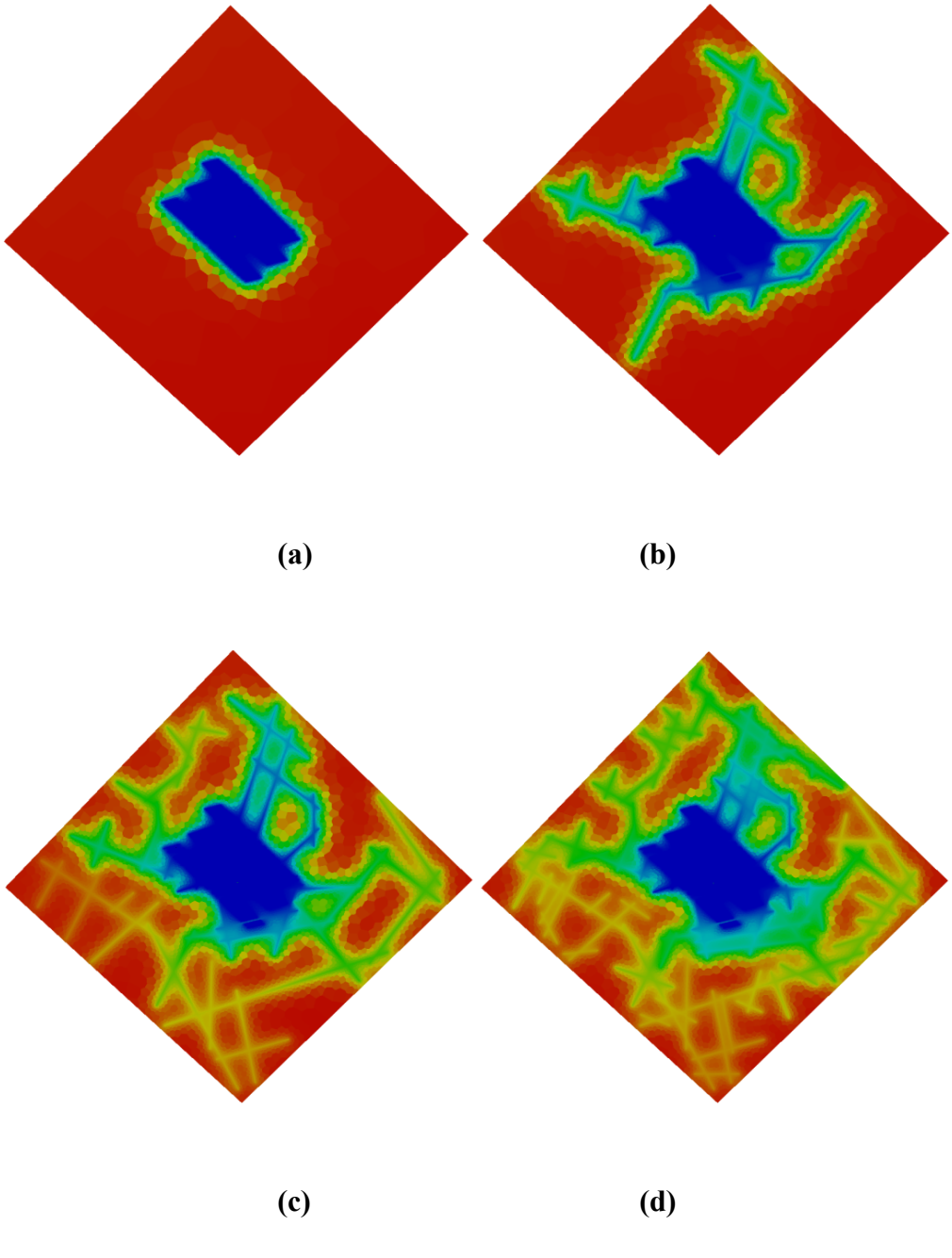

**(a)** **(b)**

**(c)** **(d)**

**Fig. 124 – Pressure graph comparison for different natural fracture scenarios; CPU consumption equals to 2.7 hours for no NF (a), 6.9 hours for 20 NF (b), 10.1 hours for 40 NF (c), and 12.9 hours for 80 NF (d), respectively.**

# CHAPTER VII

# APPLICATION OF EOR TECHNIQUES IN DISCRETE FRACTURE NETWORKS

## *7.1 Model Validation against Tartan Grid Solutions*

In order to validate the proposed fracture discretization scheme for modeling complex fracture networks, a detailed $CO_2$ huff-n-puff comparison between developed fracture discretization approach (unstructured) and conventional discretization approach (structured) will be performed.

| | | | |
|---|---|---|---|
| Matrix Porosity | 0.06 | Reservoir Length, ft. | 5000 |
| Matrix Permeability, md | 1.00E-04 | Reservoir Width, ft. | 1800 |
| Rock Compressibility, psi-1 | 3.00E-06 | Reservoir Height, ft. | 100 |
| Hydraulic Fracture Permeability, md | 100 | Reference Datum Depth, ft. | 12050 |
| Hydraulic Fracture Half Length, ft. | 240 | Reference Pressure, psi | 6000 |
| Hydraulic Fracture Width, ft. | 0.01 | Water Density, lb./ft3 | 62.4 |
| Hydraulic Fracture Porosity | 0.3 | Water Compressibility, psi-1 | 3.36E-06 |
| Reservoir Top Depth, ft. | 12000 | Water Viscosity, cp | 0.2053 |
| Three-phase Kro Calculation Method | STONE 2 | Water Formation Volume Factor | 1.0803 |

**Table 21 – Reservoir and fracture properties.**

**Table 21** to **Table 24** summarize simulation input parameters, which include reservoir and fracture properties, relative permeability curves, EOS input parameters, and binary interaction coefficients. The reservoir consists of 40 vertical and orthogonal hydraulic fractures, which will be discretized by a commercial simulator using conventional tartan grid, as well as by the developed unstructured grid discretization approach.

| Sw | Krw | Krow | Sg | Krg | Krog |
|---|---|---|---|---|---|
| 0.25 | 0 | 1 | 0 | 0 | 1 |
| 0.3 | 0 | 0.656 | 0.05 | 0.001 | 0.826 |
| 0.356 | 0.002 | 0.385 | 0.113 | 0.009 | 0.633 |
| 0.413 | 0.009 | 0.208 | 0.175 | 0.038 | 0.465 |
| 0.469 | 0.021 | 0.1 | 0.238 | 0.084 | 0.323 |
| 0.525 | 0.038 | 0.041 | 0.3 | 0.15 | 0.207 |
| 0.581 | 0.059 | 0.013 | 0.363 | 0.234 | 0.116 |
| 0.625 | 0.079 | 0.005 | 0.375 | 0.255 | 0.103 |
| 0.638 | 0.084 | 0.003 | 0.425 | 0.338 | 0.052 |
| 0.694 | 0.115 | 0 | 0.488 | 0.459 | 0.013 |
| 0.75 | 0.15 | 0 | 0.55 | 0.6 | 0 |
| 1 | 1 | 0 | 0.75 | 0.8 | 0 |

**Table 22 –Oil and gas relative permeability curves.**

**Fig. 125a** is the top view of the unstructured PEBI grid, and **Fig. 125b** is the top view of structured Cartesian grids by the commercial simulator. In total, there are 290,000 cells for the structured grid, and 108,805 cells for the unstructured grid. The

well first produces for 7665 days at a constant bottom-hole pressure of 3000 psi, which is followed by ten huff-n-puff cycles. Each cycle consists of 6 months of $CO_2$ injection at a rate of 2 MMscf/d, followed by a three-month soaking, then one year of production. Total simulated production time is around 15,000 days.

| Component | Molar Weight, g/gmol | Critical Temperature, K | Critical Pressure, psi | Critical Gas Compressibility Factor | Acentric Factor |
|---|---|---|---|---|---|
| $CO_2$ | 44.01 | 304.2 | 1070.16 | 0.2736 | 0.2250 |
| N2-C1 | 16.21 | 189.67 | 665.028 | 0.2898 | 0.0084 |
| C2-C4 | 44.79 | 412.17 | 639.303 | 0.2561 | 0.1481 |
| C5-C7 | 83.46 | 556.92 | 554.043 | 0.2618 | 0.2486 |
| C8-C12 | 120.52 | 667.52 | 456.288 | 0.2488 | 0.3279 |
| C13-C19 | 220.34 | 673.76 | 283.563 | 0.2830 | 0.5672 |
| C20-C30 | 321.52 | 792.4 | 226.086 | 0.2701 | 0.9422 |

**Table 23 – Compositional data for the Peng-Robinson EOS equation.**

**Fig. 126** shows cumulative oil production up to 15,000 days. The black curve from the developed unstructured discretization approach shows a reasonable match with the red curve of the structured grids by the commercial simulator. The blue curve represents the case where there is no huff-n-puff. In addition, a good match of oil production rate between two discretization approaches is illustrated in **Fig. 127**. During each production cycle after $CO_2$ soaking, we observe good matches between

unstructured grids and structured grids. Therefore, the developed discretization scheme is accurate enough to reproduce results of commercial simulators.

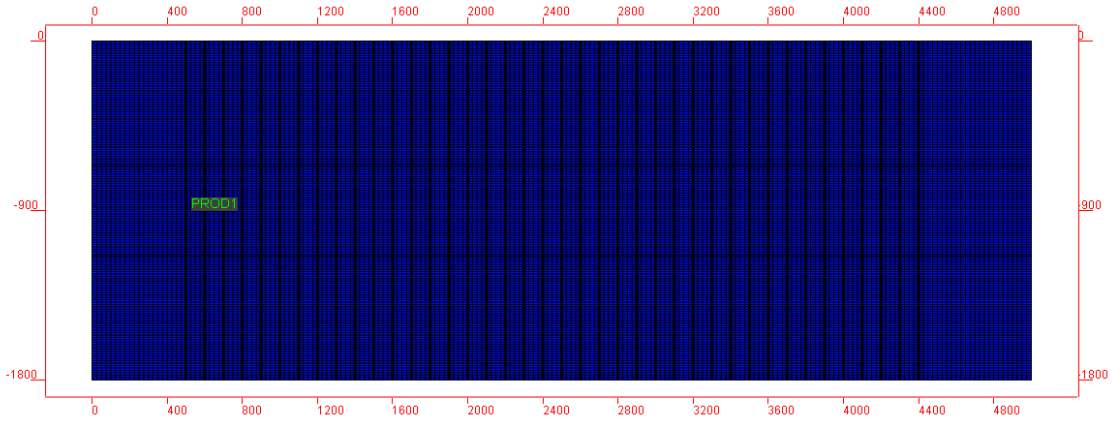


**(a)**

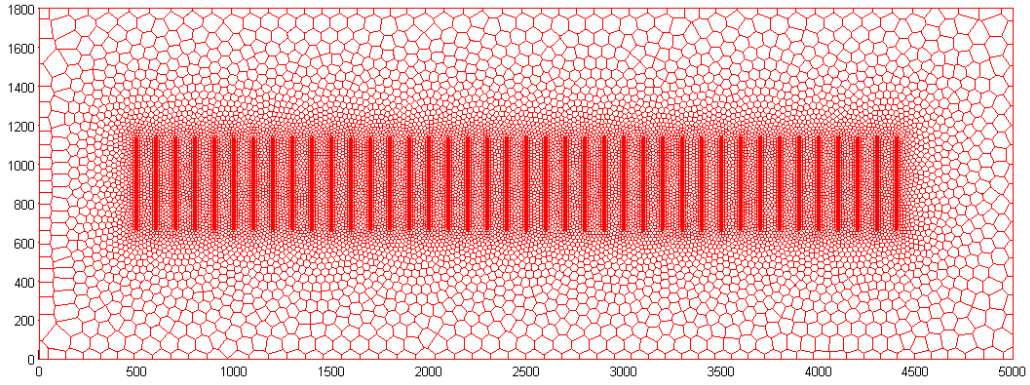


**(b)**

**Fig. 125 – Comparison of top view between structured Cartesian grids with 290,000 cells (a) and unstructured 2.5D PEBI grids with 108,805 cells (b).**

| COMPONENT | $CO_2$ | N2-C1 | C2-C4 | C5-C7 | C8-C12 | C13-C19 |
|---|---|---|---|---|---|---|
| N2-C1 | 0.1013 | | | | | |
| C2-C4 | 0.1317 | 0 | | | | |
| C5-C7 | 0.142 | 0 | 0 | | | |
| C8-C12 | 0.1501 | 0 | 0 | 0 | | |
| C13-C19 | 0.1502 | 0 | 0 | 0 | 0 | |
| C20-C30 | 0.1503 | 0 | 0 | 0 | 0 | 0 |

**Table 24 – Binary interaction coefficient of each component.**

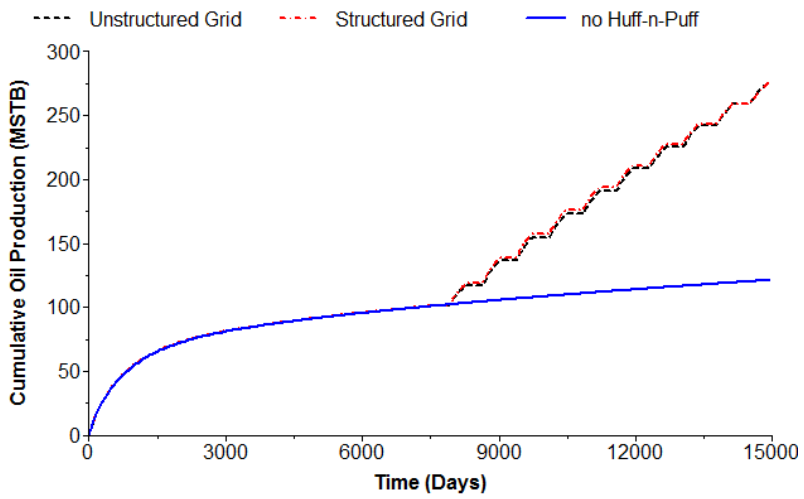


**Fig. 126 – Comparison of cumulative oil production between structured and unstructured discretization approaches.**

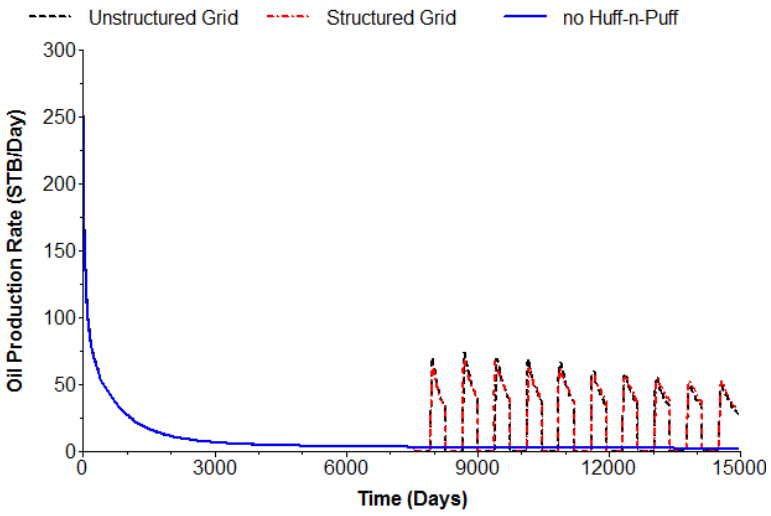


**Fig. 127 – Comparison of oil rate between structured and unstructured discretization approaches.**

*7.2 Comparison between Explicit and Dual Continuum Models*

Dual continuum models can be used to represent simple sugar-cube concepts for naturally fractured reservoirs. For modeling complex fracture networks, dual continuum approaches are able to match production history by tuning parameters such as fracture spacing and fracture permeability without explicitly honoring fracture geometry, resulting in inaccurate pressure calculations and oil recovery. In this section, we will see if we can apply the dual continuum models to represent complex fracture networks or discrete fracture networks (DFNs) during $CO_2$ huff-n-puff. The fractal-based approach was applied to generate stochastically distributed natural fractures. **Table 25** summarizes input parameters for generating three DFN realizations. **Fig. 128** shows reservoir and fracture geometry as well as fracture discretization. Each DFN model consists of 40 vertical hydraulic fractures, and stochastically generated natural fractures.

| | |
|---|---|
| Number of Natural Fracture Sets | 2 |
| Minimum Fracture Length (ft.) | 0.03 * reservoir domain size |
| Fracture Fractal Density | 1.9 |
| Fracture Fractal Length | 1.8 |
| Constant Density Term | 1.5 |
| Scale Ratio | 3 |
| Multifractal Dimension | 2 |

**Table 25 – Input parameters for generating stochastic discrete fracture networks.**

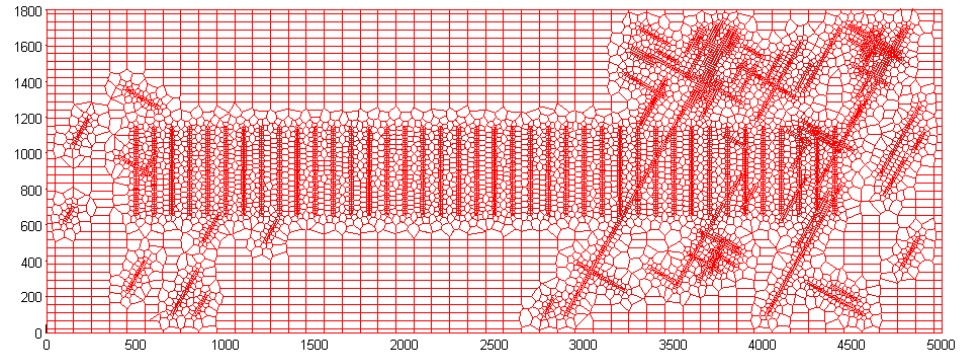


**(a)**

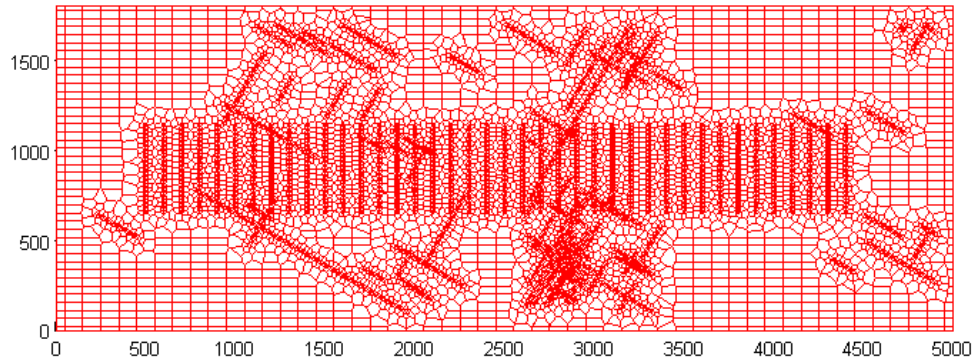


**(b)**

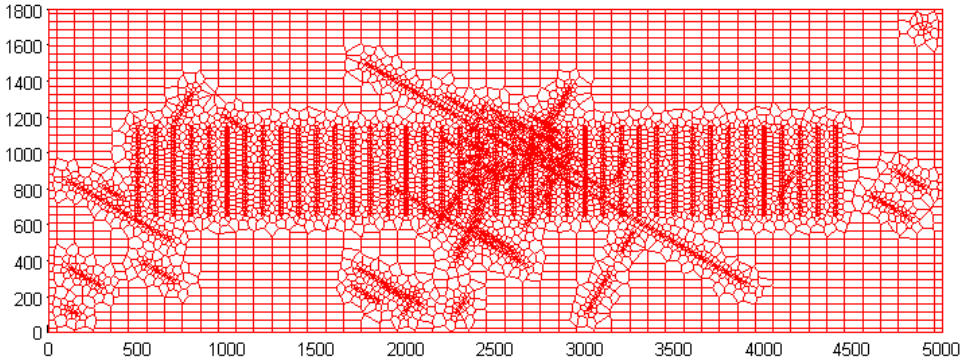


**(c)**

**Fig. 128 – Three random realizations of stochastically generated fractured network. From the top to the bottom, DFN_1 (a), DFN_2 (b), and DFN_3 (c).**

With the same simulator input parameters as seen in the previous section, we performed $CO_2$ huff-n-puff for all three DFN models. **Fig. 129** shows the comparison of cumulative oil production among three DFN models, the previous DFN model without natural fractures (**Fig. 125**), and a corresponding dual porosity model. The blue curve represents cumulative oil production for the DFN model without natural fractures. The pink curve, green curve, red curve represent the three DFN models with natural fractures, respectively.

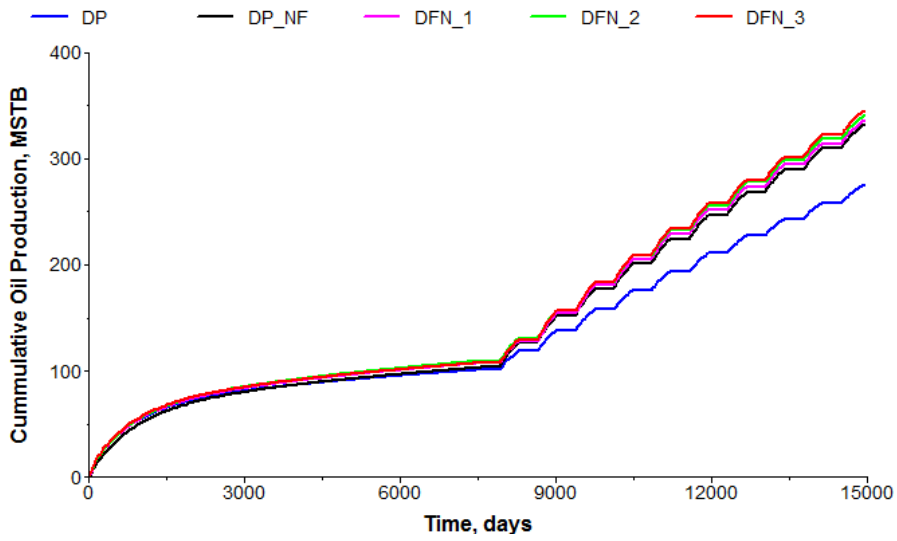


**Fig. 129 – Comparison of cumulative oil production among three DFN models (DFN_1, DFN_2, and DFN_3), the matched dual porosity model (DP_NF), and the DFN model without natural fractures (DP) from Fig. 5.**

The black curve is the matched corresponding dual porosity model with parameters listed in **Table 26**. Before huff-n-puff, the DFN model without natural

fractures show lower cumulative oil production than the other models. However, after the huff-n-puff treatment starts, we see a significant difference between the DFN model without natural fractures (blue curve) and the three DFN models with natural fractures.

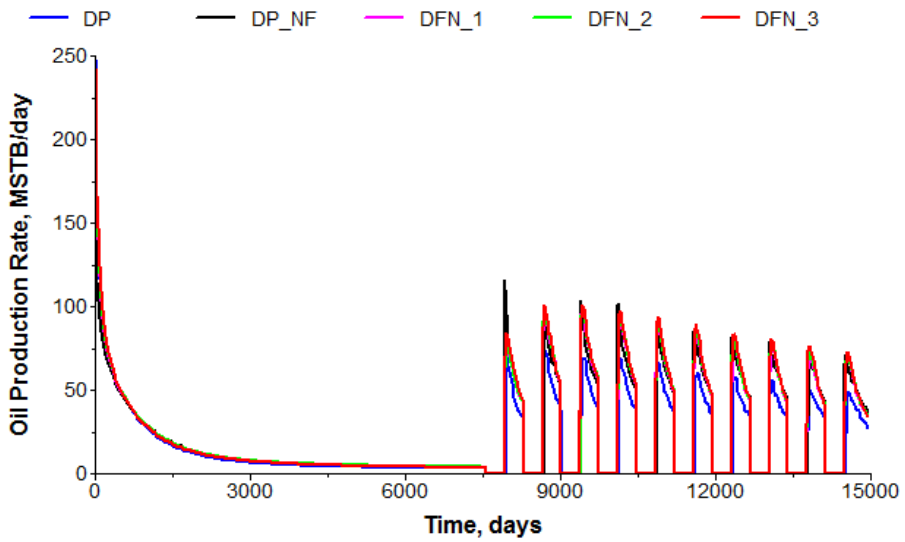


**Fig. 130 – Comparison of oil production rate among three DFN models (DFN_1, DFN_2, and DFN_3), the matched dual porosity model (DP_NF), and the DFN model without natural fractures (DP) from Fig. 5.**

The existence of natural fractures increases the sweep efficiency of the injected $CO_2$. The regions far away from hydraulic fractures can be swept by the injected $CO_2$, and therefore more oil is produced from the DFN model with natural fractures. The three DFN models with natural fractures show very similar cumulative oil production performance, because they were generated with the same input parameters. Besides, by varying natural fracture parameters of the dual porosity model, we found that natural

fracture permeability of 0.00003 mD and fracture porosity of 0.000005 provides a reasonable match between three DFN models and the dual porosity model. Similarly, from oil production rate plot in **Fig. 130**, we reach the same conclusions. We were able to find a corresponding dual porosity model to match production performance of the complicated DFN models for $CO_2$ huff-n-puff studies.

| | | | |
|---|---|---|---|
| Matrix Porosity | 0.06 | Natural Fracture Spacing Lx, ft. | 25 |
| Matrix Permeability, md | 0.0001 | Natural Fracture Spacing Ly, ft. | 25 |
| Rock compressibility | 3.00E-06 | Natural Fracture Spacing Lz, ft. | 20 |
| Hydraulic Fracture permeability, md | 100 | Natural Fracture Porosity | 0.00005 |
| Hydraulic Fracture half length, ft. | 240 | Natural Fracture Permeability Kx, md | 0.00003 |
| Hydraulic Fracture width, ft. | 0.01 | Natural Fracture Permeability Ky, md | 0.00003 |
| Hydraulic Fracture porosity | 0.3 | Natural Fracture Permeability Kz, md | 0.00003 |

**Table 26 – Input parameters for the matched dual porosity model.**

**Fig. 131** illustrates pressure graphs of the three DFN models and the matched dual porosity model. The dual porosity model shows very smooth pressure graph front. However, for all three DFN models, the pressure front depends on how the natural fractures are distributed. We observe pressure depletion in the regions far away from the horizontal wellbore because of the existence of natural fractures. Even though we could roughly match cumulative oil production of the DFN models with the dual porosity

model, the pressure depletion is uniform in **Fig. 131 (d)**, whereas the pressure depletion is very heterogeneous due to natural fracture distribution along the well. Inevitably, this fracture heterogeneity introduces inaccuracy for production forecast.

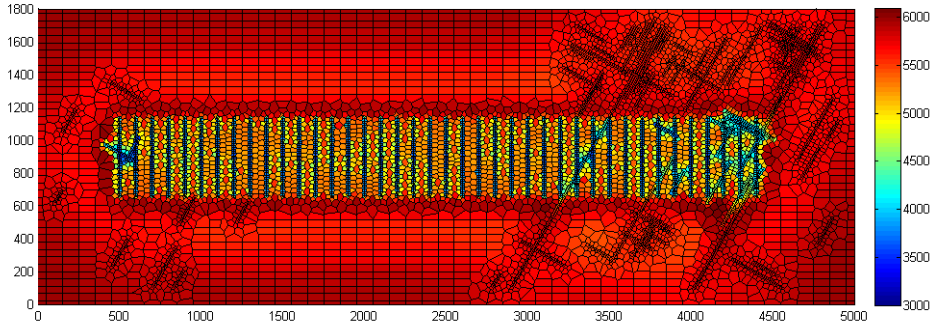


**(a)**

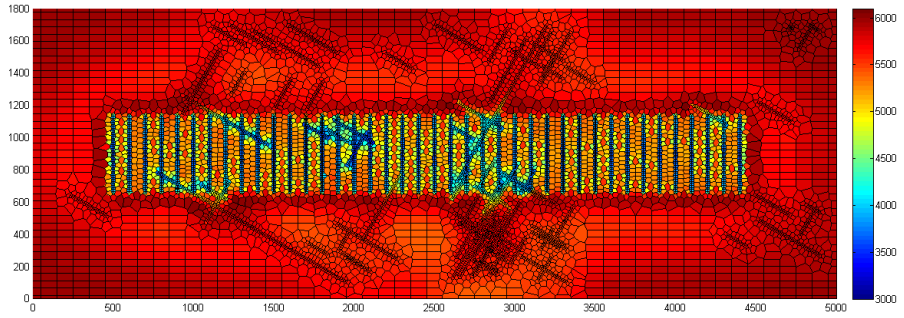


**(b)**

**Fig. 131 – Comparison of pressure graphs among three DFN models and the matched dual porosity model.**

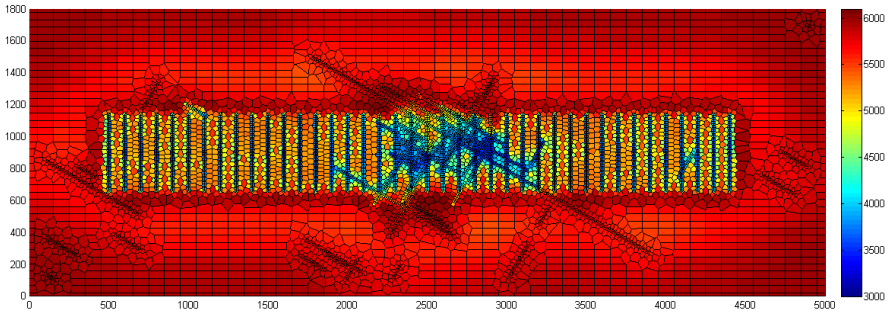


**(c)**

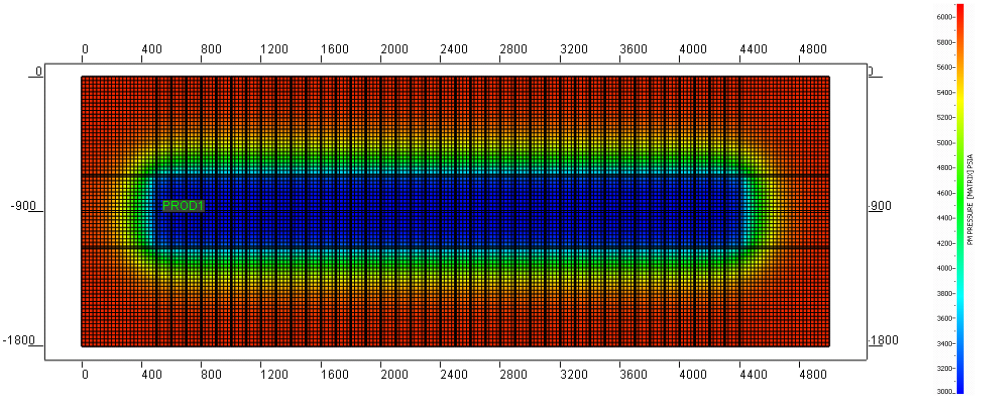


**(d)**

**Fig. 131 – Continued.**

Therefore, when it comes to modeling complex fracture networks, explicit models not only accurately predict production performance, but also capture distribution of injected gas depending on fracture characterization. Dual continuum models tend to smooth the pressure front as shown in **Fig. 131 (a)** to **(d),** thus it is not accurate enough to model complex fracture networks.

*7.3 $CO_2$ Huff-n-Puff for the Microseismic-Constraint Characterization Approach*

In section 7.1, we see an orthogonal hydraulic fracture in a single stage, which is not usually the case in the field. Intersections between induced hydraulic fractures and in-situ natural fractures obviously results in complex fracture networks. The next task is to investigate $CO_2$ huff-n-puff behavior in complex fracture networks.

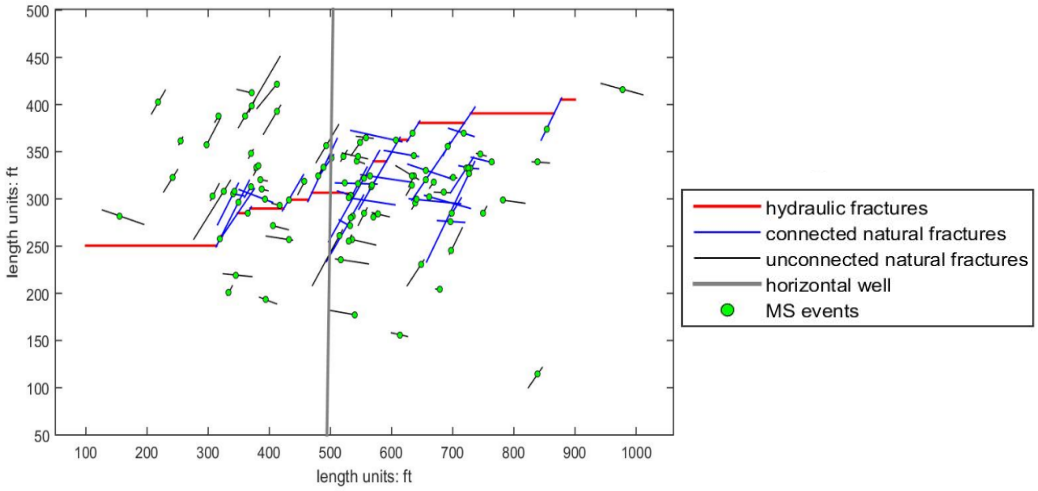


**Fig. 132 – Complex fracture geometry that is generated from microseismic and core data.**

The compositional PVT fluid model is the same as seen in section 7.1. In addition, the fracture geometry of a single stage will be generated based on microseismic and core data using the algorithms by Sotelo Gamboa (2014). In **Fig. 132**, the green dots represent the locations of microseismic events. Red line segments indicate hydraulic fractures, and the blue ones are the connected natural fractures. The solid black line

segment indicates the well trajectory. The remaining black line segments are the disconnected natural fractures, which were assumed to make no contribution to well production. The well produces from both hydraulic fractures and connected natural fractures.

| | | | |
|---|---|---|---|
| Matrix Porosity | 0.06 | Reservoir Length, ft. | 1011 |
| Matrix Permeability, md | 0.0001 | Reservoir Width, ft. | 451 |
| Total Pore Volume, MM bbl. | 1.48 | Reservoir Height, ft. | 300 |
| Hydraulic Fracture Permeability, md | 3984 | Reservoir Top, ft. | 10000 |
| Hydraulic Fracture Width, ft. | 0.01 | Initial Reservoir Pressure, psi | 6000 |
| Hydraulic Fracture Porosity | 0.3 | Initial Oil Saturation | 0.75 |
| $CO_2$ Soaking Length, days | 15 | $CO_2$ Injection Length, days | 30 |
| $CO_2$ Injection Rate, Mscf/day | 500 | Production Length before Huff-n-puff, days | 1000 |

**Table 27 – Reservoir and fracture properties.**

**Table 27** shows input reservoir and fracture properties as well as $CO_2$ injection related parameters. The total pore volume from the simulator shows around 1.48 MM bbl. reservoir barrels of fluids. Considering $CO_2$ is injected for 30 days at a rate of 500 Mscf/day, the total injected $CO_2$ is around 2.4 reservoir pore volumes. **Fig. 133** shows the unstructured mesh after applying the proposed fracture discretization algorithms in section 3.2, which are designed to honor and model complex fracture geometry.

**Fig. 134** to **Fig. 136** show production performance as well as the pressure graph of the complex fracture network. From **Fig. 135**, the changes in oil saturation are below

0.01, which is due to the ultra-low reservoir permeability. Correspondingly, the reservoir pressure in **Fig. 134** depletes significantly and reaches BHP of 3000 psi around the fractures. **Fig. 136** shows comparison of cumulative oil production (COP), oil production rate (QOP) between two cases with and without $CO_2$ huff-n-puff. With $CO_2$ huff-n-puff, a spike increase in oil production rate is observed, which is followed by a steep decline. After soaking, it takes 181 days for the production rate to return to the case without huff-n-puff. Cumulative oil production shows better performance (26.7 M bbl. after huff-n-puff) with an incremental oil around 438.61 STB at the end of 5000 days' production, which represents 1.64 % increase in oil production. The $CO_2$ utilization rate is around 0.56 Mscf/STB.

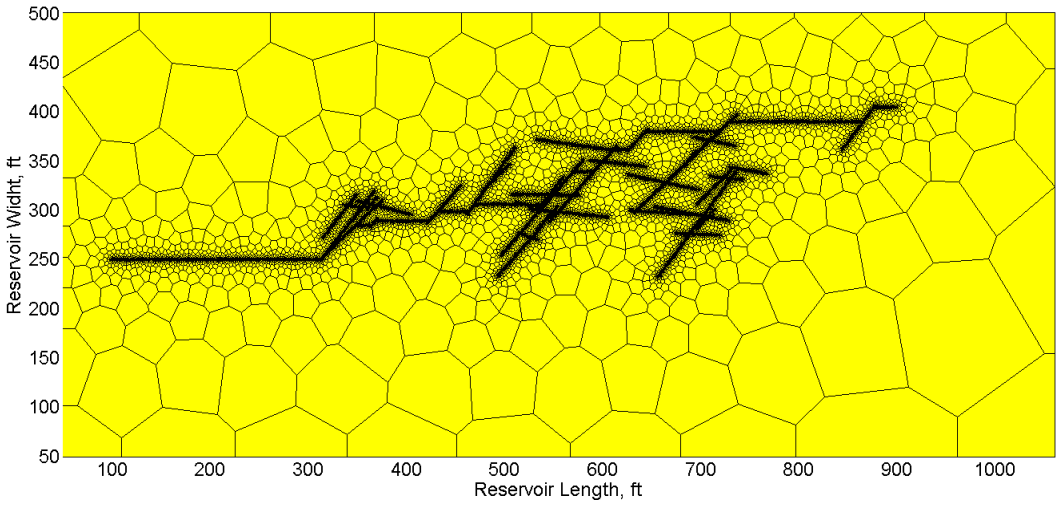


**Fig. 133 – Discretization of the complex fracture network with unstructured PEBI grids.**

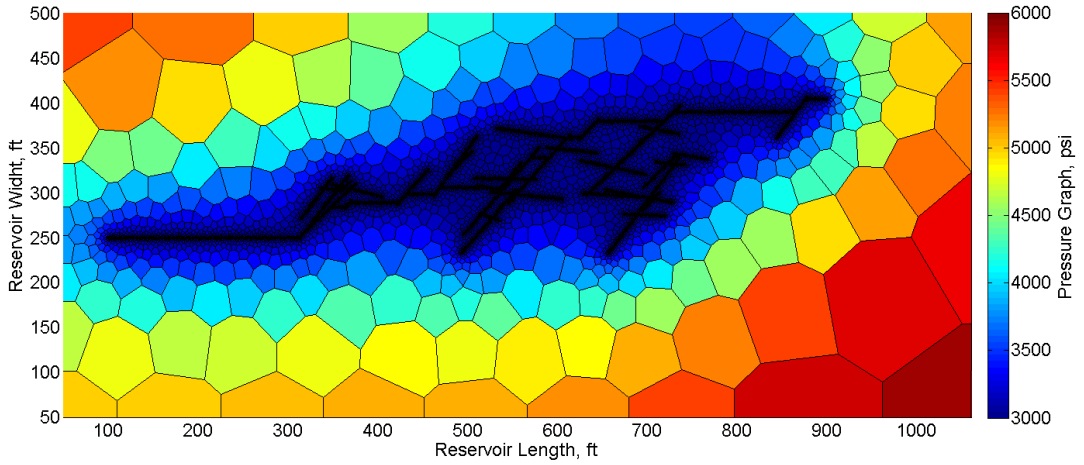


**Fig. 134 – Pressure graph at the end of the huff-n-puff simulation.**

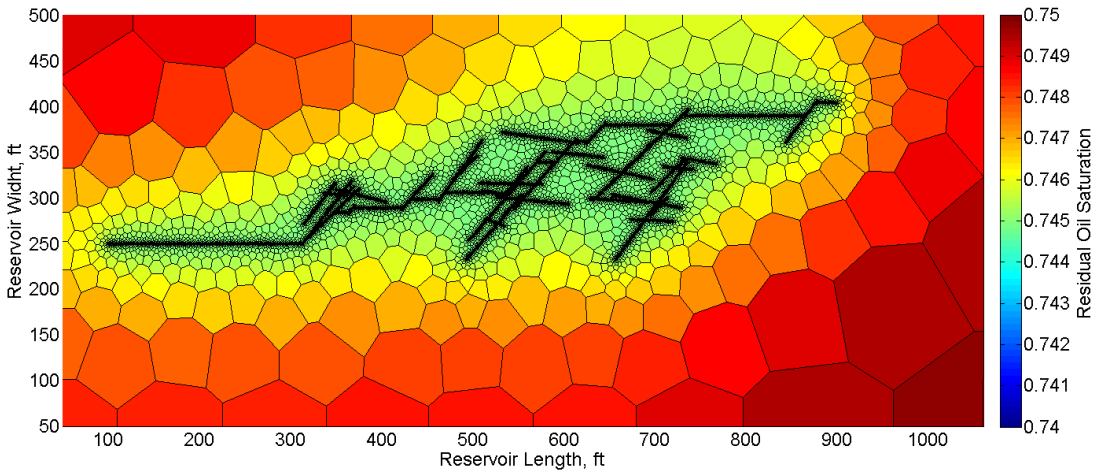


**Fig. 135 – Oil Saturation at the end of the huff-n-puff simulation.**

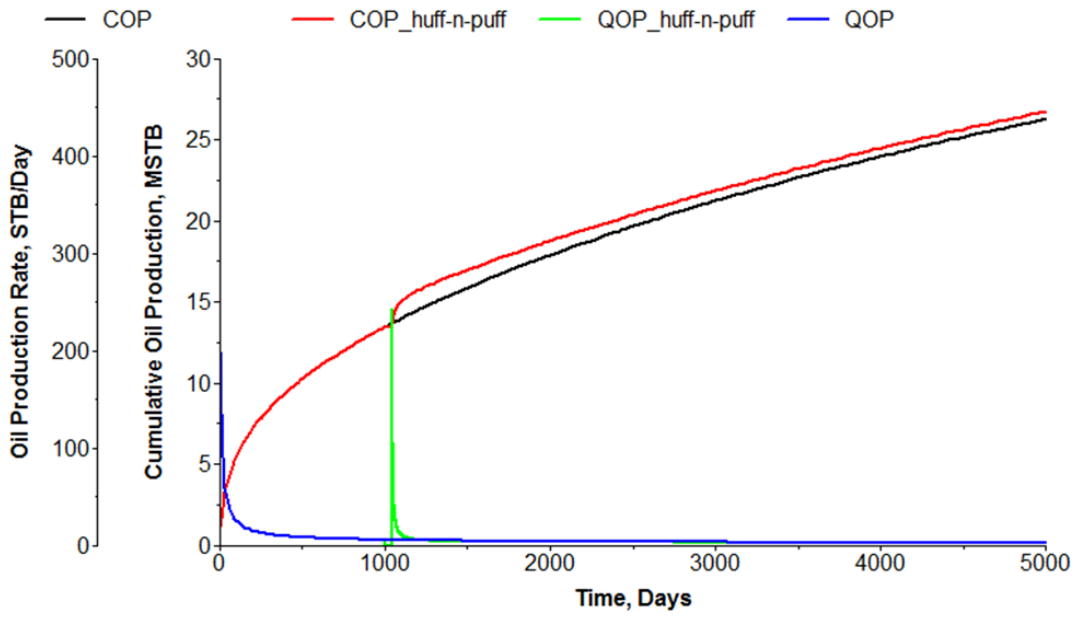


**Fig. 136 – Cumulative oil production and oil production rate at the end of the huff-n-puff simulation.**

# CHAPTER VIII

# CONCLUSIONS AND RECOMMENDATIONS

Throughout this study, two important aspects regarding discrete fracture networks are investigated, which are fracture characterization and fracture simulation. In terms of fracture characterization, both in-situ natural fractures and induced hydraulic fractures are required to be properly understood. Currently, literature publications in petroleum industry tend to over-emphasize the importance of hydraulic fracture propagation, overlooking the other essential input data – in-situ natural fracture distributions.

In order to deal with natural fracture characterization, we demonstrate three available techniques, which are stochastic fractal-based, microseismic-constrained, and outcrop-based. Note that these approaches are not independent from each other. For example, stochastic fractal-based approach is combined with microseismic information in section 4.2 to generate more realistic fracture networks. If there is no available microseismic monitoring data, probably we have to resort to stochastic-based or outcrop-based approaches. In order to properly select natural fracture characterization techniques, it is required to have a good understanding of available data resources.

In terms of modeling hydraulic fractures, this work incooperates a fast proxy model for fracture propagation. We also admit there are more accurate numerical approaches for modeling fracture propagations, such as finite-element method (FEM) and boundary-element method (BEM). However, the fast proxy model probably gives us

a much faster and easier approach to evaluate uncertainties associate with natural fractures, and to perform history matching with production data.

The proposed gridding and discretization approach bridges the gaps between fracture characterization and fracture simulation. Even though PEBI grid is not a new grid system in petroleum industry, it has not been extensively applied to model complex fracture networks due to the lack of detailed implementation algorithms. This work addresses this point in a detailed manner. Moreover, we apply the proposed approaches to model both synthetic and field applications, and provide practical guidance on how to select an approximate mesh to model complex fracture networks from the standpoint views of accuracy and CPU performance.

When it comes to fracture simulation, we present results of nonuniform fracture aperture and well-testing behaviors of complex fracture networks. For simplicity, current researchers consider fracture conductivity as a combined property for fracture permeability and fracture aperture. After the detailed numerical study (**Fig. 64**), we do observe some discrepancy among cases with the same fracture conductivity, even though the differences might be acceptable from the engineering point of view. It is still necessary to obtain a realistic fracture aperture as a model input.

For well-testing responses of complex fracture networks, the history-matched well testing model could provide some clues about the underlying complex fracture networks. A proper understanding of model responses after the sensitivity analysis facilitates us to interpret well production behavior in scenarios where discrete fracture networks are not possible to build. However, we don't recommend run similar well tests

in the field, because of the extremely long build-up period. Instead, pre-fracturing fall-off test (i.e., mini-frac) might be a good alternative to obtain reservoir properties in order to design a hydraulic fracturing job.

Lastly, the potential of $CO_2$ EOR in complex fracture network is investigated. Note that for the field-scale simulation, we don't consider diffusion as the important recovery mechanism. Instead, gas expansion and oil swelling contribute to field-scale production from the matrix into the fractures. To sum up, we have the following main conclusions:

- The proposed integrated workflow can easily conform to available data resources such as core data, microseismic data, outcrop data, and other reservoir and rock properties.
- The gridding and discretization approach with unstructured PEBI grids can handle complex fracture networks with variable length, spacing, aperture, fracture clustering, and low-angle fracture intersections. This approach is proven to be robust, efficient and accurate for both synthetic and field cases.
- Sensitivity analysis of natural fracture related parameters and unstructured gridding related parameters demonstrate that more attention should be paid to fracture characterization. Fracture geometry and properties significantly affect production performance. The higher the natural fracture density, the better the production performance. Natural fracture length and strike show optimal values in order to yield the best production performance.

- The Eagle Ford field example shows that gridding won't affect the accuracy too much. It is feasible to yield a good unstructured grid in terms of accuracy and CPU performance by reducing the background mesh density, replacing the background unstructured grids with structured grids, and removing unnecessary fracture refinement.
- Non-uniform fracture aperture does affect production performance. Numerical simulation of lab-measured nonuniform fracture aperture distributions demonstrates that production is strongly stress-dependent. The same fracture conductivity does not yield the same production performance for complex fracture networks.
- Complex fracture networks could be history-matched with simple well testing models, which provide some guidance regarding information of the complex fracture networks. The matched well testing model doesn't show the classic "V" shape for the pressure derivative plots. The sensitivity analysis of well testing models show that the 'V' shape becomes more obvious with the increase in fracture half-length, lambda and omega, and decrease in reservoir flow capacity.
- $CO_2$ huff-n-puff studies show that complex fracture networks could by matched with dual continuum models in terms of production profiles. Pressure profile maps vary significantly from uniform pressure distribution to nonuniform pressure distribution depending on the natural fracture characterization. Thus, we were able to demonstrate that discrete fracture networks are more appropriate than dual continuum models for $CO_2$ EOR in unconventional shale reservoirs.

In the following, we summarize the areas, which require further work.

- Apply the fracture propagation proxy model for multiple stages of a horizontal well. In the microseismic-constrained approach, only a single stage is studied in this work. Multiple stages are required in order to better history match the production.
- Apply the proposed gridding and discretization approaches to a third dimension with arbitrary dip angles of natural fracture systems. For most cases, hydraulic fractures are vertical. For non-vertical fractures, 3D PEBI grids need to be developed to model natural fracture networks.
- Develop the Virtual Finite Element Method (VEM) for fracture geomechanics. In order to ensure smooth transitions among fracture geomechanics, reservoir simulation, and reservoir geomechanics with PEBI grids, VEM is the most promising approach because shape functions are for arbitrary polyhedrons.
- Investigate well testing behavior for fracture characterization techniques other than outcrop-based approaches. For example, it would be interesting to study well-testing responses of fractal-based and microseismic-based fracture networks.
- Investigate history-matching approaches for complex fracture networks. Even though fracturing design might be more important than history matching of conventional shale reservoirs, the latter will help us better design nearby and infill wells.

# REFERENCES


Abass, H. H., Hedayati, S., Meadows, D. L. 1996. Nonplanar Fracture Propagation from a Horizontal Wellbore: Experimental Study. *SPE Production & Facilities* **11** (3):133–137. SPE-24823-PA. http://dx.doi.org/10.2118/24823-PA.

Al-Kobaisi, M., Ozkan, E., Kazemi, H. 2006. A Hybrid Numerical/Analytical Model of a Finite-Conductivity Vertical Fracture Intercepted by a Horizontal Well. *SPE Reservoir Evaluation & Engineering* **9** (04):345-355. http://dx.doi.org/10.2118/92040-PA.

Beckner, B. L., Chan, H. M., McDonald, A. E. et al. 1991. Simulating Naturally Fractured Reservoirs Using a Subdomain Method. Presented at the SPE Symposium on Reservoir Simulation, Anaheim, California, 17–20 February. http://dx.doi.org/10.2118/21241-MS.

Belytschko, T., Organ, D., Gerlach, C. 2000. Element-Free Galerkin Methods for Dynamic Fracture in Concrete. *Computer Methods in Applied Mechanics and Engineering* **187** (3–4):385–399. http://dx.doi.org/10.1016/S0045-7825(00)80002-X.

Branets, L. V., Ghai, S. S., Lyon, S. L. et al. 2008. Challenges and Technologies in Reservoir Modeling. *Communications in Computational Physics* **6**:23.

Cipolla, C. L., Fitzpatrick, T., Williams, M. J. et al. 2011. Seismic-to-Simulation for Unconventional Reservoir Development. Presented at the SPE Reservoir Characterisation and Simulation Conference and Exhibition, Abu Dhabi, UAE, 9–11 October. http://dx.doi.org/10.2118/146876-MS.

Dean, R. H., Lo, L. L. 1988. Simulations of Naturally Fractured Reservoirs. *SPE Reservoir Engineering* **3** (2):638–648. http://dx.doi.org/10.2118/14110-PA.

Dershowitz, W. S., Pointe, P. R. L., Doe, T. W. 2004. Advances in Discrete Fracture Network Modeling. *Proc.*, U.S. EPA/NGWA Fractured Rock Conference, Portland, Maine, 13–15 September, 882–894. http://clu-in.org/products/siteprof/2004fracrockconf/cdr_pdfs/indexed/group1/882.pdf.

Du, S., Yoshida, N., Liang, B. et al. 2015. Dynamic Modeling of Hydraulic Fractures Using Multisegment Wells. Presented at the SPE Liquids-Rich Basins

Conference–North America, Midland, Texas, USA, 2–3 September. http://dx.doi.org/10.2118/175540-MS.

Fardin, N., Stephansson, O., Jing, L. 2001. The Scale Dependence of Rock Joint Surface Roughness. *International Journal of Rock Mechanics and Mining Sciences* **38** (5):659–669. http://dx.doi.org/10.1016/S1365-1609(01)00028-4.

Fayers, F. J. 1989. Extension of Stone's Method 1 and Conditions for Real Characteristics in Three-Phase Flow. *SPE Reservoir Engineering* **4** (04):437–445. http://dx.doi.org/10.2118/16965-PA.

Ferrill, D. A., McGinnis, R. N., Morris, A. P. et al. 2014. Control of Mechanical Stratigraphy on Bed-Restricted Jointing and Normal Faulting: Eagle Ford Formation, South-Central Texas. *AAPG Bulletin* **98** (11):2477-2506.

Fung, L. S. K., Ding, X. Y., Dogru, A. H. 2014. Unconstrained Voronoi Grids for Densely Spaced Complex Wells in Full-Field Reservoir Simulation. *SPE Journal* **19** (05): 803–815. SPE-163648-PA. http://dx.doi.org/10.2118/163648-PA.

Gale, J. F. W., Laubach, S. E., Olson, J. E. et al. 2014. Natural Fractures in Shale: A Review and New Observations. *AAPG Bulletin* **98** (11):2165–2216. http://dx.doi.org/10.1306/08121413151.

Gamboa, E. S. 2014. *Natural Fracture Characterization by Source Mechanism Estimation and Semi-Stochastic Generation of Discrete Fracture Networks Using Microseismic and Core Data* M.S. Thesis, Texas A&M University, College Station.

Heinemann, Z. E., Brand, C. W., Munka, M. et al. 1991. Modeling Reservoir Geometry with Irregular Grids. *SPE Reservoir Engineering* **9** (02):225–232. http://dx.doi.org/10.2118/18412-PA.

Jiang, J., Younis, R. M. 2015. Numerical Study of Complex Fracture Geometries for Unconventional Gas Reservoirs Using a Discrete Fracture-Matrix Model. *Journal of Natural Gas Science and Engineering* **26**:1174-1186. http://dx.doi.org/10.1016/j.jngse.2015.08.013.

Kappa. 2016. Saphir Software (accessed April 20 2016).

Karimi-Fard, M., Durlofsky, L. J., Aziz, K. 2003. An Efficient Discrete Fracture Model Applicable for General Purpose Reservoir Simulators. Presented at the SPE

Reservoir Simulation Symposium, Houston, Texas, 3-5 February. 79699. http://dx.doi.org/10.2118/79699-ms.

Kazemi, H., Merrill, L. S., Jr., Porterfield, K. L. et al. 1976. Numerical Simulation of Water-Oil Flow in Naturally Fractured Reservoirs. *Society of Petroleum Engineers Journal* **16** (6):317–326. http://dx.doi.org/10.2118/5719-PA.

Kim, T., Putra, E., Schechter, D. 2007. Analyzing Tensleep Natural Fracture Properties Using X-Ray Ct Scanner. *Archives of Mining Sciences* **52** (1):3–20. http://mining.archives.pl/index.php/content/view/342/87/lang,en/.

Kim, T. H., Lee, K. S. 2015. Pressure-Transient Characteristics of Hydraulically Fractured Horizontal Wells in Shale-Gas Reservoirs with Natural- and Rejuvenated-Fracture Networks. *Journal of Canadian Petroleum Technology* **54** (04):245-258. http://dx.doi.org/10.2118/176027-PA.

Kim, T. H., Schechter, D. 2009. Estimation of Fracture Porosity of Naturally Fractured Reservoirs with No Matrix Porosity Using Fractal Discrete Fracture Networks. *SPE Reservoir Evaluation & Engineering* **12** (2):232–242. SPE-110720-PA. http://dx.doi.org/10.2118/110720-PA.

Kuchuk, F., Biryukov, D. 2015. Pressure-Transient Tests and Flow Regimes in Fractured Reservoirs. *SPE Reservoir Evaluation & Engineering* **18** (02):187-204. http://dx.doi.org/10.2118/166296-PA.

Kulatilake, P. H. S. W., Um, J. 1999. Requirements for Accurate Quantification of Self-Affine Roughness Using the Roughness–Length Method. *International Journal of Rock Mechanics and Mining Sciences* **36** (1):5–18. http://dx.doi.org/10.1016/S0148-9062(98)00170-3.

Kappa Reading Room Brochure. 2015. Kappa Unconventional Resources, October 2013, http://www.kappaeng.com/documents/flip/ur-brochure/ (accessed Apri 23 2015).

Li, L., Lee, S. H. 2008. Efficient Field-Scale Simulation of Black Oil in a Naturally Fractured Reservoir through Discrete Fracture Networks and Homogenized Media. *SPE Reservoir Evaluation & Engineering* **11** (4):750–758. http://dx.doi.org/10.2118/103901-PA.

Mirzaei, M., Cipolla, C. L. 2012. A Workflow for Modeling and Simulation of Hydraulic Fractures in Unconventional Gas Reservoirs. Presented at the SPE

Middle East Unconventional Gas Conference and Exhibition, Abu Dhabi, UAE, 23-25 January. 153022. http://dx.doi.org/10.2118/153022-ms.

Moinfar, A., Varavei, A., Sepehrnoori, K. et al. 2013. Development of an Efficient Embedded Discrete Fracture Model for 3d Compositional Reservoir Simulation in Fractured Reservoirs. *SPE Journal* **19** (2):289–303. http://dx.doi.org/10.2118/154246-PA.

Moog, G. 2013. *Advanced Discretization Methods for Flow Simulation Using Unstructured Grids*. PhD, Stanford University, CA.

Muralidharan, V., Chakravarthy, D., Putra, E. et al. 2004. Investigating Fracture Aperture Distributions under Various Stress Conditions Using X-Ray Ct Scanner. Presented at the Canadian International Petroleum Conference, Calgary, Alberta, 8–10 June. PETSOC-2004-230. http://dx.doi.org/10.2118/2004-230.

Muralidharan, V., Schechter, D. S., Chakravarthy, D. et al. 2004. Investigating Fracture Aperture Distributions under Various Stress Conditions Using X-Ray Ct Scanner. Presented at the Canadian International Petroleum Conference, Calgary, Alberta, 8–10 June. http://dx.doi.org/10.2118/2004-230.

Olorode, O. M., Freeman, C. M., Moridis, G. J. et al. 2012. High-Resolution Numerical Modeling of Complex and Irregular Fracture Patterns in Shale Gas and Tight Gas Reservoirs. Presented at the SPE Latin America and Caribbean Petroleum Engineering Conference, Mexico City, Mexico, 16–18 April. http://dx.doi.org/10.2118/152482-ms.

Olson, J. E., Wu, K. 2012. Sequential Vs. Simultaneous Multizone Fracturing in Horizontal Wells: Insights from a Non-Planar, Multifrac Numerical Model. Presented at the SPE Hydraulic Fracturing Technology Conference, The Woodlands, Texas, 6–8 February. http://dx.doi.org/10.2118/152602-MS.

Persson, P.-O., Strang, G. 2004. A Simple Mesh Generator in Matlab. *SIAM review* **46** (2):329–345. http://www.jstor.org/stable/20453511.

Priest, S. D. 1993. *Discontinuity Analysis for Rock Engineering*, first edition. London: Chapman & Hall.

Pruess, K., Oldenburg, C., Moridis, G. 1999. Tough2 User's Guide Version 2. *Lawrence Berkeley National Laboratory*.

Romain, M., Caumon, G., Levy, B. et al. 2011. Building Centroidal Voronoi Tessellations for Flow Simulation in Reservoirs Using Flow Information. Presented at the SPE Reservoir Simulation Symposium, The Woodlands, Texas, USA, 21–23 February. http://dx.doi.org/10.2118/141018-MS.

Rossen, R. H. 1977. Simulation of Naturally Fractured Reservoirs with Semi-Implicit Source Terms. *Society of Petroleum Engineers Journal* **17** (3):201–210. http://dx.doi.org/10.2118/5737-PA.

Robert Schneiders. 2015. Mesh Generation & Grid Generation on the Web, http://www.robertschneiders.de/meshgeneration/meshgeneration.html (accessed 24 April 2015).

Sheng, M., Li, G., Shah, S. N. et al. 2012. Extended Finite Element Modeling of Multi-Scale Flow in Fractured Shale Gas Reservoirs. Presented at the SPE Annual Technical Conference and Exhibition, San Antonio, Texas, 8–10 October. http://dx.doi.org/10.2118/159919-MS.

Sotelo Gamboa, E. 2014. *Natural Fracture Characterization by Source Mechanism Estimation and Semi-Stochastic Generation of Discrete Fracture Networks Using Microseismic and Core Data*. Master of Science, Texas A&M University, College Station (December 2014).

Sun, J., Schechter, D. S. 2015a. Investigating the Effect of Improved Fracture Conductivity on Production Performance of Hydraulic Fractured Wells through Field Case Studies and Numerical Simulations. *Journal of Canadian Petroleum Technology* **54** (06):442–449. SPE-169866-PA.

Sun, J., Schechter, D. S. 2015b. Optimization-Based Unstructured Meshing Algorithms for Simulation of Hydraulically and Naturally Fractured Reservoirs with Variable Distribution of Fracture Aperture, Spacing, Length and Strike. *SPE Reservoir Evaluation & Engineering* **18** (04):463–480. SPE-170703-PA.

Sun, J., Zou, A., Sotelo, E. et al. 2016. Numerical Simulation of Co2 Huff-N-Puff in Complex Fracture Networks of Unconventional Liquid Reservoirs. *Journal of Natural Gas Science and Engineering* **31**:481–492. http://dx.doi.org/10.1016/j.jngse.2016.03.032.

Tamagawa, T., Matsuura, T., Anraku, T. et al. 2002. Construction of Fracture Network Model Using Static and Dynamic Data. Presented at the SPE Annual Technical

Conference and Exhibition, San Antonio, Texas, 29 September–2 October. SPE-77741-MS. http://dx.doi.org/10.2118/77741-MS.

Verma, S., Aziz, K. 1997. A Control Volume Scheme for Flexible Grids in Reservoir Simulation. Presented at the SPE Reservoir Simulation Symposium, Dallas, Texas, 8–11 June. http://dx.doi.org/10.2118/37999-MS.

Vestergaard, H., Olsen, H., Sikandar, A. S. et al. 2008. The Application of Unstructured-Gridding Techniques for Full-Field Simulation of a Giant Carbonate Reservoir Developed with Long Horizontal Wells. *SPE Reservoir Evaluation & Engineering* **11** (06):958–967. SPE-120887-PA. http://dx.doi.org/10.2118/120887-PA.

Wan, T., Sheng, J. 2015. Compositional Modelling of the Diffusion Effect on Eor Process in Fractured Shale-Oil Reservoirs by Gasflooding. *Journal of Canadian Petroleum Technology* **54** (02):107 - 115. http://dx.doi.org/10.2118/2014-1891403-PA.

Wang, Y., Shahvali, M. 2016. Discrete Fracture Modeling Using Centroidal Voronoi Grid for Simulation of Shale Gas Plays with Coupled Nonlinear Physics. *Fuel* **163**:65–73. http://dx.doi.org/10.1016/j.fuel.2015.09.038.

Warpinski, N. R., Branagan, P. T. 1989. Altered-Stress Fracturing. *Journal of Petroleum Technology* **41** (9):990–997. SPE-17533-PA. http://dx.doi.org/10.2118/17533-PA.

Warpinski, N. R., Mayerhofer, M., Agarwal, K. et al. 2013. Hydraulic-Fracture Geomechanics and Microseismic-Source Mechanisms. *SPE Journal* **18** (4): 766–780. SPE-158935-PA. http://dx.doi.org/10.2118/158935-PA.

Warren, J., Root, P. J. 1963. The Behavior of Naturally Fractured Reservoirs. *SPE Journal* **3** (3):245–255. SPE-426-PA. http://dx.doi.org/10.2118/426-PA.

Wu, Y.-S., Pruess, K. 1988. A Multiple-Porosity Method for Simulation of Naturally Fractured Petroleum Reservoirs. *SPE Reservoir Engineering* **3** (1):327–336. http://dx.doi.org/10.2118/15129-PA.

Xue, W., Ghassemi, A. 2009. Poroelastic Analysis of Hydraulic Fracture Propagation. Presented at the 43rd U.S. Rock Mechanics Symposium & 4th U.S. - Canada Rock Mechanics Symposium, Asheville, North Carolina, 28 June–1 July. ARMA-09-129. https://www.onepetro.org/conference-paper/ARMA-09-129.

Yan, B., Killough, J. E., Wang, Y. et al. 2013. Novel Approaches for the Simulation of Unconventional Reservoirs. Presented at the Unconventional Resources Technology Conference, Denver, Colorado, USA, 12–14 August. http://dx.doi.org/10.1190/URTEC2013-131.

Yu, W., Lashgari, H., Sepehrnoori, K. 2014. Simulation Study of Co2 Huff-N-Puff Process in Bakken Tight Oil Reservoirs, 17-18 April. http://dx.doi.org/10.2118/169575-MS.